

EARTHQUAKE FOCAL MECHANISM ANALYSIS OF CENTRAL  
ANATOLIA

A THESIS SUBMITTED TO  
THE GRADUATE SCHOOL OF NATURAL AND APPLIED SCIENCES  
OF  
MIDDLE EAST TECHNICAL UNIVERSITY

BY

SEDA BİRSOY

IN PARTIAL FULFILLMENT OF THE REQUIREMENTS  
FOR  
THE DEGREE OF MASTER OF SCIENCE  
IN  
GEOLOGICAL ENGINEERING

DECEMBER 2018



Approval of the thesis:

**EARTHQUAKE FOCAL MECHANISM ANALYSIS OF CENTRAL ANATOLIA**

submitted by **SEDA BİRSOY** in partial fulfillment of the requirements for the degree of **Master of Science in Geological Engineering Department, Middle East Technical University** by,

Prof. Dr. Halil Kalıpçılar  
Dean, Graduate School of Natural and Applied Science \_\_\_\_\_

Prof. Dr. Erdin Bozkurt  
Head of Department, Geological Engineering \_\_\_\_\_

Assist. Prof. Dr. A. Arda Özacar  
Supervisor, Geological Engineering Dept., METU \_\_\_\_\_

**Examining Committee Members:**

Prof. Dr. Erdin Bozkurt  
Geological Engineering Dept., METU \_\_\_\_\_

Assist. Prof. Dr. A. Arda Özacar  
Geological Engineering Dept., METU \_\_\_\_\_

Prof. Dr. Nuretdin Kaymakçı  
Geological Engineering Dept., METU \_\_\_\_\_

Assoc. Prof. Dr. Gonca Örgülü  
Geophysical Engineering Dept., İstanbul Technical Uni. \_\_\_\_\_

Assoc. Prof. Dr. Zeynep Gülerce  
Civil Engineering Dept., METU \_\_\_\_\_

Date: 10/12/2018

**I hereby declare that all information in this document has been obtained and presented in accordance with academic rules and ethical conduct. I also declare that, as required by these rules and conduct, I have fully cited and referenced all material and results that are not original to this work.**

Name, Last name: Seda Birsoy

Signature :

## **ABSTRACT**

### **EARTHQUAKE FOCAL MECHANISM ANALYSIS OF CENTRAL ANATOLIA**

Birsoy, Seda

M.Sc., Department of Geological Engineering

Supervisor: Assist. Prof. Dr. A. Arda Özacar

December 2018, 181 pages

Anatolian interior is characterized by large lateral and vertical displacements and a complex tectonic history. Especially, Central Anatolia is located between escape tectonics in the east and extensional deformation in the west. The nature of this transition is still under much debate and requires detailed analysis of active tectonic stresses within the region. In this study, regional moment tensor inversion is performed for 29 earthquakes with  $M > 3.5$  recorded between 2013-2015 by a temporary broadband seismic network. Resultant focal mechanisms are later used for stress tensor inversion to map the active stress field. Our focal mechanisms solutions indicate dominantly strike-slip and normal faulting across the region. Stress analysis conducted for sub-regions revealed strike-slip regime along East Anatolian Fault Zone (EAFZ) and across the interior parts of Anatolian plate (North of  $38^\circ$  latitude) where maximum principle stress ( $\sigma_1$ ) rotates clockwise from NW-SE to NE-SW towards east. On the other hand, earthquakes occurring near Adana Basin and İskenderun Gulf where three plates merge, display scattered seismicity and high ( $>35\%$ ) CLVD components associated to tectonic complexity and principal stress directions support a transtensional regime producing simultaneous NE-SW trending left-lateral strike-slip and E-W trending normal faulting.

Keywords: Central Anatolian Fault Zone, focal mechanism, moment tensor inversion,  
stress tensor inversion

## ÖZ

### ORTA ANADOLU'NUN DEPREM ODAK MEKANİZMA ANALİZİ

Birsoy, Seda

Yüksek Lisans, Jeoloji Mühendisliği Bölümü

Tez Yöneticisi: Dr. Öğr. Üy. A. Arda Özacar

Aralık 2018, 181 sayfa

Anadolu'nun iç kısımları, büyük yanal ve düşey yer değiştirmeler ve karmaşık bir tektonik tarihçe ile karakterize edilmiştir. Özellikle Orta Anadolu, doğuda kaçış tektoniği ile batıda gerilme deformasyonu arasında yer almaktadır. Bu geçişin niteliği, hala çok tartışılmakta ve bölgedeki aktif tektonik streslerin ayrıntılı analizini gerektirmektedir. Bu çalışmada, 2013-2015 yılları arasında geçici geniş bantlı sismik ağ ile kaydedilen ve  $M > 3.5$  olan 29 deprem için bölgesel moment tensör ters çözüm yöntemi uygulanmıştır. Elde edilen odak mekanizması çözümleri daha sonra stres tensörü ters çözümünde aktif gerilme alanını haritalamak için kullanılmıştır. Odak mekanizması çözümlerimiz, bölgeye doğrultu atımlı ve normal faylanmaların hakim olduğuna işaret etmektedir. Altbölgeler için yapılan stres analizi, Doğu Anadolu Fay Zonu (DAFZ) boyunca ve maksimum asal gerilmenin ( $\sigma_1$ ) doğuya doğru saat yönünde KB-GD'dan KD-GB'ya döndüğü Anadolu plakasının iç kısımlarında ( $38^\circ$  enleminin kuzeyi) doğrultu atımlı rejiminin etkin olduğunu göstermiştir. Öte yandan, üç tabakanın birleştiği Adana Havzası ve İskenderun Körfezi yakınlarında meydana gelen depremler, dağınık sismisite ve tektonik karmaşıklıkla ilişkili olan yüksek (>% 35) CLVD bileşenleri sunar ve asal gerilme yönleri, KD-GB yönelimli sol yönlü doğrultu atımlı faylanma ve D-B yönelimli normal faylanmayı eş zamanlı üreten bir transformasyonel rejimi desteklemektedir.

Anahtar sözcükler: Orta Anadolu Fay Zonu, odak mekanizma çözümü, moment tensor ters çözümü, gerilme tensörü ters çözümü

To My Family

## ACKNOWLEDGMENTS

First of all, I would like to express my sincere appreciation to my advisor Dr. A. Arda Özacar for his strong belief, constant guidance and precious criticism during the completion of my M.Sc. studies.

I owe a deep sense of gratitude to Bizhan Abgarmi for his valuable suggestions and help, never-ending patience and overwhelming attitude at all stages of my studies. When I met obstacles, I have always felt his support and encouragement. I am actually grateful.

I would like to thank to my colleague Syed Tanvir Shah who helped much at the last stages of my thesis. I am glad to meet him.

I am indebted to Yüksel Proje A.Ş. for allowing me to have my master's degree. I owe immense gratitude to Mr. Mustafa Kemal Akman and Mr. Ali Bayram who encouraged me to begin this study. I also thank to Barış Görbil with whom we shared the road from work to school and also similar experiences.

I would like to express my deepest gratitude to my family who let me chase my dreams from İstanbul all the way to Ankara even though they were scared and I was a little girl. My special thanks are extended to my entire family for their wholeheartedly support, love and patience toward me.

I also owe a great debt of thanks to my one and only sister, Seval. Her existence gave me happiness and comfort during my studies.

I would like to thank to my 'girlz' Sanem Elidemir and Çidem Argunhan Atalay for their precious and joyful friendship, love and patience during this tough journey.

I am truly grateful to my dearest Güneş Şahin. I found my way with her lovely support and precious love during my studies.

Lastly, there is a special person I would like to thank and without him this thesis could not be completed: my beloved Varol Birsoy. I continued and survived with his unwavering support. I am truly grateful for his everlasting faith and all the things that he did to motivate me to complete this study.

Finally, I would like to represent my thanks to everyone who helped me during my studies.

## TABLE OF CONTENTS

ABSTRACT .....	v
ÖZ.....	vii
ACKNOWLEDGMENTS.....	x
TABLE OF CONTENTS .....	xii
LIST OF TABLES .....	xiv
LIST OF FIGURES.....	xv
CHAPTERS	
1. INTRODUCTION .....	1
1.1 Purpose and Scope .....	1
1.2 Study Area .....	2
1.3 Data and Methods of the Study.....	3
1.4 Organization of the Thesis .....	4
2. TECTONIC SETTING .....	5
2.1 Paleotectonic Evolution .....	5
2.1.1 Izmir – Ankara – Erzincan Suture Zone .....	6
2.1.2 Inner Tauride Suture Zone .....	7
2.1.3 Bitlis – Zagros Suture Zone .....	8
2.2 Active Tectonic Setting.....	8
2.2.1 Central Anatolian Fault Zone.....	8
2.2.2 East Anatolian Fault Zone .....	11
2.2.3 Dead Sea Fault Zone .....	13
2.2.4 Tuz Gölü Fault Zone .....	15
2.2.5 Malatya – Ovacık Fault Zone .....	16

2.2.6 Cyprean Arc .....	17
2.3 Seismicity of the Region.....	17
2.3.1 Historical Seismicity.....	17
2.3.2 Instrumental Seismicity .....	23
<b>3. REGIONAL MOMENT TENSOR INVERSION ANALYSES</b>	<b>39</b>
3.1 Methodological Background .....	39
3.1.1 Focal Mechanism.....	39
3.1.2 Seismic Moment Tensor .....	41
3.2 Moment Tensor Inversion.....	48
3.2.1 Methodology.....	49
3.2.2 Data.....	52
3.2.3 Results.....	56
<b>4. STRESS TENSOR ANALYSIS</b>	<b>77</b>
4.1 Stress Tensor Inversion.....	77
4.1.1 Stress Tensor Analysis by Slick Method .....	78
4.1.2 Stress Tensor Analysis by Win-Tensor .....	81
4.2 Determination of Tectonic Domains in the Study Area .....	86
4.2.1 Sub-region 1.....	88
4.2.2 Sub-region 2.....	90
4.1.3 Sub-region 3.....	92
4.1.4 Sub-region 4.....	94
4.1.5 Sub-region 5.....	96
4.1.6 Sub-region 6.....	98
4.1.7 Sub-region 7.....	101
4.1.8 Sub-region 8.....	103
<b>5. DISCUSSION AND CONCLUSION</b>	<b>109</b>
<b>REFERENCES.....</b>	<b>117</b>
<b>APPENDIX A .....</b>	<b>137</b>
<b>APPENDIX B .....</b>	<b>151</b>

## LIST OF TABLES

### TABLES

Table 2. 1 Historical earthquakes of the region. ....	19
Table 3. 1 Tabulated form of global PREM model.....	55
Table 3. 2 Our moment tensor inversion results .....	64
Table 3. 3 The resultant source parameters of 29 earthquakes analyzed in this study. .....	67
Table 3. 4 Types of tectonic regimes. ....	72
Table 3. 5 P, T, SHmax, SHmin axes and stress regimes of our focal mechanism solutions. ....	73
Table 4. 1 Comparison of stress tensor inversion results by Michael's method (1987) in ZMAP and by P-,B-,T-axes and Right Dihedron methods in Win-Tensor for the entire region and the sub-regions.....	106

## LIST OF FIGURES

### FIGURES

Figure 1. 1 Tectonic map of Turkey with active faults; provinces, blocks and major sutures; and relative plate motions according to Eurasian plate .....	2
Figure 1. 2 General view of study area.. .....	3
Figure 2. 1 Topographic map showing faults, sutures, volcanism; and the seismic stations in the study area.. .....	9
Figure 2. 2 Topographic map showing historical events (BC148-AD1899).. .....	18
Figure 2. 3 a) Magnitude vs. time plots of events in the earthquake catalog, b) cumulative number of earthquakes plotted in time.....	24
Figure 2. 4 At the top, local seismicity in the study area. At the bottom, depth (left) and time (right) distribution of earthquakes are shown with histograms....	25
Figure 2. 5 Cumulative moment release as a function of time.....	26
Figure 2. 6 Histogram of the hourly number of events a) all events; b) $M \geq 2.0$ c) $M \geq 2.5$ d) $M \geq 3.0$ .....	29
Figure 2. 7 Quarry contamination detection map for the earthquakes with $M < 3.0$ ..30	
Figure 2. 8 Quarry contamination detection map for the earthquakes with $M \geq 3.0$ . 32	
Figure 2. 9 (a) Cumulative frequency – magnitude distribution (FMD) plot and (b) recurrence time of earthquakes with different magnitudes occurred in the study area. ....	35
Figure 2. 10 Map view of the distribution of focal mechanism solutions for 171 events in the study area. ....	36
Figure 2. 11 Rake based ternary diagram of the focal mechanism catalog with 171 data. ....	38
Figure 2. 12 P- and T- axes orientations of 171 earthquakes occurred in the study area between 1938 – 2017. ....	38
Figure 3. 1 The focal mechanisms and their related fault geometries .....	40
Figure 3. 2 Equivalent body forces in 2D fault geometry.....	42
Figure 3. 3 The force couples showing the components of seismic moment tensor..	43

Figure 3. 4 Force systems, moment tensors and radiation patterns of sources .....	46
Figure 3. 5 Examples of moment tensors and their stereographic focal mechanism plots .....	47
Figure 3. 6 (a) raw and (b) processed three component broadband seismic waveforms of the event 22.02.2014.....	53
Figure 3. 7 Plot of P and S wave velocities of global PREM model .....	54
Figure 3. 8 Moment tensor inversion solution of the event 16.06.2013. ....	57
Figure 3. 9 Comparison of observed and synthetic waveforms for the event 16.06.2013. .....	57
Figure 3. 10 Plot of correlation vs time shift, source position and focal mechanism of the event 16.06.2013. ....	58
Figure 3. 11 Depth correlation plot of the event 16.06.2013. ....	58
Figure 3. 12 Moment tensor inversion solution of the event 22.02.2014. ....	59
Figure 3. 13 Comparison of observed and synthetic waveforms for the event 22.02.2014.....	59
Figure 3. 14 Plot of correlation vs time shift, source position and focal mechanism of the event 22.02.2014. ....	60
Figure 3. 15 Depth correlation plot of the event 22.02.2014. ....	60
Figure 3. 16 Moment tensor inversion solution of the event 26.07.2013. ....	61
Figure 3. 17 Comparison of observed and synthetic waveforms for the event 26.07.2013.....	61
Figure 3. 18 Plot of correlation vs time shift, source position and focal mechanism of the event 26.07.2013. ....	62
Figure 3. 19 Depth correlation plot of the event 26.07.2013. ....	62
Figure 3. 20 Fault plane solutions of 29 focal mechanisms resulted in this study.....	66
Figure 3. 21 Rake-based ternary diagram of our focal mechanism solutions. ....	69
Figure 3. 22 Distribution of P- and T-axes orientations of our solutions.....	69
Figure 3. 23 Maximum horizontal stress $S_{Hmax}$ map of the study area constructed using our focal mechanism solutions.....	70
Figure 3. 24 Rose diagrams of maximum ( $S_{Hmax}$ ) and minimum ( $S_{Hmin}$ ) horizontal stresses of our focal mechanism solutions on equal area display by Win- Tensor.....	71

Figure 3. 25 Faulting type histogram for our 29 resultant focal mechanism solutions .....	72
Figure 3. 26 Earthquakes having multiple focal mechanism solutions in the study area. .....	74
Figure 4. 1 The results of stress tensor inversion by Michael’s method for (a) the resultant (29) and (b) all the focal mechanisms (200) data.....	80
Figure 4. 2 The results of stress tensor inversion by (a) Michael’s method; (b) P-, B-, T-axes method; and (c) Right Dihedron method for the resultant focal mechanisms (29). .....	84
Figure 4. 3 The results of stress tensor inversion by (a) Michael’s method; (b) P-, B-, T-axes method; and (c) Right Dihedron method for the all focal mechanisms (200). .....	85
Figure 4. 4 Sub-regions of the study area. ....	87
Figure 4. 5 Close up map view of Sub-region 1 showing focal mechanism solutions. ....	88
Figure 4. 6 The results of stress tensor inversion by (a) Michael’s method; (b) P-, B-, T-axes method; and (c) Right Dihedron method in Sub-region 1.....	89
Figure 4. 7 Close up map view of Sub-region 2 showing focal mechanism solutions. ....	90
Figure 4. 8 The results of stress tensor inversion by (a) Michael’s method; (b) P-, B-, T-axes method; and (c) Right Dihedron method in Sub-region 2.....	91
Figure 4. 9 Close up map view of Sub-region 3 showing focal mechanism solutions. ....	92
Figure 4. 10 The results of stress tensor inversion by (a) Michael’s method; (b) P-, B- , T-axes method; and (c) Right Dihedron method in Sub-region 3.....	93
Figure 4. 11 Close up map view of Sub-region 4 showing focal mechanism solutions. ....	94
Figure 4. 12 The results of stress tensor inversion by (a) Michael’s method; (b) P-, B- , T-axes method; and (c) Right Dihedron method in Sub-region 4.....	95
Figure 4. 13 Close up map view of Sub-region 5 showing focal mechanism solutions. ....	96

Figure 4. 14 The results of stress tensor inversion by (a) Michael’s method; (b) P-, B-, T-axes method; and (c) Right Dihedron method in Sub-region 5.....	97
Figure 4. 15 Close up map view of Sub-region 6 showing focal mechanism solutions. ....	99
Figure 4. 16 The results of stress tensor inversion by (a) Michael’s method; (b) P-, B-, T-axes method; and (c) Right Dihedron method in Sub-region 6.....	100
Figure 4. 17 Close up map view of Sub-region 7 showing focal mechanism solutions. ....	101
Figure 4. 18 The results of stress tensor inversion by (a) Michael’s method; (b) P-, B-, T-axes method; and (c) Right Dihedron method in Sub-region 7.....	102
Figure 4. 19 Close up map view of Sub-region 8 showing focal mechanism solutions. ....	104
Figure 4. 20 The results of stress tensor inversion by (a) Michael’s method; (b) P-, B-, T-axes method; and (c) Right Dihedron method in Sub-region 8.....	105
Figure 5. 1 Rake-based ternary diagram of all the focal mechanism solutions (200) in the study area.....	109
Figure 5. 2 Distribution of P- and T-axes orientations of all the focal mechanism solutions (200).....	110
Figure 5. 3 Faulting type histogram for the entire data set. ....	111
Figure 5. 4 Stress map of the study area based on maximum horizontal stress axes ( $S_{Hmax}$ ) of focal mechanism solutions of (a) individual focal mechanisms of World Stress Map (WSM) database (b) entire data (200) in the study area .....	112
Figure 5. 5 Rose diagrams of maximum ( $S_{Hmax}$ ) and minimum ( $S_{Hmin}$ ) horizontal stresses of entire focal mechanism solutions (200) by equal area display in Win-Tensor .....	113
Figure 5. 6 Simplified map for the results of horizontal projections of principle stresses for the sub-regions by Right Dihedron method.....	114

# CHAPTER 1

## INTRODUCTION

### 1.1 Purpose and Scope

Central Anatolia is shaped by a series of decisive faults and fault systems and characterized by young volcanism. It is one of the most tectonically active regions of the world where damaging earthquakes can threaten several highly populated cities such as Adana, Konya, Gaziantep, Mersin also including Akkuyu nuclear power plant site. Although, the active tectonic structures in the area deserve upmost attention, they are under much debate due to merge of complex tectonic processes and presences of rather limited seismic data. Recently, a temporary seismic deployment including over 70 broadband stations provided a unique opportunity to study the nature of earthquakes occurring in the region.

In this study, new broadband data which samples the area more densely will be used to determine focal mechanism solutions of earthquakes with  $M > 3.5$  recorded between 2013 and 2015. This will increase the number of available focal mechanism solutions for the region and provide sufficient data to conduct stress tensor inversions in the scope of this thesis which will give more insight on the present tectonic stress field controlling the Central Anatolia (Figure 1.1).

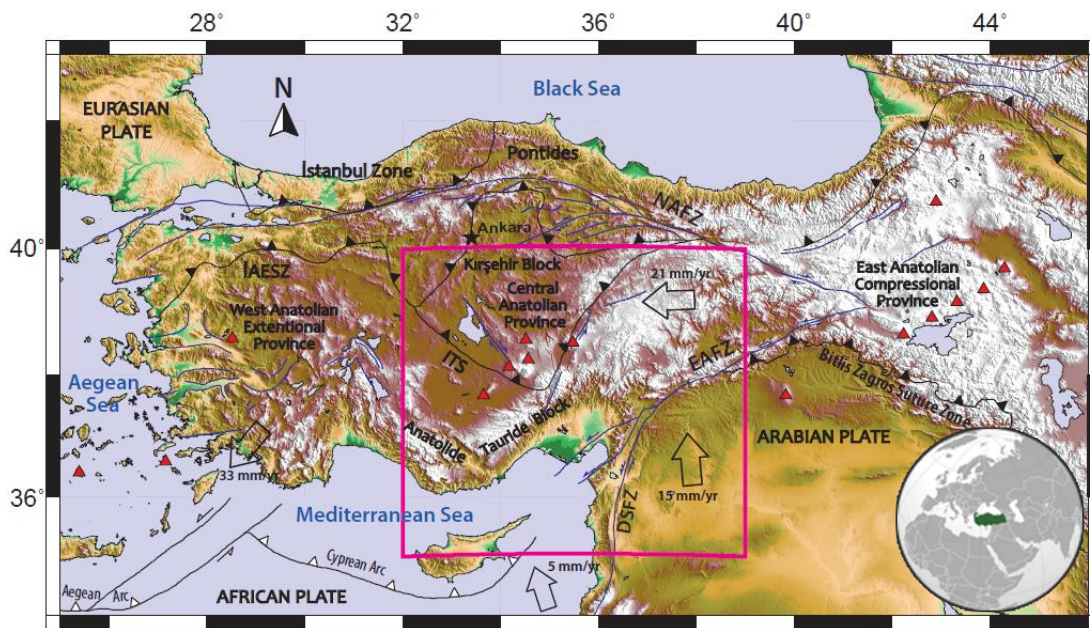


**Figure 1. 1** Generalized tectonic map of Turkey including neotectonic structures and provinces (from Bozkurt, 2001), major sutures (from Okay and Tüysüz, 1999); and relative plate motions respect to Eurasian plate (from Reilinger et al., 2006). Black lines with black triangles represent suture zones; black lines with white triangles are trenches; purple lines are active faults. Red triangles indicate Holocene volcanoes. The study area is outlined by pink box. DSFZ: Dead Sea Fault Zone, EAFZ: East Anatolian Fault Zone, IAESZ: Izmir-Ankara-Erzincan Suture Zone, ITS: Inner Tauride Suture Zone, NAFZ: North Anatolian Fault Zone.

## 1.2 Study Area

The study area is located in Central Anatolia region within the latitudes between 35°N and 40°N and longitudes between 32°E and 39°E. The area lies in the junction of African, Arabian and Anatolian plates which results in a complex tectonic evolution including ongoing tectonic escape and subduction. The study area contains 19 cities which have approximately 30% of the population of Republic of Turkey according to the Turkish Statistical Institute (2016). Note that part of the capital city Ankara is also located on the northwestern edge of the study area (Figure 1.2).

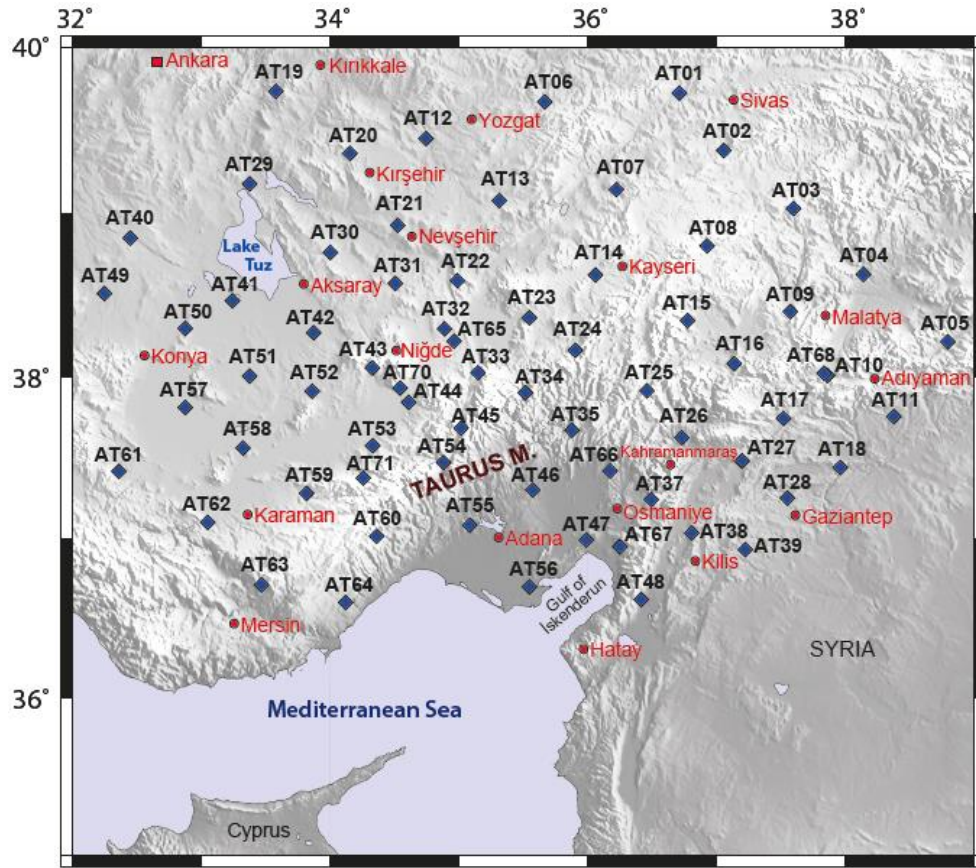


**Figure 1. 2** Topographic map of the study area. CD-CAT Project broadband seismic stations are indicated by blue diamonds. Cities are written in red.

### 1.3 Data and Methods of the Study

Parameters of earthquakes occurred in the study area are collected from Kandilli Observatory and Earthquake Research Institute (KOERI), United States Geological Survey (USGS) and Incorporated Research Institutions for Seismology (IRIS). Broadband seismic data recorded in the study area are gathered from temporarily deployed passive seismic network in the scope of the Continental Dynamics / Central Anatolian Tectonics: Surface to mantle dynamics during collision to escape (CDCAT) project. Waveform records taken from CDCAT network are converted from velocity – time domain to displacement – time using the Seismic Analysis Code (SAC) program (Goldstein et al., 2003). The regional moment tensor inversions of the waveforms are

conducted by using the software ISOLA-GUI (Zahradnik and Sokos, 2016). Later, stress tensors inversions are carried out using Michael (1984) approach in ZMAP program (Wiemer, 2001) and using Win-Tensor program of Delvaux and Sperner (2003) separately which allowed us to compare results and investigate the accuracy of the methods.

#### **1.4 Organization of the Thesis**

This thesis is divided into 5 chapters. After introduction part, thesis continues with Chapter 2 which is the tectonic setting of the region and gives information about the geology, major tectonic structures and seismicity of the study area. Chapter 3 presents the moment tensor inversion analysis method in detail. Chapter 4 deals with the stress tensor inversions applied using focal mechanism solutions. In Chapter 5, all the results of the analyses in this thesis are compiled and discussed.

## CHAPTER 2

### TECTONIC SETTING

#### 2.1 Palaeotectonic Evolution

The present-day Anatolia is located in the intersection area of Eurasian, African and Arabian plates within the Alpine-Himalayan mountain belt. In the past, the region was lying between two mega-continents called Laurasia (Northern Pangea) and Gondwana (Southern Pangea) where rifting led to the formation of two Tethyan oceans known as Paleotethys and Neotethys (Şengör, 1979a; 1987; Şengör and Yılmaz, 1981; Okay and Tüysüz, 1999; Stampfli, 2000; Bozkurt and Mittwede, 2001). During Alpine orogeny, several branches of Tethyan oceanic basins closed and several small-scale continental nappes are accreted. Thus, the landmass of Anatolia is made up of highly deformed, metamorphosed and non-metamorphosed lithospheric fragments distinguished by suture zones and/or metamorphic belts (Şengör and Yılmaz, 1981; Okay and Tüysüz, 1999; Pourteau et al., 2010; Lefebvre, 2011). In the region, the northern branch of Neotethyan ocean was sutured through Late Paleocene – Late Burdigalian forming the İzmir – Ankara – Erzincan and Inner Tauride suture zones and the southern branch where northward subducting Arabian plate collided with Eurasian plate was closed during the late Middle Miocene along the Bitlis-Zagros suture (Yılmaz, 1993; Elmas, 1996a; Yılmaz and Yıldırım, 1996; Bozkurt and Mittwede, 2001). Considering the effect of paleo-structures on forming the present day tectonics setting, the positions of these suture zones across Turkey is shown in Figure 1.1.

### **2.1.1 Izmir – Ankara – Erzincan Suture Zone**

İzmir – Ankara – Erzincan suture zone is a 2000 km long ophiolitic belt boundary trending east-west and thrusting toward southern direction over the Anatolides and Taurides. According to Şengör and Yılmaz (1981), İzmir – Ankara – Erzincan suture is separating Turkey into two parts as the Pontides in the north and the Tauride-Anatolide platform in the south. In the Pontides, Sakarya Block exposes a wide area which comprises of a mixture of Precambrian to Paleozoic crystalline basement, late Triassic blueschists and eclogites, and Jurassic to Eocene non-metamorphic sedimentary cover units (Tekeli, 1981; Okay and Monié, 1997; Pourteau et al., 2010).

The Anatolide-Tauride Block occupies in the western and southern parts of Turkey and has two divisions as Taurides and Anatolides by the Tertiary suture in the southeast Turkey from Arabian plate (Robertson et al., 2006). The Tauride Mountains were originated from the fragments of Gondwana continent since Triassic time; whereas the Anatolian terrane was emanated by Eurasian continent (Şengör and Yılmaz, 1981; Özgül, 1984). The Taurides are comprised of the non-metamorphic sedimentary units including large platform carbonates (Özgül, 1984; van Hinsbergen et al., 2016); and the Anatolides represent metamorphic rocks and exhumed massifs such as Kırşehir Block, Tavşanlı zone, Afyon zone, Menderes massif in Turkey (Okay, 1984; Pourteau et al., 2010).

The Kırşehir Block is located in the northeast part of the Central Anatolia with its currently triangular form and also known as the Central Anatolian Crystalline Complex (Göncüoğlu et al., 1991; Lefebvre, 2011). Some researchers interpreted that the high temperature condition and the granitoid intrusions of the Kırşehir Block evolved because of lithospheric delamination or slab breakoff (van Hinsbergen et al., 2016; and references therein). Mafic and ultramafic bodies extending across the Kırşehir Block are considered as the remnants of large ophiolitic slab (Yalınız et al., 1996; Okay and Tüysüz, 1999).

### 2.1.2 Inner Tauride Suture Zone

According to previous studies, the northern branches of Neotethyan ocean were closed at multiple stages along the Izmir – Ankara – Erzincan suture and the Inner Tauride suture (Şengör and Yılmaz, 1981; Görür et al., 1984; Dilek et al., 1999; Okay and Tüysüz, 1999; Bozkurt and Mittwede, 2001). Since the Anatolide – Tauride Block and the Kırşehir Block are separated from each other by Cenozoic – Quaternary sedimentary basins rather than an ophiolitic belt, some researchers questioned the existence of Inner Tauride ocean branch (Yalınız et al., 1996; references therein).

HP-LT metamorphism along the passive continental margin of Anatolides is thought to be a witness to the Inner Tauride suture between Kırşehir Block and the Anatolide-Tauride Block. According to Pourteau et al. (2010); there are some subjects supporting the Inner Tauride ocean: (1) Southeastern and southwestern parts of Kırşehir Block are composed of Cenozoic – Quaternary sedimentary basins which are referred to arc-related events and southern margins of these basins known as Ulukışla basin, shows subduction-related geochemical properties (Görür et al., 1984). (2) Southwestern margin of Kırşehir Block is composed of Late Cretaceous calc-alkaline granitoids indicating subduction-related environment and a member of volcanic-arc granitoids group. Also, Central Anatolian intrusive rocks are grouped as syn- to postcollisional triggered granitoids rather than the collisional interval between the Kırşehir Block and the Pontides (Akıman et al, 1993). (3) Close metamorphic sole ages (between 90 – 100 Ma) of Lycian, Kütahya and Tauride ophiolites denote that they are parts of same oceanic basin. However, some disjointed ophiolites unlike Lycian, Kütahya and Tauride ophiolites are seen at the upper parts of the Kırşehir Block. Therefore, it is suggested that the Anatolide-Tauride Block and Kırşehir Block were originated from different sources. Anatolide-Tauride ophiolites are thought to be derived from the oceanic branch between Kırşehir Block and Anatolide-Tauride Block while Central Anatolian ophiolites are the parts of northern Ankara – Erzincan Zone (Şengör and Yılmaz, 1981).

### **2.1.3 Bitlis – Zagros Suture Zone**

The Bitlis – Zagros Suture Zone is formed by continental collision between Arabian and Eurasian plates during the Middle Miocene – early Late Miocene. It lies from the north of Arabian platform through the southeastern Turkey to the Zagros Mountains in Iran (Dewey and Şengör, 1979; Şengör and Yılmaz, 1981; Hempton, 1984). Major thrust zones along the suture zone divided it into three. The first is the Arabian platform which has been made up of Lower Paleozoic – Miocene aged autochthonous sedimentary succession and Late Cretaceous – Eocene aged ophiolitic nappes. The second is known as zone of imbrication including several thrusts and third is named as nappe region. Thus, the upper tectonic parts of southeast Anatolian orogeny are composed of ophiolitic and metamorphic units from bottom to top which are overlain by back-arc basin formations and nappe emplacements (Yılmaz, 1993). Ongoing convergence led to the tectonic escape forming NAFZ, MOFZ and EAFZ, but it is also partly compensated along Bitlis suture (Bozkurt, 2001; and references therein).

## **2.2 Active Tectonic Setting**

### **2.2.1 Central Anatolian Fault Zone**

The Central Anatolian Fault Zone (CAFZ) is a sinistral active shear zone developed by the reactivation and propagation of palaeotectonic “Ecemiş Corridor” in the Plio-Quaternary times due to continuing convergence of the Arabian and Eurasian plates towards each other. The CAFZ cuts across the eastern Anatolian Plateau in NE and SW direction and probably reaches to west of Cyprus by passing through Anamur and Eastern Mediterranean Sea floor (Figure 2.1) (Koçyiğit and Beyhan, 1998; Bozkurt, 2001).

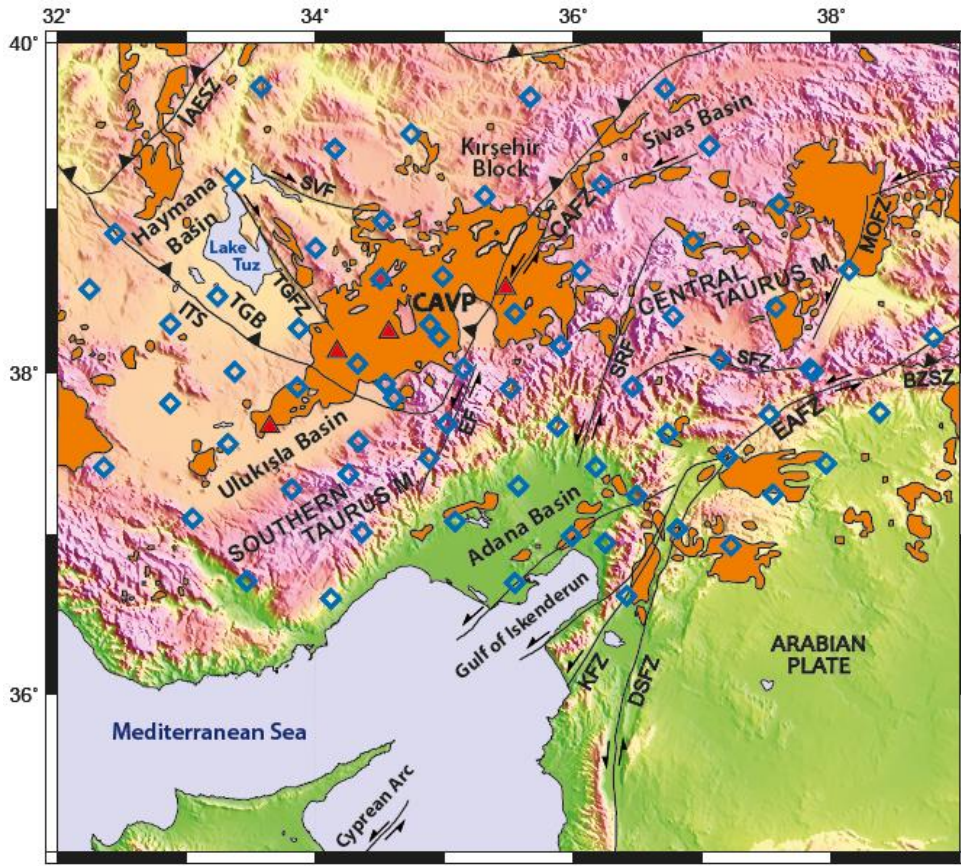


**Figure 2. 1** Topographic map showing faults, sutures (simplified from Bozkurt, 2001), volcanism (taken from Abgarmi et al., 2017); and the seismic stations in the study area. CD-CAT Project broadband seismic stations are indicated by blue unfilled diamonds. Black lines with black filled triangles represent suture zones. Red triangles are Holocene volcanoes and orange polygons show Neogene recent volcanic deposits. BZSZ: Bitlis Zagros Suture Zone, CAFZ: Central Anatolian Fault Zone, CAVP: Central Anatolian Volcanic Province, DSFZ: Dead Sea Fault Zone, EAFZ: East Anatolian Fault Zone, EF: Ecemiş Fault, IAESZ: İzmir-Ankara-Erzincan Suture Zone, ITS: Inner Tauride Suture, KFZ: Karasu Fault Zone, MOFZ: Malatya-Ovacık Fault Zone, SFZ: Sürgü Fault Zone, SRF: Sarız Fault, SVF: Savcılı Fault, TGB: Tuz Gölü Basin, TGFZ: Tuz Gölü Fault Zone.

Koçyiğit and Beyhan (1998) describes the CAFZ as a 730 km long, 2 to 80 km wide sinistral intracontinental megashear zone cutting across the Central Anatolia and bounded by the Eastern Mediterranean Sea in the south and the Erzincan city in the northeast. It is a young, important neotectonic structure which is initiated in the middle Pliocene and formed from several segments (Dirik, 2001). Its displacement differs according to the palaeotectonic and neotectonic periods. Koçyiğit and Beyhan (1998) claim sinistral displacements of about 75 km for late Paleozoic – early Mesozoic

period, 4 to 24 km for Miocene period and 3.1 km for the Quaternary deposits and drainage systems. However, there are some speculations about the present day slip rate along CAFZ. The slip rate of about 3 mm/yr was calculated by finite element model by Kasapoğlu (1987). Koçyiğit and Beyhan (1998) and Westaway (1999) debate about this slip rate whether such an active zone exists in the region or whether all relative motion between Central Anatolia and Arabia proceeds to be the future boundary of East Anatolian Fault Zone (Aktuğ et al., 2013).

The northern part of CAFZ includes NE trending left-lateral strike-slip faults and related pull apart basins (Yılmaz and Yılmaz, 2006). CAFZ is related to a large intervening pull-apart basin, named as the Erciyes pull-apart basin by Koçyiğit and Beyhan (1998). According to Koçyiğit and Erol (2001), the basin has a 35 km width, 120 km length and 1.2 km depth. It is formed due to releasing double bend along CAFZ and is hosting the Erciyes Dağı in the central part and is filled by the Plio-Quaternary volcanic units of this stratovolcano complex. The ESE boundaries of the Erciyes pull-apart basin is characterized by normal – slip faults which intersect a series of acidic domes, volcanic cones and the crater of Erciyes stratovolcano (Şaroğlu et al., 1992; Koçyiğit and Beyhan, 1998; Koçyiğit and Erol, 2001).

The northeastern part of CAFZ overlays on the western part of the Sivas basin which is one of the largest Tertiary basin of Anatolia. It was formed by the Inner Tauride ocean closure and its northern part was shaped by İzmir – Ankara – Erzincan Suture frontal thrust and also Sivas to Kızılırmak segments of CAFZ (Şengör and Yılmaz, 1981; Koçyiğit and Beyhan, 1998). The Sivas Basin is extending from Kayseri in the west to Erzincan in the east and is filled by two main sedimentary groups: the first was completed at the end of late Palaeogene and consisting of continental deposits with evaporates; while the second was initiated with marine incursion during Early Miocene to Late Neogene and again formed by continental deposits (Temiz et al., 1993). In the northeastern side of Central Anatolia, Haymana basin is located in the Ankara part of İzmir – Ankara suture and near western-northwestern side of Kırşehir Block and emerged during the Late Cretaceous to Eocene (Gürer et al., 2016; Görür et al., 1984).

The widespread units of İzmir – Ankara suture are filling the Haymana basin (Koçyiğit, 1991).

In according to the paper of Şengör et al. (1985), Central Anatolian is named as ‘Ova’ Province due to its inactive seismic characteristics. Some earthquake record indicate that the eastern part of the Central Anatolia has relatively less seismic activity. However, some moderate size earthquakes were recorded through time such as 1717 and 1835 Ecemiş, 9 March 1902 Çankırı (Ms=5.5), May 1914 Gemerek (M=5.6), 1938 Kırşehir (M=6.8), 21 February 1940 Erciyes (M=5.3), 13 April 1940 Yozgat – Kayseri (M=5.3), 14 August 1996 Mecitözü – Çorum (M=5.6) within this zone. It is reported that 28.05.1914 Gemerek earthquake was felt strongly in Kayseri, Sivas and Tokat cities and caused life loss and serious damages on structures. The 21.02.1940 Erciyes (Kayseri) earthquake was happened in the Erciyes Mountain with its 18 shocks. It is reported that 37 people lost their life and five villages and one county were destroyed, 10,000 km<sup>2</sup> area were affected during the earthquake.

### **2.2.2 East Anatolian Fault Zone**

The East Anatolian Fault Zone is a transform fault and resulted from the continued northward convergence of Arabia toward Eurasia since the late Miocene (Şengör et al., 1985; Dewey et al., 1986; Hempton, 1987; Westaway, 1994). It is the boundary between the Anatolian and the Eurasian plates and between the Arabian and the African plates and thought as the conjugate structure of NAFZ (Figure 2.1) (Bozkurt, 2001). This African-Arabian plate motion is correlated with the sinistral Dead Sea Fault Zone at a slip rate of 4.5 – 4.8 mm/yr (Reilinger et al., 2006).

The sinistral characteristic of the fault zone participates to the westward motion of Anatolia. The East Anatolian Fault Zone has numerous pull-apart basins, conjugate fractures, folding and important thrust component. The EAFZ comprises some pure strike-slip faults parallel to plate motion and some oblique to the plate motion. This stepover geometry also creates strike-slip faults and needs dispensed shortening

around (Bozkurt, 2001). According to Reilinger et al. (2006), the East Anatolian Fault has 550 km length and  $9.7 \pm 0.9$  mm/yr slip rate according to geodesy studies. Westaway and Arger (2001) estimates that its total offset ranges between 8 and 30 km comparingly much less than the North Anatolian Fault offset with varying  $85 \pm 5$  km to 20-25 km (Barka et al., 2000; Bozkurt, 2001 and references therein).

In the review paper of Bozkurt (2001), the age of the East Anatolian Fault Zone is disputed by four different groups: first, it is located in the Late Miocene – Early Pliocene (Şengör et al., 1985; Dewey et al., 1986; Hempton, 1987; Arpat and Şaroğlu, 1972; Lyberis et al., 1992; Perinçek and Çemen, 1990); second, it is initiated in the Late Pliocene (Şaroğlu et al., 1992); third, it began to form 1.8 Ma ago (Yürür and Chorowicz, 1998); last, the fault zone is activated approximately 3 Ma by the abandonment of Malatya – Ovacık Fault Zone (Westaway and Arger, 1998). The age of 1.8 Ma is depended on Quaternary volcanism near the south of Kahramanmaraş by Yürür and Chorowicz (1998) who also correlated this volcanism to extensional regime and so the present strike-slip faulting geometry. However, Arger et al., (2000) suggested that the same volcanism is Miocene aged and there has no obvious evidence of extension or strike-slip faulting.

This NE-trending left-lateral transform fault zone constructs two triple junction points: Karlıova triple junction with the North Anatolian fault zone (NAFZ) in the northeast and Kahramanmaraş triple junction with the Dead Sea fault zone (DSFZ) in the southwest. The NAFZ and DSFZ are the well-defined faults and their nature, age and offset information are clearly established, on the other hand, the age, total offset and geometry of the EAFZ has debates as it getting closer to the triple junction point. Westaway, 1994; Hempton, 1987; Westaway and Arger, 1996; Taymaz et al., 1991; Arger et al., 2000; Koçyiğit et al., 1998; Gürsoy et al., 1998; Yurtmen et al., 2000 claim that the EAFZ extends from Karlıova to Cyprus by transferring Osmaniye, Yumurtalık and Gulf of İskenderun in the southwest direction. Westaway (1994) states that Africa, Arabia and Turkey come across at the triple junction near Kahramanmaraş city where SSW-trending sinistral faults are located at the edges of the Arabian and Turkish plates. Some authors claim that the existing faults running from Karlıova

through Osmaniye, Yumurtalık and Gulf of İskenderun to Cyprus are not related to the EAFZ since they are the boundary between the Anatolian and African plates and they meet with the EAFZ in the more eastern part of the triple junction (Bozkurt, 2001).

Some important earthquakes with magnitudes greater than 6.5 which had occurred along the EAFZ are compiled including, January 1544 (M>6.7), 29 May 1789 (M>7.0), 3 May 1874 (M>7.1), 3 March 1875 (M=6.7), 2 March 1893 (M>7.1), 4 December 1905 (M=6.8), 13 September 1905 (M=6.8), 1945 (M=5.7) and 1952 (M=5.3) in Adana – Misis, 22 May 1971 (M=6.9) and 6 September 1975 (M=6.7), 24 November 1976 (M=7.3, 1979 (M=5.1) Adana – Kozan,) 30 October 1983 (M=6.8), 5 May 1986 (M=5.8), 6 June 1986 (M=5.6), 1986 (M=5.0) Gaziantep, 1989 (M=4.9) Iskenderun, 1991 (M=5.2) Kadirli – Adana, 1994 (M=5.0) Adana – Ceyhan, 27 June 1998 (M=6.2) Adana – Ceyhan, 17 January 2001 (M=4.9) Osmaniye (Taymaz et al., 1991b; Ambraseys, 1989; Westaway, 1994; Tüysüz, 2005).

### **2.2.3 Dead Sea Fault Zone**

Dead Sea Fault Zone is a N-S trending, dominantly left-lateral with extensional component, intraplate, strike-slip fault zone. It is more than 1000 km long, and has approximately 105 km of total offset between Lebanon and the Gulf of Aqaba in the south and 70 – 80 km in the Turkey – Syria border region in the north (Figure 2.1) (Westaway, 2004; Bozkurt, 2001; Rojay et al., 2001). The Dead Sea Fault Zone (DSFZ) follows a linear path in northward direction from the Red Sea more or less parallel to the eastern margins of Mediterranean Sea and then reaches to Turkey (Perinçek and Çemen, 1990; and references therein). The East Anatolian and Dead Sea fault zones come across in southeastern Turkey.

The DSFZ can be represented as the most significant tectonic system of the Middle East region which generates one of the most seismically active region. Its motion moves along the fault from the Red Sea in the south where oceanic spreading takes

place, to the Taurus – Zagros collision boundary in Turkey and Iran to the north (Rojay et al., 2001; Ben-Avraham et al., 2005).

The Dead Sea Fault Zone consists of two approximately N-trending linear segments in the north. The NNE trending Karasu fault zone links the N-S-trending Gharb segment of DSFZ and the NE-trending EAFZ. The Karasu Rift is located between Kahramanmaraş and Antakya in southern Turkey. It is NNE-SSW trending, 150 km long and 10 to 25 km wide structure. In the western margins of the valley, small-scale pull-apart basins are formed between en-echelon left-lateral strike-slip faults with a height of up to 2 km. In the eastern margins, N-S trending strike-slip faults are dominantly observed where the topography reaches the maximum value of 800 m (Rojay et al., 2001).

The Karasu segment is a left-lateral strike-slip fault with 150 km in length. The DSFZ creates rift depressions and the Karasu Rift Valley is one of these rifts in the study area, existing within the EAFZ and the DSFZ and also representing the one of the volcanic centers along the transform (Parlak et al., 1998). An intense and widespread igneous activity is recorded from the Gulf of Aqaba to the Amik basin (Bozkurt, 2001).

Big earthquakes occurred during historical period along the DSFZ are as follows: BC 69 (I=IX), 13 December 115 (I=IX), 245 (I=X), 334 (I=IX), 14 September 458 (I=IX), 10 September 506 (I=IX), 29 May 526 (I=IX), 30 September 587 (I=IX), 8 April 859 (I=IX), 867 (I=IX), 10 August 1114 (I=IX), 13 August 1822 (I=X), and 2 April 1872 (I=IX) (Tüysüz, 2005). According to Westaway (1994), some important earthquakes with magnitudes greater than 6.5 have occurred during instrumental period in the northern Dead Sea Fault Zone, including, 15 August 1157 (M>7.0), 29 June 1170 (M>7.0), 22 February 1404 (M is large), 29 April 1407 (M>7.0), 26 April 1796 (M=6.6), 3 April 1872 (M<7.2) and 13 August 1822 (M>7.4) (Ambraseys and Barazangi, 1989). Additionally, Rojay et al., (2001) mentioned the recent earthquake that occurred in January 22, 1997 with M=5.5 in the west of Antakya (Erdik et al., 1997).

## 2.2.4 Tuz Gölü Fault Zone

Tuz Gölü Fault Zone (TGFZ) is one of the most outstanding deformation zone in Central Anatolia trending in NW-SE direction and extending along the eastern margin of Lake Tuz (Figure 2.1). It is an approximately 200 km long, 5 to 25 km wide, right lateral strike-slip fault zone with a significant normal component (Koçyiğit and Beyhan, 1998; Koçyiğit and Erol, 2001; Bozkurt, 2001; Dirik and Göncüoğlu, 1996). The initiation time of Tuz Gölü Fault Zone is disputable. Çemen et al. (1999) and Görür et al. (1984) claim that the movement along TGFZ began in Late Cretaceous, while Dellaloğlu and Aksu (1984) establish that the fault zone became its activity in the Miocene.

Tuz Gölü Fault Zone shapes the eastern boundary of Tuz Gölü and comprises step-like half-graben and horst-graben structures (Dirik and Göncüoğlu, 1996). In the NNE direction of Tuz Gölü, the Savcılı Fault (SVF) is located in the Kırşehir Block between the İzmir – Ankara – Erzincan and Inner Tauride suture zones. It extends in WNW-ESE direction as a left-lateral structure (Lefebvre et al., 2013).

In the middle of the Central Anatolia, Tuz Gölü Basin (TGB) is situated as the largest intracontinental basin. The Tuz Gölü Basin is emerged at the same time with the Haymana basin during the Late Cretaceous to Eocene (Gürer et al., 2016; Görür et al., 1984). As a result of Tuz Gölü Fault Zone, the thick sedimentary deposits of the Tuz Gölü Basin (TGB) can be collocated with the crystalline rocks of the Kırşehir Block which are covering the Inner Tauride Suture (ITS) trace on the surface in the southwest (Abgarmi et al., 2017; Çemen et al., 1999). Studies conducted on the sedimentary sequences of Tuz Gölü near the town Aksaray revealed the absence of palaeochannels that could drain Tuz Gölü (Özsayın et al., 2013; and references therein).

Tuz Gölü Basin continues toward the eastern direction and turns into Ulukışla Basin where Ecemiş Fault (EF) forms the boundary in the east. The Ulukışla basin experienced N-S and E-W extension from latest Cretaceous-Paleocene until ~56 Ma. These N-S compressional forces resulted the folded structure of Bolkar Mountains

during Eocene-Oligocene and secondary structures in the basin as well (Gürer et al., 2016).

Neotectonic activity of extensional fault systems controls the deformation in TGB. Volcanic activity, alignment of cinder cones, right-lateral offset of lava flows, travertine occurrences and fault-controlled terrace deposits are the controlling structures of the southern segment of Tuz Gölü Fault Zone (Dirik and Göncüoğlu, 1996; Toprak and Göncüoğlu, 1993b). As Pasquare et al. (1988) and Toprak and Göncüoğlu (1993b) denote that the Quaternary Hasan Dağ which is another important composite volcano beside Erciyes Dağı, has been formed along TGFZ by intersecting NE-SW trending faults. Additionally, the dextral strike-slip fault mechanism of southern segment can be supported by the clockwise patterns of streams, striated fault planes and right-lateral offsets of volcanic rocks (Dirik and Göncüoğlu, 1996).

### **2.2.5 Malatya – Ovacık Fault Zone**

The Malatya – Ovacık Fault Zone (MOFZ) is 240 km long left-lateral strike-slip fault zone which is comprising of two segments with more or less equal lengths: Ovacık segment lying through WSW direction along the margin of Ovacık Valley and Malatya segment is extending through WNW margin of Malatya Basin towards Anatolian Plate (Figure 2.1) (Westaway et al., 2008). In the North, MOFZ and NAFZ meets in the Erzincan basin (Bozkurt, 2001). Westaway and Arger (2001) claimed that the MOFZ developed as a plate boundary between Anatolian Arabian boundary at 5 Ma. The modern EAFZ and the eastern segments of the NAFZ were developed near Erzincan at approximately 3 Ma which triggered the abandonment of the MOFZ.

At the most southern edge of MOFZ, Sürgü Fault Zone (SFZ) was evolved which is unusually trending approximately in the E-W direction. The SFZ is one of the bifurcations of the EAFZ in the east and delimits several NNE–SSW trending faults in the region including Sarız Fault (SRF) (Koç and Kaymakçı, 2013). The Sarız Fault (SRF) locates between the CAFZ and EAFZ by being bounded by left-lateral strike-

slip faults and provides the internal deformation of Central Taurus Mountains (Abgarmi et al., 2017; Kaymakçı et al., 2010).

### **2.2.6 Cyprean Arc**

Cyprean Arc is the active convergent plate boundary in the eastern Mediterranean and triggered by the subduction of African plate in the southern Anatolia toward the north direction (Figure 2.1). The eastern part of Cyprean Arc is characterized by strike-slip faults forming positive flower structures in a wide area rather than a form of sharp plate boundary between Anatolian and African plates (Bozkurt, 2001; and references therein). Since the eastern section of the Cyprean Arc was affected by differential dynamics of African, Arabian and Anatolian plate motions; it displays no well-defined arc-trench system and has the most disputable movement (Wdowinski et al., 2006). In the easternmost section near İskenderun Gulf, dip-slip events near the major strike-slip faults are commonly recorded which are explained by segmentation and geometrical complexity in strike-slip fault systems. In the west, Cyprus arc turns towards north and display a more pronounced deep and intermediate seismic activity below the Antalya Basin associated to active subduction. According to recent studies that utilized passive seismic imaging techniques, gently dipping Cyprus slab in south, becomes close to vertical beneath Taurus Mountains (Biryol et al. 2011; Abgarmi et al. 2017; Portner et al., 2018).

## **2.3 Seismicity of the Region**

### **2.3.1 Historical Seismicity**

Historical seismicity catalogs comprise the data recorded from the first human descriptions until the beginning of the instrumental catalog records. Historical events in Central Anatolia are gathered for the years BC 148 – AD 1899 and plotted on the topographic map (Figure 2.2) and listed in Table 2.1. It can be seen that these

earthquakes are mostly clustered on Antakya vicinity probably because of the well-records of the churches in the region. Besides, some of them are well-correlated with the southern branch of East Anatolian Fault Zone. The intensities of these historical events are varying from V to X. The most destructive earthquake (I=X) has occurred in Antakya in 245 AD.

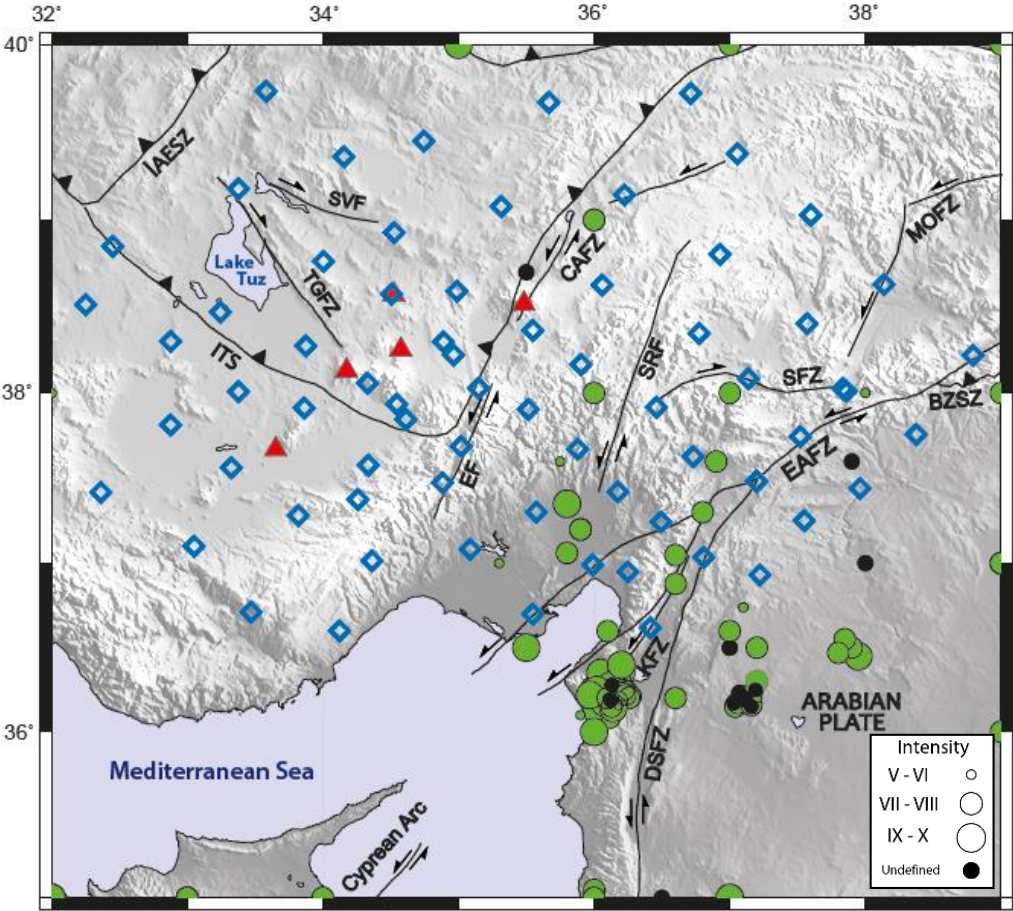


**Figure 2. 2** Topographic map showing historical events (BC148-AD1899). Earthquakes are denoted by green circles scaled to their intensities. Black circles indicate unknown intensities. CD-CAT Project seismic stations are shown by blue unfilled diamonds. Red triangles are Holocene volcanoes. Labels are explained in Figure 2. 1.

**Table 2. 1** Historical earthquakes of the region (OZ00 = Öztemir et al., 2000; A94 = Ambraseys et al., 1994; T15 = Tülüveli, 2015; AFAD = deprem.afad.gov.tr).

No	Date	N (°)	E (°)	Intensity	Location	Reference
1	BC 148	36.25	36.10	VIII	Antakya	OZ00
2	BC 131	37.05	36.60	VII	Islahiye	OZ00
3	BC 69	36.25	36.10	IX	Antakya	OZ00
4	BC 37	36.25	36.10	VIII	Antakya	OZ00
5	BC 26	35.00	32.00	VII	Cyprus	AFAD
6	BC 15	35.00	32.00	IX	Cyprus	AFAD
7	37	36.24	36.10	VIII	Antakya	OZ00
8	53	35.00	36.00	VIII	Antakya	AFAD
9	79	36.25	36.10	VII	Antakya	OZ00
10	110	36.25	36.10	VIII	Antakya, Samandağ	OZ00
11	115	36.25	36.10	IX	Antakya and vicinity	OZ00
12	117	36.25	36.10	VII	Antakya	OZ00
13	128	37.30	36.80	VIII	Islahiye, Maraş	OZ00
14	220	36.25	36.10	VIII	Antakya	OZ00
15	245	36.25	36.10	X	Antakya	OZ00
16	272	36.25	36.10	VIII	Antakya	OZ00
17	290	37.06	35.80	VIII	Ceyhan, İçel	OZ00
18	334	36.25	36.10	IX	Antakya, Beyrut	OZ00
19	341	36.25	36.10	VIII	Antakya	OZ00
20	342	35.00	32.00	IX	Cyprus	AFAD
21	343	35.00	33.00	VIII	Nicosia, Cyprus	AFAD
22	345	36.25	36.10	VII	Antakya	OZ00
23	363	36.25	36.10	V	Antakya	OZ00
24	387	36.25	36.10	VI	Antakya	OZ00
25	396	36.25	36.10	VIII	Antakya	OZ00
26	434	35.00	36.00	VIII	Syria	AFAD
27	458	36.25	36.10	IX	Antakya and N.Syria	OZ00
28	477	35.00	36.00	VII	Syria	AFAD
29	506	36.25	36.10	IX	Antakya, Samandağ	OZ00
30	517	37.20	35.90	VIII	Anazarba, Adana	OZ00
31	518	36.88	36.60	VIII	Antakya	OZ00
32	524	37.20	35.90	VIII	Anazarba, Adana	OZ00
33	526	36.25	36.10	IX	Antakya, Samandağ	OZ00
34	526	36.25	36.10	VI	Antakya	OZ00
35	527	36.25	36.10	VI	Antakya	OZ00
36	529	36.25	36.10	IX	Antakya and vicinity	OZ00

**Table 2. 1 (cont'd)** Historical earthquakes of the region (OZ00 = Özt Demir et al., 2000; A94 = Ambraseys et al., 1994; T15 = Tülüveli, 2015; AFAD = deprem.afad.gov.tr).

No	Date	N (°)	E (°)	Intensity	Location	Reference
37	532	35.00	37.00	VII	Antakya	AFAD
38	553	36.25	36.10	VII	Antakya	OZ00
39	557	36.25	36.10	VII	Antakya	OZ00
40	561	37.20	35.90	VIII	Anazarba, Antakya	OZ00
41	579	36.25	36.10	VII	Antakya and vicinity	OZ00
42	581	36.25	36.10	VI	Antakya	OZ00
43	583	36.25	36.10	?	Antakya	OZ00
44	587	36.25	36.10	IX	Antakya	OZ00
45	715	36.50	37.90	IX	Syria	OZ00
46	716	36.25	36.10	VII	Antakya	OZ00
47	718	37.00	39.00	VIII	Urfa	AFAD
48	775	36.25	36.10	VII	Antakya, Aleppo	OZ00
49	791	36.20	36.10	VIII	Aleppo	OZ00
50	835	36.25	36.10	VII	Antakya	OZ00
51	859	36.25	36.10	IX	Antakya, Şam	OZ00
52	860	37.00	38.00	?	East Anatolia	A94
53	867	36.25	36.10	IX	Antakya	OZ00
54	963	36.60	37.00	VIII	Aleppo, N Syria	OZ00
55	972	36.25	36.10	VII	Antakya	OZ00
56	1003	37.00	39.00	VIII	Urfa and vicinity	AFAD
57	1037	37.00	39.00	VII	Urfa	AFAD
58	1042	36.50	37.90	VIII	Syria	OZ00
59	1053	36.25	36.10	VIII	Antakya	OZ00
60	1072	36.25	36.10	VIII	Antakya	OZ00
61	1089	36.50	37.90	VIII	Syria	OZ00
62	1091	36.25	36.10	VII	Antakya and Urfa	OZ00
63	1109	36.50	37.90	VIII	Syria	OZ00
64	1114	36.50	35.50	IX	Ceyhan, Antakya	OZ00
65	1114	36.25	36.10	?	Antakya	OZ00
66	1114	37.60	36.90	VIII	Maraş, Harran	OZ00
67	1138	36.30	37.20	VIII	Aleppo, Mesopotamia	OZ00
68	1138	36.50	37.00	?	North Syria	A94
69	1139	36.20	37.10	?	Aleppo	AFAD
70	1140	36.00	39.00	VIII	Syria	AFAD
71	1152	35.00	36.00	VII	Hama	AFAD
72	1157	35.00	36.00	VII	Damascus	AFAD
73	1157	35.00	37.00	IX	Hama	AFAD
74	1170	35.00	36.50	?	North Syria	A94

**Table 2.1 (cont'd)** Historical earthquakes of the region (OZ00 = Özt Demir et al., 2000; A94 = Ambraseys et al., 1994; T15 = Tülüveli, 2015; AFAD = deprem.afad.gov.tr).

No	Date	N (°)	E (°)	Intensity	Location	Reference
75	1183	35.00	32.00	IX	Antakya	AFAD
76	1190	36.25	36.10	VIII	Antakya and vicinity	OZ00
77	1204	36.20	37.10	VIII	Aleppo, Tyr	OZ00
78	1205	39.00	36.00	VIII	Kayseri	AFAD
79	1212	36.25	36.10	VI	Antakya	OZ00
80	1222	36.74	37.10	VI	Kilis	OZ00
81	1254	40.00	39.00	VIII	Refahiye, Erzincan	AFAD
82	1268	37.35	35.80	IX	Kozan, Ceyhan	OZ00
83	1287	36.00	36.00	VIII	Latakia, Syria	AFAD
84	1290	36.00	36.00	VI	Latakia, Syria	AFAD
85	1355	36.00	36.00	VI	Latakia, Syria	AFAD
86	1491	35.00	32.00	?	Mediterranean	AFAD
87	1544	38.00	37.00	VIII	Maraş	AFAD
88	1567	35.00	33.00	VII	Nicosia	AFAD
89	1577	35.00	33.00	VIII	Nicosia	AFAD
90	1598	40.00	35.00	IX	Amasya	AFAD
91	1643	37.60	37.9	?	Adiyaman	T15
92	1714	39.00	36.00	VII	Kayseri	AFAD
93	1717	38.70	35.50	?	Kayseri	T15
94	1718	35.00	33.00	VIII	Cyprus	AFAD
95	1719	36.20	37.10	VIII	Aleppo and N. Syria	OZ00
96	1726	36.25	36.10	VI	Iskenderun&vicinity	OZ00
97	1735	35.00	34.00	VIII	Cyprus	AFAD
98	1737	36.25	36.10	VII	Antakya	OZ00
99	1741	35.00	34.00	VII	Magosa, Cyprus	AFAD
100	1752	36.00	36.00	IX	Latakia	AFAD
101	1754	40.00	37.00	VII	Sivas	AFAD
102	1759	36.20	37.10	?	Aleppo, Syria	OZ00
103	1759	36.20	37.10	?	Aleppo, Syria	OZ00
104	1759	36.20	37.10	?	Aleppo, Syria	OZ00
105	1764	36.20	37.10	?	Aleppo, Syria	OZ00
106	1778	36.20	37.10	?	Aleppo	OZ00
107	1783	36.20	37.10	V	Aleppo	OZ00
108	1795	36.20	37.10	VII	Aleppo	OZ00
109	1822	36.40	36.20	IX	Antakya, Aleppo	OZ00
110	1822	36.20	37.10	?	Aleppo	OZ00

**Table 2.1 (cont'd)** Historical earthquakes of the region (OZ00 = Özt Demir et al., 2000; A94 = Ambraseys et al., 1994; T15 = Tülüveli, 2015; AFAD = deprem.afad.gov.tr).

No	Date	N (°)	E (°)	Intensity	Location	Reference
111	1830	36.20	37.10	V	Aleppo	OZ00
112	1831	36.20	37.10	VI	Aleppo	OZ00
113	1835	38.00	36.00	VIII	Kayseri	AFAD
114	1844	36.20	37.10	VII	Aleppo, Syria	OZ00
115	1844	36.20	37.10	V	Aleppo, Syria	OZ00
116	1846	36.20	37.10	VI	Aleppo	OZ00
117	1847	36.60	36.10	VII	Iskenderun	OZ00
118	1854	36.20	36.60	VII	Antakya, Aleppo	OZ00
119	1855	37.60	35.75	VI	Ceyhan, Adana	OZ00
120	1866	38.00	39.00	VIII	S of Caspian Lake	AFAD
121	1866	38.00	32.00	VI	Konya	AFAD
122	1872	36.25	36.10	IX	Antakya, Samandağ	OZ00
123	1872	36.20	36.10	VII	Antakya	OZ00
124	1873	36.50	37.20	VII	Nisiros Isl., Mediterranean	OZ00
125	1873	36.10	35.90	VI	Antakya, Samandağ	OZ00
126	1875	36.20	36.10	VII	Antakya vicinity	OZ00
127	1884	36.30	37.20	VII	Aleppo and N.Syria	OZ00
128	1887	40.00	37.00	VI	Tokat	AFAD
129	1890	40.00	39.00	IX	Refahiye, Erzincan	AFAD
130	1890	38.00	38.00	VI	Malatya	AFAD
131	1894	36.20	36.10	V	Antakya vicinity	OZ00
132	1896	37.00	35.30	VI	Adana, Mersin	OZ00

### 2.3.2 Instrumental Seismicity

The historical seismicity catalogs take part in long-term seismic hazard assessment, while the instrumental seismicity catalogs are developed by dense seismic networks and used as resources in statistical seismology (Woessner et al., 2010). The study area covers significant tectonic structures, such as active major faults, deactivated faults and narrow to broad shear zones. In this respect, the spatial distribution of instrumental seismicity in the region helps us to define the distribution of active faults. Therefore, an earthquake catalog is compiled from Boğaziçi University Kandilli Observatory and Earthquake Research Institute Regional Earthquake-Tsunami Monitoring Center (KOERI-RETMC) from January, 1900 to December, 2017 covering the area with latitudes of 35°N – 40°N and longitudes of 32°E – 39°E. The catalog data includes 27662 events with a magnitude range of 0.7 to 6.6 and depths up to 160 km. The graphs of magnitude vs. time and cumulative number of earthquakes in time are drawn for this compiled data. According to Figure 2.3a, it is seen that only the earthquakes with  $M > 4.0$  could be recorded until 1960s. The data became denser after 1967, and the events with  $M > 2.5$  also began to be recorded after 1978. The data seems much denser by the inclusion of the events with  $M > 0.7$  which are begun to be recorded in 2000s. According to Figure 2.3b, the number of recorded earthquakes increase at the beginning of 1960s, and a drastic change occurs in 1995. The locations of all earthquakes in the catalog are plotted so that their spatial distributions can be followed on the local seismicity map (Figure 2.4). The epicentral distribution of the earthquakes well correlates with the mapped tectonic structures in the study area.

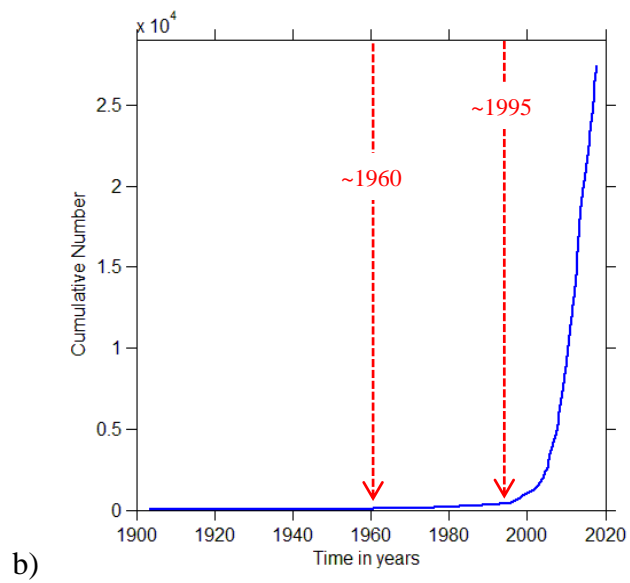
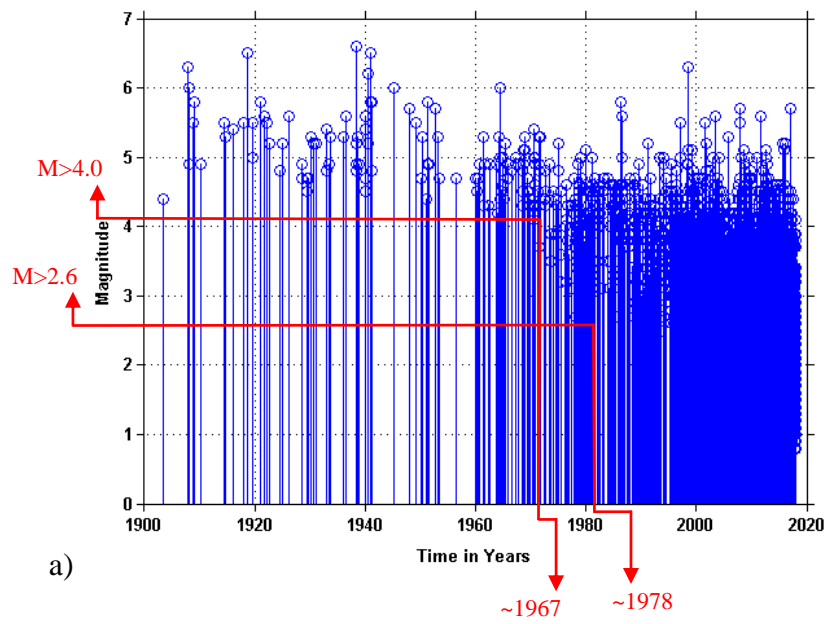


**Figure 2.3** a) Magnitude vs. time plots of events in the earthquake catalog, b) cumulative number of earthquakes plotted in time.

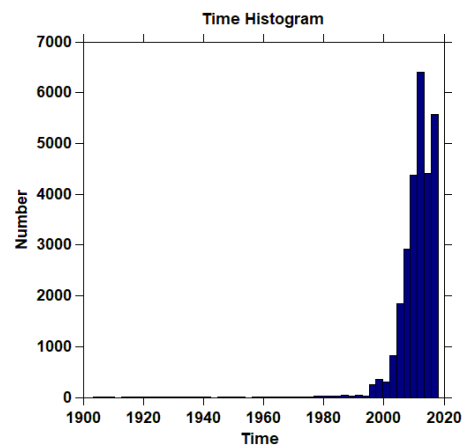
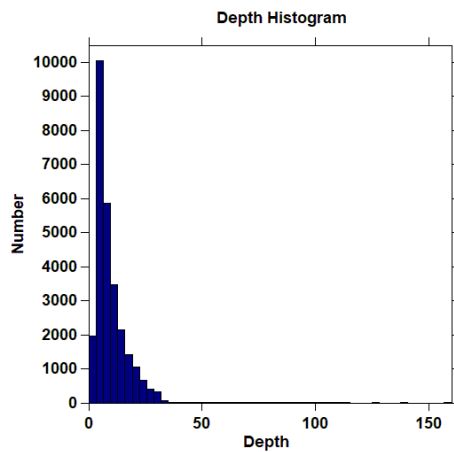
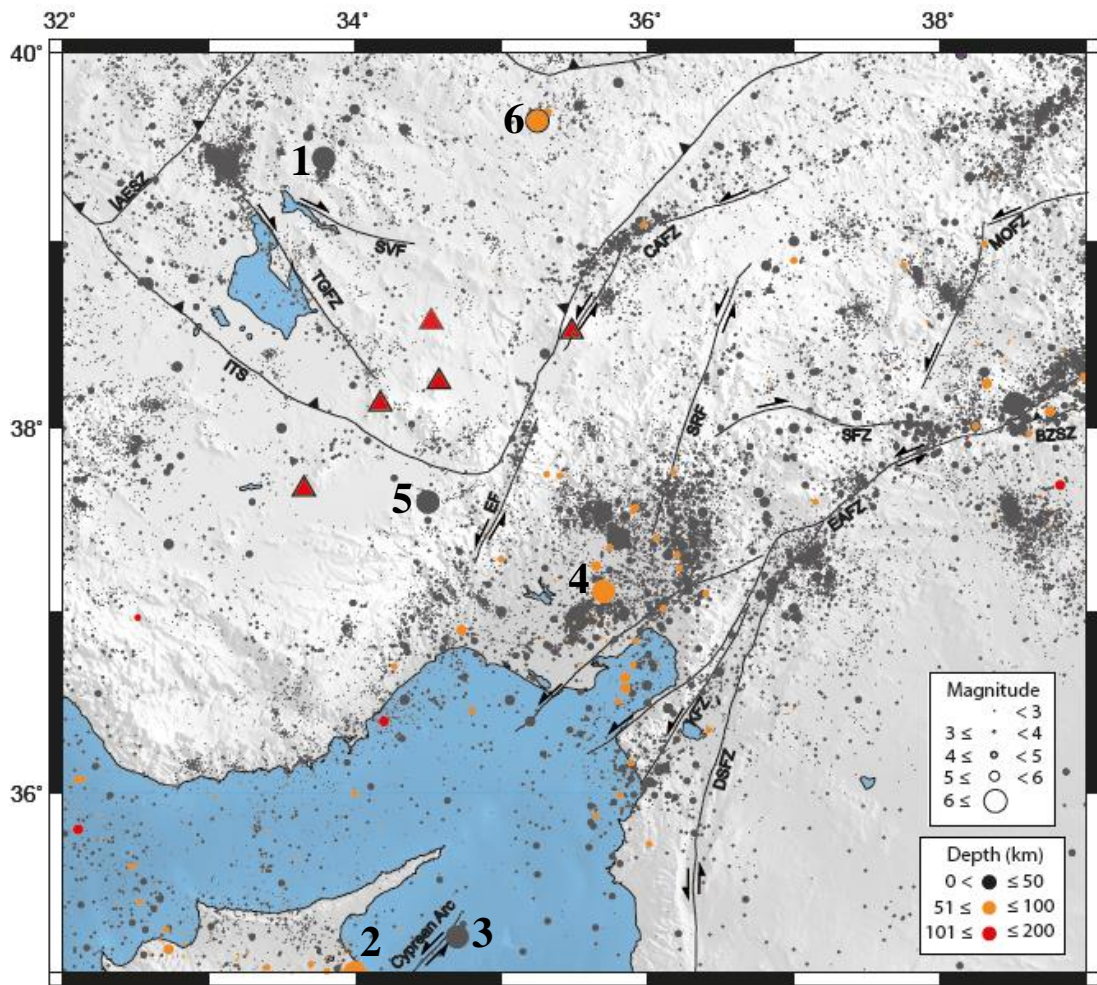


**Figure 2. 4** At the top, local seismicity in the study area. Earthquake symbols are scaled to their magnitudes and colored according to their depths. Numbers indicate the earthquakes with  $M > 6.0$ . Labels are explained in Figure 2. 1. At the bottom, depth (left) and time (right) distribution of earthquakes are shown with histograms.

Most of the seismicity with the earthquakes shallower than 50 km are situated along the major fault zones and in Adana Basin with their fore- and aftershocks. The events with the depths between 50 – 100 km are concentrated along Cyprean Arc and in the Mediterranean Sea basin, and the seismicity deeper than 100 km occur rarely in the Mediterranean Sea basin and near Bitlis-Zagros Suture Zone. Among the data, events with  $M > 6$  are individually marked on the map. The graph of change in time due to cumulative moment release is plotted and six events with the highest magnitudes are shown on Figure 2.5. The sudden drastic increases in cumulative moments refer to main shock occurrences.

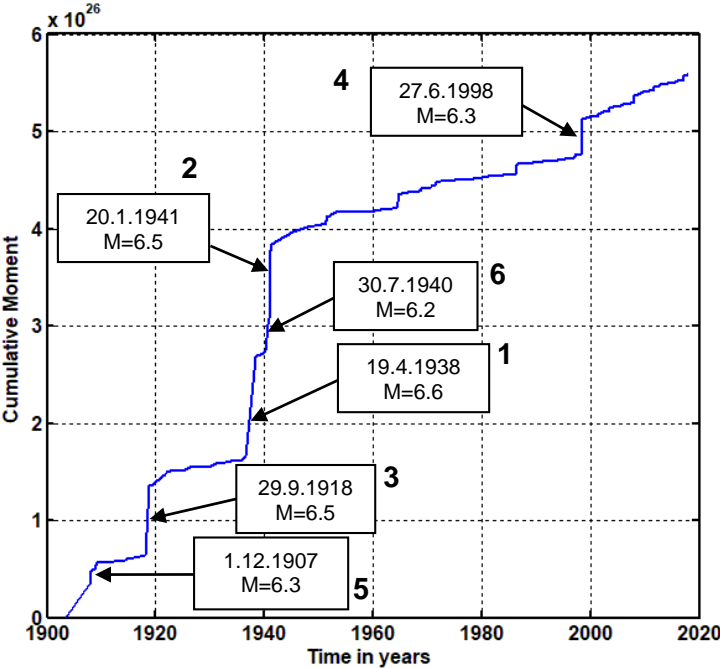


**Figure 2. 5** Cumulative moment release as a function of time.

According to Figure 2.5, the highest value is created by 19.04.1938 earthquake ( $M = 6.6$ ) in Kırşehir with approximately  $1.3 \times 10^{26}$  moment release. The earthquake was triggered by Akpınar Fault locating at the northeast of TGFZ and north of Savcılı Fault. This earthquake caused 204 life-loss and 770 collapsed and heavily damaged

buildings (Şahin, 2016). The second event is the most catastrophic earthquake in Cyprus in 20.01.1941 ( $M = 6.5$ ) causing 24 people injured and many collapsed buildings. The third earthquake is 29.09.1918 in northern Syria near Cyprus. It is depicted as the most damaged earthquake felt in Syria (Zohar et al., 2016). The fourth highest value is created by 27.06.1998 earthquake with  $M=6.3$  in Adana which is triggered by East Anatolian Fault strike-slip mechanism (Schwarz et al., 2000) and resulted in 146 life-loss and 4,000 collapsed and heavily damaged buildings (Pelling, 2003). The other most recognizable patterns are generated by 01.12.1907 ( $M=6.3$ ) earthquake in Ulukışla (Niğde) and 30.07.1940 ( $M=6.2$ ) earthquake in Sorgun (Yozgat) corresponding to a drastic increase of cumulative moments in a short time interval.

### **2.3.2.1 Catalog Declustering**

Time-dependent nature of seismic processes is a clear evidence of temporal clustering. The earthquakes are divided into foreshocks, main shock and aftershock sequences as assumingly only the main shocks are the result of time-independent process (Console et al., 2010; and references therein). To study the time-independent seismicity, declustering algorithms are commonly utilized by many seismological studies. Among these algorithms, Gardner and Knopoff (1974) and Reasenberg (1985) approaches are the most well-known ones. These methods are mainly resulted from the limitations in space-time properties of the major events seismicity (Omori, 1894; Utsu, 1969).

According to Gardner and Knopoff (1974), events of a given catalog are ordered in descending magnitude and space-time windows are defined as a function of magnitude for each event assigning largest windows to the potential main shock events and eliminating foreshocks and aftershocks present within the given time window from the catalog (Talbi et al., 2013). Reasenberg (1985) states that there is an interaction zone centered on each earthquake that can be defined by spatial and temporal parameters. Thus the aftershocks occur within the interaction zone of a former earthquake. The spatial parameter is based on the source dimension as the temporal parameter is related

to non-homogeneous Poisson process for aftershocks using Omori which is the description of average temporal attitude of aftershock sequences.

For this study the ZMAP software is used to utilize both Gardner and Knopoff (1974) and Reasenberg (1985) algorithms. After applying Gardner and Knopoff (1974) method, a declustered catalog is found with a total number of 14596 events out of 27662. On the other hand, Reasenberg (1985) algorithm is resulted in a declustered catalog with a total of 23096 events out of 27662. For the next stages of this study, Reasenberg (1985) method is applied to the catalog.

### **2.3.2.2 Detection and Removal of Mine and Quarry Blast Events**

Because the earthquake catalogs can include quarry blasts and mine explosions, the blast contamination of the area is analyzed by ZMAP software. It is expected that the blast activities to occur in daytime (Wiemer and Wyss, 2000 and reference therein), and thus will cause an artificial increase on the number of detected events during day time. Event distribution of the catalog can be detected by the histograms of hourly number of events. In order to detect such event distributions, the time distribution of events in the KOERI catalog is analyzed in hourly bases. In Figure 2.6, the catalog is gradually eliminated in a descending order of magnitude ranges and it is obvious that the number of daytime events is decreasing while the minimum magnitude of the catalog is increased. Figure 2.6a indicates a contaminated catalog by quarry blasts since it peaks between 7.00 to 17.00 hours that are accepted as the working time in a day. In Figure 2.6d, the catalog covers the events with  $M \geq 3.0$ , and it is resulted that the number of daytime events and the number of nighttime events are individually almost similar for each hour unlike the other plots. Thus the magnitude range for the instrumentally recorded blasts is accepted as  $M < 3.0$  which is the maximum limit for the explosion threshold in the region.

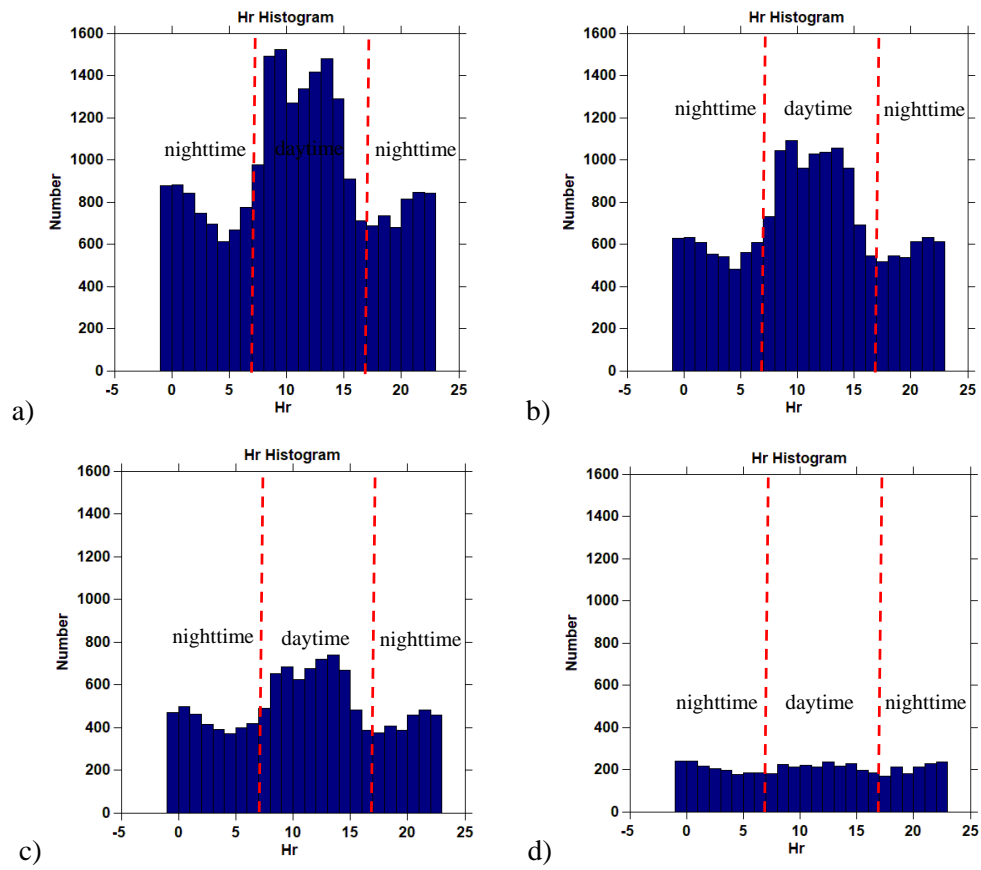


**Figure 2. 6** Histogram of the hourly number of events a) all events; b)  $M \geq 2.0$  c)  $M \geq 2.5$  d)  $M \geq 3.0$

In order to evaluate the spatial distribution of blasts present in the catalog, the day and night time ratio of events with  $M < 3.0$  are computed and mapped in the region using ZMAP software (Figure 2.7). The resultant blast contamination map revealed 19 areas characterized by significantly high day/night ratio ( $>80$ ) anomalies located across the study area.

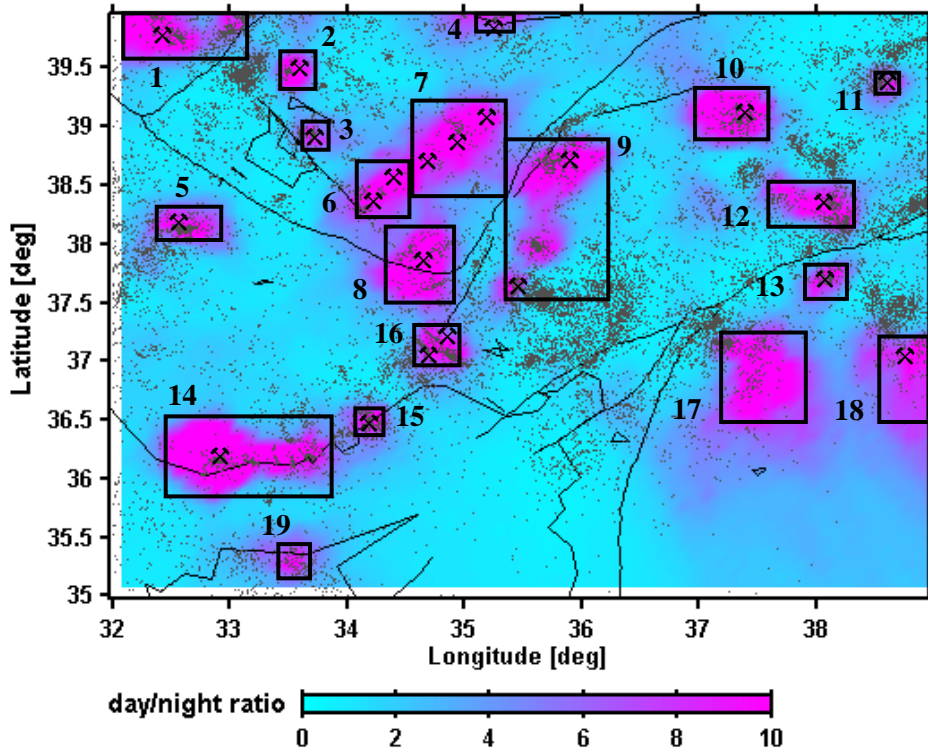


**Figure 2. 7** Quarry contamination detection map for the earthquakes with  $M < 3.0$ . (Hammer symbol indicates the cities with mine sites taken from MTA).

In order to verify the source of the detected blast, the quarry facilities located in these areas are identified from General Directorate of Mineral Research and Explorations (MTA) Mineral Maps and other resources. The collected quarry information for each area numbered in map is listed below accordingly;

1. Limestone, marble, natural stone and ballast (andesite, basalt, etc.), sand-gravel, cement raw materials, brick-tile building stone and gypsum mines in Ankara
2. Marble mine sites in Kırıkkale
3. Limestone and gypsum mine sites in Ankara
4. Marble mine sites in Yozgat
5. Limestone, marble, calcite, mercury, pumice, brick-tile building stone and dolomite mines in Konya
6. Pumice and gypsum mines in Aksaray and pumice mine sites in Nevşehir

7. Kaolinite, marble and pumice mine sites in Nevşehir, marble, limestone, kaolinite and natural stone (andesite, basalt, etc.) mines in Kayseri, marble mines in Yozgat
8. Marble, calcite, mercury, antimony, iron, copper-lead-zinc, gypsum mines in Niğde
9. Marble, natural stone (andesite, basalt, etc.), zinc, iron, lead, chromite, limestone, pumice, in Kayseri and chromite and iron mines in Adana
10. Limestone, celestite, gypsum, marble, chromite, salt water, ballast (andesite, basalt, etc.) and talc mines in Sivas
11. Chromite, iron and manganese mines in Erzincan
12. Marble, limestone, iron and gypsum mines in Malatya
13. Limestone, barite, and chromite mines in Adıyaman
14. Marble, barite, dolomite mine sites in Mersin
15. Limestone, dolomite and barite mines in Erdemli (Mersin)
16. Limestone and zinc mines in eastern Mersin and quartzite and limestone mine sites in Pozantı (Adana)
17. Crushed stone and sand quarries in Gaziantep (Provincial Environmental Status Report, 2010). This region also includes north of Aleppo in where bomb blasts have happened because of civil war in Syria.
18. Limestone, dolomite and marble mine sites in Şanlıurfa and bomb blasts in Syria.
19. Ballast quarries in Kyrenia Mountains in Cyprus (Necdet and Göker, 1996; LGC News, 2018).

Additionally, quarry contamination detection map is plotted for the events with  $M \geq 3.0$  to see if areas characterized by large magnitude blasts still remain (Figure 2.8). The resultant map shows no sign of blast, indicating that the catalog including events with  $M \geq 3.0$  is free from any blast contamination. Therefore, the contaminated data ( $M < 3.0$ ) with a total number of 18116 events out of 23096 events are removed from the declustered catalog. Note that the resultant catalog with a total of 4980 events is studied in the following stages.

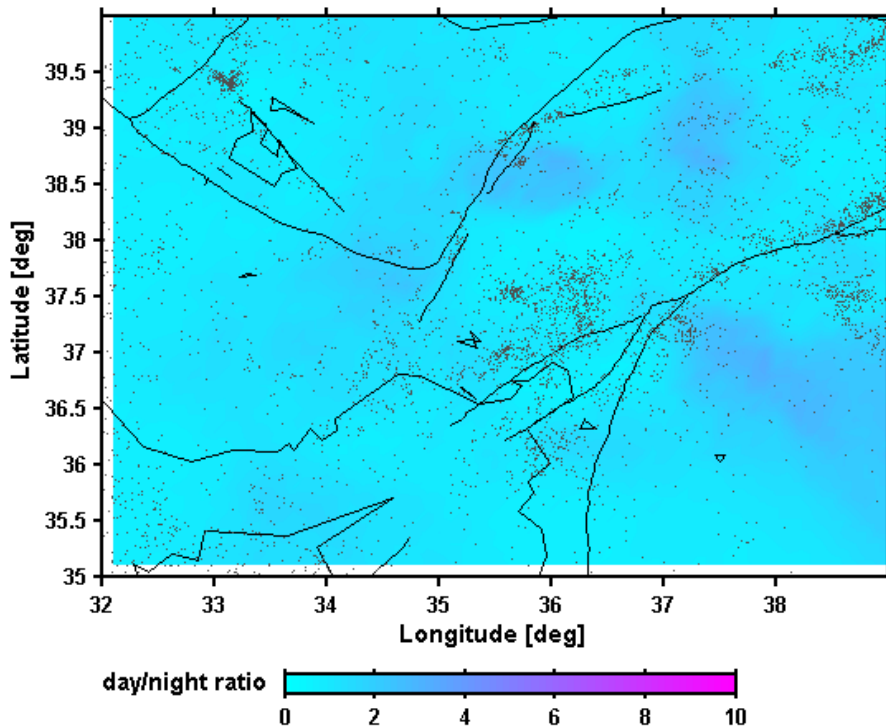


**Figure 2. 8** Quarry contamination detection map for the earthquakes with  $M \geq 3.0$ .

### 2.3.2.3 Earthquake Statistics

The estimation of earthquake hazard in related regions is very important for engineering projects. Probabilistic seismic hazard analysis is the most well-known method for this evaluation which needs the input parameter of the relative size distribution of earthquakes. First, Ishimoto and Iida (1939) in Japan and later Gutenberg and Richter (1944) in the USA appraised a power-law relationship to describe the size distribution of earthquakes also known as the Frequency Magnitude Distribution (FMD)

$$\log_{10} N = a - bM \quad (1)$$

where  $N$  is the expected total number of earthquakes occurring in a region in a specific time period related to their magnitude,  $M$  and the  $a$ - and  $b$ -values are the constants.

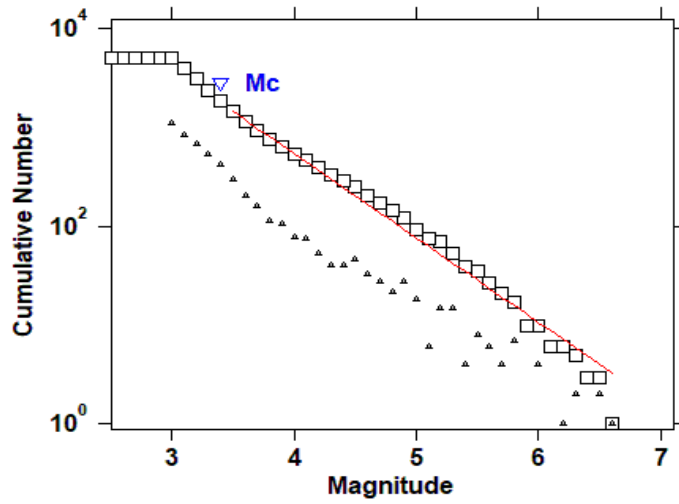
The a-value is the intercept which represents the seismic rate and differs extremely from region to region. On the other hand, the b-value is equal to the slope of the best-fit line of the frequency–magnitude distribution (FMD) equation and so related to the relative size distribution of earthquakes (Sanchez et al., 2004; Kalyoncuoğlu, 2006).

Since the b-value is known as the seismicity parameter, many research study publications are available for it in the literature. Aki (1965) claimed that b-value has an inverse proportion with the average fault length rupturing in the earthquake (Sanchez et al., 2004). According to Kalyoncuoğlu (2006) paper; Utsu (1965) claimed that the b-value is almost same for both large and small earthquakes in the world. Evernden (1970) estimated a global range for b-value between 0.8 and 1.2. Many researchers assigned b-values for specific regions such as Sweden (Bath, 1983), central California (Turcotte, 1986; Shi and Bolt, 1982), China (Wang, 1994), East African rift system (Kebede and Kulhanek, 1994). The b-value is practically assumed as close to 1 in the Earth's crust and computed as closer to 2 in the volcanic areas (Sanchez et al., 2004 and references therein). However, Frohlich and Davis (1993) suggested that b-value is more or less unity in seismically active regions. Many researches denoted that b-value has a dependency of the spacing or clustering of epicenters or fault segment distribution (Huang and Turcotte, 1988; Lapenna et al., 1998; Nanjo et al., 1998). Wiemer et al. (1998) claimed that the increase in b-value occurs with depth in volcanic regions, while it decreases with depth in non-volcanic regions. Wyss et al. (2000) suggested that the b-value has no systematic relation with depth. Manakou and Tsapanos (2000) suggested that low b-values correspond to large faults because of low heterogeneity, large strain rate and high velocity for the deformation. According to Main et al. (1992) high heterogeneous areas with low stress intensity are responsible for the higher b-values.

Besides these seismotectonic implications of b-value, an incomplete catalog can also cause substantial deviations in b-value. Missing events are mostly increasing with narrowing magnitude range which results in decrease of b-value for small-magnitude events (Kalyoncuoğlu, 2006; and references therein). A minimum magnitude known

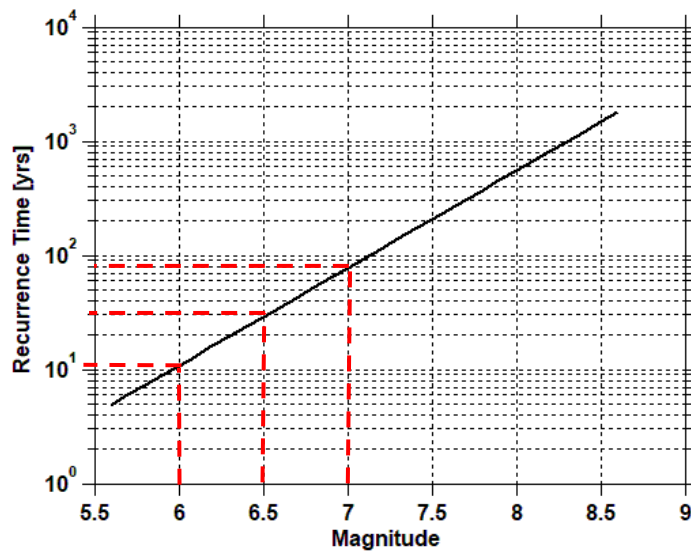
as the magnitude of completeness,  $M_c$  exists in all catalogs above which there is a 100% chance of recording all the earthquakes (Sanchez et al., 2004).

The maximum likelihood method is used to calculate b-value by ZMAP software which results in more constant mean values and more symmetric distribution of b-values in comparison with the weighted least squares approach as the other commonest method (Wiemer and Wyss, 1997). FMD calculation is applied for the catalog ( $M \geq 3.0$ ) declustered by Reasenber (1985) method. The a- and b- values are plotted in Figure 2.9a and calculated as 0.85 and 6.14, respectively. High a-values denote relatively high earthquake productivity and high b-values are corresponding to continuously releasing stress pattern related to small earthquakes occurring in the region. The return periods of earthquakes with different magnitudes are shown in Figure 2.9b. The occurrences of earthquakes with magnitudes 6.0, 6.5 and 7.0 are calculated as 10, 30 and 80 years, respectively. The earthquakes greater than 7.0 magnitudes are expected to occur within every ~100 years. This analysis indicates a remarkable earthquake hazard potential in the study area.



Maximum Likelihood Estimate, Uncertainties by bootstrapping  
 b-value =  $0.85 \pm 0.09$ , a value = 6.14, a value (annual) = 4.08  
 Magnitude of Completeness =  $3.4 \pm 0.29$

a)



b)

**Figure 2. 9** (a) Cumulative frequency – magnitude distribution (FMD) plot and (b) recurrence time of earthquakes with different magnitudes occurred in the study area.

**2.3.2.4 Focal Mechanisms**

The focal mechanism solutions of the earthquakes occurred in the study area are compiled from the literature for the years 1938 – 2017 and this compiled catalog data is comprising of 171 events. The distribution of focal mechanism solutions has an important role in describing the tectonic stress field properties in the region. The catalog is plotted on the map (Figure 2.10) and the list of the solutions is represented in Table A.1 including the references of each focal mechanism solution.

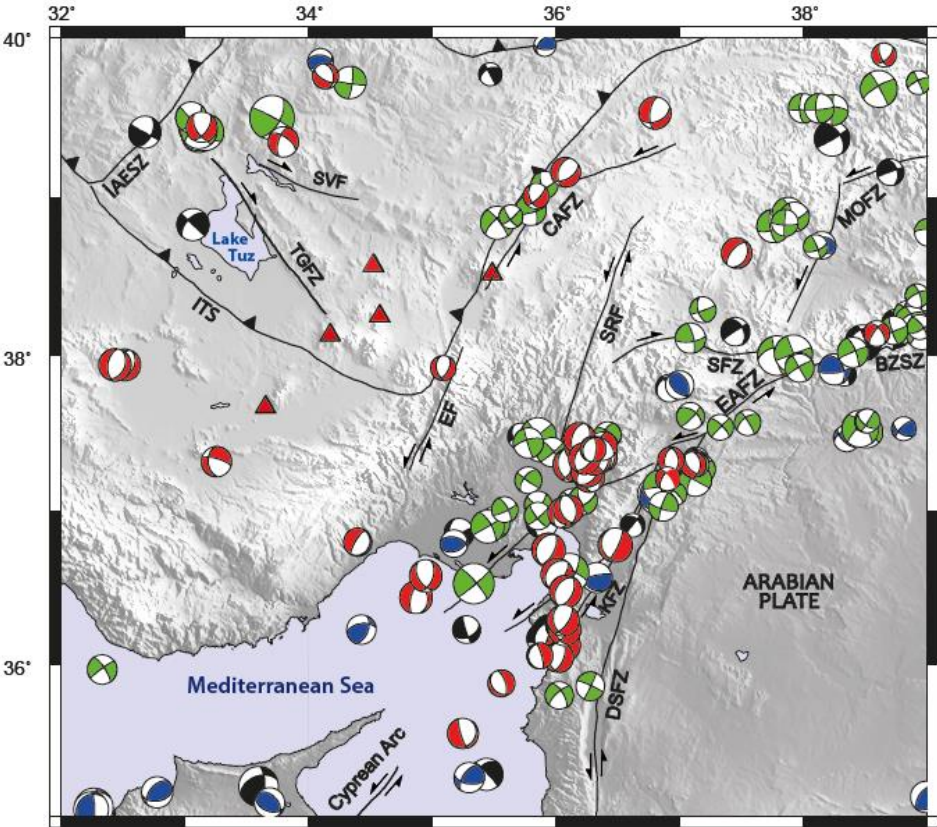


**Figure 2. 10** Map view of the distribution of focal mechanism solutions for 171 events in the study area. Focal mechanism symbols are scaled to their magnitudes. Focal mechanism colors are grouped as; red: NF and NS; green: SS; blue: TF and TS; black: unidentified. (References are given in Table A.1). Red triangles show Holocene volcanoes (taken from Abgarmi et al., 2017). Labels are explained in Figure 2. 1.

It is clearly seen that the spatial variation of focal mechanism solutions is directly associated with active seismic structures in the study area and their type of mechanisms are corresponding to the ongoing tectonic stress field along the faults. The study area is dominantly under the effects of strike-slip and normal faulting indicating the predominant extensional forces in the region. Some solutions are normal faults with strike-slip components and some are strike-slip faults with normal components. There are minor amounts of reverse faulting with strike-slip components along the Cyprean Arc and Bitlis – Zagros Suture Zone due to the subduction.

The focal mechanisms are mostly concentrated along the EAFZ as an indication of the most seismically active structure in the region. Along the EAFZ, the focal mechanisms are generally left-lateral in NE-SW trending whereas the northern branch of EAFZ in the Gulf of Iskenderun is mainly represented by sinistral NE-SW trending strike-slip faulting, and the southern branch dominantly consists of normal faults with NS orientation. There is a complex region where the EAFZ, BZSZ and DSFZ coincide with each other leading to the combination of strike-slip, normal and slightly reverse faulting. The CAFZ region is characterized by NE-SW trending normal faulting with strike-slip component and left-lateral strike-slip mechanism with normal component. The northern part of TGFZ is involving NS trending normal faulting with minor strike-slip component and sinistral strike-slip solutions in SW direction. The cluster in the north of MOFZ is dominated by E-W trending left lateral strike-slip faults and there are few approximately N-S trending normal faults with minor strike-slip component. On the other hand, there are reverse solutions with strike-slip component generally trending N-S and NE-SW direction in Cyprus region which are related to Cyprean Arc.

The faulting types are plotted in ternary diagram based on rake values and their distribution pattern can be seen in Figure 2.11. The diagrams show that the transtensional stress regime is dominant in the region since both the strike slip and the normal faulting mechanism are the most common. According to P- and T-axes orientations of these earthquakes which are plotted on lower hemisphere projection (Figure 2.12), the region is under the regime of N-S compression, and E-W extension.

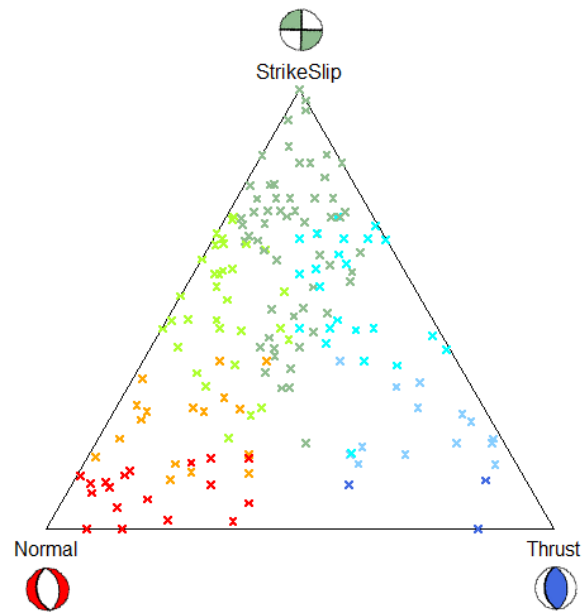


**Figure 2. 11** Rake based ternary diagram of the focal mechanism catalog with 171 data.

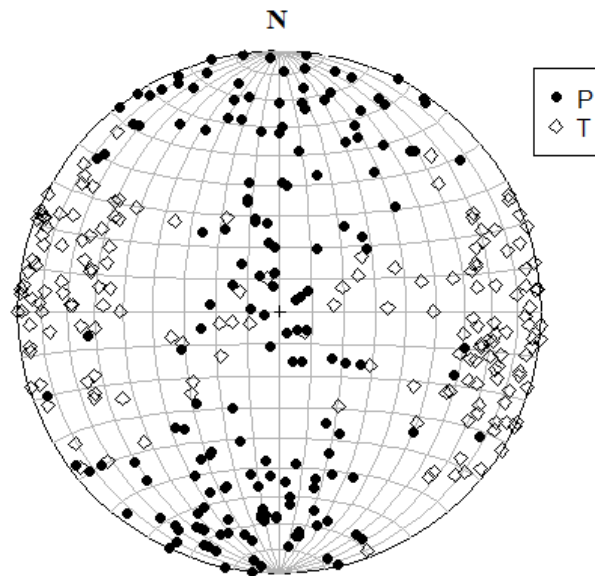


**Figure 2. 12** P- and T- axes orientations of 171 earthquakes occurred in the study area between 1938 – 2017. Black diamonds show P-axis and white diamonds indicate T-axis.

## CHAPTER 3

### REGIONAL MOMENT TENSOR INVERSION ANALYSES

#### 3.1 Methodological Background

##### 3.1.1 Focal Mechanism

In seismology, to determine the characteristics of a seismic source is a major case for research studies. Earthquake focal mechanism solutions allow researchers to reach valuable information about the stress of the Earth's crust. Spatially well-distributed seismograms record the amplitudes and shapes of radiated seismic waves at various distances and azimuths to construct an appropriate focal mechanism diagram which releases information about the fault geometry and slip amount, slip direction, origin time, focal depth, epicentral location, size of the earthquake. This analysis is known as focal mechanism (Stein and Wysession, 2003). In the literature there are numerous methods to estimate focal mechanisms such as first motion (polarity) of P- and S-waves (body waves), waveform modeling and moment tensor inversion (e.g., Stein and Wysession, 2003). All these methods are commonly utilizing the pattern of radiated seismic rays which are affected by the fault orientation and slip direction (Barth et al., 2008).

The first motion polarity is accepted as the simplest method which is based on the idea of the direction of the first P-wave arrival which differs depending on the location of the seismic station and related seismic source. The sphere of focal mechanism is divided into four quadrants with two compressional and two dilatational (Figure 3.1).

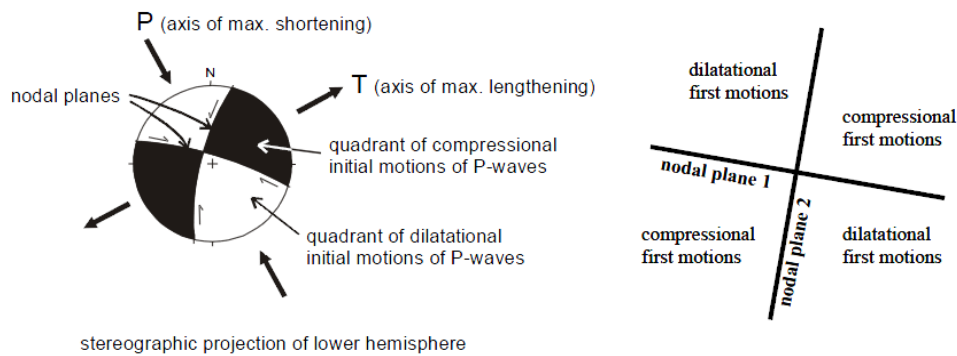
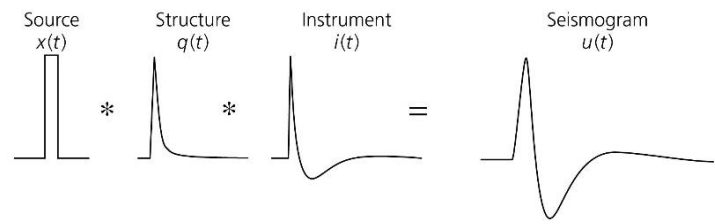


**Figure 3. 1** The focal mechanisms and their related fault geometries (taken from Barth et al., 2008).

The black colored quadrant regions symbolize the compressional P-wave motions including the maximum lengthening axis which is called as tension axis (T). The white quadrant regions stand for the tensional T-wave motions with the maximum shortening stress direction which is known as the pressure axis (P). The compressional quadrants are characterized by the “upward” motion of the first waves where they are recorded “toward” the receiver. Contrarily, the extensional (dilatational) quadrants are the “downward” regions where the first waves in the ground are recorded “away” from the station. The boundaries between the compressional and dilatational quadrants are called as nodal planes which are perpendicular to each other and defining the direction of fault geometry. One of the nodal planes is the fault plane and the other becomes the auxiliary plane which is known as intermediate stress axis (B) or null axis.

On the other hand, waveform modeling compares the observed body waves and surface waves and the synthetic waveforms which are created by a forward modeling or an inversion technique to determine a best fitting model for the data. The determination of the depth of earthquakes and the rupture processes can be done by waveform modeling rather than the first motion method. The created synthetic waveforms are composed of ground motion records such as the earthquake source, the earth structure, and the seismometer as indicated below:



$$x(t) * q(t) * i(t) = u(t) \quad (2)$$

where  $x(t)$  is the source time function corresponding to the signals that are penetrated into the ground,  $q(t)$  is indicating the impacts of the earth structure that the waves are propagating through,  $i(t)$  is the instrument response of the seismometer to the ground motion for different frequencies (Stein and Wysession, 2003).

The source time function can be defined as the signals of an earthquake source which are known as body-wave pulses generated by the earthquake rupture. In real life, faults are resulted in complex source time functions rather than impulses at each point. Since each point does not break at the same time and slip is not instantaneous along a finite fault, the total signal cannot be accepted as an impulse. To simplify the case, the earthquake is accepted as a single point source and represented by a ramp function which models the displacement on the fault as a ramp. The slip starts at time zero and ends at the rising point in ramp function model. So, the length of finite faults is estimated as the sum of the total number of earthquake point sources with rise and rupture times (Stein and Wysession, 2003; Clinton, 2004).

### 3.1.2 Seismic Moment Tensor

The seismic moment tensor is simply the mathematical representation of a seismic source and allows researchers to know about the rupture process and the fault source parameters by inversion modeling. The most significant feature of the moment tensor is giving a complete definition of equivalent forces of a seismic point source. The observed seismic waves can be created when they release energy rapidly through the earth in the seismic wave frequency band. The rapid release is required to activate the propagating seismic waves; otherwise slow deformations in the crust is recorded by

other methods (Stein and Wysession, 2003). Figure 3.2 shows all the equivalent forces of a single force, single and double couple forces.

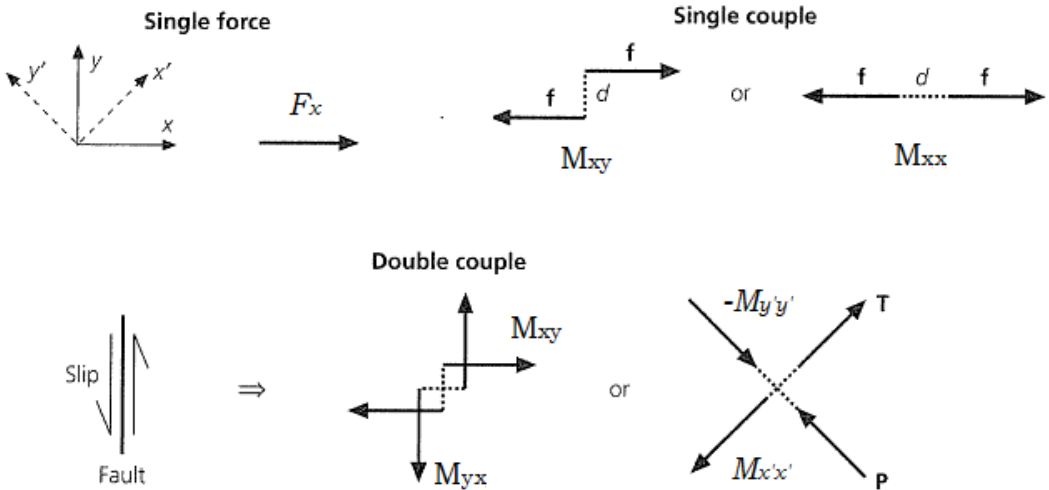


**Figure 3. 2** Equivalent body forces in 2D fault geometry.  $M_{xx}$  is force dipole with no torque exerted.  $M_{xy}$  represents the forces with torque. Slip on a fault can be expressed by superposition of couples like  $M_{xy}$  and  $M_{yx}$  or dipoles like  $M_{x'x'}$  and  $M_{y'y'}$  with their pressure (P) and tension (T) axes (Stein and Wysession, 2003).

Single force events include earthquakes related to the release of gravitational potential energy such as landslides, collapse of caverns, volcanic eruptions, and explosions. Fukao (1995) identifies non-tectonic earthquakes triggered by the release of energy rather than elastic strain energy, and all the released energy is used in seismic processes without static strain energy conversion. These events can better be explained by single-forces corresponding to a case where the source is buried and completely enclosed by the dislocation surface (Fukao, 1995).

Single couples are the first earthquake source models which are composed of a pair of force acting together, used in the early 1950s until the recognition that this model cannot explain the S-wave radiation (Şen, 2014; and references therein). Single-couple model states that the earthquakes occurring due to slip on a fault and this slip is similar

to the single couple including two forces with the motions on opposite sides of the fault (Aki and Richards, 2002). Because the single couple does not have zero total force and moment, it could not continue to represent a shear fracture or an internal source (Udias et al., 2014).

The double couple is first established in the early 1960s and modeling the radiated energy pattern at the earthquake source. This model is based on two force couples with equal moments in opposite directions. These force couples are normal to each other and generates no net moment (Aki and Richards, 2002). The double couple assumes that a slip occurs along the single fault with a single motion direction. The double couple of equivalent body forces acting on the fault plane in an isotropic medium are represented in Figure 3.3 considering their varying combinations.

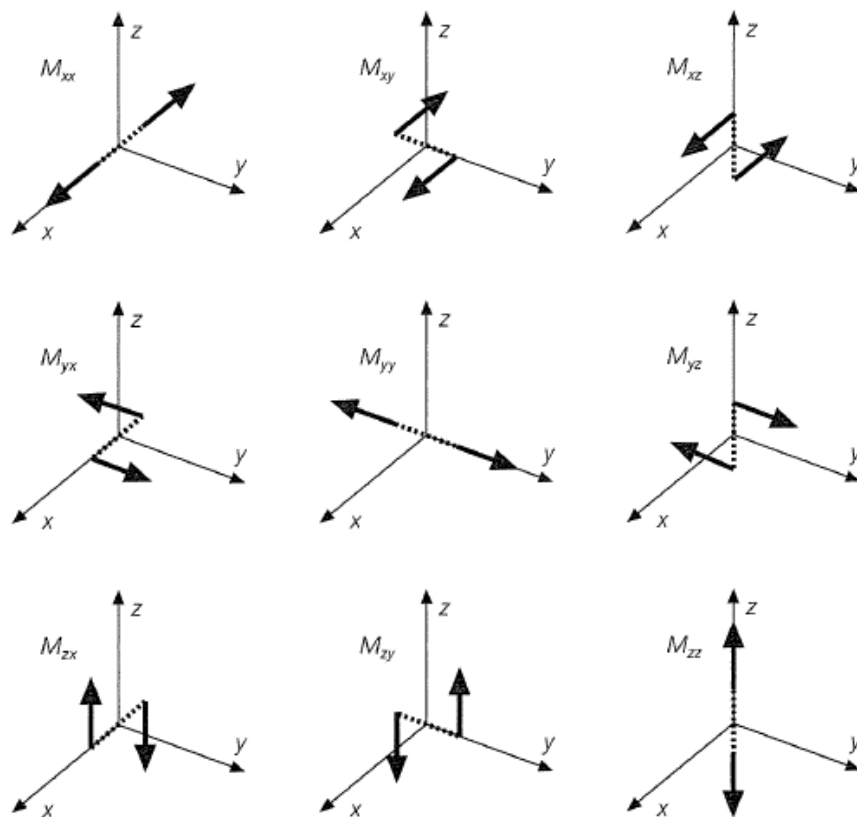


**Figure 3. 3** The force couples showing the components of seismic moment tensor (from Aki and Richards, 1980).

Scalar seismic moment tensor of the earthquake ( $M_0$ ) is the magnitude of body-force equivalents which is associated with the size of the event and has dimensions of torque.

The seismic moment tensor,  $M$  whose components are body-force equivalents can be defined by a 3 x 3 matrix as follows:

$$M = \begin{bmatrix} M_{xx} & M_{xy} & M_{xz} \\ M_{yx} & M_{yy} & M_{yz} \\ M_{zx} & M_{zy} & M_{zz} \end{bmatrix} \quad (3)$$

According to the law of momentum conservation, the non-diagonal elements should be symmetric leaving six independent pairs (Aki and Richards, 2002). Rotating the moment tensor into an eigenvector system by matrix diagonalization thus results in three forces: the pressure (P) axis, the tension (T) axis, and the null (B) axis, with eigenvalues,  $\lambda_T \geq \lambda_B \geq \lambda_P$ , respectively (Barth, 2007; and references therein). P- and T-axes are known as the directions of the compressional and dilatational quadrants, respectively; whereas B-axis is parallel to the direction of two nodal plane intersection.

The analysis of eigenvalues and eigenvectors give information about the equivalent forces of the moment tensor (Okal, 2011). To define the moment tensor of a fault, the definitions of the normal and slip vectors which are normal vectors of two nodal planes are used regarding to strike, dip and slip directions as in the following:

$$\begin{aligned} M_{xx} &= -M_0(\sin \delta \cos \lambda \sin 2\phi + \sin 2\delta \sin \lambda \sin^2 \phi) \\ M_{yy} &= M_0(\sin \delta \cos \lambda \sin 2\phi - \sin 2\delta \sin \lambda \cos^2 \phi) \\ M_{zz} &= M_0(\sin 2\delta \sin \lambda) \\ M_{xy} &= M_0(\sin \delta \cos \lambda \cos 2\phi + \frac{1}{2}(\sin 2\delta \sin \lambda \sin 2\phi)) \\ M_{xz} &= -M_0(\cos \delta \cos \lambda \cos \phi + \cos 2\delta \sin \lambda \sin \phi) \\ M_{yz} &= -M_0(\cos \delta \cos \lambda \sin \phi - \cos 2\delta \sin \lambda \sin \phi) \end{aligned} \quad (4)$$

The sum of eigenvalues denotes the volume change of the source. If the sum of eigenvalues is  $M > 0$ , moment tensor is called isotropic representing a volume change.

The eigenvector of the maximum eigenvalue is introduced by the T-axis, as the minimum eigenvalue leads to the P-axis, and the intermediate is represented by B-axis (Bock, 2012). If the sum of eigenvalues is  $M = 0$ , the moment tensor has only deviatoric components which is divided into major and minor double couple; or a double couple (DC) and a compensated linear vector dipole (CLVD) (Jost and Herrmann, 1989; and references therein).

$$\begin{aligned}
M_{\text{dev}} &= \begin{pmatrix} \lambda_1 & 0 & 0 \\ 0 & \lambda_2 & 0 \\ 0 & 0 & \lambda_3 \end{pmatrix}; |\lambda_1| \geq |\lambda_2| \geq |\lambda_3| \\
&= \begin{pmatrix} \lambda_1 & 0 & 0 \\ 0 & -\lambda_1 & 0 \\ 0 & 0 & 0 \end{pmatrix} + \begin{pmatrix} 0 & 0 & 0 \\ 0 & -\lambda_3 & 0 \\ 0 & 0 & \lambda_3 \end{pmatrix} \\
&\quad \text{major DC} \qquad \qquad \text{minor DC} \\
&= \begin{pmatrix} \frac{2\lambda_1 + \lambda_3}{2} & 0 & 0 \\ 0 & -\frac{2\lambda_1 + \lambda_3}{2} & 0 \\ 0 & 0 & 0 \end{pmatrix} + \begin{pmatrix} -\frac{\lambda_3}{2} & 0 & 0 \\ 0 & -\frac{\lambda_3}{2} & 0 \\ 0 & 0 & \lambda_3 \end{pmatrix} \quad (5) \\
&\quad \text{DC} \qquad \qquad \qquad \text{CLVD}
\end{aligned}$$

The double couple percentage,  $p$  can be calculated from the ratio of the minimum eigenvalue to the maximum eigenvalue or minor to major double couple moments:

$$p = (1 - 2\varepsilon) * 100\% \qquad \varepsilon = \frac{|\lambda_3|}{|\lambda_1|} = \frac{|M_{0\text{min}}|}{|M_{0\text{max}}|} \quad (6)$$

The most stable part of a moment tensor is the double couple (DC) component, a high  $p$  value means a high DC-percentage with a stable result. To obtain a pure CLVD system,  $p = 0\%$  which means  $\varepsilon = 0.5$ . To get a pure DC system,  $p$  should be 100% and  $\varepsilon = 0$ . It is important to note that earthquake source locations errors, presence of lateral heterogeneities and the rupture plane variations may lead to unstable inversion and thus low DC-percentage (Barth, 2007; Zhang and Lay, 1990). The force couple systems, moment tensors and radiation patterns of these moment tensors are shown in Figure 3.4.

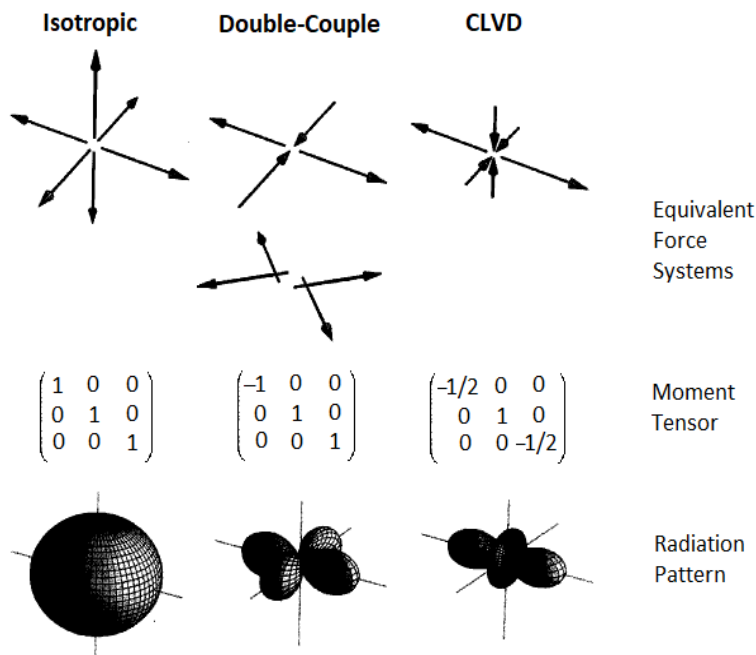


**Figure 3. 4** Force systems, moment tensors and radiation patterns of sources (Julian et al, 1998).

Moment tensors can be represented by stereographic projections. Figure 3.5 denotes the representative moment tensors and their focal mechanisms. The first row is showing isotropic moment tensor (an explosion on the left and an implosion on the right). The second, third and fourth rows are examples of pure double-couple mechanisms. The second row shows a left lateral strike-slip N-S on the left and NW-SE on the right. The third row is vertical dip-slip with the strike E-W on the left and N-S on the right. The fourth row indicates a 45° dipping pure reverse striking E-W on the left and N-S on the right. The last two rows stand for CLVD sources (Stein and Wysession, 2003).

Moment tensor	Beachball	Moment tensor	Beachball
$\frac{1}{\sqrt{3}} \begin{pmatrix} 1 & 0 & 0 \\ 0 & 1 & 0 \\ 0 & 0 & 1 \end{pmatrix}$		$-\frac{1}{\sqrt{3}} \begin{pmatrix} 1 & 0 & 0 \\ 0 & 1 & 0 \\ 0 & 0 & 1 \end{pmatrix}$	
$-\frac{1}{\sqrt{2}} \begin{pmatrix} 0 & 1 & 0 \\ 1 & 0 & 0 \\ 0 & 0 & 0 \end{pmatrix}$		$\frac{1}{\sqrt{2}} \begin{pmatrix} 1 & 0 & 0 \\ 0 & -1 & 0 \\ 0 & 0 & 0 \end{pmatrix}$	
$\frac{1}{\sqrt{2}} \begin{pmatrix} 0 & 0 & -1 \\ 0 & 0 & 0 \\ -1 & 0 & 0 \end{pmatrix}$		$\frac{1}{\sqrt{2}} \begin{pmatrix} 0 & 0 & 0 \\ 0 & 0 & -1 \\ 0 & -1 & 0 \end{pmatrix}$	
$\frac{1}{\sqrt{2}} \begin{pmatrix} -1 & 0 & 0 \\ 0 & 0 & 0 \\ 0 & 0 & 1 \end{pmatrix}$		$\frac{1}{\sqrt{2}} \begin{pmatrix} 0 & 0 & 0 \\ 0 & -1 & 0 \\ 0 & 0 & 1 \end{pmatrix}$	
$\frac{1}{\sqrt{6}} \begin{pmatrix} 1 & 0 & 0 \\ 0 & -2 & 0 \\ 0 & 0 & 1 \end{pmatrix}$		$\frac{1}{\sqrt{6}} \begin{pmatrix} -2 & 0 & 0 \\ 0 & 1 & 0 \\ 0 & 0 & 1 \end{pmatrix}$	
$\frac{1}{\sqrt{6}} \begin{pmatrix} 1 & 0 & 0 \\ 0 & 1 & 0 \\ 0 & 0 & -2 \end{pmatrix}$		$-\frac{1}{\sqrt{6}} \begin{pmatrix} 1 & 0 & 0 \\ 0 & 1 & 0 \\ 0 & 0 & -2 \end{pmatrix}$	

**Figure 3. 5** Examples of moment tensors and their stereographic focal mechanism plots (Stein and Wyssession, 2003).

Some complicated tectonic environments can be source for CLVD mechanism. For instance, the inflation of a magma dyke in tectonic areas are modeled as a crack opening under tension. Multiple faulting events can cause the formation of CLVD mechanism which occur in volcanic areas where faulting meets with magmatic processes. The locations of two ordinary double-couple earthquakes are very close to each other, their seismic signals are superposed and thus create a CLVD source in that region. Additionally, moment tensor inversion analysis is not good at solving isotropic component of shallow earthquake, thus the seismic wave pattern will be more similar to CLVD (Stein and Wyssession, 2003).

### 3.2 Moment Tensor Inversion

The valuable information about earthquakes such as tectonic regime, fault type, source location, origin time, moment magnitude and focal mechanism can be analyzed from seismic moment tensors, so that accurate and quick estimations of moment tensors are extremely important in source parameter studies. The centroid moment tensor (CMT) is the quantitative calculation of focal mechanisms and has two types:

**Global Centroid Moment Tensor (CMT):** It works on moderate – large earthquakes by using their waveform data taken from global broadband seismic networks (Bonita et al., 2015). CMT catalog moment tensors are systematically calculated for the earthquakes with  $M > 5.0$  up to four-month delay. The moment tensors for earthquakes with  $M > 5.5$  are determined rapidly and spread quickly which are known as quick CMTs.

**Regional Centroid Moment Tensor (RCMT):** It determines the seismic source characteristics by well-defining the earthquake size and source geometry. The RCMT modified algorithm is set up to model intermediate surface waves for moderate events ( $\sim 4.5 < M < 5.5$ ) at regional distance by considering the intermediate surface waves and also body waves. The surface waves in the inversion are filtered by 35-60 s, due to magnitude. The body waves are modelled separately and simultaneously. In body wave modelling, 3D heterogeneous mantle structure is included whereas global phase velocity maps are preferred for surface waves (Pondrelli et al., 2012; and references therein).

In this study, regional centroid moment tensor inversion is performed using seismograms are recorded at regional distance by temporary CAT seismic network to study the present-day seismicity in Central Anatolia which led to 29 new regional CMTs solutions calculated for the events with the magnitudes between 3.5 – 4.6 during 2 years period (2013 – 2015).

### 3.2.1 Methodology

In this study, the moment tensor inversion analysis is executed by ISOLA (ISOLated Asperities) program package (Sokos and Zahradnik, 2008). ISOLA code uses multiple point-source approach and iterative deconvolution method (Kikuchi and Kanamori, 1991) by considering the full-wave seismograms to evaluate the correlation between observed and synthetic waveforms for the determination of the centroid moment tensor (Zahradnik and Sokos, 2016).

The synthesized seismograms are determined in terms of three trigonometric parameters of strike, dip and slip angle which makes the equation harder to be solved by forward modeling. Thus, this problem can be solved in a much easier way by inverse modeling with the formula:

$$u_i(t) = \sum_{j=1}^6 G_{ij}(t)m_j \quad (7)$$

In Equation 6, the sum of Green's function is in terms of the source indicated by vector,  $m$  with components of moment tensor; and the seismogram of  $i^{\text{th}}$  seismometer shown by  $G_{ij}(t)$  including the Earth structure between the source and the receiver.

The Green's function can calculate the boundary conditions by the evaluation of Bouchon's (1981) discrete wavenumber method. Since there are plenty of seismograms in the analysis, this equation is proposed as a vector-matrix;

$$u = Gm \quad (8)$$

where  $u$  is the data vector,  $G$  is the Green's function matrix and  $m$  is the model vector. Since the  $G$  has not a square structure, it cannot be inverted into a matrix. The seismograms are linear functions and their inversion is possible to estimate the best fitting moment tensor components for the observed seismograms in terms of the least squares method by using generalized inversion,  $G$ ;

$$m = (G^T G)^{-1} G^T u \quad (9)$$

where T and -1 indicate transposition matrix and inversion of the system matrix ( $G^T G$ ), respectively. The inversion process is technically carried out by ISOLA software to calculate the predicted seismograms by processing the observed seismograms (Krizova et al., 2013). The correlation between the observed (u) and the synthetic (s) seismograms can be improved by the grid search method. The grid search looks for the minimum residual error for the trial source position by the least square method. The best-fitting result between real (observed) and predicted (synthetic) seismograms will be measured by the L2-norm misfit equation;

$$\text{misfit} = \int (u - s)^2 \quad (10)$$

ISOLA user can make an optimization by predefining a set of trial source positions and time via the grid search method. This optimization process can be applied to every point which are known as subevents of complex source models.

This point source contribution to the model is called as subevent which are calculated by ISOLA in terms of the iterative deconvolution (Kikuchi and Kanamori, 1991). The codes search for the subevent 1, and find it by fitting the data as well as possible. Once a subevent is found, the corresponding synthetics are subtracted from the real data and thus the residual data is obtained. Next, the residual data is processed in the same way and subevent 2 is found, etc. Thus the resulting synthetic seismogram is estimated by the original data minus the last residual seismogram. This iterative application gives a single (best-fitting) set of subevents.

To understand the quality of waveform fit between the observed and synthetic data, variance reduction (VR) is calculated by the formula in terms of observed and the synthetic waveforms;

$$VR = 1 - \frac{\sum_k (obs_k - syn_k)^2}{\sum_k obs_k^2} \quad (11)$$

VR quantifies the improvement of fit between observed and synthetic waveforms and can also be written in terms of correlation ( $\text{Corr}^2 = \text{VR}$ ). It is worth to note that the fit of waveforms with large amplitudes and usage of limited waveforms may result in misleading high variance reductions.

The condition number (CN) is another control point for the solution quality and directly related to observed waveforms ( $u$ ) and model parameter ( $m$ ). Thus, it is estimated from the Green's function matrix ( $G$ ) as the ratio between maximum and minimum singular values of  $G$ . As ISOLA does not decompose  $G$  in its singular values, condition number is estimated from;

$$\text{CN} = \sqrt{\frac{\text{max}_{eigenval}}{\text{min}_{eigenval}}} \quad (12)$$

where  $\text{max}_{eigenval}$  and  $\text{min}_{eigenval}$  are the maximum and minimum eigenvalues of  $(G^T G)$ , respectively. There is a reverse relationship between CN and the quality of the inversion.

The variability of focal mechanism solutions is a measurement for the solution quality in the close region of the solution in terms of source position and time. This spatial temporal variation of correlation and focal mechanism is named as correlation plot in ISOLA (Sokos and Zahradnik, 2013). The correlation plot has two attributes: FMVAR and STVAR. The focal mechanism variability index (FMVAR) is the stability of focal mechanism in spatial temporal grid search within a highly correlated region. The space – time variability index (STVAR) is the stability of the source position and time plot of the solutions within a given correlated region. Small values of FMVAR and STVAR are preferable for stable inversions (Sokos and Zahradnik, 2013; Michele et al., 2014).

Besides focal mechanism and moment magnitude, the centroid depth estimation is another important product of the moment tensor inversion. The grid search method determines the centroid depth which is known as the center of gravity of the faulted area. For smaller events, centroid and hypocenter positions are very close to each other. The centroid depth determination is more difficult and more reliable than the centroid

position, because the depth calculation is dependent on P and S wave records from the near stations. When the spatial resolutions of long waves are limited, the centroid position is also uncertain (Zahradnik and Jansky et al., 2008; Sokos et al., 2012).

### **3.2.2 Data**

Moment tensor solutions of the earthquakes are estimated from the inversion of regional broadband seismograms. The bandpass-filtered broadband seismograms are recorded by 71 stations of CDCAT Project seismic network. The station locations and their codes can be seen in Table A.2. The complete 3-component broadband waveforms are used with the motion directions of up-down, north-south and east-west. These records are operated without separating the wave groups as P, S or L in which the surface waves are dominant. First, the BHZ, BHE and BHN components of waveforms were synchronized due to their reference times. P-arrivals were picked up automatically in Seismic Analysis Code (SAC) program (Goldstein et al., 2003) and the data was cut 50 s before and 200 s after the P-onset to window the signal. The mean and trend in the dataset were removed and taper was applied to exclude the artifact signals during processing. The bandpass filter is applied between 0.05 and 2 Hz to remove unwanted data. The plots of raw and processed data for the event 22.02.2014 are given in Figure 3.6 as an example.

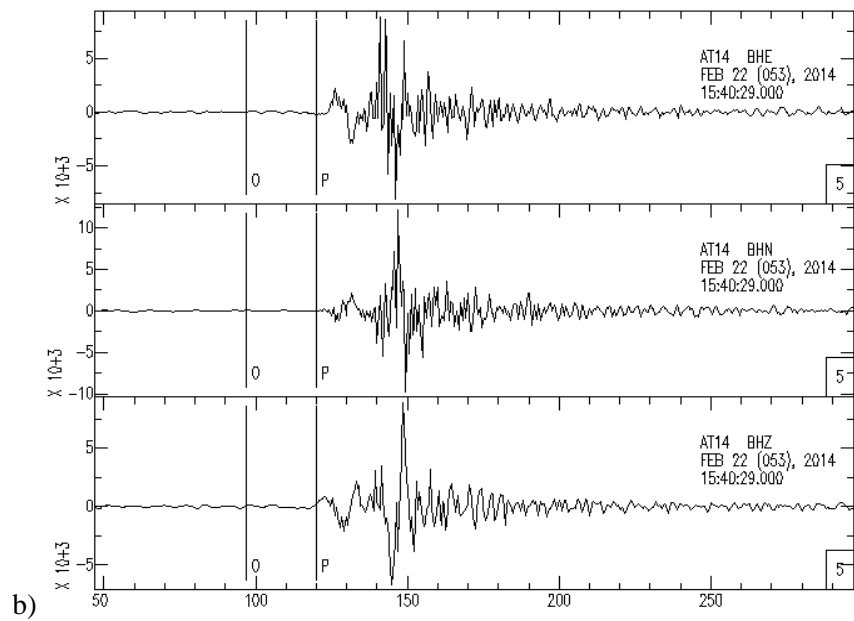
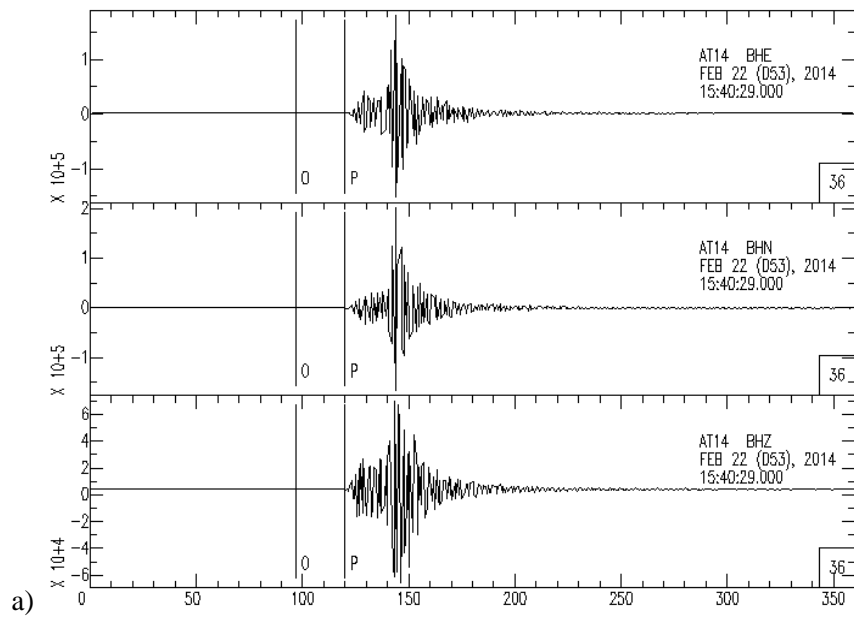


**Figure 3. 6** (a) raw and (b) processed three component broadband seismic waveforms of the event 22.02.2014.

The SAC formatted waveform records are converted to ASCII format via ISOLA program. To remove the instrument response, ISOLA creates files of poles, zeros and A0 which is known as normalization constant for instrument correction in the data. A complex transform function is applied to the complex waveform record to convert it into time. As event information, the hypocenter position is entered to the program with the latitude, longitude and depth of the event. The origin time is accepted as time zero and shifted 20 s before the true hypocenter time which means a decrease in origin time by 20 s shift to the right side of  $t=0$  to escape from numerical complications. During data selection, only events recorded with a good azimuthal coverage ( $> 120^\circ$ ) are used. Among recording stations, the ones with similar epicentral distances are preferred to stabilize the inversion. The distance between the epicenters and the station locations is not exceeding 300 km in this study. According to Zahradnik and Jansky et al. (2008), the waveforms have less impact on the crustal model for relatively near-regional epicentral distances ( $<300$  km) and for low frequencies. Thus, a simplified Preliminary Reference Earth Model (PREM) (after Dziewonski and Anderson, 1981) is utilized and shown in Figure 3.7 and the values of velocity in terms of depth are tabulated (Table 3.1).

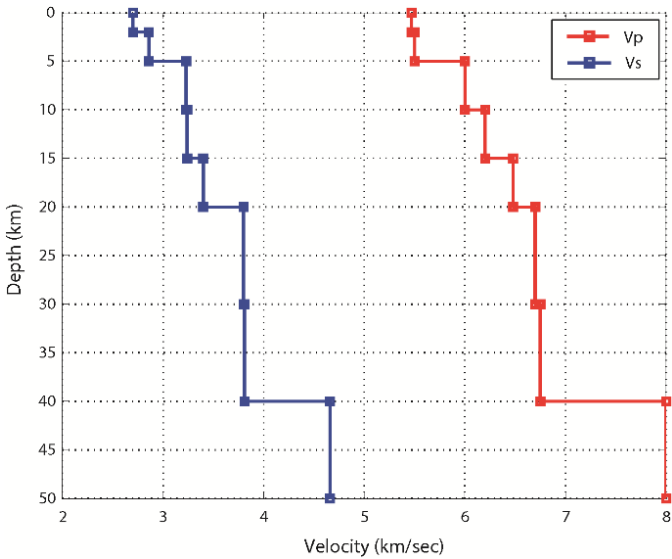


**Figure 3. 7** Plot of P and S wave velocities of global PREM model (simplified from Dziewonski and Anderson, 1981).

**Table 3. 1** Tabulated form of global PREM model (simplified from Dziewonski and Anderson, 1981).

<b>Depth (km)</b>	<b>Vp (km/sec)</b>	<b>Vs (km/sec)</b>	<b>Density (g/cm<sup>3</sup>)</b>
0	5.47	2.70	2.56
2	5.50	2.86	2.80
5	6.00	3.23	2.94
10	6.20	3.24	2.94
15	6.48	3.40	2.98
20	6.70	3.80	2.98
30	6.75	3.81	2.98
40	8.00	4.66	3.36

In ISOLA, trial source positions are created for the spatial grid search. In this study, trial sources below epicenter option is chosen and 10 trial source positions below epicenter are set up as recommended. In case of large number of shallow earthquakes in the data, the starting depth and depth step are chosen as 0.9 and 2 km, respectively.

ISOLA calculates the Green's function by the helps of maximum frequency ( $f_{\max}$ ) and elementary moment rate functions. The prescribed maximum frequency is needed to be greater than any frequency range used in waveforms inversion to avoid artificial effects of the spectral cutoff. Since the frequency band range assigned during the inversion is 0.06 – 0.12 Hz except few events with 0.06 – 0.11 Hz and 0.07 – 0.11 Hz, the maximum frequency is selected as 0.15 Hz in Green function computation. The elementary moment rate function has two options as delta and triangle functions. Because ISOLA does not assign any particular slip-rate time function for the simplicity, the slip rate is estimated by the Green function calculation. If the triangle function is chosen, the duration should be assumed. Thus delta function representing an impulsive force that is acceptable for the analyzed earthquake magnitude range is chosen in our calculations.

In the inversion stage, the inverted velocity data is converted into displacement and fitted to synthetic displacement data (Zahradnik and Sokos, 2016). Any mismatched components of the waveforms are deselected, and different frequency ranges are assigned for different stations in the same event for better correlation. A moment tensor can be decomposed into three modes: double-couple (DC), compensated linear vector dipole (CLVD) and voluminal (VOL). In ISOLA, the moment tensor (MT) inversion may have three solutions: full MT inversion (DC+CLVD+VOL), deviatoric MT inversion (DC+CLVD; VOL=0), DC-constrained MT inversion (DC; VOL=0; CLVD=0). Many examples are established for the synthetics with DC% equal to 50 and 100 which do not create a distinguishable difference in their seismogram data, the quantitative measure of their fit with real data is almost similar (Sokos and Zahradnik, 2009). Since there are young volcanoes in the region, we have applied the full MT inversion.

### **3.2.3 Results**

In the content of this study, 29 earthquakes in Central Anatolia are analyzed by moment tensor inversion method. ISOLA delivers the plots of moment tensor inversion, waveform comparison, correlation vs time shift and correlation vs depth. For instance, the outputs of the events 16.06.2013 and 22.02.2014 which are strike-slip faulting and normal faulting with high DC percentages are shown in Figure 3.8 – 3.15, respectively. As an example for low DC %, the outputs of the event 27.07.2013 which is strike-slip faulting with normal component are shown in Figure 3.16 – 3.19.

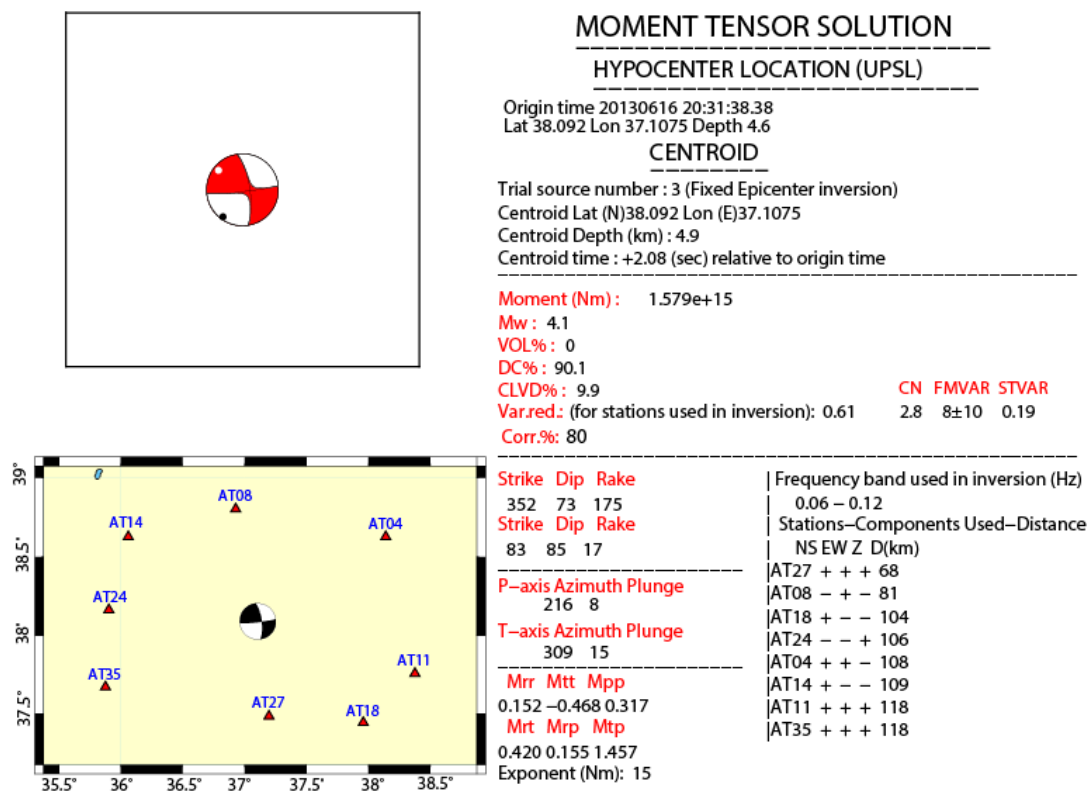


**Figure 3. 8** Moment tensor inversion solution of the event 16.06.2013.

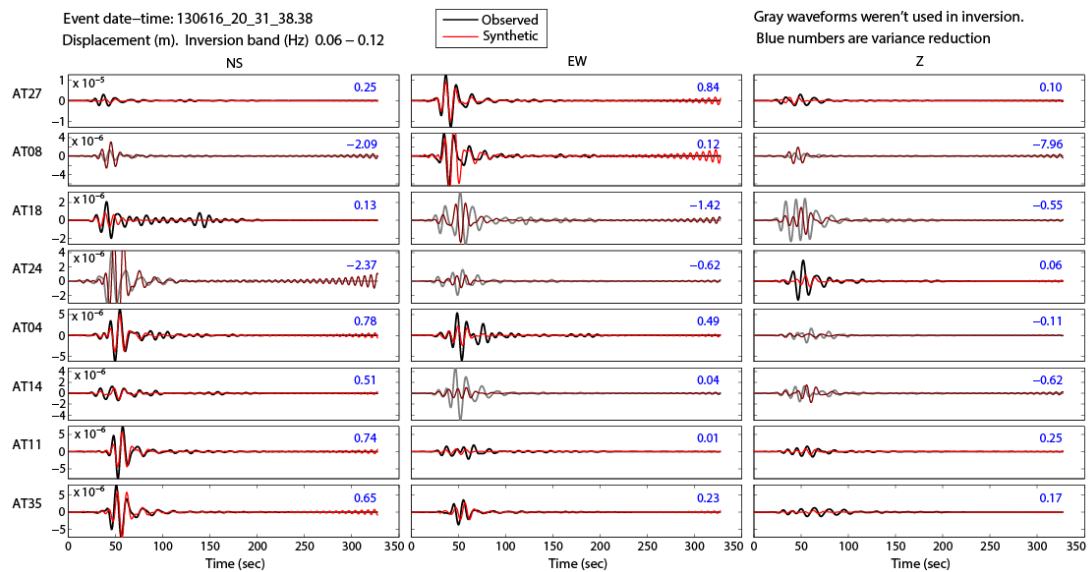


**Figure 3. 9** Comparison of observed and synthetic waveforms for the event 16.06.2013.

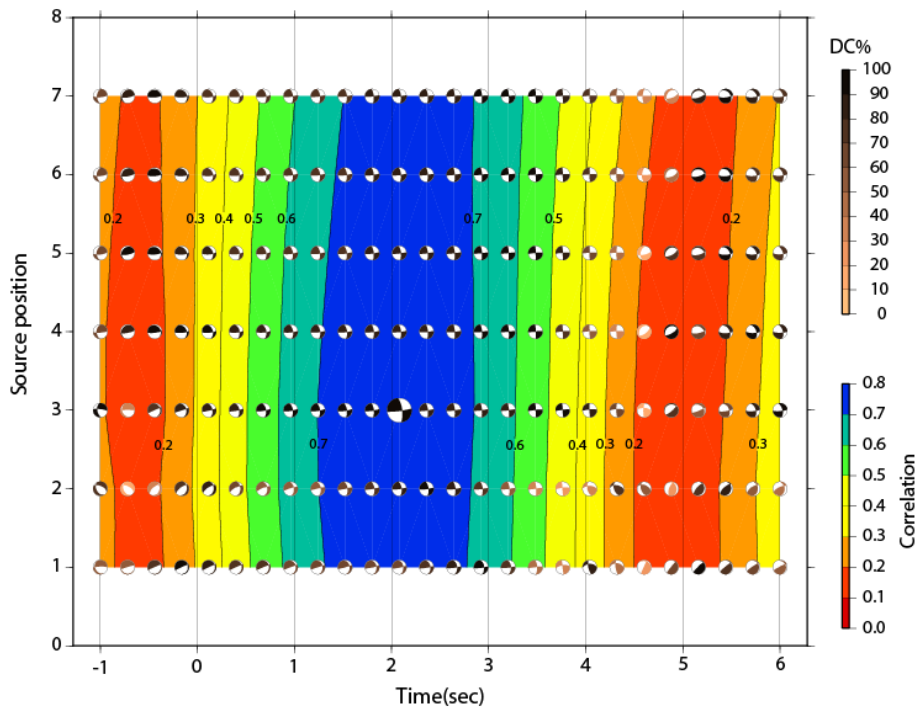


**Figure 3. 10** Plot of correlation vs time shift, source position and focal mechanism of the event 16.06.2013. Largest correlation is in the middle of blue area. Focal mechanism color changes due to DC%.

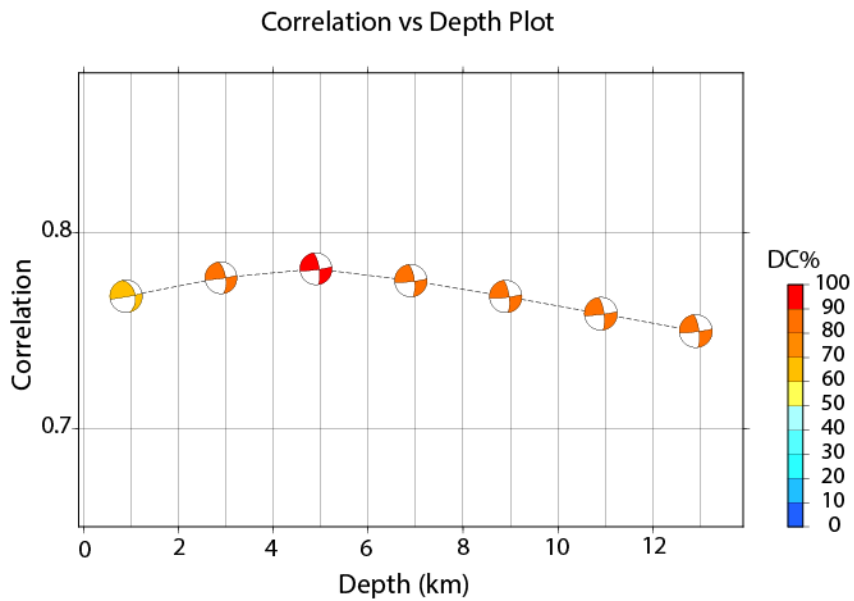


**Figure 3. 11** Depth correlation plot of the event 16.06.2013. Focal mechanism colors represent the DC%.

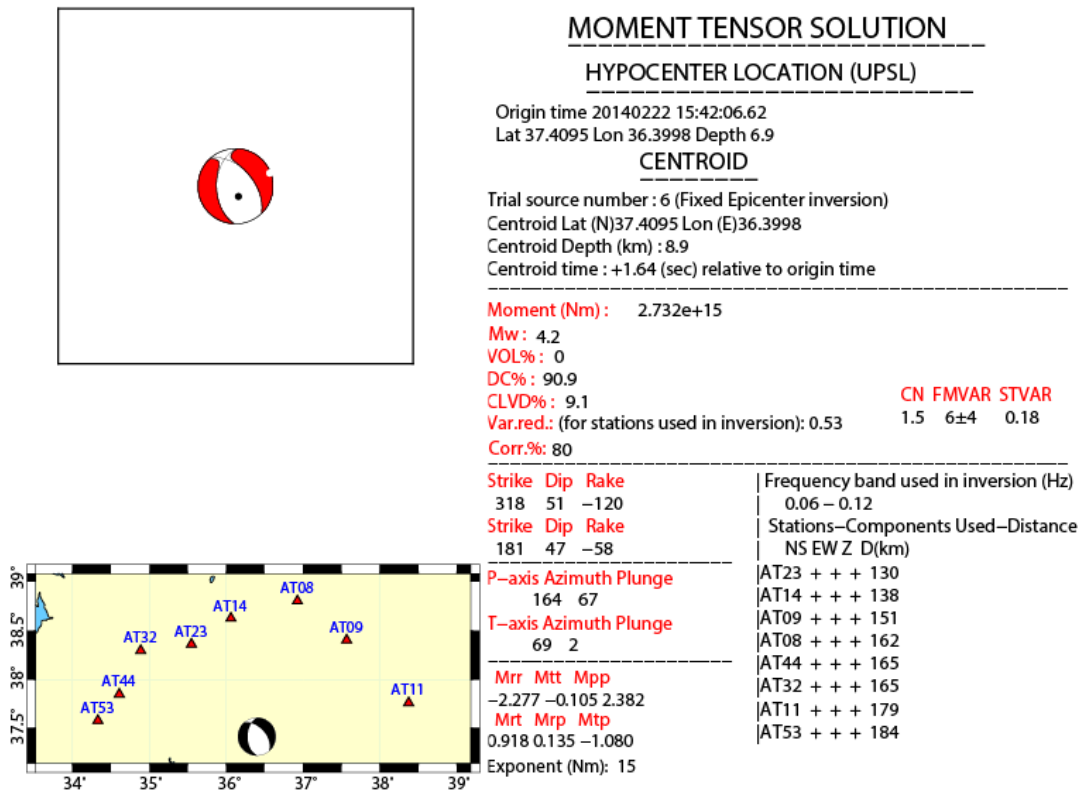


Figure 3. 12 Moment tensor inversion solution of the event 22.02.2014.

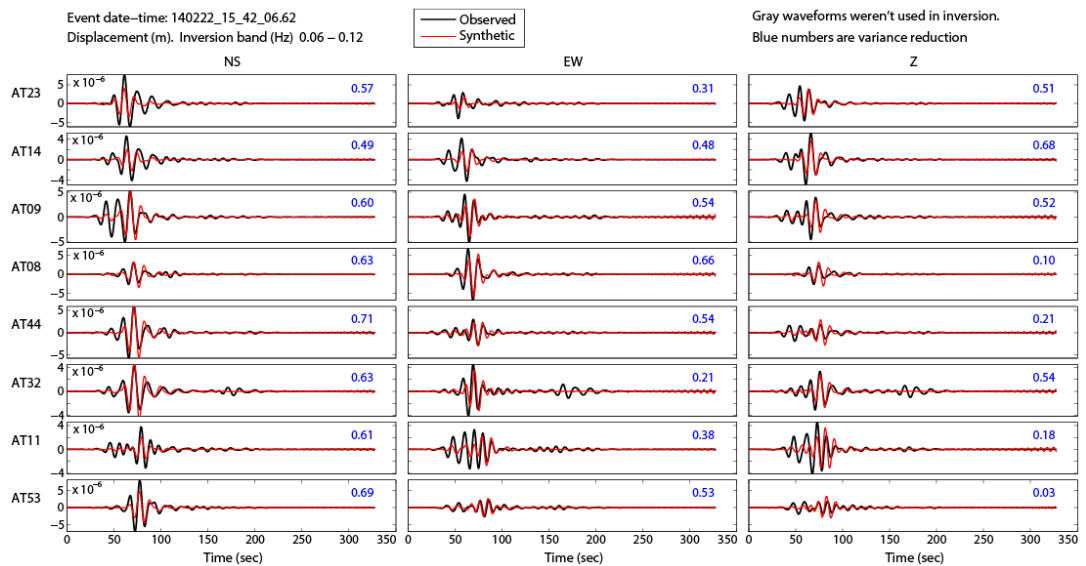
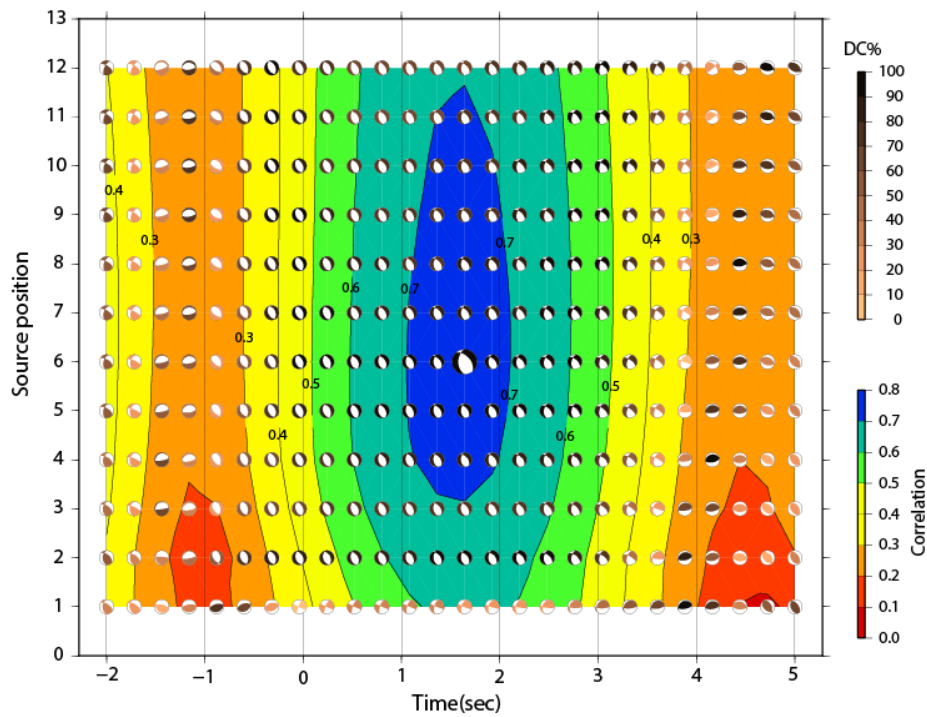
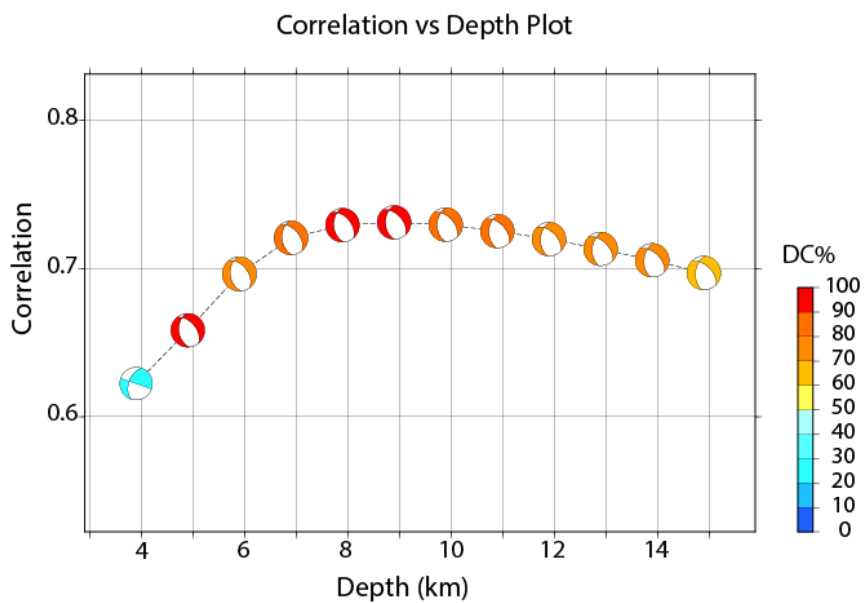


Figure 3. 13 Comparison of observed and synthetic waveforms for the event 22.02.2014.



**Figure 3. 14** Plot of correlation vs time shift, source position and focal mechanism of the event 22.02.2014. Largest correlation is in the middle of dark blue area. Focal mechanism color changes due to DC%.



**Figure 3. 15** Depth correlation plot of the event 22.02.2014. Focal mechanism colors represent the DC%.



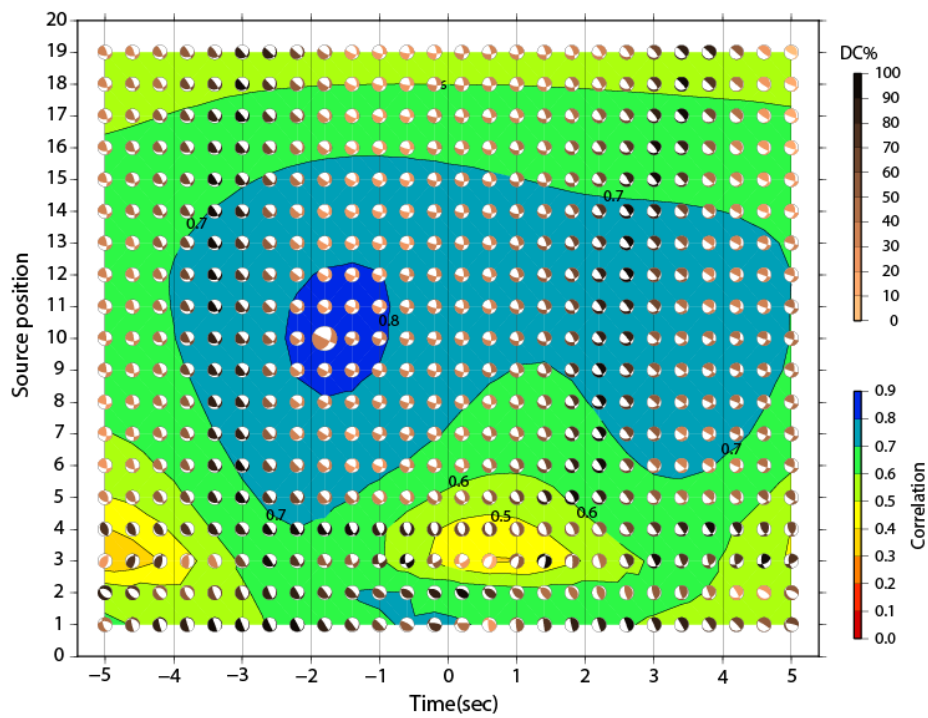


**Figure 3.18** Plot of correlation vs time shift, source position and focal mechanism of the event 26.07.2013. Largest correlation is in the middle of blue area. Focal mechanism color changes due to DC%.

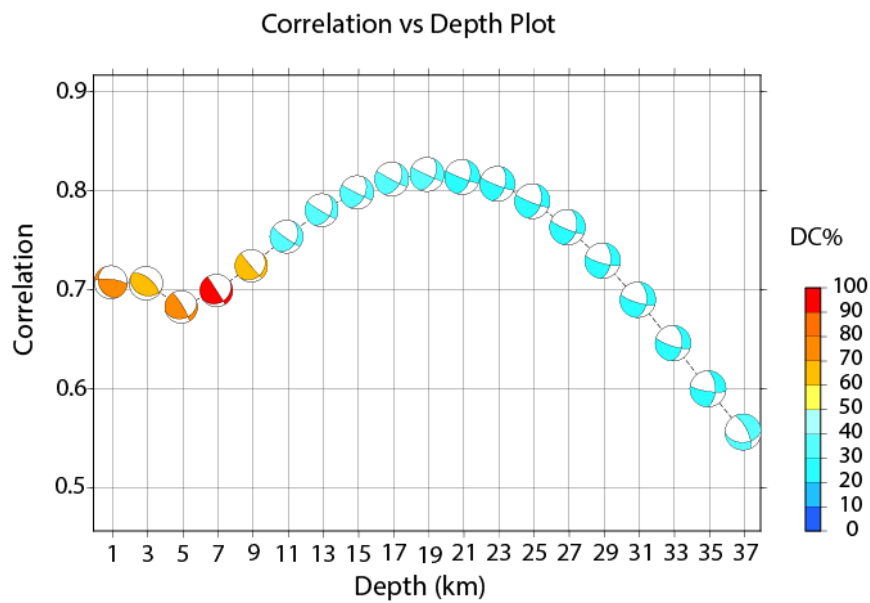


**Figure 3.19** Depth correlation plot of the event 26.07.2013. Focal mechanism colors represent the DC%.

The moment tensor solution delivers origin time, latitude and longitude, centroid depth, moment (Nm), moment magnitude (Mw), DC% and CLVD%, variance reduction (VR) for all the stations used in the inversion, the largest correlation (Corr.%) for the result, condition number (CN), focal mechanism variability index (FMVAR), space – time variability index (STVAR), strike, dip and rake values for each nodal planes, azimuth and plunge of P- and T-axes, moment tensor components, frequency band range and station components used in the inversion.

According to the results, DC% varies between 18.80 – 99.10 % and 10 of these values are bigger than 80%. CLVD% ranges between 0.90 – 81.20 % and seven of these values are greater than 50%. No voluminal (VOL) solution is obtained suggesting that none of them are volcanic events. Events 4, 7, 16 and 18 have fairly low DC% ( $\leq 35$ ) components. The inversion solution plots of event 4 are represented as example in Figure 3.16 – 3.19. Low DC% might be related to complex faulting and the existence of non-planar motions. Condition number (CN) indicates the inversion stability and its values are varying between 1.40 – 3.40 in the results. Low CN numbers ( $< 5$ ) associates with highly stable inversions while  $CN > 10$  are the indicators of less stable solutions (Triantafyllis et al., 2016). FMVAR values are smaller than  $40^\circ$  which express a good qualified focal mechanism solution except two results. STVAR values are between 0.07 – 0.27 ( $< 30$ ) representing a good space-time resolution. The variance reduction (VR) is corresponding to the waveform match (perfect match = 1) ranging between 0 – 1 and our results are between 0.26 – 0.67 (4 of them is below 0.30) expressing good level of waveform fit. Variance reduction for individual waveforms can be seen in the plots of observed and synthetic waveforms and this individual variance in the individual waveforms have faced values below zero due to the ill-posed correlations (Figure 3.9, 3.13, 3.17). Most of the time these ill-posed correlations are eliminated by deselecting the station components except few values close to zero. All the moment tensor inversion results are given in Table 3.2.

**Table 3. 2** Our moment tensor inversion results

No	Date	Moment (Nm)	DC %	CLVD %	Corr %	CN	FMVAR (°)	STVAR	VR
1	25.05.2013	4.519e+14	92.4	7.6	70	3.4	51±32	0.18	0.45
2	04.06.2013	4.489e+15	79.8	20.2	90	2.0	5±2	0.07	0.66
3	16.06.2013	1.579e+15	90.1	9.9	80	2.8	8±10	0.19	0.61
4	26.07.2013	3.815e+15	32.3	67.7	90	3.2	35±27	0.20	0.67
5	27.07.2013	4.257e+14	87.9	12.1	60	1.7	11±7	0.13	0.26
6	06.08.2013	6.160e+14	60.5	39.5	60	1.8	9±7	0.15	0.29
7	18.09.2013	3.264e+15	18.8	81.2	60	2.5	16±10	0.08	0.31
8	23.10.2013	6.155e+15	53.1	46.9	80	1.6	31±23	0.12	0.49
9	07.11.2013	1.122e+15	82.5	17.5	70	2.0	9±6	0.15	0.40
10	08.11.2013	3.191e+14	97.8	2.2	60	1.5	11±4	0.16	0.32
11	10.01.2014	1.239e+15	51.8	48.2	80	1.9	35±34	0.27	0.51
12	07.02.2014	7.598e+14	99.1	0.9	60	2.2	13±21	0.10	0.28
13	14.02.2014	9.500e+15	68.1	31.9	70	1.8	9±7	0.20	0.39
14	22.02.2014	2.732e+15	90.9	9.1	80	1.5	6±4	0.18	0.53
15	02.03.2014	7.245e+14	78.1	21.9	80	2.1	10±5	0.13	0.56
16	02.03.2014	6.279e+15	29.2	70.8	70	2.1	11±8	0.09	0.49
17	01.05.2014	2.002e+15	69.7	30.3	70	1.8	7±7	0.20	0.43
18	09.06.2014	1.077e+16	35.4	64.6	70	2.1	11±16	0.13	0.45
19	12.07.2014	8.082e+14	71.8	28.2	60	1.9	14±18	0.10	0.29
20	11.08.2014	5.681e+14	83.0	17.0	80	2.7	16±12	0.13	0.53
21	28.08.2014	6.307e+14	74.6	25.4	60	2.2	6±3	0.12	0.30
22	03.09.2014	1.527e+15	44.0	56.0	80	2.8	38±38	0.11	0.52
23	08.01.2015	4.977e+15	50.4	49.6	80	1.9	28±24	0.19	0.58
24	22.01.2015	1.032e+15	87.9	12.1	60	3.4	24±16	0.16	0.33
25	10.02.2015	1.214e+16	47.0	53.0	80	2.5	16±18	0.18	0.52
26	26.03.2015	5.972e+14	70.8	29.2	80	1.6	6±6	0.10	0.56
27	26.03.2015	7.556e+14	76.8	23.2	70	1.4	6±4	0.08	0.47
28	28.03.2015	6.894e+14	41.0	59.0	70	3.0	40±37	0.23	0.40
29	28.03.2015	3.811e+15	80.1	19.9	80	3.3	8±5	0.14	0.54

Map showing the resultant focal mechanism solutions is given in Figure 3.20 and resultant source parameters are represented in Table 3.3. In the map, earthquakes characterized by high (>35%) CLVD component which are label with magenta color, are mainly located near İskenderun Gulf and Adana Basin indicating the tectonic complexity present at the southwestern continuation of EAFZ. This high degree of complexity is also in agreement with highly scattered seismicity (Fig. 2.4) and variable focal mechanism solutions indicating strike-slip and normal faulting occurring simultaneously (Fig. 2.10, 3.20). Note that moment tensor inversion solution of each earthquake is also given separately in Appendix B.

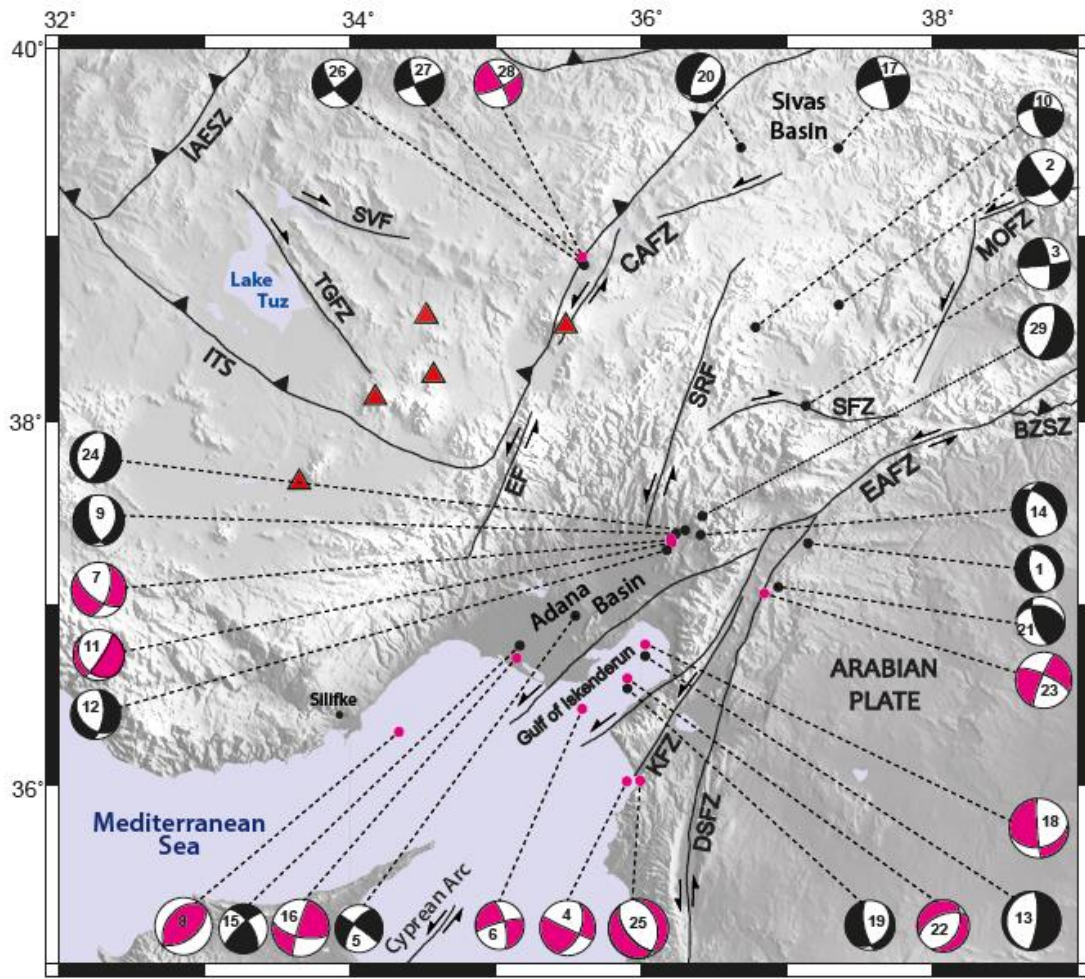


**Figure 3.** 20 Fault plane solutions of 29 focal mechanisms resulted in this study. The focal mechanisms are scaled to their magnitudes. Magenta focal mechanisms have CLVD  $\geq 35\%$ . Red triangles denote Holocene volcanoes (taken from Abgarmi et al., 2017). Labels are explained in Figure 2. 1.

**Table 3. 3** The resultant source parameters of 29 earthquakes analyzed in this study. (#St. = number of stations used in moment tensor inversion).

No	Date	Lon. E (°)	Lat. N (°)	Mw	Depth (km)	Nodal Plane 1			Nodal Plane 2			# St.
						Strike (°)	Dip (°)	Rake (°)	Strike (°)	Dip (°)	Rake (°)	
1	25.05.2013	37.14	37.34	3.7	4.9	324	37	-110	168	56	-76	7
2	04.06.2013	37.33	38.63	4.4	30.9	52	58	-5	145	85	-148	8
3	16.06.2013	37.11	38.09	4.1	4.9	352	73	175	83	85	17	8
4	26.07.2013	35.89	36.03	4.3	18.9	116	88	-142	24	52	-3	7
5	27.07.2013	35.55	36.97	3.7	18.9	215	66	-3	306	87	-156	10
6	06.08.2013	35.59	36.42	3.8	12.9	347	72	-170	253	80	-18	7
7	18.09.2013	36.20	37.38	4.3	22.9	127	61	-144	17	59	-34	8
8	23.10.2013	34.33	36.30	4.5	6.9	53	51	99	219	40	79	9
9	07.11.2013	36.24	37.40	4.0	13.9	23	36	-56	163	60	-112	8
10	08.11.2013	36.78	38.51	3.6	6.9	167	68	152	268	64	25	9
11	10.01.2014	36.20	37.31	4.0	12.9	33	80	-63	142	29	-159	8
12	07.02.2014	36.20	37.30	3.9	14.9	6	64	-59	131	39	-137	8
13	14.02.2014	36.03	36.72	4.6	14.9	6	75	-90	187	15	-89	8
14	22.02.2014	36.40	37.41	4.2	8.9	318	51	-120	181	47	-58	8
15	02.03.2014	35.16	36.78	3.8	8.9	325	64	16	228	76	153	6
16	02.03.2014	35.17	36.76	4.5	20.9	103	64	172	197	82	26	6
17	01.05.2014	37.35	39.47	4.1	6.9	344	86	-167	253	77	-4	8
18	09.06.2014	36.01	36.77	4.6	16.9	176	85	-125	79	36	-8	8
19	12.07.2014	35.90	36.55	3.9	18.9	39	30	-44	170	70	-112	9
20	11.08.2014	36.68	39.45	3.8	4.9	60	30	-56	203	66	-107	8
21	28.08.2014	36.90	37.11	3.8	14.9	161	69	122	280	37	36	9
22	03.09.2014	35.93	36.61	4.1	16.9	29	42	-120	246	54	-66	5
23	08.01.2015	36.85	37.08	4.4	10.9	295	74	-171	203	82	-16	8
24	22.01.2015	36.31	37.40	3.9	4.9	19	65	-83	182	26	-105	10
25	10.02.2015	35.98	36.03	4.7	22.9	348	37	-67	140	56	-106	7
26	26.03.2015	35.61	38.89	3.8	14.9	332	82	165	64	75	8	11
27	26.03.2015	35.60	38.89	3.9	18.9	158	72	-178	67	88	-18	9
28	28.03.2015	35.62	38.89	3.8	4.9	146	72	-170	53	80	-19	10
29	28.03.2015	36.41	37.48	4.3	18.9	16	69	-90	195	21	-90	7

Events 16, 15, 5, 12, 11, 7, 9, 24, 14 and 29 are associated with the northern branch of EAFZ. Events 16 and 5 are strike-slip mechanisms with minor normal faulting having E-W extension and N-S compression, event 15 is strike-slip mechanism with minor reverse faulting, events 24 and 29 are pure normal faulting, events 12, 11, 7, 9 and 14 are normal faulting with minor strike-slip mechanisms. Events 6, 19, 22, 13 and 18 are located between the north and south branches of EAFZ. Events 6 and 18 are strike-slip mechanisms with normal components, while events 19 and 22 are normal mechanisms with minor strike-slip components. Event 13 is the pure normal faulting. Event 1 occurs very close to the intersection point of EAFZ and DSFZ and has pure normal mechanism having WSW-ENE extensional forces. Events 21 and 23 are located along the DSFZ and their mechanisms are reverse faulting with minor strike-slip component and strike-slip mechanism with minor normal faulting, respectively. Events 4 and 25 that are located closely along the sinistral Karasu Fault indicate strike-slip and normal mechanisms, respectively displaying interaction between strike-slip motions and extension. Event 8 is situated at the coastline of Silifke with pure reverse faulting in NE-SW direction. In the northern parts of the study area, events 26, 27 and 28 are located along the CAFZ having strike-slip mechanisms with minor normal faulting. The locations of events 17 and 20 are at the northeastern part of CAFZ and their mechanisms are strike-slip faulting and normal faulting with minor strike-slip component, respectively. Events 2, 3, and 10 are located between SRF, SFZ and MOFZ. Events 2 and 3 are strike slip faults with normal components, as event 10 is strike-slip faulting with reverse component.

The rake based distributions of focal mechanism solutions for 29 earthquakes are plotted on the ternary diagram in Figure 3.21. Their P- and T- axes orientation distributions are also plotted using the lower hemisphere projection in Figure 3.22. According to these plots, strike-slip and normal faulting are the most dominant mechanisms and consistent with the characteristics of the related faults and extensional regime in the region. The lower hemisphere projection of the data indicates a transition between strike-slip faulting and normal faulting due to E-W directed extension.

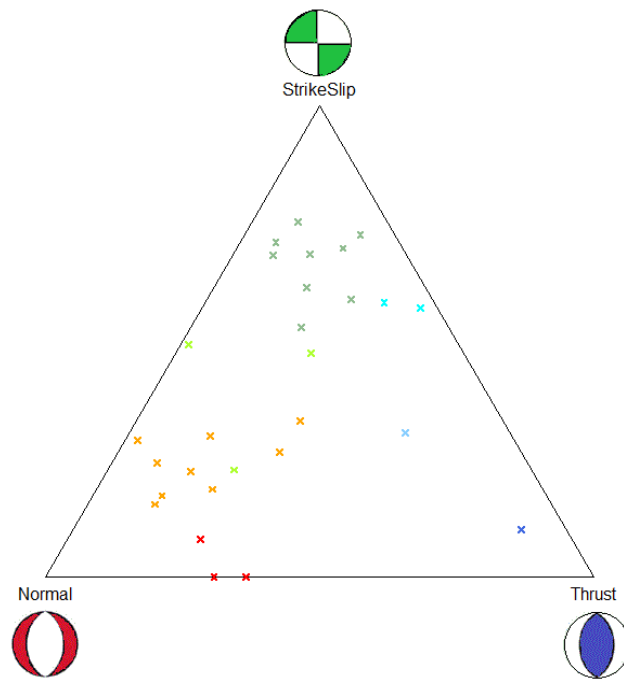


**Figure 3. 21** Rake-based ternary diagram of our focal mechanism solutions.

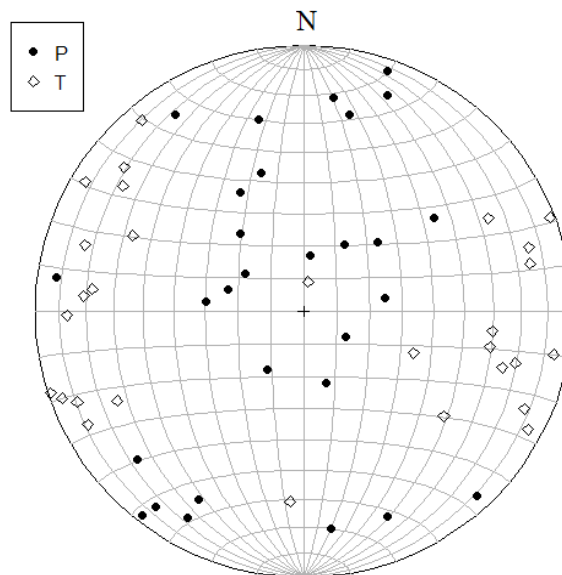


**Figure 3. 22** Distribution of P- and T-axes orientations of our solutions.

The relationship between the earthquakes and the tectonic stresses may be complicated but the earthquakes are the main indicators where the stress is concentrated (Zhao and Müller, 2001). Thus a well-constrained tectonic stress field map helps to identify the faults with orientations and monitor the seismic activity (Heidbach et al., 2011; and references therein). For this purpose, we have calculated the maximum horizontal stress direction ( $S_{Hmax}$ ) from resultant moment inversion solutions of each earthquake using the approach of Lund and Townend's (2007) via Win-Tensor program (Delvaux and Sperner, 2003). The resultant  $S_{Hmax}$  directions are then plotted in Figure 3.24 by following the protocol of the World Stress Map Project (Heidbach et al., 2008). The rose diagrams of  $S_{Hmax}$  and  $S_{Hmin}$  are also established for the resultant data which suggested that the horizontal stress regime of the region is dominated by N-S compression and E-W extension (Figure 3.25).

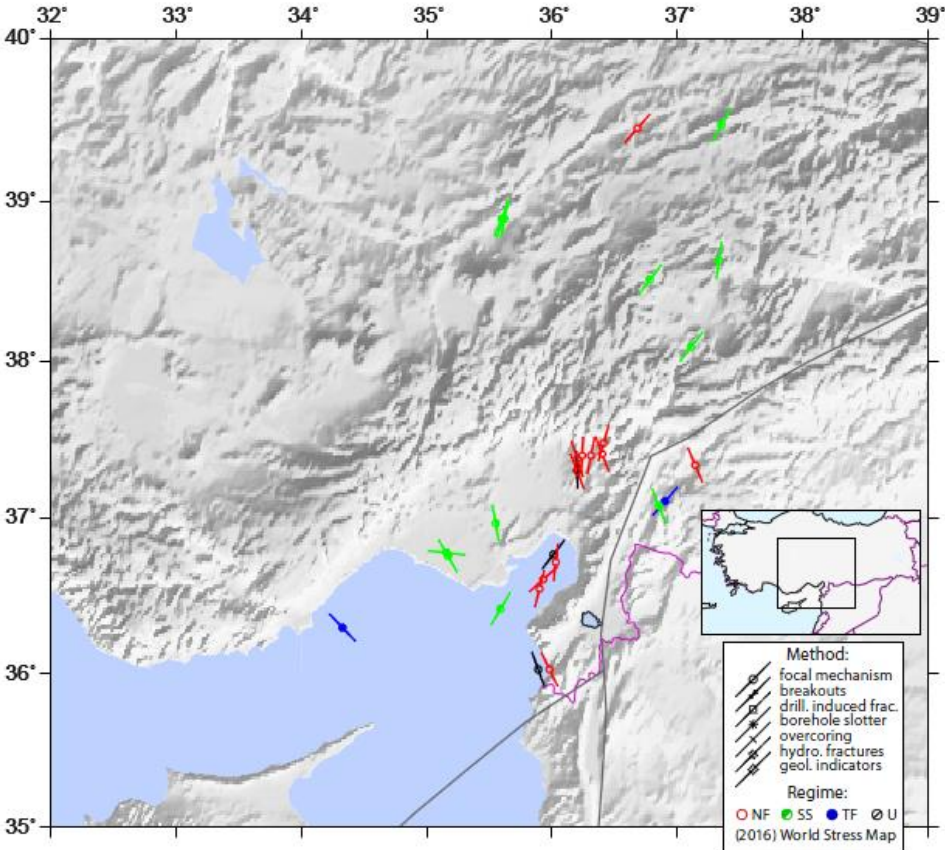


**Figure 3. 23** Maximum horizontal stress  $S_{Hmax}$  map of the study area constructed using our focal mechanism solutions.

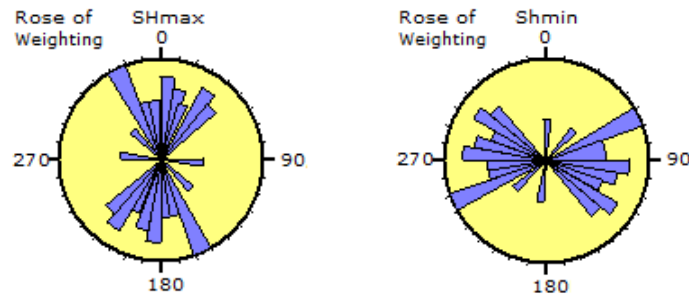


**Figure 3. 24** Rose diagrams of maximum ( $S_{Hmax}$ ) and minimum ( $S_{Hmin}$ ) horizontal stresses of our focal mechanism solutions on equal area display by Win-Tensor (Delvaux and Sperner, 2003).

For individual events, stress regime can be categorized using compressional and extensional forces defining P-B-T axes by assuming that  $\sigma_1$  is corresponding to P, and  $\sigma_3$  to T so that P and T axes lies in the movement plane including the fault-plane normal (Reches, 1987). In this respect, Zoback (1992) classified stress regimes in to five categories (NF: Normal faulting, NS: Transtension, SS: Strike-slip faulting, TS: Transpression, TF: Thrust faulting) based on the orientations of P-B-T axes (Table 3.4). Following this classification, stress regimes of every resultant solution is assigned and plotted as a histogram (Fig. 3.26). Among the resultant solutions, the percentage of strike-slip faulting is the greatest among the data with 41% value. The normal faulting is at the second place with 38% which is very close to the strike-slip mechanism. 10 % of the solutions falls into unidentified category while 7% is in thrust faulting, 5% is in transtension (normal faulting with strike-slip component) and none at transpression (reverse faulting with strike-slip component). Note that P-B-T axes,  $S_{Hmax} / S_{Hmin}$  directions and stress regimes of each resultant solution are also give in Table 3.5.

The resulted focal mechanism solutions in this study are compared to the solutions of Global Centroid Moment Tensor (CMT), the European-Mediterranean Seismological Centre (EMSC) and USGS sources. Two solutions from Global CMT and USGS catalogs and nine solutions from EMSC catalog are for events that we have applied regional moment tensor inversion. The focal mechanisms of these common earthquakes are shown on map seen in Figure 3.27.

**Table 3. 4** Types of tectonic regimes (Zoback, 1992; retrieved from Barth et al., 2008).

P/S1-axis	B/S2-axis	T/S3-axis	Regime	S <sub>H</sub> -azimuth
p1 > 52		p1 < 35	NF	azimuth of B-axis
40 < p1 < 52		p1 < 20	NS	azimuth of T-axis+90
p1 < 40	p1 > 45	p1 < 20	SS	azimuth of T-axis+90
p1 < 20	p1 > 45	p1 < 40	SS	azimuth of P-axis
p1 < 20		40 < p1 < 52	TS	azimuth of P-axis
p1 < 35		p1 > 52	TF	azimuth of P-axis

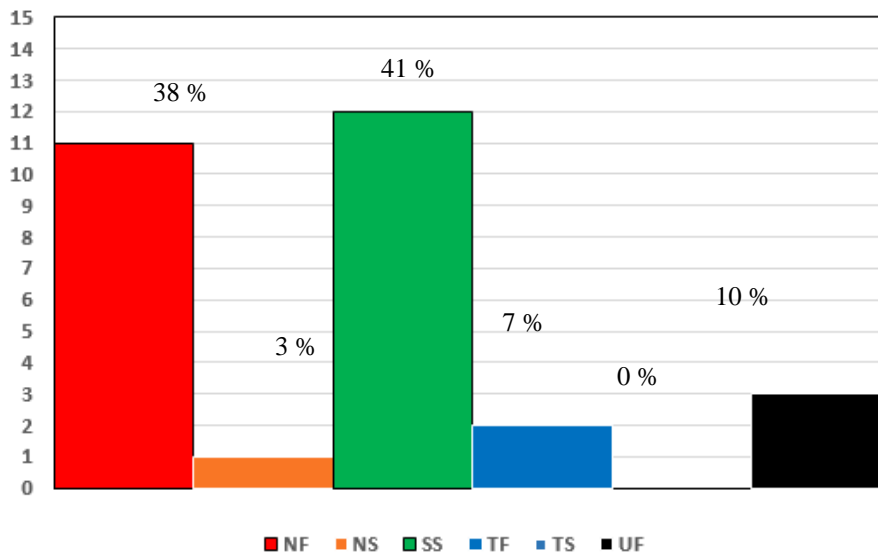


**Figure 3. 25** Faulting type histogram for our 29 resultant focal mechanism solutions

**Table 3. 5** P, T, SHmax, SHmin axes and stress regimes of our focal mechanism solutions. (Paz = P-axis azimuth, Ppl = P-axis plunge, Taz = T-axis azimuth, Tpl = T-axis plunge; NF = normal faulting, NS = predominately normal faulting with strike-slip component, SS = strike-slip faulting, TF = thrust (reverse) faulting, UF = undefined).

No	Date	P axis		T axis		SH axis		Regime Code
		Paz	Ppl	Taz	Tpl	Max az.	Min az.	
1	25.05.2013	119	75	248	10	157	67	NF
2	04.06.2013	13	25	274	18	8	98	SS
3	16.06.2013	216	8	309	15	37	127	SS
4	26.07.2013	347	28	243	24	160	70	UF
5	27.07.2013	173	19	78	15	170	80	SS
6	06.08.2013	209	20	301	6	30	120	SS
7	18.09.2013	343	45	251	2	162	72	NS
8	23.10.2013	137	6	7	81	136	46	TF
9	07.11.2013	31	67	269	13	3	93	NF
10	08.11.2013	218	2	126	35	37	127	SS
11	10.01.2014	331	48	101	30	178	88	UF
12	07.02.2014	320	58	74	14	159	69	NF
13	14.02.2014	276	60	96	30	6	96	NF
14	22.02.2014	164	67	69	2	159	69	NF
15	02.03.2014	279	8	184	29	96	6	SS
16	02.03.2014	328	13	63	24	150	60	SS
17	01.05.2014	209	12	118	6	28	118	SS
18	09.06.2014	54	39	294	31	37	127	UF
19	12.07.2014	48	59	276	22	14	104	NF
20	11.08.2014	83	65	306	19	41	131	NF
21	28.08.2014	228	18	111	54	41	131	TF
22	03.09.2014	212	69	320	6	48	138	NF
23	08.01.2015	158	17	250	5	159	69	SS
24	22.01.2015	303	69	103	20	11	101	NF
25	10.02.2015	6	73	242	10	154	64	NF
26	26.03.2015	19	5	287	17	18	108	SS
27	26.03.2015	21	14	114	11	22	112	SS
28	28.03.2015	9	20	101	6	9	99	SS
29	28.03.2015	286	66	106	24	16	106	NF

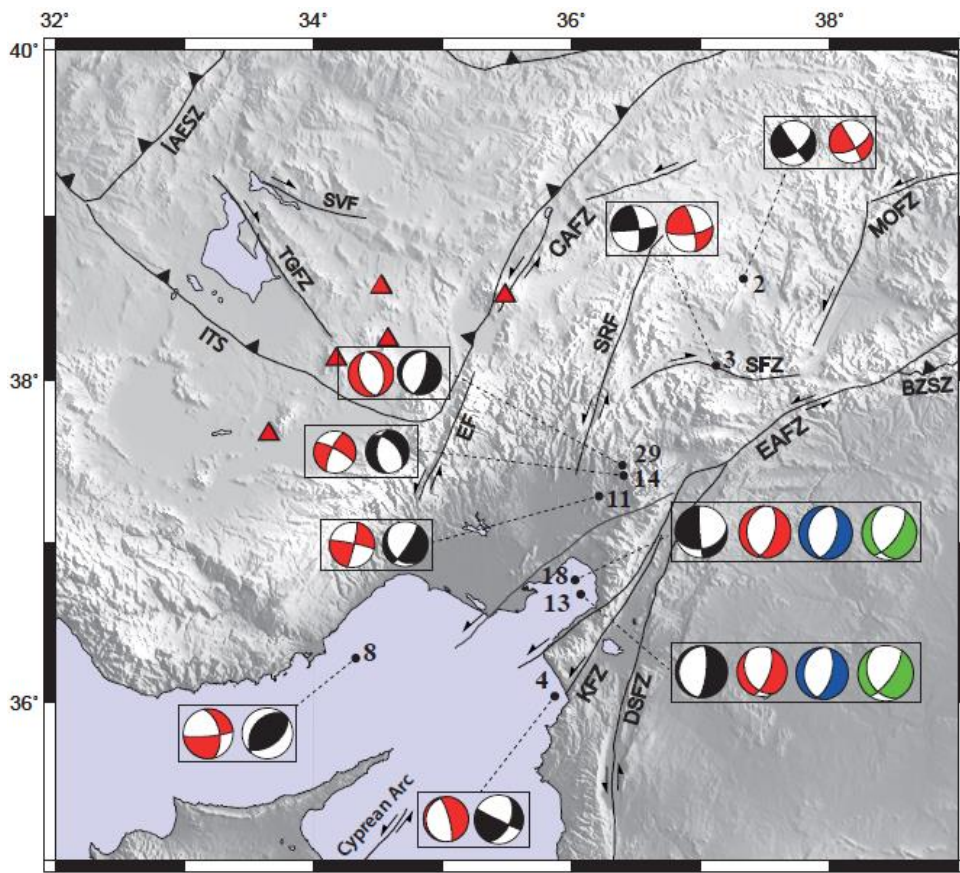


**Figure 3. 26** Earthquakes having multiple focal mechanism solutions in the study area. (The reference databases of focal mechanisms are shown by different colors: red=EMSC, green=GCMT, blue=USGS and our solutions are in black). The focal mechanisms are scaled to their magnitudes. Red triangles indicate Holocene volcanoes (taken from Abgarni et al., 2017). Labels are explained in Figure 2. 1.

The well-fitting results are Events 2, 3, 13 and 29. The resultant focal mechanisms of Event 2 and 3 fit well with the EMSC solution, Event 13 is well-fitted with USGS result but EMSC and GCMT has minor strike-slip components. Event 29 is found as pure normal faulting by EMSC which is consistent with the resultant. However, the resultant is trending NE-SW direction while the EMSC result is in NNW-SSE direction.

The result of event 18 is more or less consistent with the GCMT result which are normal faulting with minor strike-slip component, but the results of EMSC and USGS are pure normal faulting which are identical to each other. Events 11 and 14 are resulted as normal faulting with minor strike-slip component, but the EMSC results are strike-slip faulting with minor normal component.

Apart from these seven resultants, the solutions of Event 4 and 8 are different from the results of this study. Event 4 is located at the end of southern branch of East Anatolian Fault Zone and it is strike-slip faulting with normal component. The EMSC result is pure normal faulting trending in NNW-SSE direction which is inconsistent with the trend of EAFZ. Event 8 is resulted as pure reverse faulting trending in NE-SW direction while the EMSC is resulted as strike-slip faulting with normal component. Both events are located at the south of the station layout of our seismic network thus they have poor azimuthal coverage due to absence of any station in the south. Thus, our solutions of these two events should be interpreted with caution.



## CHAPTER 4

### STRESS TENSOR ANALYSIS

#### 4.1 Stress Tensor Inversion

The stress tensor inversion analysis is preferred to determine the orientation of best fitting stress tensor of a specified region from fault plane solutions. There are numerous stress inversion techniques have been formulated from the focal mechanism solutions (Angelier, 1979; 1984; 2002; Gephart and Forsyth, 1984; Michael, 1984, 1987; Gephart, 1990; Rivera and Cisternas, 1990; Delvaux and Sperner, 2003). The stress tensor inversion of the observed focal mechanisms provides the parameters of the azimuth and plunges of the three principal stresses and the relative magnitudes of the stress axes which is named as stress ratio (R) and forces the shape of stress ellipsoid. The stress ratio, R corresponds to the ratio of all three principal stresses by the equation  $R = (\sigma_2 - \sigma_3) / (\sigma_1 - \sigma_3)$  where  $\sigma_1$ ,  $\sigma_2$ ,  $\sigma_3$  are the maximum, intermediate and minimum principal compressive stresses, respectively.

All these techniques release the best-fitting stress tensor by utilizing the observed focal mechanism and they aim to minimize the discrepancy between the resulted shear stress direction and the slip direction for all the earthquakes in the data. But these techniques differ in their best model definition and the fault plane ambiguity (Karasözen et al., 2014). The most well-known inversion algorithms are developed by Gephart and Forsyth (1984) and Michael (1984, 1987).

Hardebeck and Hauksson (2001) studied these two methods for the comparison in terms of synthetic focal mechanism data sets. Hardebeck and Hauksson (2001) resulted that (1) the accuracy of both models that is significant in the estimation of the stress parameters is satisfying; and (2) the accuracy of both models is affected in a positive

way with increasing data. However, there are some differences about these models: Michael's method (1984, 1987) is good at very noisy data sets whereas Gephart and Forsyth's method (1984) is good at high-quality data sets. Michael's approach (1984, 1987) determines the uncertainty more appropriately (Görgün et al., 2010; and references therein) while Gephart and Forsyth's approach (1984) develops more reliable stress orientations.

#### **4.1.1 Stress Tensor Analysis by Slick Method**

Stress tensor analysis by Slick method (Michael, 1984; 1987) is executed by a linear least-square inversion calculation. This method uses bootstrap resampling approach to determine the maximum, intermediate and minimum principle axes orientations and stress magnitude where the fault plane is selected randomly among two nodal planes. P- and T-axes of a single focal mechanism solution may change due to the principal stress directions. Hence the maximum compressive stress orientation can locate in any direction in the dilatational quadrant, they may have poor constrained principal stresses. The aim of Michael's Slick Method is to calculate the best fitting stress tensor for the observed focal mechanisms (Shah, 2015; Görgün et al., 2010). Minimizing the average of the individual angular misfit ( $\beta$ ) between the determined and the observed fault planes and the slip direction is the way to calculate the best fitting stress tensor (Tselentis et al., 2006). The misfit value and the variance affect the level of stress field heterogeneity. High variance value means poor quality in stress orientation fitting. To avoid this, the region should be divided into smaller tectonic domains displaying minimal internal variations (Shah, 2015). Wiemer et al. (2002) suggested the threshold boundary of the stress tensor variance as 0.20 to obtain a homogeneous stress field from the focal mechanisms solutions. In this study, the maximum value for the beta is accepted as  $35^\circ$  for a relatively uniform stress field.

For the study area, the stress tensor inversion analyses are carried out by ZMAP software package (Wiemer, 2001) which utilizes Michael's (1987) slick method for

stress tensor inversions. We have run stress inversions using only other solutions (29 events) and using the entire data (200 events). The output plots are given in Figure 4.1.

In Figure 4.1a, the maximum principal stress ( $\sigma_1$ ), S1 is sub-horizontally orienting in N-S direction; the intermediate principle stress ( $\sigma_2$ ), S2 is sub-vertical and striking in NNE-SSW direction; the minimum principal stress ( $\sigma_3$ ), S3 is horizontally striking in ESE-WNW direction. The faulting style is strike-slip mechanism with the stress ratio, R of 0.76 which is between moderate and high values indicating varying characteristics. The variance value is determined as 0.19 which is close to the limit boundary but still corresponds to the homogeneity in the study area. The beta value ( $\sim 38^\circ$ ) indicates some spatial variation in the stress field for the resultant data of 29 events.

Figure 4.1b is plotted by utilizing the entire data of 200 earthquake solutions in the region. The maximum principal stress ( $\sigma_1$ ), S1 is horizontally striking in NNE-SSW direction; the intermediate principle stress ( $\sigma_2$ ), S2 is vertically oriented in N-S direction; and the minimum principal stress ( $\sigma_3$ ), S3 is horizontal and striking ESE-WNW direction. The dominant faulting is strike-slip mechanism with the stress ratio, R of 0.67 which is close to moderate values suggesting that  $\sigma_2$  value is close to the average value of  $\sigma_1$  and  $\sigma_3$  in magnitude. The variance (0.15) is less than the threshold limit value of 0.20 but the beta ( $34.83^\circ$ ) is almost equal to  $35^\circ$ . The resultant variance and beta values are reasonably representing the entire stress field in the study area and indicating some heterogeneity in the region. For a homogeneous stress field, sub-regions in the study area will be defined and studied individually.

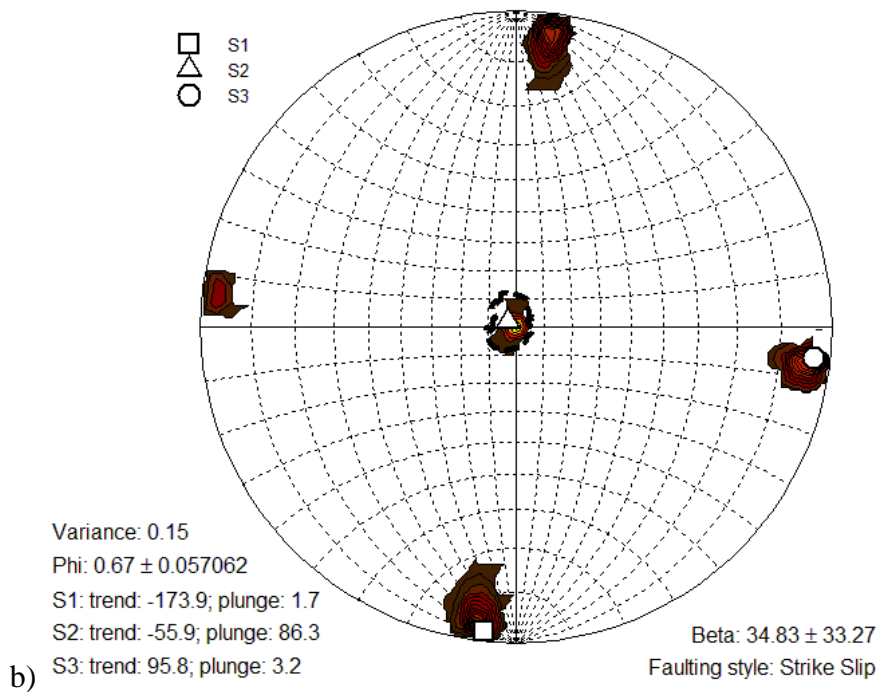
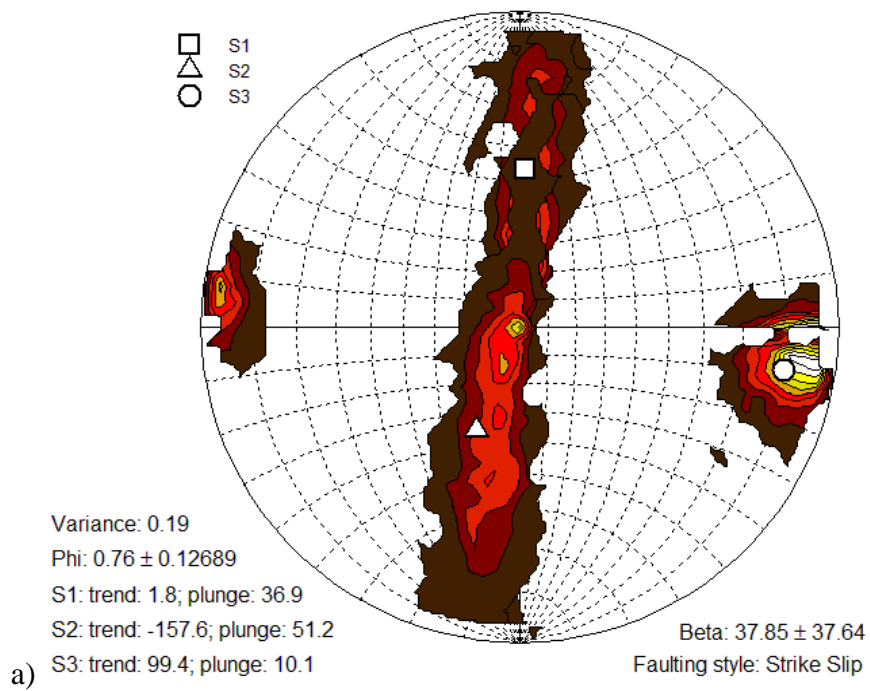


**Figure 4. 1** The results of stress tensor inversion by Michael's method for (a) our focal mechanism solutions (29) and (b) all the focal mechanisms (200) data.

#### 4.1.2 Stress Tensor Analysis by Win-Tensor

Win-Tensor (Windows version of Tensor) program is developed by Delvaux and Sperner (2003) to calculate the stress tensor by analyzing fault-plane solutions to construct a relationship between the fault and the principle stress axes. The right dihedral method (Angelier and Mechler, 1977) places the compression axis (P) by considering the position of the most compressive principal stress ( $\sigma_1$ ). The stress tensor parameters can be estimated by an improved version of “Right Dihedron method” by eliminating the mismatched nodal planes from the stress regime if the data set is symmetric and complete. Despite an asymmetrical and incomplete data set, dynamic rotation optimization will provide the original stress tensor which suggests that a full information about the stress conditions can be estimated by using a minor slip data extracted from a homogeneous fault environment which are generating the slip (Delvaux, 1993). The resulted stress tensor is utilized by the Rotational Optimization approach to minimize the angular deviation between the observed and the computed slip directions and maximize the shear stress magnitude on the focal planes, since the data sets are composite in general with heterogeneous subsets inside them (D’Amico, 2018; Shah, 2015; Delvaux, 1993). The resultant parameters of stress tensor inversion are: (i) the maximum compressional principal stress axis,  $\sigma_1$ , (ii) the intermediate compressional principal stress axis,  $\sigma_2$ , (iii) the minimum compressional principal stress axis,  $\sigma_3$ , (iv) the stress ratio, R. According to Delvaux et al. (1997), the orientation of principal stress axes and the shape of the stress ellipsoid (R) are the elements of stress regime function.

In Win-Tensor program, P-, B-, T- axes and Right Dihedron methods are utilized and their results are compared. P-, B-, T- axes method uses the average orientation areas of P, B and T kinematic axes for all the individual data (Delvaux, 2011). This method considers homogeneous rock material and newly formed faults. Right Dihedron method uses the compression and extension areas to determine the orientation of principle stresses taking average of P dihedral orientations for  $\sigma_1$  axis and T dihedral orientations for  $\sigma_3$  axis assuming that the used data represent the same stress regime

(Delvaux, 2011). Both methods give similar results and directly determine the stress axes orientation and relative magnitude by rotational optimization process.

The stress conditions of the study area are determined by using P-, B-, T- axes and Right Dihedron methods for the resultant (29) and the entire data set (200) by Win-Tensor program represented in Figure 4.2 and Figure 4.3, respectively. In Figure 4.2a, the result is obtained from P-, B-, T- axes method leading that the region is under the effects of  $\sigma_1$ : 44/005,  $\sigma_2$ : 46/183,  $\sigma_3$ : 01/274 with  $R=0.73$ . It has the characteristics of normal to strike-slip regime. The red outward arrows show the extension in E-W to WNW-ESE direction and so that the compression in more or less N-S direction. In Figure 4.2b, the result from Right Dihedron method shows that the region is characterized by  $\sigma_1$ : 38/008,  $\sigma_2$ : 52/198,  $\sigma_3$ : 05/102 with  $R=0.80$  having the mechanism of strike-slip faulting. The red outward arrows are indicating WNW-ESE extensional and NNE-SSW oriented compressional forces. In Figure 4.3a, the result is obtained from P-, B-, T- axes method indicating that the region is under the effects of  $\sigma_1$ : 01/007,  $\sigma_2$ : 89/220,  $\sigma_3$ : 00/097 with  $R=0.76$ . The red outward arrows show the extension in WNW-ESE direction and so that the compression in NNE-SSW direction. In Figure 4.3b, the result from Right Dihedron method shows that the region is characterized by  $\sigma_1$ : 24/005,  $\sigma_2$ : 66/171,  $\sigma_3$ : 05/273 with  $R=0.74$ . The red outward arrows are ~E-W oriented extensional and ~N-S oriented compressional forces. Both methods have the characteristics of strike-slip regime. All results release high values of stress ratio ( $>0.73$ ) indicating significantly larger  $\sigma_2$  compare to  $\sigma_3$ .

The quality of World Stress Map rank (QRw) and the tensor quality rank (QRt) are varying from A: good to E: very poor and found as D and E for the data sets of this study. Small amount of fault-slip data used in the analysis and the insufficiency in variety of orientations among the data may be resulted in very poor quality. Counting deviation (CD) value is developed by the improved Right Dihedron method showing how well the individual counting nets are coherent with the average counting net. Low CD values ( $<40\%$ ) have negative contribution whereas high CD values ( $>40\%$ ) bring positive effect on the tensor. The resultant CD values range between 32.9 – 41.5 %.

In comparison, these two methods differ in the dominant stress regime of the study area, as one of the tensor results of P-, B-, T- axes method releases strike slip faulting with normal component rather than pure strike slip faulting results of Right Dihedron method. Both methods expose anticlockwise shift due to the dominant E-W extension in the study area.

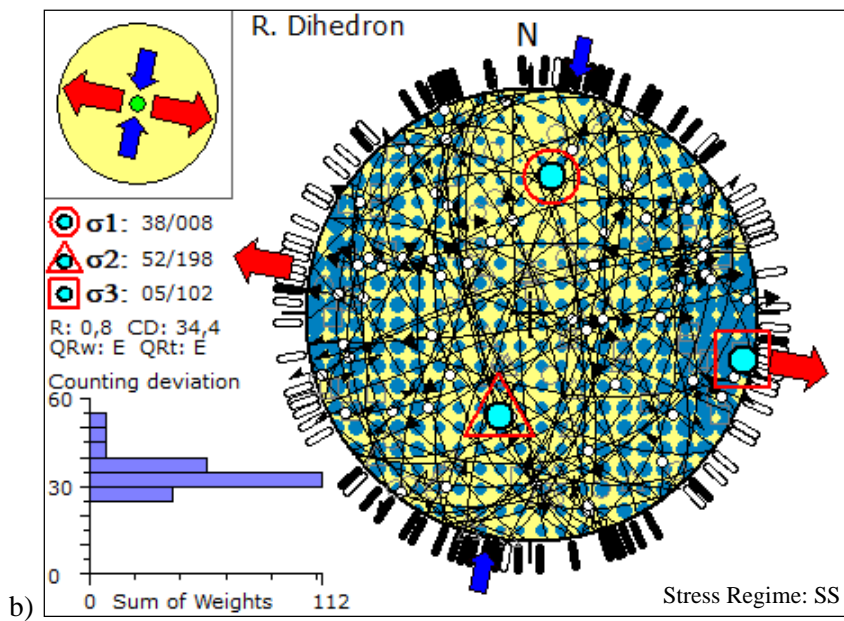
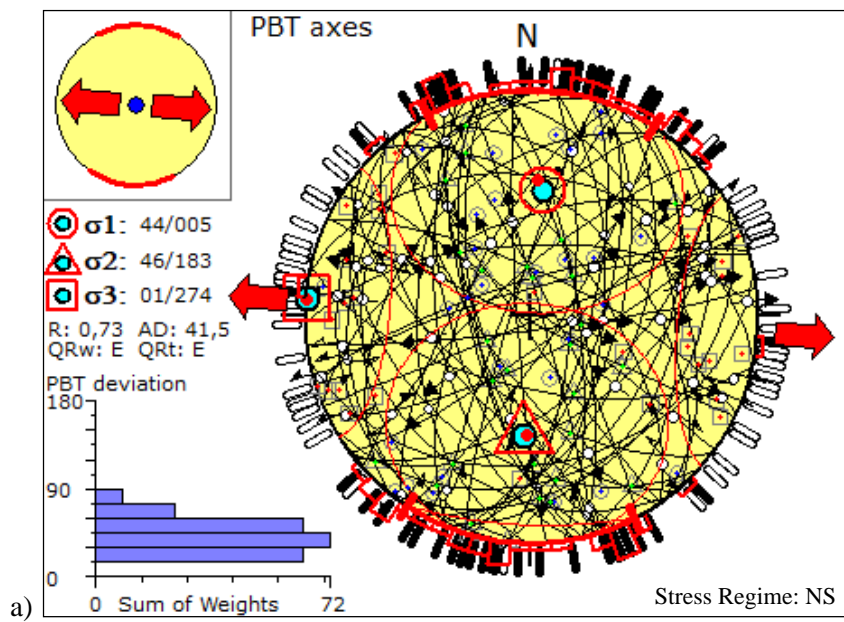


**Figure 4. 2** The results of stress tensor inversion by (a) P-, B-, T-axes method; and (b) Right Dihedron method for our focal mechanism solutions (29).

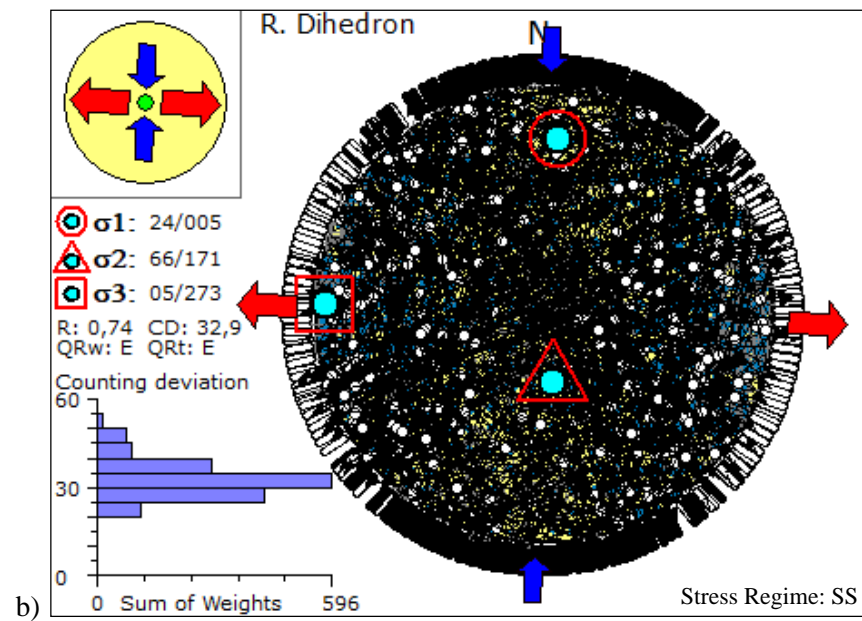
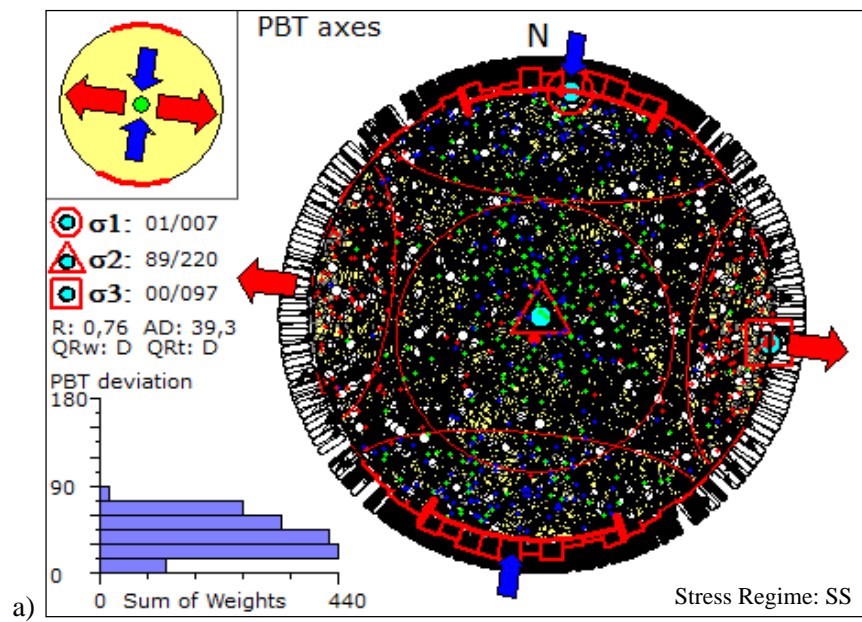


**Figure 4. 3** The results of stress tensor inversion by (a) P-, B-, T-axes method; and (b) Right Dihedron method for the all focal mechanisms (200).

## 4.2 Determination of Tectonic Domains in the Study Area

In the study area, regions with similar stress conditions are defined and sub-regions are outlined in Figure 4.4. Eight sub-regions having similar homogeneous strains are identified by considering the epicentral distance of focal mechanisms and spatial variations of earthquake occurrences and thus the related tectonic properties in these seismogenic areas. Sub-region 1 is selected near Istanbul – Ankara – Erzincan Suture Zone, Tuz Gölü Fault Zone and Savcılı Fault (SVF) having dominantly strike-slip solutions. Sub-region 2 is comprising of the earthquakes with dominantly strike-slip solutions triggered by CAFZ. In Sub-region 3, the earthquakes with dominantly strike-slip mechanism which occurred between MOFZ, Sarız Fault and Sürgü Fault are studied. Sub-region 4 is dominated by strike-slip earthquake solutions where the EAFZ and BZSZ coincide. Sub-region 5 is identified as the junction area of EAFZ, BZSZ and the northernmost parts of the DSFZ in where the earthquakes with strike-slip solutions has occurred most. In Sub-region 6, the earthquakes locating along the southern branch of EAFZ and the northeastern continuation of Cyprian Arc are analyzed which are mostly normal faulting and strike-slip with normal component. Sub-region 7 is consisting of the earthquakes with strike-slip and normal faulting solutions occurred along the northern branch of EAFZ in Adana Basin. In Sub-region 8, reverse faulting earthquake solutions are dominant which are locating in the north part of Cyprus.

To determine the characterizing stress field patterns of each sub-region in the study area, Michael's (1987) method by ZMAP and P-, B-, T- axes and Right Dihedron methods by Win-Tensor (Delvaux and Sperner, 2003) are applied. All the results are compared in the following section.

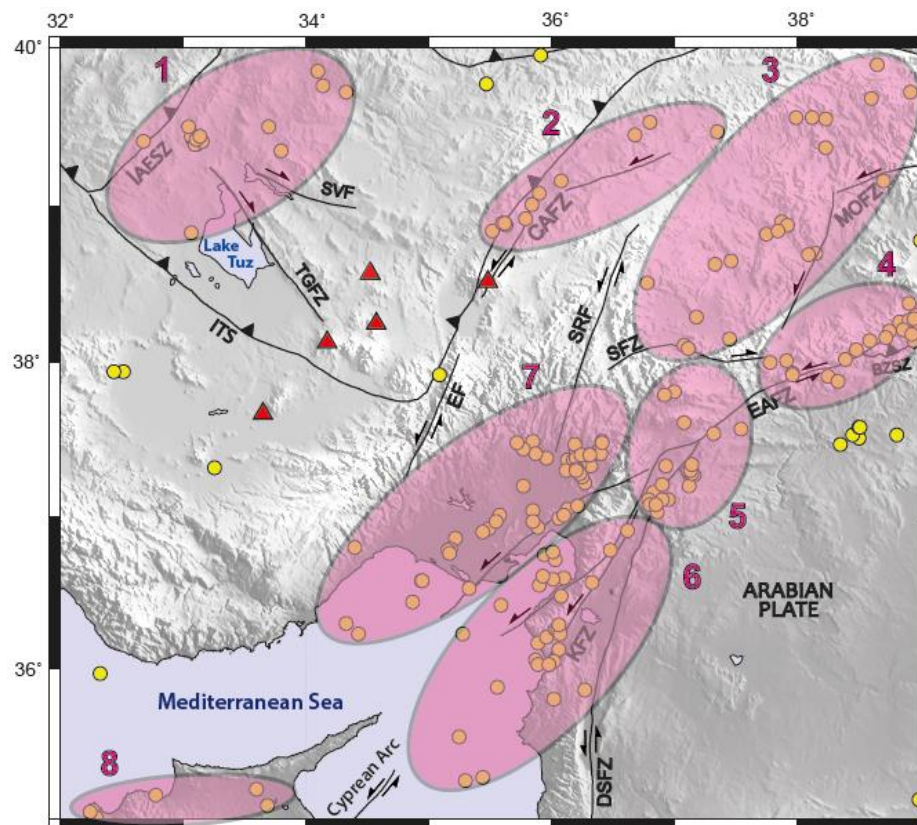


**Figure 4.** 4 Sub-regions of the study area. Yellow circles denote earthquakes with focal mechanism solutions. Black lines with black filled triangles represent suture zones. Red triangles represent Holocene volcanoes. (taken from Abgarmi et al., 2017). Labels are explained in Figure 2. 1.

### 4.2.1 Sub-region 1

The focal mechanism solutions of Sub-region 1 has 17 events which are shown on the distribution map in Figure 4.5. Due to stress tensor solutions (Figure 4.6), the region is characterized by strike-slip faulting with WSW-ENE oriented extension and NNW-SSE oriented compression.  $\sigma_1$  and  $\sigma_3$  principal stresses are almost horizontal;  $\sigma_2$  is almost vertical in all stress tensor results. The variance and beta values are calculated as 0.037 ( $< 0.20$ ) and  $13.64^\circ$  ( $< 35^\circ$ ), respectively; indicating a uniform stress field in the region. The stress ratio,  $R$  is varying between 0.46 – 0.56 which suggest that the magnitude of  $\sigma_2$  is close to the average value of  $\sigma_1$  and  $\sigma_3$ .

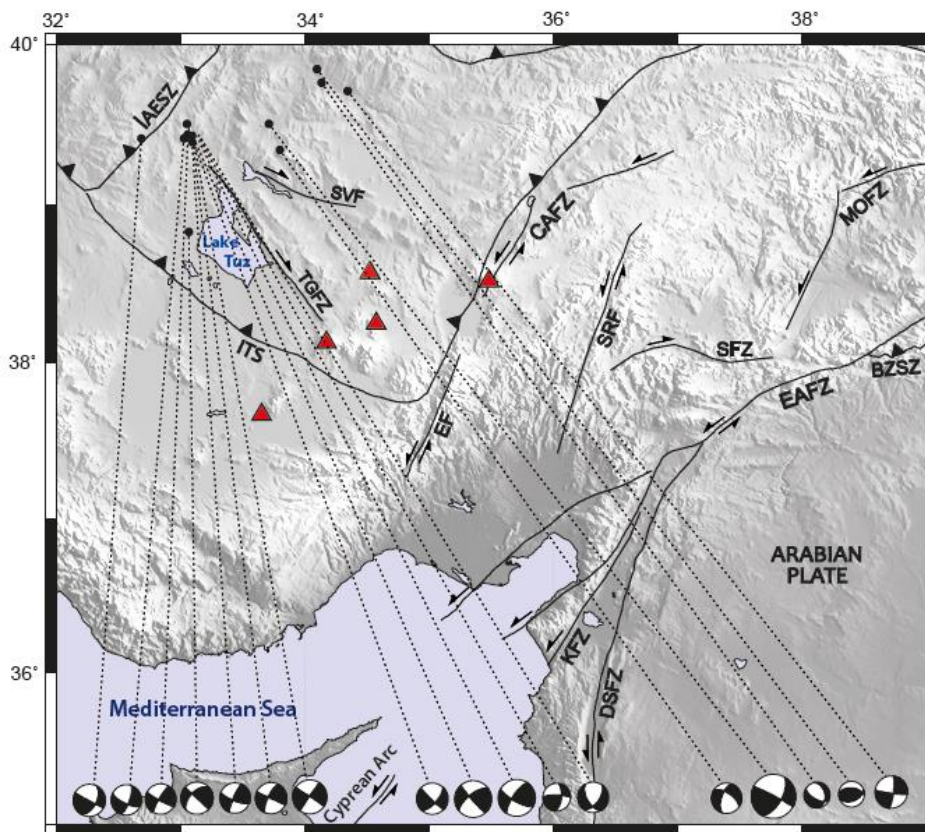


**Figure 4. 5** Map showing focal mechanism solutions of Sub-region 1. Red triangles denote Holocene volcanoes. (taken from Abgarmi et al., 2017). Labels are explained in Figure 2. 1.

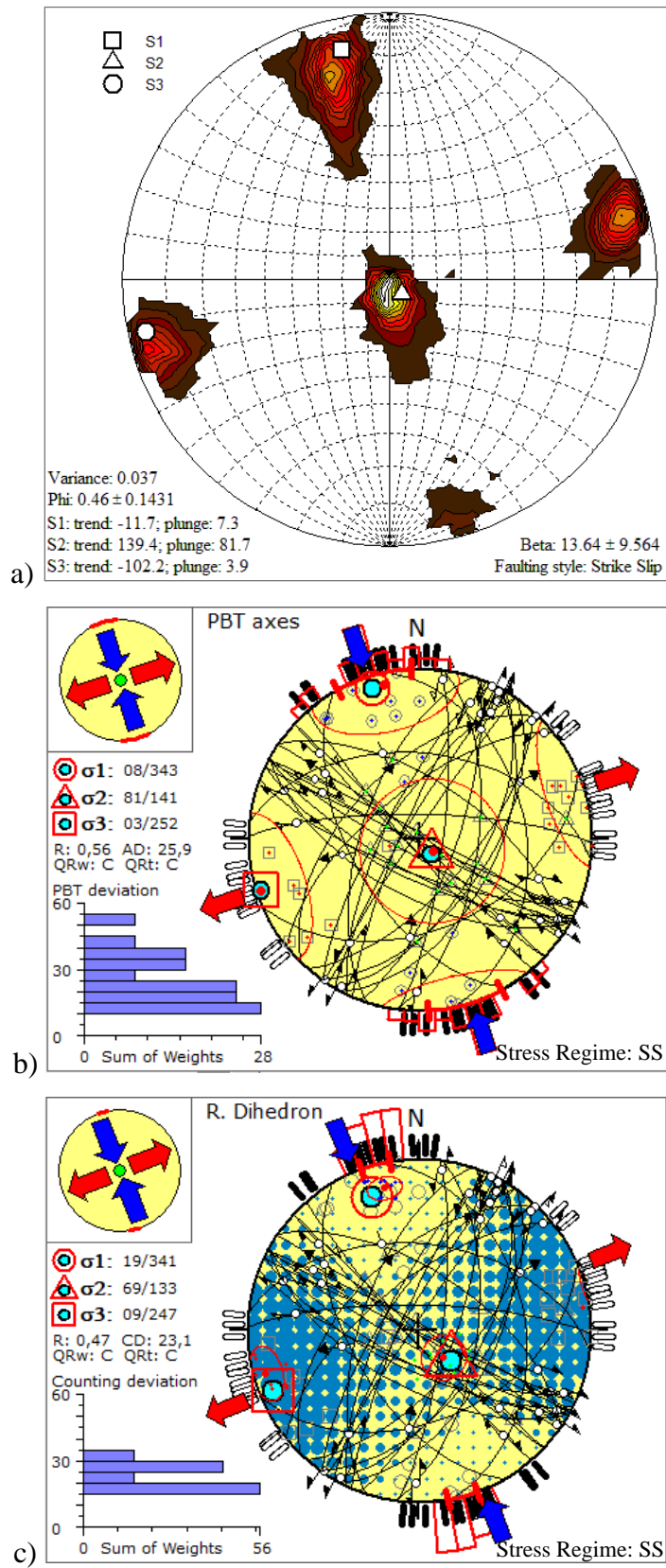


**Figure 4. 6** The results of stress tensor inversion by (a) Michael's method; (b) P-, B-, T-axes method; and (c) Right Dihedron method in Sub-region 1.

#### 4.2.2 Sub-region 2

Sub-region 2 contains 12 earthquake solutions which are distributed at the northern parts of the Central Anatolian Fault Zone (Figure 4.7). The region is dominated by strike-slip faulting with NW-SE orienting extension and NE-SW orienting compression (Figure 4.8). The stress tensor inversion results indicate that  $\sigma_1$  is sub-horizontal by trending in NE-SW direction,  $\sigma_3$  is horizontal in NW-SE direction and  $\sigma_2$  is vertically oriented. The resultant stress ratio R values differ between 0.63-0.81. Low variance 0.028 ( $< 0.20$ ) and beta 11.61 ( $< 35^\circ$ ) values represent a uniform stress field in this sub-region.

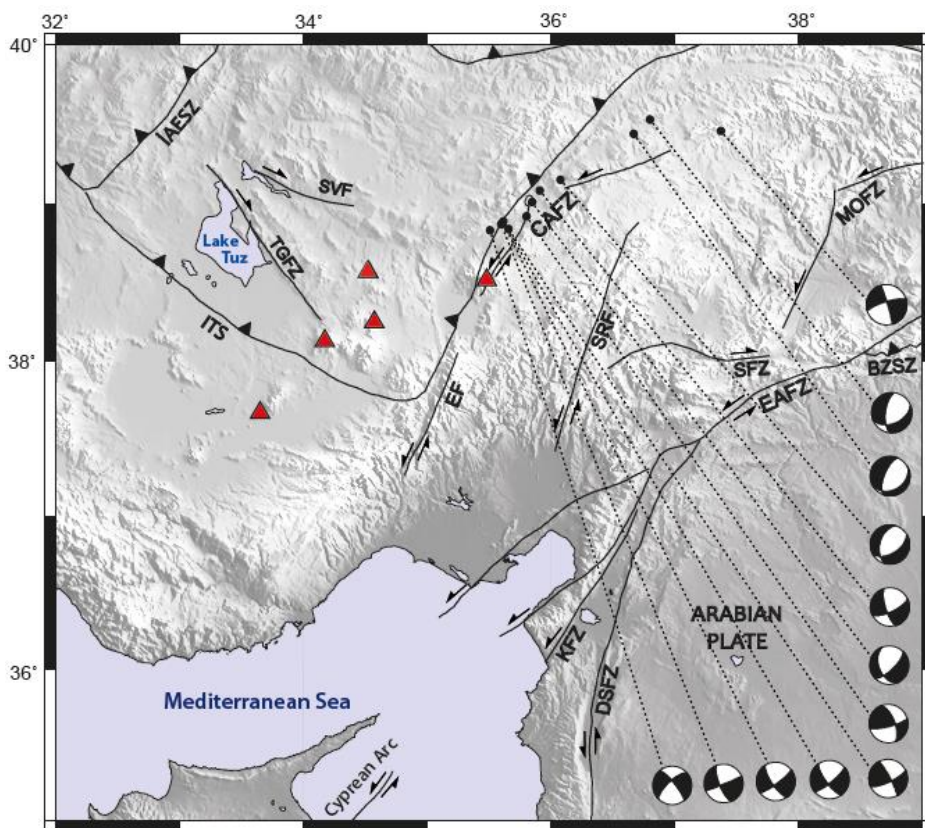


**Figure 4. 7** Map showing focal mechanism solutions of Sub-region 2. Red triangles denote Holocene volcanoes. (taken from Abgarmi et al., 2017). Labels are explained in Figure 2. 1.

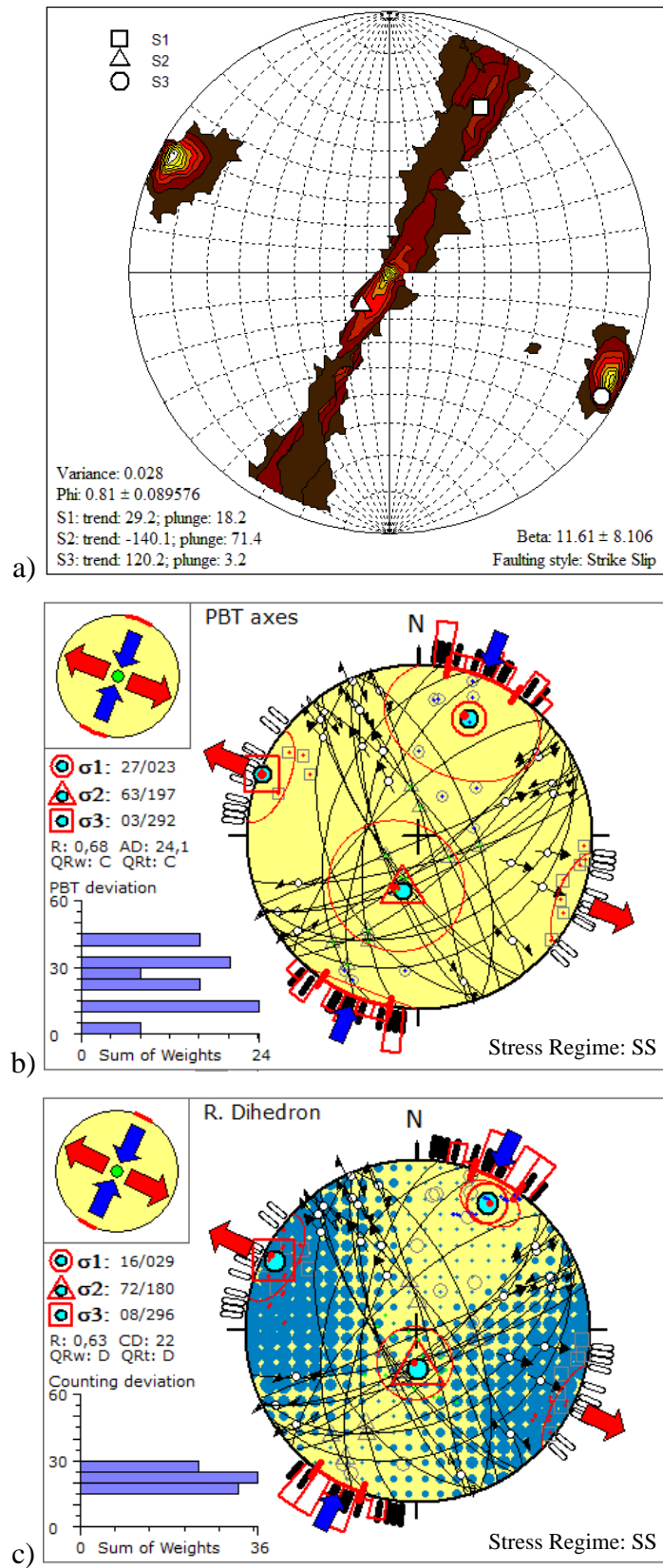


**Figure 4. 8** The results of stress tensor inversion by (a) Michael's method; (b) P-, B-, T-axes method; and (c) Right Dihedron method in Sub-region 2.

### 4.1.3 Sub-region 3

Sub-region 3 involves focal mechanism solutions for 22 earthquakes and their distribution can be seen in Figure 4.9. This area is located between the CAFZ and MOFZ in Sivas Basin which is dominantly affected by strike-slip faulting. Due to the stress tensor inversion results (Figure 4.10), the region is characterized by strike-slip faulting with NW-SE oriented extension and NE-SW oriented compression. The principal stresses  $\sigma_1$  and  $\sigma_3$  are horizontal whereas  $\sigma_2$  is vertical. The stress ratio (R) ranges between 0.54 and 0.62 as moderate values which suggest that  $\sigma_2$  value is close to the average values of  $\sigma_1$  and  $\sigma_3$ . Low variance 0.058 ( $< 0.20$ ) and beta 17.29 ( $< 35^\circ$ ) represent uniform stress field in this sub-region.

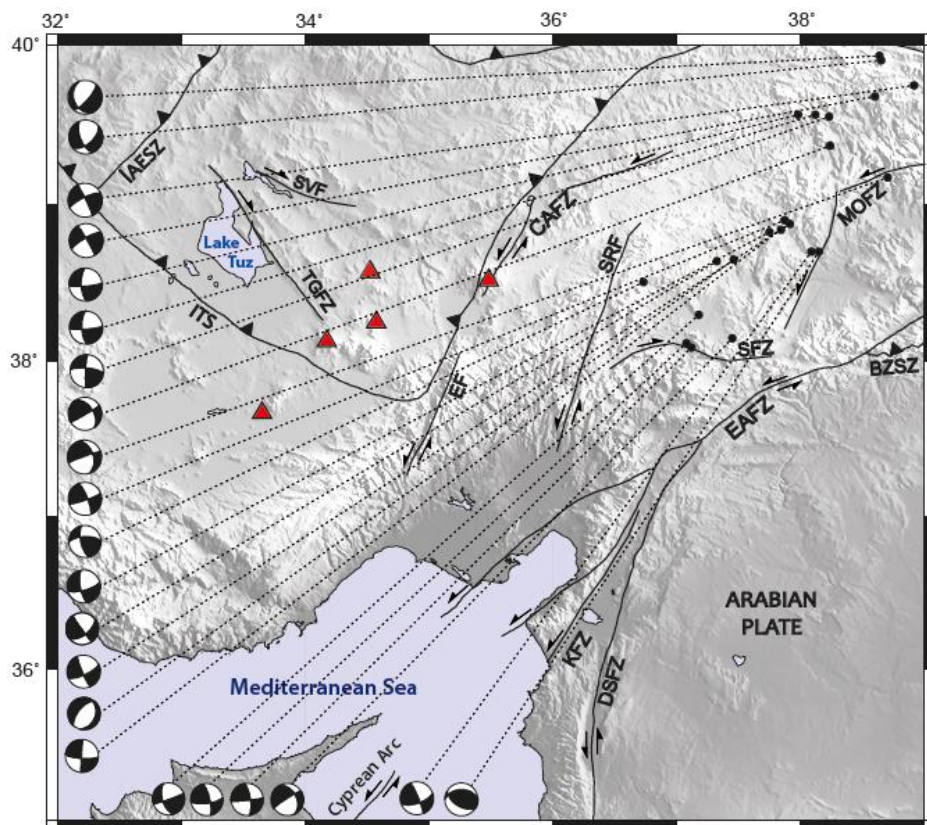


**Figure 4. 9** Map showing focal mechanism solutions of Sub-region 3. Red triangles denote Holocene volcanoes. (taken from Abgarmi et al., 2017). Labels are explained in Figure 2. 1.

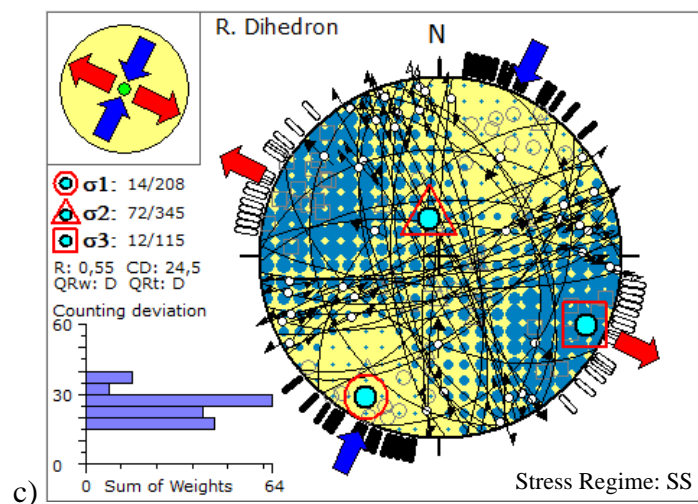
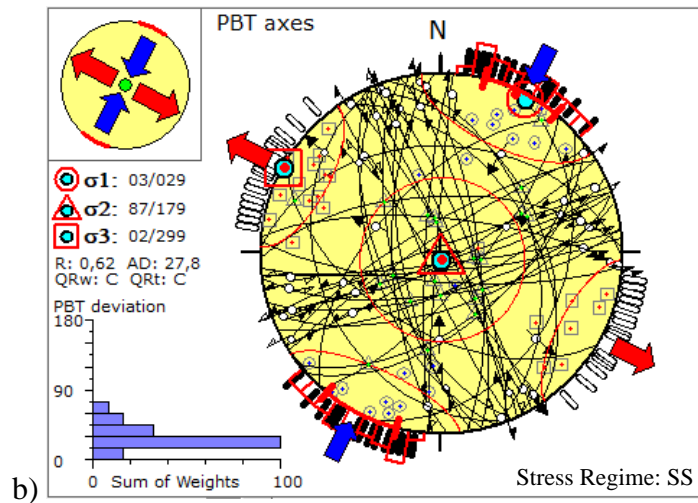
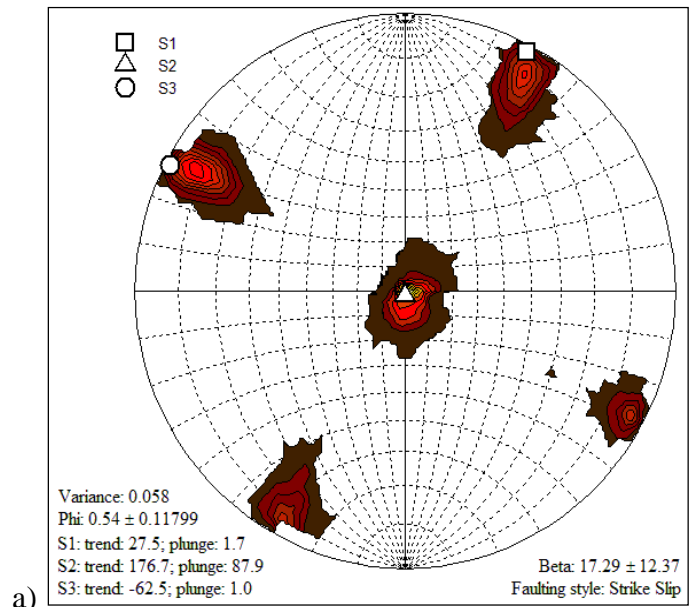


**Figure 4. 10** The results of stress tensor inversion by (a) Michael's method; (b) P-, B-, T-axes method; and (c) Right Dihedron method in Sub-region 3.

#### 4.1.4 Sub-region 4

Sub-region 4 covers a focal mechanism solution catalog of 20 earthquakes which are distributed at the intersection area of EAFZ and BZSZ (Figure 4.11). This region is characterized by strike-slip faulting with WNW-ESE oriented extension and NNE-SSW oriented compression (Figure 4.12). The stress tensor inversion results suggest that the principal stresses  $\sigma_1$  and  $\sigma_3$  are approximately horizontal while  $\sigma_2$  is vertically trending. The resultant stress ratio, R ranges between moderate values of 0.53 and 0.62 indicating that  $\sigma_2$  value and the average values of  $\sigma_1$  and  $\sigma_3$  are close to each other in magnitude. Sub-region 4 is represented by uniform stress field regarding low variance 0.031 ( $< 0.20$ ) and beta 11.56 ( $< 35^\circ$ ) values.

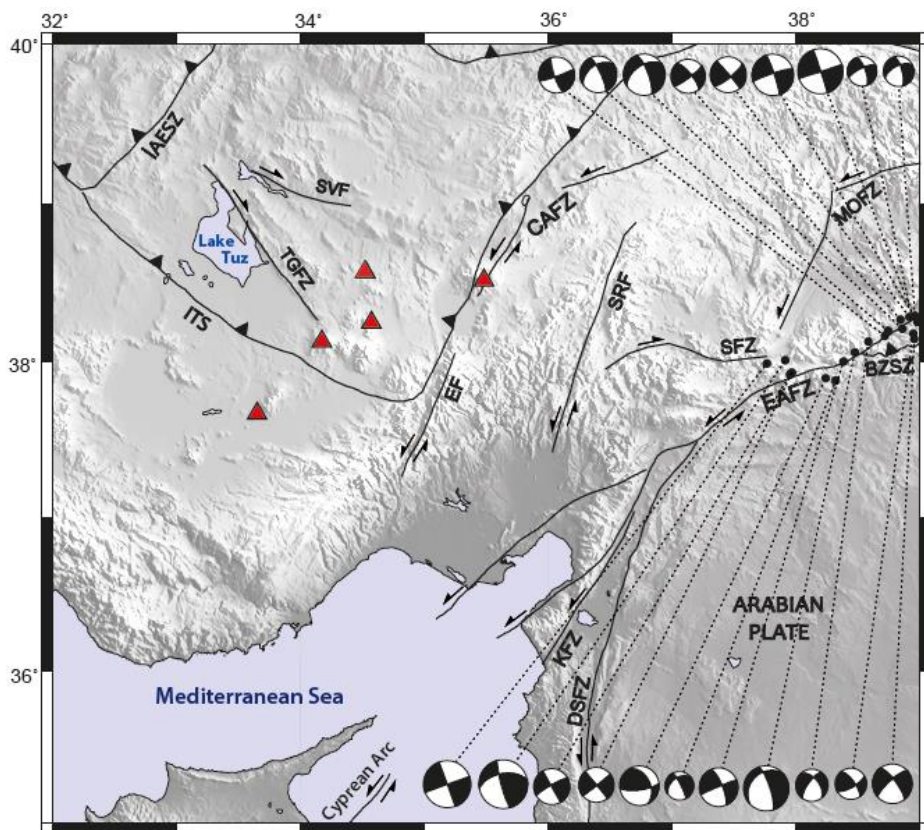


**Figure 4. 11** Map showing focal mechanism solutions of Sub-region 4. Red triangles denote Holocene volcanoes. (taken from Abgarmi et al., 2017). Labels are explained in Figure 2. 1.

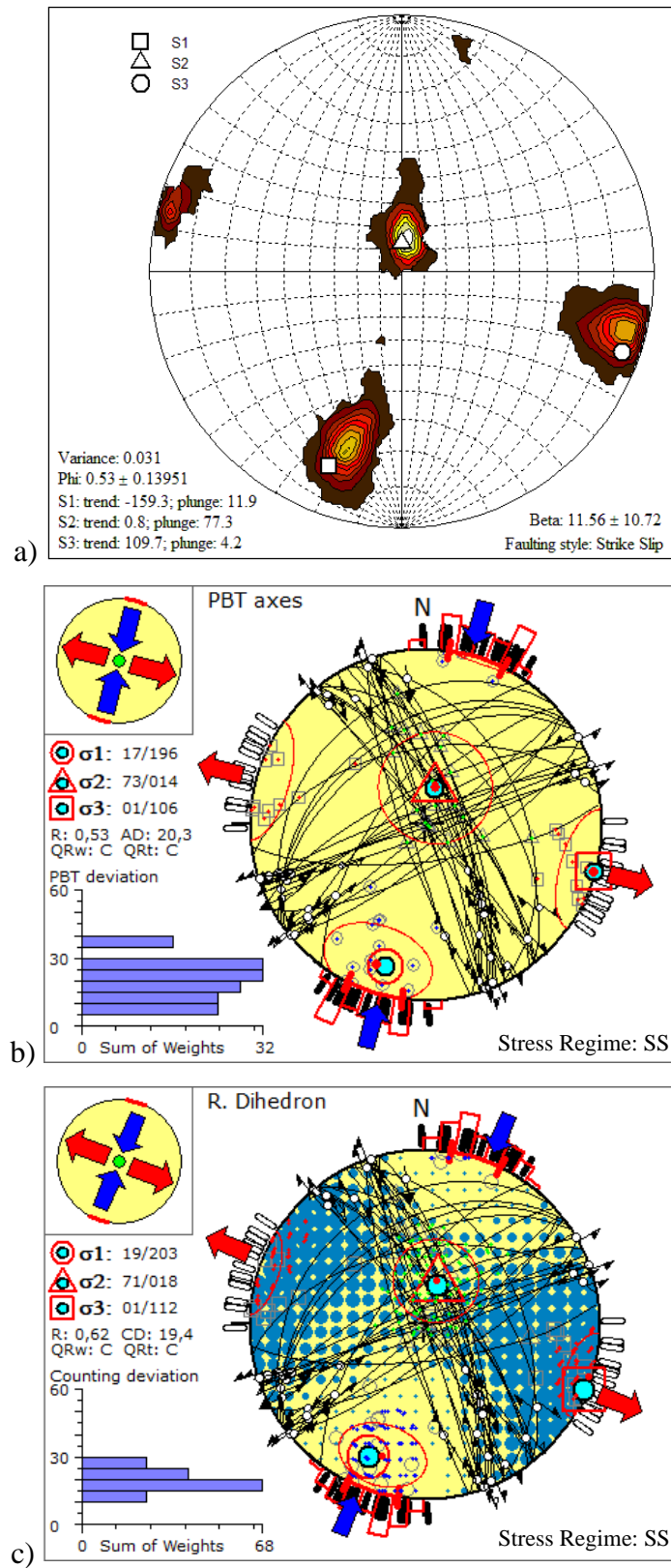


**Figure 4. 12** The results of stress tensor inversion by (a) Michael's method; (b) P-, B-, T-axes method; and (c) Right Dihedron method in Sub-region 4.

#### 4.1.5 Sub-region 5

Sub-region 5 comprises of focal mechanism solutions for 26 earthquakes which are distributed along the intersection area of EAFZ and DSFZ (Figure 4.13). The dominant faulting style is strike-slip mechanism with E-W oriented extension and N-S compression (Figure 4.14). The stress inversion results show that  $\sigma_1$  and  $\sigma_3$  are horizontal and  $\sigma_2$  is vertical. The resultant stress ratio, R values vary between a moderate range of 0.41 – 0.48 suggesting that the average values of  $\sigma_1$  and  $\sigma_3$  are close to  $\sigma_2$  in magnitude. The variance value 0.17 is close to the threshold value (0.20), whereas the beta value 38.96 is exceeding the limit value ( $35^\circ$ ). A heterogeneous stress pattern is expected in this sub-region which is compatible with the existence of different fault zones in this intersection area.

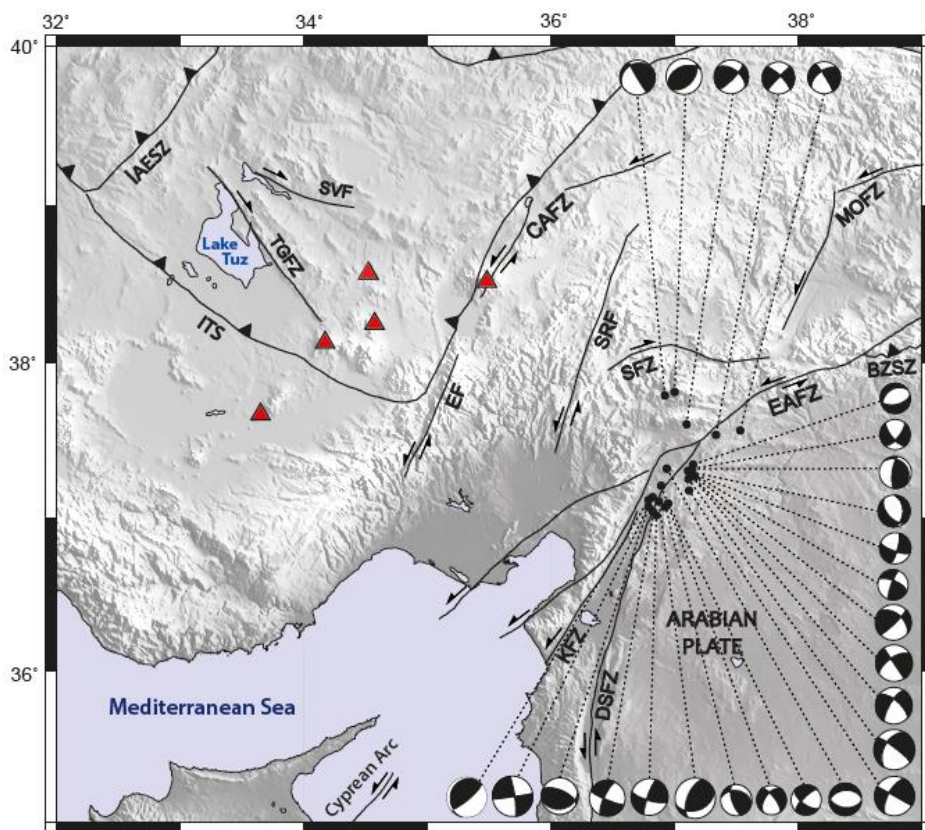


**Figure 4. 13** Map showing focal mechanism solutions of Sub-region 5. Red triangles denote Holocene volcanoes. (taken from Abgarmi et al., 2017). Labels are explained in Figure 2. 1.

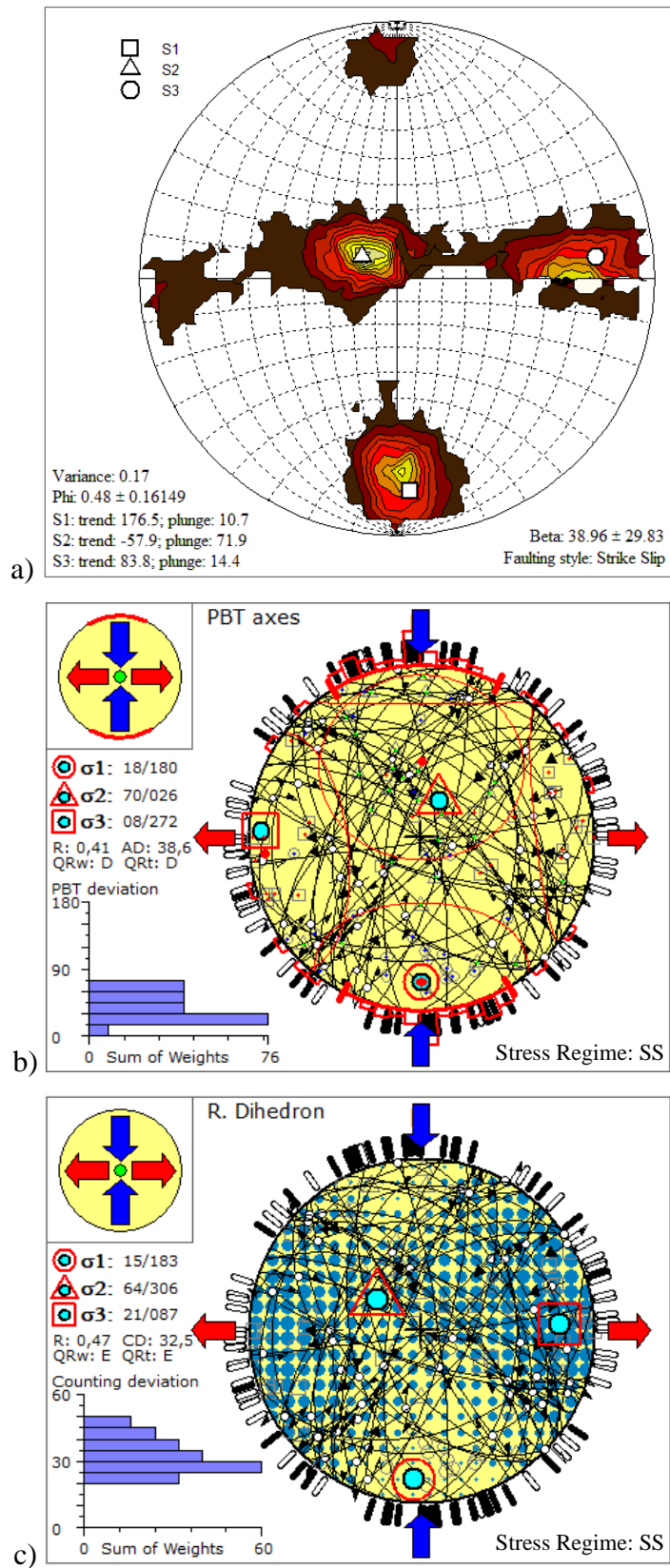


**Figure 4. 14** The results of stress tensor inversion by (a) Michael's method; (b) P-, B-, T-axes method; and (c) Right Dihedron method in Sub-region 5.

#### 4.1.6 Sub-region 6

Sub-region 6 consists of focal mechanism solutions for 30 earthquakes which are located along the southern branch of EAFZ (Figure 4.15). The stress tensor inversion results vary noticeably from one method to another. According to Michael's method  $\sigma_1$  deviates from vertical significantly and indicates normal to strike-slip faulting whereas both P-B-T axes and right Dihedron methods positioned  $\sigma_1$  close to vertical indicating pure normal faulting. In contrast,  $\sigma_3$  is oriented horizontal in every inversion suggesting WNW-ESE extension (Figure 4.16). The calculated stress ratio, R values are ranging between 0.77 – 0.94 indicating that  $\sigma_2$  is significantly larger than  $\sigma_3$  in magnitude. The resulted variance (0.17) is close to permissible limit value (0.20) and the beta (38.70) is exceeding the limit value (35°). These results lead a heterogeneous stress pattern which can be correlated with the varying faulting type in this region.

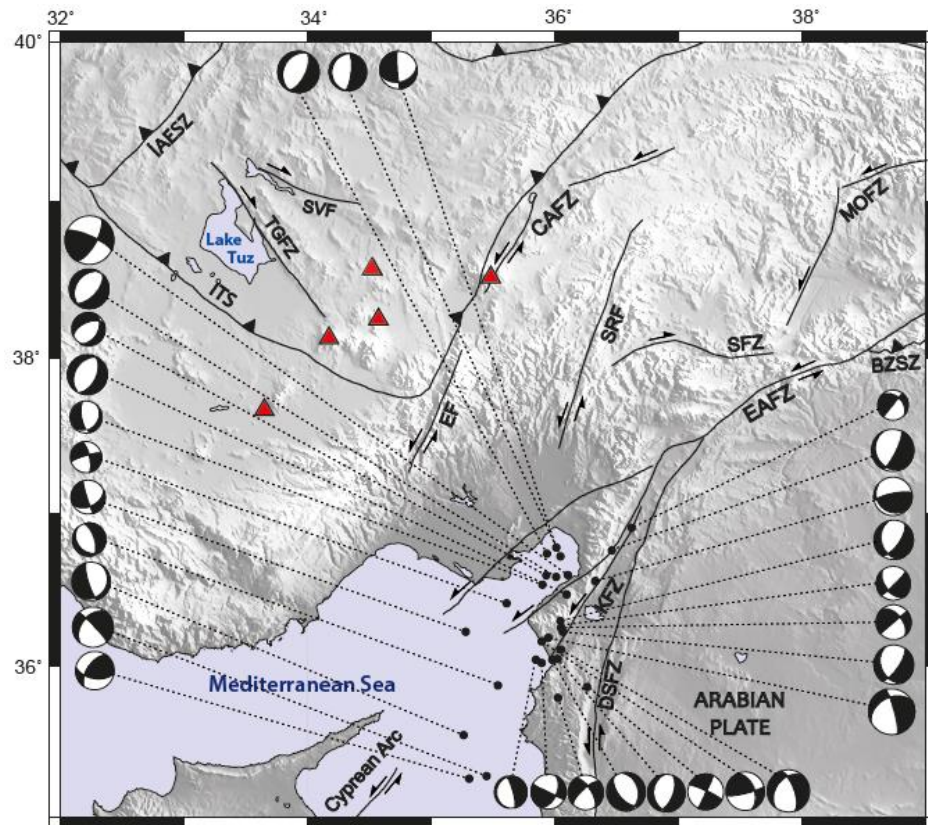


**Figure 4. 15** Map showing focal mechanism solutions of Sub-region 6. Red triangles denote Holocene volcanoes. (taken from Abgarmi et al., 2017). Labels are explained in Figure 2. 1.

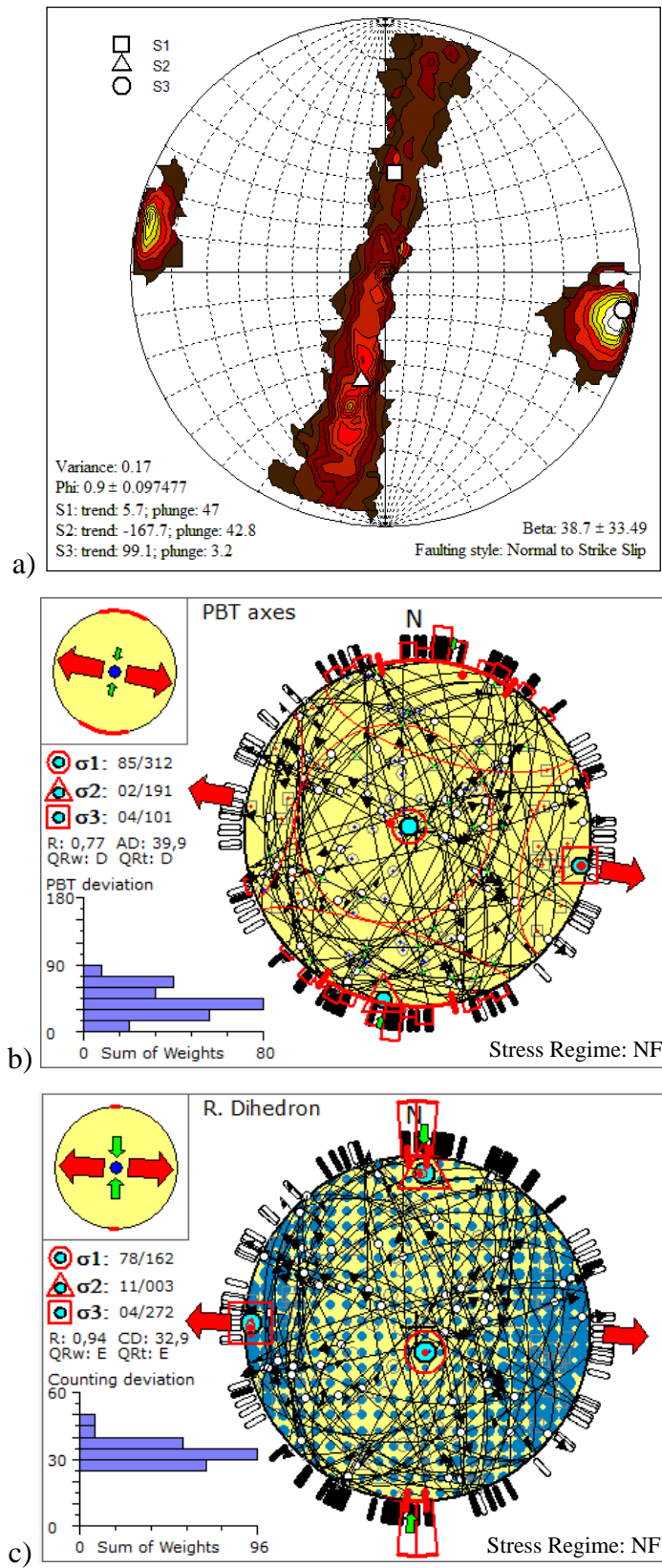


**Figure 4. 16** The results of stress tensor inversion by (a) Michael's method; (b) P-, B-, T-axes method; and (c) Right Dihedron method in Sub-region 6.

#### 4.1.7 Sub-region 7

Sub-region 7 is composed of 52 earthquake focal mechanism solutions which are located in Adana Basin along the northern branch of EAFZ (Figure 4.17). Similar to sub-region 6, inversion results vary noticeably. According to Michael's method  $\sigma_1$  is oriented horizontal in N-S direction indicating pure strike-slip faulting whereas both P-B-T axes and right Dihedron methods positioned  $\sigma_1$  oblique indicating normal to strike-slip faulting (transtension). In contrast,  $\sigma_3$  is oriented horizontal in every inversion suggesting W-E extension (Figure 4.18). The resultant variance 0.14 ( $< 0.20$ ) and beta  $31^\circ$  ( $< 35^\circ$ ) values are lower than the boundary limits suggesting a homogeneous stress pattern in the region. The stress ratio (R) values are changing between 0.84 – 0.89 indicating that  $\sigma_2$  is significantly larger than  $\sigma_3$  in magnitude.

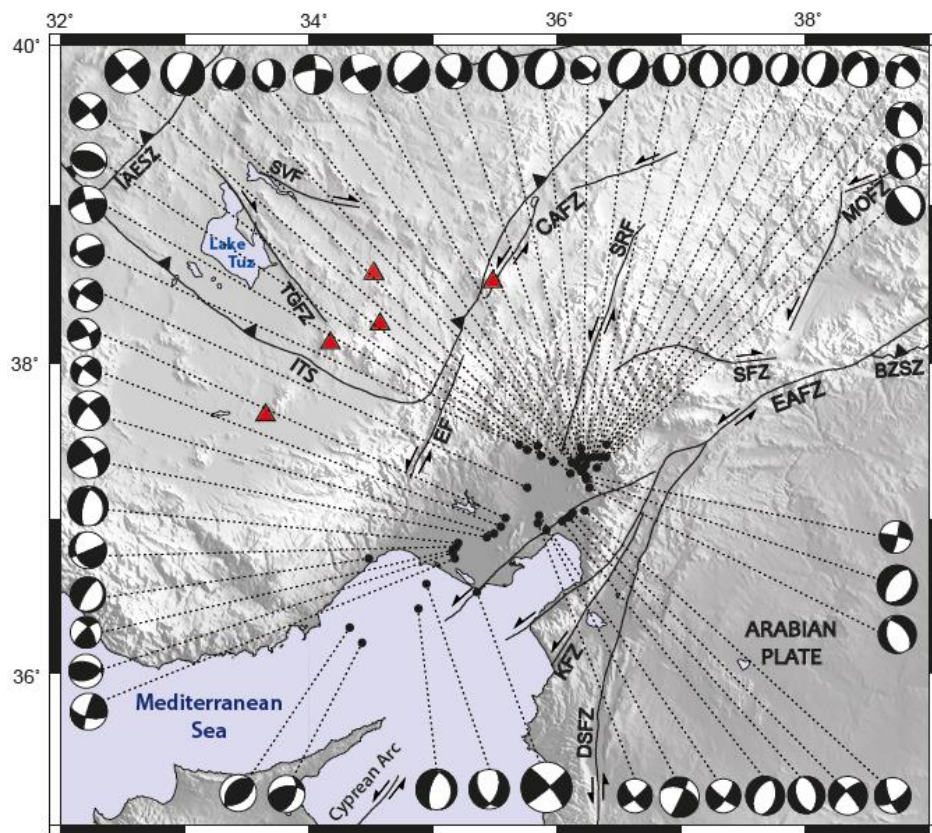


**Figure 4. 17** Map showing focal mechanism solutions of Sub-region 7. Red triangles denote Holocene volcanoes. (taken from Abgarmi et al., 2017). Labels are explained in Figure 2. 1.

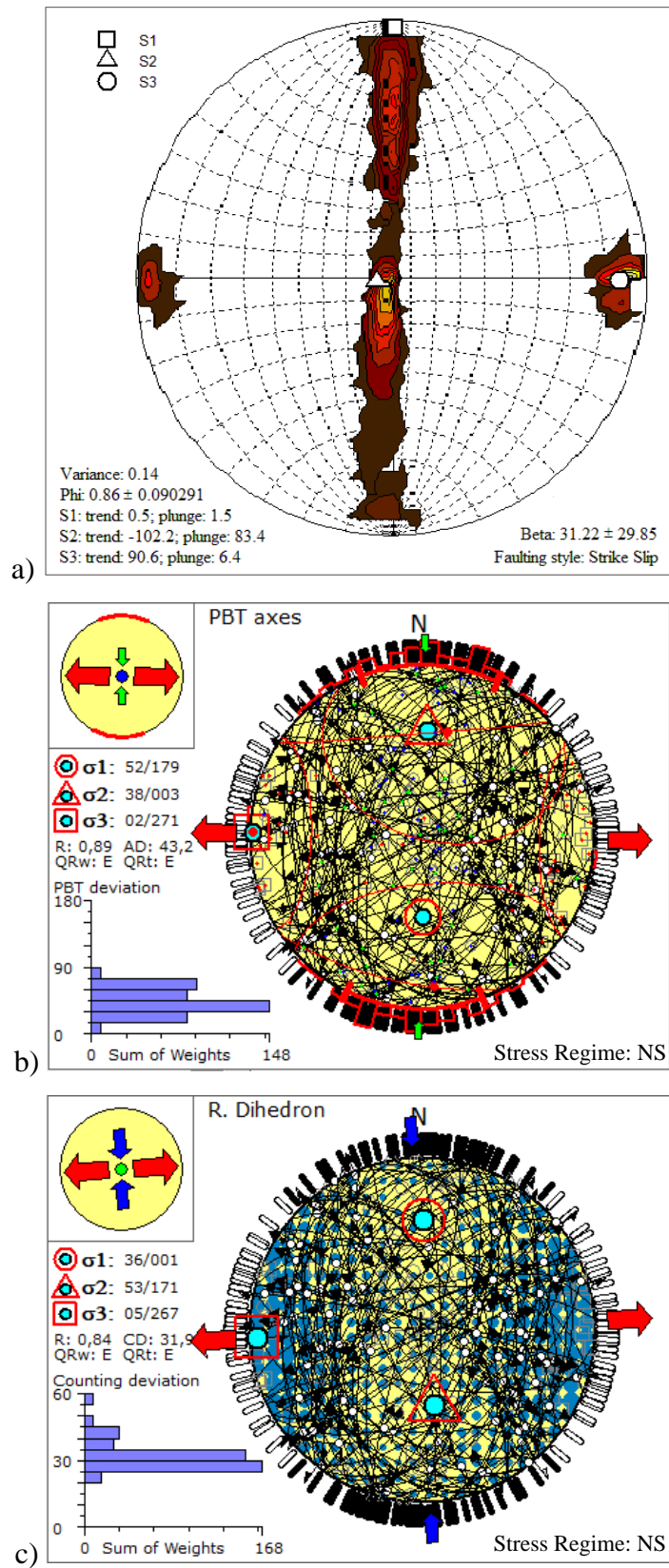


**Figure 4. 18** The results of stress tensor inversion by (a) Michael's method; (b) P-, B-, T-axes method; and (c) Right Dihedron method in Sub-region 7.

#### 4.1.8 Sub-region 8

Sub-region 8 covers a catalog of 6 earthquake focal mechanism solutions located at the Northern Cyprus (Figure 4.19). The stress tensor analysis results suggest that the principal stresses  $\sigma_1$  and  $\sigma_2$  are sub-horizontal and  $\sigma_3$  is sub-vertical. Thus the dominant faulting style is reverse mechanism (Figure 4.20). In this sub-region, the results of Michael's (1987) and Delvaux and Sperner (2003) differs in compression orientation. Michael's method (1987) reveals WNW-ESE oriented compression while Win-Tensor gives NNW-SSE oriented compression which is consistent with the Cyprus Arc. Similarly, the estimated stress ratio, R values are found in a wide range of 0.63 to 0.91. Although, the resultant variance 0.14 ( $< 0.20$ ) and beta 25.73 ( $< 35^\circ$ ) values are lower than the threshold limits regarding a homogeneous stress pattern, earthquake data used in the inversion is very limited (six earthquakes) leading to highly variable less accurate solutions and should be treated with caution.

Note that the stress tensor inversion results for the entire region and all the sub-regions are represented in Table 4.1.

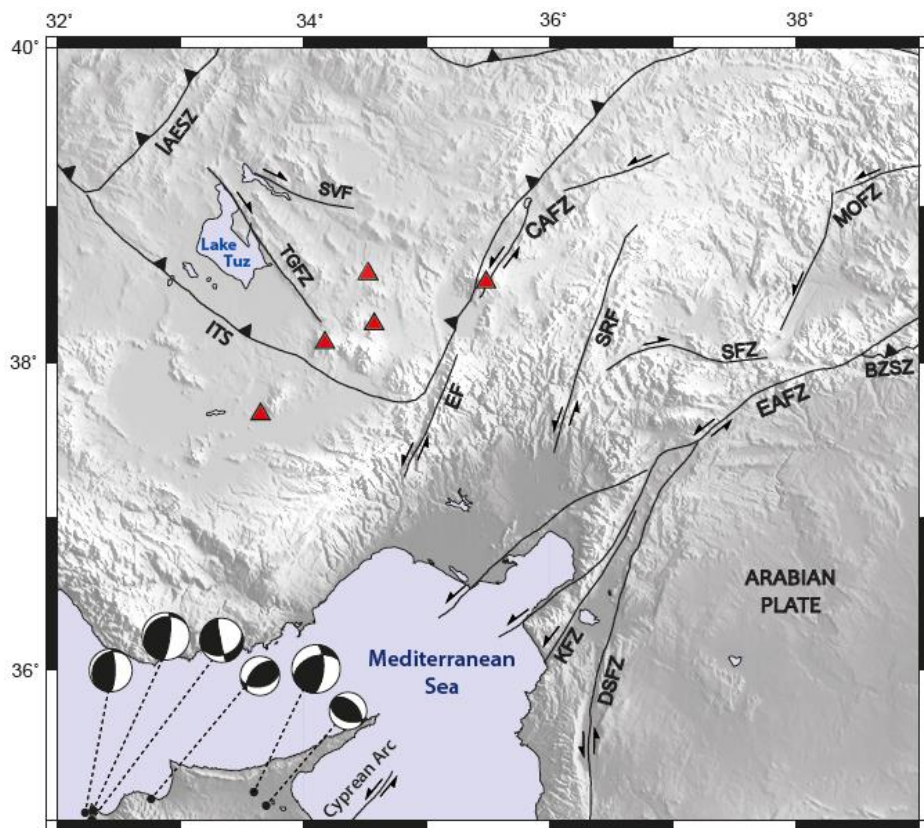


**Figure 4. 19** Map showing focal mechanism solutions of Sub-region 8. Red triangles denote Holocene volcanoes. (taken from Abgarmi et al., 2017). Labels are explained in Figure 2. 1.

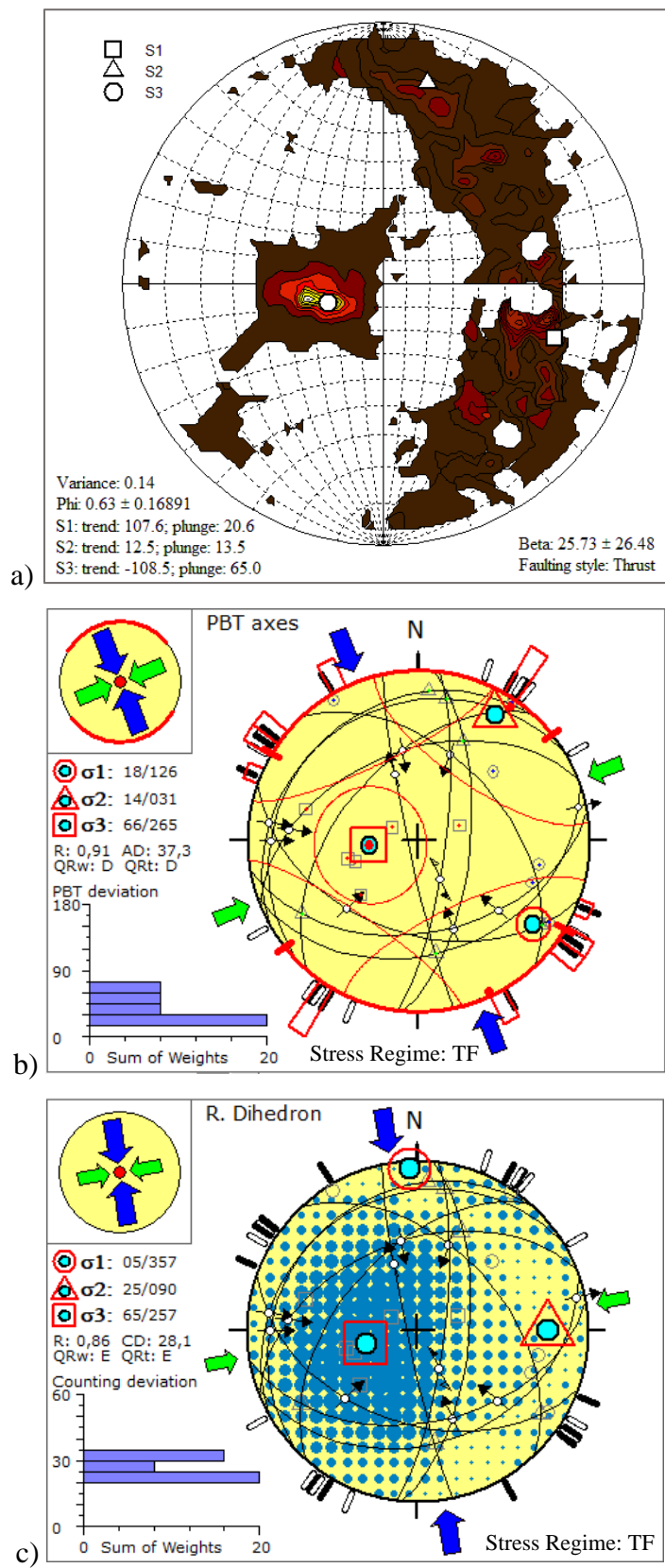


**Figure 4. 20** The results of stress tensor inversion by (a) Michael's method; (b) P-, B-, T-axes method; and (c) Right Dihedron method in Sub-region 8.

**Table 4. 1** Comparison of stress tensor inversion results by Michael's method (1987) in ZMAP and by P-,B-,T-axes and Right Dihedron methods in Win-Tensor (Delvaux and Sperner, 2003) for the entire region and the sub-regions.

Region	Method	$\sigma_1$		$\sigma_2$		$\sigma_3$		Phi (R)	Var.	Beta	Regime
		(tr)	(pl)	(tr)	(pl)	(tr)	(pl)				
Entire	Michael	186	02	304	86	96	03	0.67±0.06	0.15	34.83±33.27	SS
	PBT	007	01	220	89	097	00	0.76	-	-	SS
	R.Dihedron	005	24	171	66	273	05	0.74	-	-	SS
1	Michael	348	07	139	82	258	04	0.46±0.14	0.04	13.64±9.59	SS
	PBT	343	08	141	81	252	03	0.56	-	-	SS
	R.Dihedron	341	19	133	69	247	09	0.47	-	-	SS
2	Michael	029	18	220	71	120	03	0.81±0.09	0.03	11.61±8.11	SS
	PBT	023	27	197	63	292	03	0.68	-	-	SS
	R.Dihedron	029	16	180	72	296	08	0.63	-	-	SS
3	Michael	028	02	177	88	297	01	0.54±0.12	0.06	17.29±12.37	SS
	PBT	029	03	179	87	299	02	0.62	-	-	SS
	R.Dihedron	208	14	345	72	115	12	0.55	-	-	SS
4	Michael	201	12	001	77	110	04	0.53±0.14	0.03	11.56±10.72	SS
	PBT	196	17	014	73	106	01	0.53	-	-	SS
	R.Dihedron	203	19	018	71	112	01	0.62	-	-	SS
5	Michael	177	11	302	72	084	14	0.48±0.16	0.17	38.96±29.83	SS
	PBT	180	18	026	70	272	08	0.41	-	-	SS
	R.Dihedron	183	15	306	64	087	21	0.47	-	-	SS
6	Michael	006	47	192	43	099	03	0.90±0.10	0.17	38.70±33.49	N-SS
	PBT	312	85	191	02	101	04	0.77	-	-	NF
	R.Dihedron	162	78	003	11	272	04	0.94	-	-	NF
7	Michael	180	03	299	84	091	05	0.87±0.09	0.14	31.22±29.26	SS
	PBT	179	52	003	38	271	02	0.89	-	-	NS
	R.Dihedron	001	36	171	53	267	05	0.84	-	-	NS
8	Michael	108	21	013	14	251	65	0.63±0.17	0.14	25.73±26.48	TF
	PBT	126	18	031	14	265	66	0.91	-	-	TF
	R.Dihedron	357	05	090	25	257	65	0.86	-	-	TF

The computed stress tensor inversion solutions for each sub-region are compatible with each other for all the methods except Sub-region 8 regarding its insufficient number of data to obtain stable results. The stress ratio, R values are varying in a narrow range in Sub-region 1, 3, 4, 5 and 7; whereas it differs widely in Sub-regions 2, 6 and 8 for Michael's (1987), PBT-axes and Right Dihedron methods. These varying results in terms of different methods may be caused by limited data in Sub-region 2 and 8, and complex stress regime in Sub-region 6. As a result, the solutions of Michael's (1987) method and Right Dihedron approach are generally coherent with each other so that in the previous section Right Dihedron solutions are represented.



## CHAPTER 5

### DISCUSSION AND CONCLUSION

Finally, the entire focal mechanism solutions (200) in the study area are used to draw their rake based ternary diagram and the distribution of P- and T-axes orientation on the stereonet which are plotted based on their fault source parameters (Figure 5.1 and 5.2). The results suggest that strike-slip and normal faulting mechanisms are dominant in the region while the reverse faulting mechanism is rarely seen. The resultant P- and T-axes orientations provide that the region is under NNE-SSW oriented compression and WNW-ESE oriented extension. This state is in accordance with the tectonic regime of Central Anatolia.

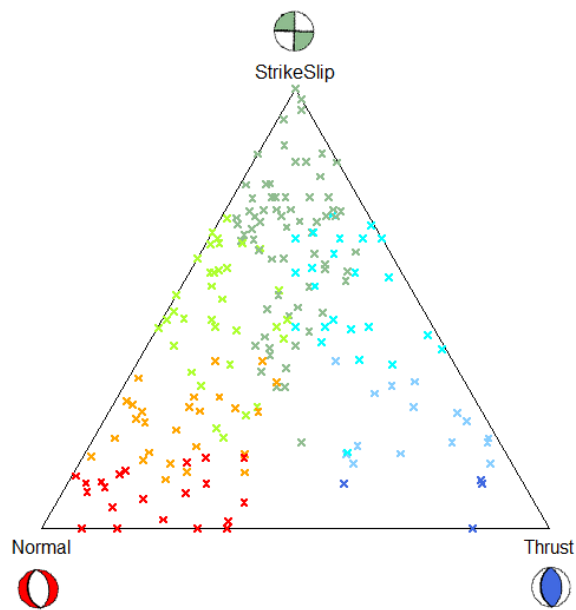


**Figure 5. 1** Rake-based ternary diagram of all the focal mechanism solutions (200) in the study area.

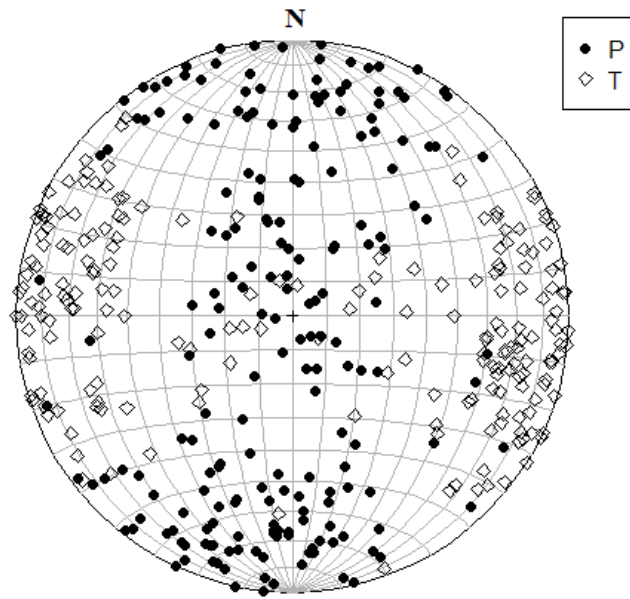


**Figure 5. 2** Distribution of P- and T-axes orientations of all the focal mechanism solutions (200). Black filled diamonds show P-axis and unfilled diamonds indicate T-axis.

According to the number of regime types for the entire data set (200) in the study area, the types of faulting are plotted as histogram (Figure 5.3). It is seen that the strike-slip faulting is the most seen regime in the study area with its 46 % among the data. The normal faulting is at the second place with its 24 %. The regime code is undefined for 14 % of the data. The reverse faulting is seen at a rate of 10 %. Predominantly normal faulting with strike slip component regime is resulted as 5 % and predominantly reverse faulting with strike slip component regime is at a rate of 1 % in the study area.

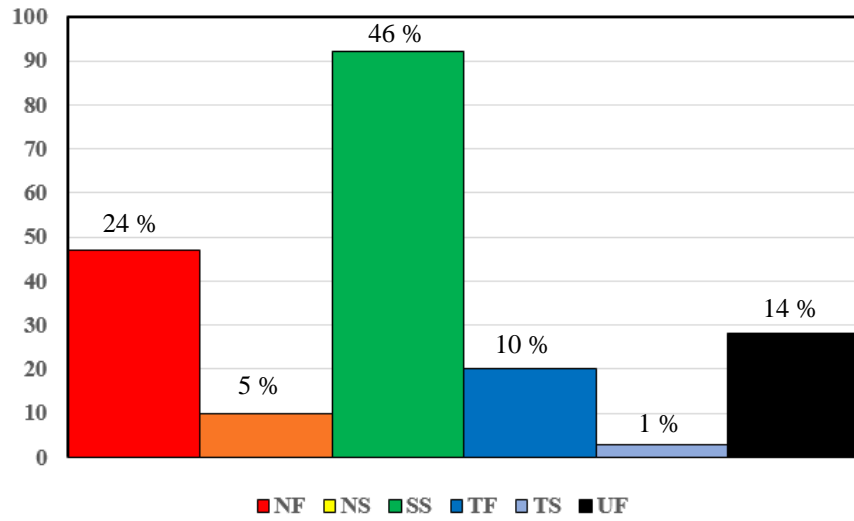


**Figure 5. 3** Faulting type histogram for the entire data set.

In order to compare the stress field results with the tectonic stress field, regime types based on  $S_{Hmax}$  orientations in the study area are plotted (Figure 5.4a) by using World Stress Map (WSM) database which depends on a web-based source program CASMO (Heidbach et al., 2008). According to WSM stress map, N-S, NNE-SSW and NW-SE oriented  $S_{Hmax}$  stresses are dominantly observed around Adana Basin and compatible with the directions of subduction along the BZSZ, EAFZ and DSFZ. In the upper central part of the study area, several NE-SW and N-S trending stresses are recorded which have similar orientations with the CAFZ. There is another cluster in the northern part of Tuz Gölü orienting mostly in NNW-SSE direction which is parallel to the TGFZ. There is rare N-S trending faulting in this part which are occurred in Ankara. Besides WSM database, the studied data of focal mechanism solutions for the entire data (200) are plotted and their contribution to WSM is represented in Figure 5.4b. It is seen that the studied data is compatible with the prevailing stress conditions and represents new information in some areas.

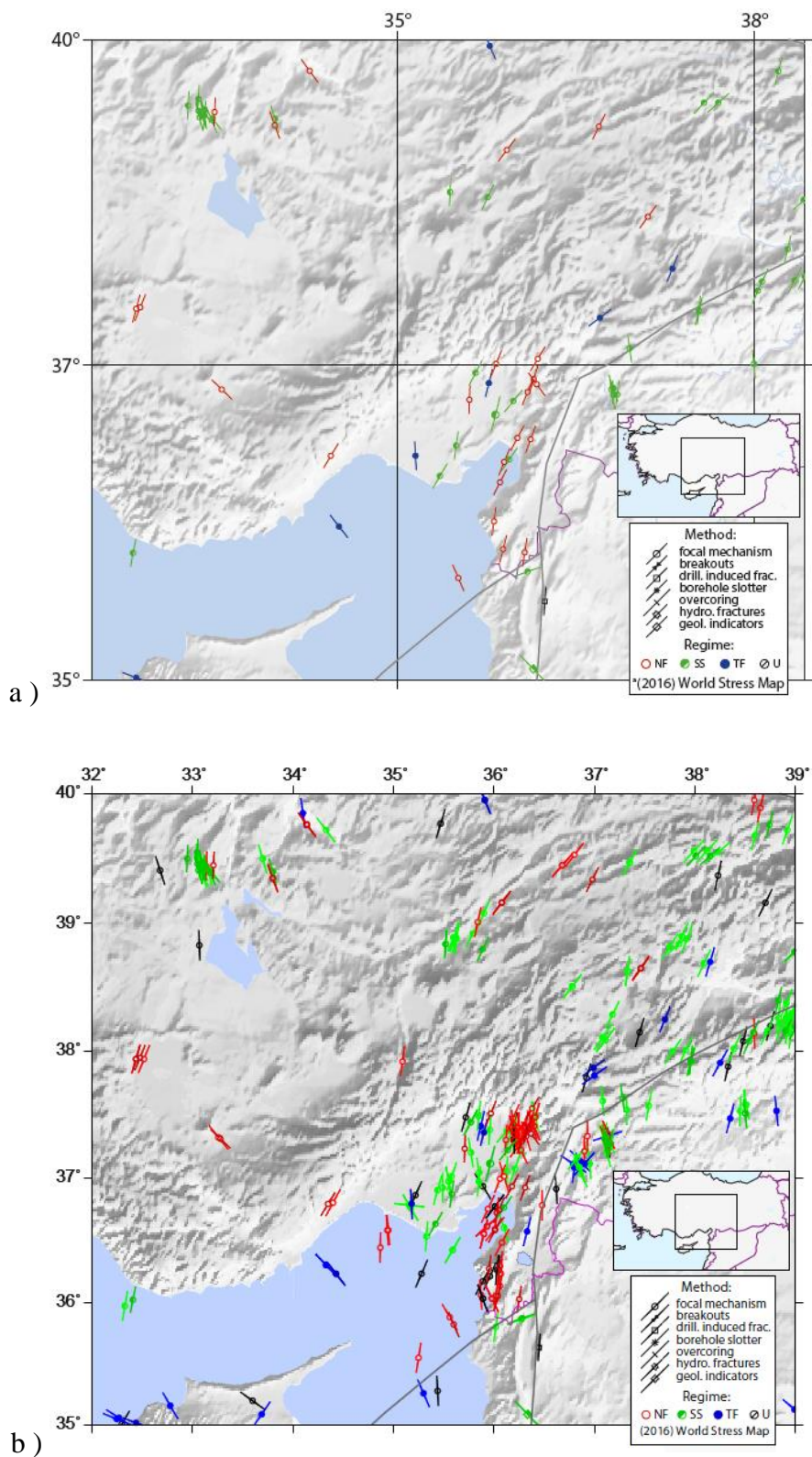


**Figure 5. 4** Stress map of the study area based on maximum horizontal stress axes ( $S_{Hmax}$ ) of focal mechanism solutions of (a) World Stress Map (WSM) database (Heidbach et al., 2008) (b) entire data used in this study including our solutions and ones compiled from literature.

In addition to WSMs of the study area, rose diagrams of  $S_{Hmax}$  and  $S_{Hmin}$  are plotted by Win-Tensor program (Figure 5.5). The results show that the stress regime is dominated by NNE-SSW oriented  $S_{Hmax}$  and WNW-ESE oriented  $S_{Hmin}$  horizontal stresses of the entire focal mechanism solutions. These results are compatible with the distributions of P- and T-axes orientations in the study area.

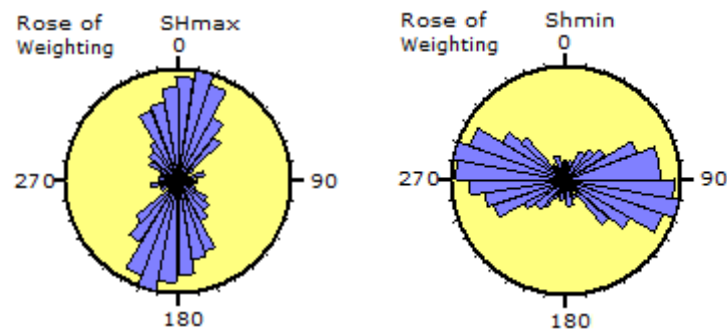


**Figure 5. 5** Rose diagrams of maximum ( $S_{Hmax}$ ) and minimum ( $S_{Hmin}$ ) horizontal stresses of entire focal mechanism solutions (200) by equal area display in Win-Tensor (Delvaux and Sperner, 2003).

In order to determine the stress variations in the entire region, eight sub-regions having approximately similar strain conditions are identified by considering the tectonic properties and the epicentral distances of focal mechanisms. Each region is analyzed to define their stress patterns by Win-Tensor. The results are individually shown on the map (Figure 5.6). The relative horizontal stresses are represented by the arrows and the vertical stresses are shown by circles in the middle of the arrows. The resultant stress field provides that  $\sigma_1$  is oriented in approximately N-S, NNE-SSW and NNW-SSW directions except Sub-region 6;  $\sigma_2$  is vertical except Sub-region 6 and 8; and  $\sigma_3$  is oriented in approximately E-W, WNW-ESE and WSW-ENE directions except Sub-region 8.

According to Figure 5.6, the stress tensor inversion solution becomes different with its  $\sigma_2$  and  $\sigma_3$  stress orientations in Sub-region 6 in where the southern branch of EAFZ and the northern parts of the DSFZ is getting close. Sub-region 6 displays a dominant extension in WNW-ESE direction and vertical compression which represent normal faulting. In sub-region 8,  $\sigma_1$  is oriented in NNW-SSE;  $\sigma_2$  is oriented in WSW-ENE; and  $\sigma_3$  is oriented vertically which indicate reverse faulting. Sub-region 6 and 8 have different stress regimes rather than the dominant strike-slip faulting which are compatible with the tectonic properties in the study area.

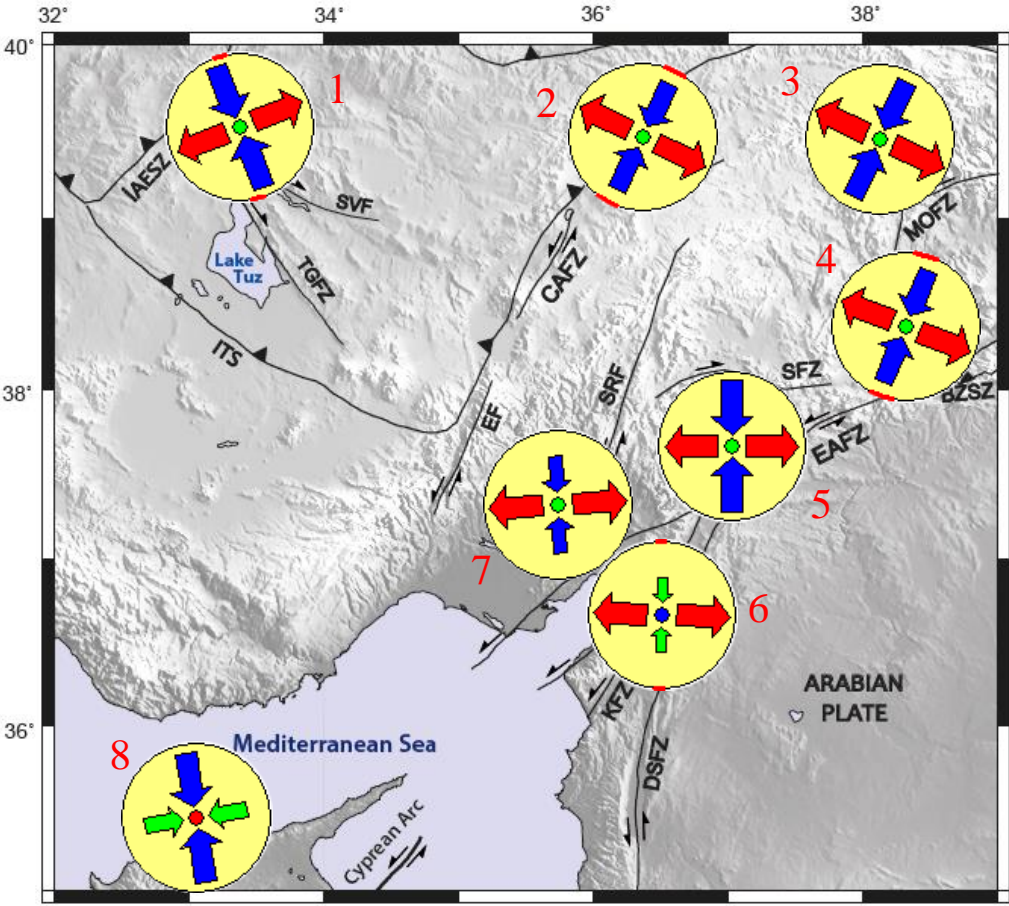


**Figure 5. 6** Simplified map for the results of horizontal projections of principle stresses for the sub-regions by Right Dihedron method (Delvaux and Sperner, 2003).  $\sigma_1$ : blue,  $\sigma_2$ : green,  $\sigma_3$ : red. Labels are explained in Figure 2. 1.

The calculated correlations in this study indicate reasonable relations in the view of tectonism and fault mechanisms in the region. However, the resultant parameters are obtained from particular data sources gathered from a limited region and time interval so that have relatively wide error ranges. The resultant correlations should be considered with caution and checked by a more general data set.



## REFERENCES

- Abgarmi, B., Delph, J. R., Özacar, A. A., Beck, S. L., Zandt, G., Sandvol, E., Türkelli, N., and Biryol, C. B., 2017. Structure of the crust and African slab beneath the central Anatolian plateau from receiver functions: New insights on isostatic compensation and slab dynamics. *Geosphere*, v. 13, no. 6, p. 1–14, doi:10.1130/GES01509.1.
- Akıman, O., Erler, A., Göncüoğlu, M. C., Güleç, N., Geven, A., Türeli, T. K., and Kadioğlu, Y. K., 1993. Geochemical characteristics of granitoids along the western margin of the central Anatolian Crystalline Complex and their tectonic implications, *Geol. J.*, 28, 371–382, doi:10.1002/gj.3350280315.
- Aki, K., 1965. Maximum Likelihood estimate of b in the formula  $\log N=a-bM$  and its confidence limits. *Bull. Earthquake Res Inst.*, Tokyo Univ. 43, 237-239.
- Aki, K., and Richards, P. G., 1980. Quantitative seismology: Theory and methods, v.1: W.H. Freeman and Co.
- Aki, K., and Richards, P. G., 2002. Quantitative Seismology, 2<sup>nd</sup> edition. University Science Books, California.
- Aktuğ, B., Parmaksız, E., Kurt, M., Lenk, O., Kılıçoğlu, A., Gürdal, M. A., and Özdemir, S., 2013. Deformation of Central Anatolia: GPS implications. *Journal of Geodynamics*, 67, 78-96.
- Ambraseys, N. N., 1989. Temporary seismic quiescence, SE Turkey. *Geophys. J.*, 96, 411–431.
- Ambraseys, N. N., and Barazangi, M., 1989. The 1759 earthquake in the Bekaa valley: Implications for earthquake hazard assessment in the Eastern Mediterranean region. *J. of Geophys. Res.*, v. 94, p. 4007–4013.
- Ambraseys, N. N., Melville, C. P., and Adams, R. D., 1994. The Seismicity of Egypt, Arabia and the Red Sea. King Abdulaziz City For Science & Technology. Cambridge University Press.
- Angelier, J., 1979. Determination of the mean principal direction of stress for a given fault population, *Tectonophysics*, 56, 17-26.

- Angelier, J., 1984. Tectonic analysis of fault slip data sets, *Geophys. Res.*, 89, B7, 5835-5848.
- Angelier, J., 2002. Inversion of earthquake focal mechanisms to obtain the seismotectonic stress IV — a new method free of choice among nodal lines. *Geophys. J. Int.*, 150, 568–609.
- Angelier, J., and Mechler, P., 1977. Sur une méthode graphique de recherche des contraintes principales également utilisable en tectonique et en séismologie: la méthode des dièdres droits. *Bull. Soc. Geol., Fr* 7:1309–1318.
- Arger, J., Mitchell, J., and Westaway, R., 2000. Neogene and Quaternary volcanism of south-eastern Turkey, in: Bozkurt E., Winchester J.A., Piper J.D.A. (Eds.), *Tectonics and magmatism in Turkey and the Surrounding Area, Geological Society Special Publication*, 173, pp. 459–487.
- Arpat, E., and Şaroğlu, F., 1972. The East Anatolian Fault System: thoughts on its development. *Min. Res. Expl. Inst. Turkey Bull.*, 78, 33–39.
- Barka, A., Akyüz, H. S., Cohen, H. A. and Watchorn, F., 2000. Tectonic evolution of the Niksar and Tasova–Erbaa pull-apart basins, North Anatolian fault zone: Their significance for the motion of the Anatolian block, *Tectonophysics*, 322, 243–264.
- Barth, A., 2007. Frequency sensitive moment tensor inversion for light to moderate magnitude earthquakes in eastern Africa and derivation of the regional stress field. Ph.D. Dissertation, University of Karlsruhe.
- Barth, A., Reinecker, J., and Heidbach, O., 2008. Stress derivation from earthquake focal mechanisms. World Stress Map Project, Guidelines: Focal mechanisms.
- Bath, M., 1983. Earthquake frequency and energy in Greece. *Tectonophysics*, 95, 233-252.
- Ben-Avraham, Z., Lazar, M., Schattner, U., and Marco, S., 2005. The Dead Sea Fault and its effect on civilization. In: Wenzel, F. (eds.) *Perspectives in Modern Seismology*, Lecture Notes in Earth Sciences, vol. 105.
- Biryol, C. B., Beck, S. L., Zandt, G., and Özacar, A. A., 2011. Segmented African lithosphere beneath the Anatolian region inferred from teleseismic P-wave

- tomography: *Geophysical Journal International*, v. 184, p. 1037–1057, <https://doi.org/10.1111/j.1365-246X.2010.04910.x>.
- Bock, G., 2012. NMSOP-GFZ: IS3.9 Moment tensor inversion and moment tensor interpretation.
- Bonita, J. D., Kumagai, H., and Nakano, M., 2015. Regional Moment Tensor Analysis in the Philippines: CMT Solutions in 2012–2013. *Journal of Disaster Research*, Vol.10, No.1.
- Bouchon, M., 1981. Numerical simulation of the acoustic and elastic wavefields radiated by a source in a fluid-filled borehole embedded in a layered medium. Earth Resources Laboratory Department of Earth, Atmospheric, and Planetary Sciences Massachusetts Institute of Technology, Cambridge.
- Bozkurt, E., 2001. Neotectonics of Turkey –a synthesis. *Geodinamica Acta*, 14, 3-30.
- Bozkurt, E., and Mittwede, S. K., 2001. Introduction to the Geology of Turkey – A Synthesis. *International Geology Review*, 43:7, 578-594, doi: 10.1080/00206810109465034.
- Canitez, N., and Üçer, S. B., 1967. A Catalogue of Focal Mechanism Diagrams for Turkey and Adjoining Areas. Vol. 25, İTÜ Maden Fak., Arz Fizigi Enstpg. 111 Vol.
- Clinton, J. F., 2004. Modern digital seismology - instrumentation, and small amplitude studies in the engineering world. Ph.D. Dissertation, California Institute of Technology.
- Console, R., Jackson, D. D., and Kagan, Y. Y., 2010. Using the ETAS model for catalog declustering and seismic background assessment. *Pure Appl. Geophys.*, 167, 819-830.
- Çemen, İ., Göncüoğlu, M. C., and Dirik, K., 1999. Structural evolution of the Tuzgölü Basin in Central Anatolia, Turkey. *J. of Geology*, v. 107, 693-706.
- D’Amico, S., 2018. Moment Tensor Solutions. Springer Natural Hazards.
- Dellaloğlu, A., and Aksu, R., 1984. Kulu-Şereflikoçhisar-Aksaray Dolayının Jeolojisi ve Petrol Olanakları, Turkish Petroleum Corporation report no. 2020, 1984 (in Turkish, unpublished).
- Delvaux, D., 1993. The TENSOR program for paleostress reconstruction: examples from the east African and the Baikal rift zones. EUG VII Strasbourg, France,

- 4-8 april 1993. Abstracts supplement N°1 to TERRA nova, V.5, P.216.
- Delvaux, D., 2011. Win-Tensor: an interactive computer program for brittle structural analysis and crustal stress reconstruction. *Geophysical Research Abstracts*, Vol. 13, EGU2011-4018, EGU General Assembly.
- Delvaux, D., and Sperner, B., 2003. Stress tensor inversion from fault kinematic indicators and focal mechanism data: the TENSOR program. In: Nieuwland, D. (Ed.), *New Insights into Structural Interpretation and Modelling*. Geol. Soc. Lond. Spec. Publ. 212, 75–100.
- Delvaux, D., Moeys, R., Stapel, G., Petit, C., Levi, K., Miroshnichenko, A., Ruzhich, V., and Sankov, V., 1997. Paleostress reconstructions and geodynamics of the Baikal region, central Asia, part 2. Cenozoic rifting. *Tectonophy.*, 282, 1–38.
- Dewey, J. F., and Şengör, A. M. C., 1979. Aegean and surrounding regions: complex multi-plate and continuum tectonics in a convergent zone. *Bull. Geol. Soc. Am.*, 90, 84-92.
- Dewey, J. F., Hempton, M. R., Kidd, W.S.F., Şaroğlu, F., and Şengör, A. M. C., 1986. Shortening of continental lithosphere: the neotectonics of eastern Anatolia – a young collision zone, in: Coward M.O., Ries A.C. (Eds.), *Collisional Tectonics. Geological Society Special Publication*, 19, Geological Society, London, pp. 3–36.
- Dilek, Y., Thy, P., Hacker, B., and Grundvig, S., 1999. Structure and petrology of Tauride ophiolites and mafic dike intrusions (Turkey): Implications for the Neotethyan ocean. *GSA Bulletin*, v. 111; no. 8; p.1192–1216.
- Dirik, K., 2001. Neotectonic evolution of the northwestward arched segment of the Central Anatolian Fault Zone, Central Anatolia, Turkey. *Geodinamica Acta*, 14, 147–158.
- Dirik, K., and Göncüoğlu, M. C., 1996. Neotectonic characteristics of Central Anatolia. *International Geology Review*, Vol. 38, p. 807 – 817.
- Disaster & Emergency Management authority Presidential of Earthquake Department.  
Retrieved from [www.deprem.gov.tr](http://www.deprem.gov.tr)
- Dziewonski, A. M., and Anderson, D. L., 1981. Preliminary reference Earth model. *Physics of the Earth and Planetary Interiors*, 25, 297-356.

- Dziewonski, A. M., Chou, T. A., and Woodhouse, J. H., 1981. Determination of earthquake source parameters from waveform data for studies of global and regional seismicity. *J. Geophys. Res.*, 86, 2825 – 28520, doi: 10.1029/JB086iB04p02825.
- Ekström, G., Nettles, M., and Dziewonski, A. M., 2012. The global CMT project 2004-2010: Centroid-moment tensors for 13,017 earthquakes. *Phys. Earth Planet. Inter.*, 200-201, 1-9. doi:10.1016/j.pepi.2012.04.002.
- Elmas, A., 1996. Geological Evolution of Northeastern Anatolia. *Int. Geol. Review*, Vol. 38, p. 881-900.
- Erdik, M., Birgören, G., Apaydın, N., and Onur, T., 1997. A probabilistic assessment of seismic hazard in Cyprus in terms of spectral amplitudes. The 29th General Assembly of the International Association of Seismology and Physics of the Earth's Interior (IASPEI 1997), paper no. 1801, Thessaloniki, Greece.
- Ergin, M., Aktar, M., and Eyidoğan, H., 2004. Present-day seismicity and seismotectonics of the Cilician Basin: eastern Mediterranean region of Turkey. *Bulletin of the Seism. Soc. of America*, V. 94, N. 3, pp. 930-939.
- European – Mediterranean RCMT Catalog. Retrieved from <http://rcmt2.bo.ingv.it>.
- Evernden, J. F., 1970. T-phase data on Kamchatka/Kurils earthquakes. *Bull. Seism. Soc. Am.*, 60, 1061-1076.
- Frohlich, C., and Davis, S., 1993. Teleseismic b-values: or, much about 1.0. *J. Geophys. Res.*, 98:631–644.
- Fukao, Y., 1995. Single-force representation of earthquakes due to landslides or the collapse of caverns. *Geophys. J. Int.*, 122, 243-248.
- Gardner, J. K., and L. Knopoff, 1974. Is the sequence of earthquakes in Southern California, with aftershocks removed, Poissonian?, *Bull. Seis. Soc. Am.*, 64, 1363–1367.
- Gasparini, P., and Vannucci, G., 2003. FPSPACK: A package of simple FORTRAN subroutines to manage earthquake focal mechanism data. *Computers & Geosciences*, 29, 893-901.
- Gaziantep Municipality, 2010. Provincial Environmental Status Report, Provincial Directorate of Environment and Forestry.

- General Directorate of Disaster Affairs Earthquake Research Dept. (GDDA-ERD).
- GEOFON Data Centre (1993): GEOFON Seismic Network. Deutsches Geo Forschungs Zentrum (GFZ).
- Gephart, J., and Forsyth, D., 1984. An improved method for determining the regional stress tensor using earthquake focal mechanism data: application to the San Fernando earthquake sequence. *J. of Geophys. Res.*, 89, 9305-9320.
- Gephart, J. W., 1990. Stress and direction of slip on fault planes. *Tectonophysics*, 8, 845–858.
- Global CMT Project (GCMT). Retrieved from [www.globalcmt.org](http://www.globalcmt.org).
- Godey, S., Mazet-Roux, G., Bossu, R., Merrer S., and Guilbert, J., 2009. Ten Years of Seismicity in the Euro-Mediterranean Region: Panorama of the EMSC Bulletin 1998-2007. *Cahiers du Cent. Eur. de Géodyn. et de Séism.*, 28, 1-14.
- Goldstein, P., Dodge, D., Firpo, M., and Minner, L., 2003. SAC2000: signal processing and analysis tools for seismologists and engineers, in *The IASPEI International Handbook of Earthquake and Engineering Seismology*, edited by W. H. K. Lee et al., London: Academic Press.
- Göncüoğlu, M. C., Toprak, V., Kuşcu, İ., Erler, A., and Olgun E., 1991. Geology of the western part of the Central Anatolian Massif, Part 1: Southern Section: Unpubl. Report No.2909, Turkish Petroleum Company Report (in Turkish).
- Görgün, E., Bohnhoff, M., Bulut, F., and Dresen, G., 2010. Seismotectonic setting of the Karadere-Düzce branch of the North Anatolian Fault Zone between the 1999 İzmit and Düzce ruptures from analysis of İzmit aftershock focal mechanisms. *Tectonophysics*, 482, 170-181.
- Görür, N., Oktay, F. Y., Seymen, I., and Şengör, A. M. C., 1984. Palaeotectonic evolution of the Tuzgölü basin complex, central Turkey: Sedimentary record of a Neo-Tethyan closure, in *The Geological Evolution of the Eastern Mediterranean*, edited by J. E. Dixon and A. H. F. Robertson, *Geol. Soc. Spec. Publ.*, 17, 467–482.
- Gutenberg, B., and Richter, C. F., 1944. Frequency of earthquakes in California, *Bull. Seism. Soc. Am.*, 34, 185–188.
- Gürer, D., van Hinsbergen, D. J. J., Matenco, L., Corfu, F., and Cascella, A., 2016. Kinematics of a former oceanic plate of the Neotethys revealed by deformation

- in the Ulukışla basin (Turkey). *Tectonics*, 35, doi:10.1002/2016TC004206.
- Gürsoy, H., Inan, S., Tatar, O., Ünlügenç, U., and Demirkol, C., 1998. Surface deformation, liquefaction-induced features and tectonic setting of 27 June 1998 Adana-Ceyhan earthquake, Third International Turkish Geology Symposium, METU-Ankara, Abstracts, p. 323.
- Hardebeck, J. L., and Hauksson, E., 2001. Stress orientations obtained from earthquake focal mechanism: What are appropriate uncertainty estimates?. *Bull. Seismol. Soc. Am.*, in press.
- Heidbach, O., Barth, A., Connolly, P., Fuchs, K., Muller, B., Tingay, M., Reinecker, J., Sperner, B., and Wenzel, F., 2011. Stress maps in a minute: The 2004 world stress map. *Journal: Transactions American Geophysical Union*, Vol 85, No 49, (3 June 2011).
- Heidbach, O., Barth, A., Müller, B., Reinecker, J., Stephansson, O., Tingay, M., and Zang, A., 2016. WSM World Stress Map. Scientific Technical Report 16-01.
- Heidbach, O., Tingay, M., Barth, A., Reinecker, J., Kurfel, D., and Müller, B., 2008. The World Stress Map database release. doi:10.1594/GFZ.WSM. last accessed May, 2018.
- Hempton M. R., 1984. Result of the detailed mapping near lake Hazar (eastern Taurus Mountains), in: Tekeli O., Göncüoğlu M.C. (Eds.), *Geology of the Taurus Belt*. Min. Res. Expl. Inst. Turkey Publ., pp. 223–238.
- Hempton, M., 1987. Constraints on Arabian plate motion and extensional history of the Red Sea. *Tectonics*, Vol. 6, No. 6, pages 687-705.
- Huang, J., and Turcotte, R., 1988. Fractal distributions of stress and strength and variations of b-value. *Earth Planet Lett.*, 91:223–230.
- Incorporated Research Institutions for Seismology (IRIS), 2014. *Seismic Analysis Code (SAC) Users Manual*, version 101.6a.
- Ishimoto, M., and Iida, K., 1939. Observations sur les séismes enregistrés par le micro-séismographe construit dernièrement (1), *Bull. Earthquake Res. Inst. Univ. Tokyo* 17, 443–478.
- Jackson, J., and McKenzie, D., 1984. Active tectonics of the Alpine – Himalayan Belt between western Turkey and Pakistan. *Geophysical Journal of Royal Astronomical Society*, 77, 185–264.

- Jost, M. L., and Herrmann, R. B., 1989. A student's guide to and review of moment tensors. *Seismological Research Letters*, Vol. 60, No.2.
- Julian, B.R., Miller, A. D., and Foulger, G. R., 1998. Non-Double-Couple Earthquakes 1. Theory, *Reviews of Geophysics*, 36, 525-549.
- Kalyoncuoğlu, U. Y., 2006. Evaluation of seismicity and seismic hazard parameters in Turkey and surrounding area using a new approach to the Gutenberg-Richter relation. *J. Seismol.*, 11:131-148.
- Kandilli Observatory and Earthquake Research Institute Regional Earthquake-Tsunami Monitoring Center (KOERI-RETMC), Boğaziçi University, "1990-2017 Earthquake Catalog". Retrieved from <http://www.koeri.boun.edu.tr/sismo/zeqdb/>
- Kandilli Observatory and Earthquake Research Institute, National Earthquake Monitoring Center (KOERI-NEMC).
- Karasözen, E., 2010. Earthquake focal mechanism and stress tensor analysis along the central segment of the North Anatolian Fault. MSc Thesis, METU.
- Karasözen, E., Özacar, A. A, Biryol, C. B., and Beck, S. L., 2014. Seismicity, focal mechanisms and active stress field around the central segment of the North Anatolian Fault in Turkey. *Geophys. J. Int.*, 196, 405-421.
- Kasapoğlu, E. K., 1987. Seismotectonic characteristics of Eastern Mediterranean: A finite elements analysis. *Hacettepe Univ. Earth Sci.*, 14, 309–317.
- Kaymakçı, N., Özmutlu, Ş., van Dijk, M., and Özçelik, Y., 2010. Surface and Subsurface Characteristics of the Çankırı Basin (Central Anatolia, Turkey): Integration of Remote Sensing, Seismic Interpretation and Gravity. *Turkish J. Earth Sci.*, V. 19, pp. 79–100.
- Kebede, F., Kulhanek, O., 1994. Spatial and temporal variations of b-values along the East African Rift System and the Southern Red Sea. *Phys. Earth Planet Int.*, 83:249–264.
- Kikuchi, M., and Kanamori, H., 1991. Inversion of complex body waves-III. *Bulletin of the Seismological Society of America*, V. 81, N. 6, pp. 2335-2350.
- Koç, A., and Kaymakçı, N., 2013. Kinematics of Sürgü Fault Zone (Malatya, Turkey): A remote sensing study. *Jour. of Geodynamics*, 65, 292– 307.

- Koçyiğit, A., 1991. An example of an accretionary forearc basin from northern Central Anatolia and its implications for the history of subduction of Neo-Tethys in Turkey. *Geologic. Soc. of America Bulletin*, v. 103, p. 22-36.
- Koçyiğit, A., and Beyhan, A., 1998. A new intracontinental transcurrent structure: the Central Fault Zone, Turkey. *Tectonophysics*, 284, 317-336.
- Koçyiğit, A., and Erol, O., 2001. A tectonic escape structure: Erciyes pull-apart basin, Kayseri, Central Anatolia, Turkey. *Geodinamica Acta*, 14, 133-145.
- Koçyiğit, A., Yılmaz, R., Aktaş, K., Erkmen, C., Nurlu, M., Baykal, M., and Kılıç, T., 1998. Seismotectonic characteristics of the 27 June 1998 Yakapınar–Ceyhan (Adana) earthquake, Turkey, Third International Turkish Geology Symposium, METU-Ankara, Abstracts, p. 321.
- Krizova, D., Zahradnik, J., and Kiratzi, A., 2013. Resolvability of isotropic component in regional seismic moment tensor inversion, *Bulletin of the Seismological Society of America*, Vol. 103, No. 4, pp. 2460-2473.
- Lapenna, V., Macchiato, M., and Telesca, L., 1998. Fluctuations and self similarity in earthquake dynamics; observational evidences in southern Italy. *Phys. Earth Planet Int.*, 106:115–127.
- Lefebvre, C., Barnhoorn, A., van Hinsbergen, D. J. J., Kaymakçı, N., and Vissers, R. L. M., 2011. Late Cretaceous extensional denudation along a marble detachment fault zone in the Kırşehir massif near Kaman, central Turkey. *J. of Structural Geol.*, 33, 1220-1236.
- Lefebvre, C., Meijers, M. J. M., Kaymakçı, N., Peynircioğlu, A., Langereis, C. G., and van Hinsbergen, D. J. J., 2013. Reconstructing the geometry of central Anatolia during the Late Cretaceous: Large-scale Cenozoic rotations and deformation between the Pontides and Taurides. *Earth and Planetary Science Letters*, v. 366, p. 83–98, <https://doi.org/10.1016/j.epsl.2013.01.003>.
- LGC News, 2018. Quarries continue to damage environment. Online news for North Cyprus, Retrieved from <https://www.lgcnews.com/quarries-continue-to-damage-environment/>

- Lund, B., and Townend, J., 2007. Calculating horizontal stress orientations with full or partial knowledge of the tectonic stress tensor. *Geophys. J. Int.*, 1328–1335.
- Lyb ris, N., Y r r, T., Chorowicz, J., Kasapođlu, E., and G ndođdu, N., 1992. The East Anatolian fault: an oblique collisional belt. *Tectonophys.*, 204, 1–15.
- Main, I. G., Meredith, P. G., and Sammonds, P. R., 1992. Temporal variations in seismic event rate and b-values from stress corrosion constitutive laws. *Tectonophysics* 211:233–246.
- Manakou, M. V., and Tsapanos, T. M., 2000. Seismicity and seismic hazard parameters evaluation in the island of Crete and surrounding area inferred from mixed data files. *Tectonophysics*, 321:157–178.
- Michael, A., 1984. Determination of stress from slip data: faults and folds. *Journal of Geophysical Research*, 89, 11517-11526.
- Michael, A. J., 1987. Use of focal mechanisms to determine stress: A control study, *J. Geophys. Res.*, 92, 357 – 368.
- Michele, M., Custodio, S., and Emolo, A., 2014. Moment Tensor Resolution: Case Study of the Irpinia Seismic Network, Southern Italy. *Bulletin of the Seismological Society of America*, Vol. 104, No. 3, pp. 1348–1357.
- Nanjo, K., Nagahama, H., and Satomura, M., 1998. Rates of aftershock decay and the fractal structure of active fault systems. *Tectonophysics*, 287:173–186.
- National Earthquake Information Center of the United States Geological Survey (NEIC – USGS).
- Necdet, M., and G ker, Z., 1996. A view to the crushstone industry of the Turkish Republic of Northern Cyprus, I. Ulusal K rmataş Sempozyumu’96, Istanbul, ISBN 975-395-196-5.
- Okal, E. A., 2011. Earthquake, Focal mechanism. Department of Earth & Planetary Sciences, Northwestern University, USA.
- Okay, A.  ., 1984. The geology of the Agvanis metamorphic rocks and neighbouring formations. *Mineral Research Exploration Institute of Turkey (MTA) Bulletin*, 99/100, 16-36.
- Okay, A.  ., and Moni , P., 1997. Early Mesozoic subduction in the eastern Mediterranean: Evidence from Triassic eclogite in northwest Turkey.

- Geology*, 25, 595-598. doi:10.1130/0091-7613(1997)025<0595:EMSITE>2.3.CO;2.
- Okay, A. İ., and Tüysüz, O., 1999. Tethyan sutures of northern Turkey. In: Durand, B., Jolivet, L., Horvath, F. and Seranne, M. (eds) *The Mediterranean Basins: tertiary Extension within the Alpine Orogen*. *Geological Society*, London, Special Publications, 156, 475-515.
- Omori, F., 1894. On the after-shocks of earthquakes. *J. Coll. Sci. Tokyo Imp. Univ.* 7: 111-200.
- Örgülü, G., Aktar, M., Türkelli, N., Sandvol, E., and Barazangi, M., 2003. Contribution to the seismotectonics of Eastern Turkey from moderate and small size events. *Geophysical Research Letters*, 30, 8040.
- Özgül, N., 1984. Stratigraphy and tectonic evolution of the Central Taurides, in *Geology of the Taurus Belt*. Proceedings of the International Tauride Symposium, edited by O. Tekeli and M. C. Göncüoğlu, pp. 77-90, Cambridge, U. K.
- Özsayın, E., Çiner, A., Rojay, B., Dirik, K., Melnick, D., Fernandez-Blanco, D., Bertotti, G., Schildgen, T. F., Garcin, Y., Strecker, M. R., and Sudo, M., 2013. Plio-Quaternary extensional tectonics of the Central Anatolian Plateau: a case study from the Tuz Gölü Basin, Turkey. *Turkish J. of Earth Sciences*, 22: doi: 10.3906/yer-1210-5.
- Öztemir, F., Necioğlu, A., and Bağcı, G., 2000. Focal mechanism solutions and seismicity for Antakya region and its surrounding. *Jeofizik*, 87-102.
- Parlak, O., Kop, A., Ünlügenç, U. C., and Demirkol, C., 1998. Geochronology and geochemistry of basaltic rocks in the Karasu Graben around Kırıkhan (Hatay), S. Turkey. *Tr. Journal of Earth Sciences*, 7, 53-612.
- Pasquaré, G., Vezzoli, S. P. L., and Zanchi, A., 1988. Continental arc volcanism and tectonic setting in Central Anatolia, Turkey. *Tectonophys.*, 146, 217-230.
- Pelling, M., 2003. *Natural Disasters and Development in a Globalizing World*. Routledge, Taylor & Francis Group, London and New York.
- Perinçek, D., and Çemen, İ., 1990. The structural relationship between the East Anatolian and Dead Sea fault zones in southeastern Turkey. *Tectonophys.*, 172, 331-340.

- Pondrelli, S., and Salimbeni, S., 2015. Regional Moment Tensor Review: An Example from the European Mediterranean Region. In *Encyclopedia of Earthquake Engineering*, pp. 1-15.
- Pondrelli, S., Ekström, G., Morelli, A., and Primerano, S., 1999. Study of source geometry for tsunamigenic events of the Euro-Mediterranean area, in *International Conference on Tsunamis*, pp. 297–307.
- Pondrelli, S., Morelli, A., and Ekström, G., 2004. European-Mediterranean Regional Centroid Moment Tensor catalog: solutions for years 2001 and 2002. *Phys. Earth Planet. Int.*, 145, 1-4, 127-147.
- Pondrelli, S., Morelli, A., Ekström, G., Mazza, S., Boschi, E., and Dziewonski, A. M., 2002. European-Mediterranean regional centroid-moment tensors: 1997-2000. *Physics of the Earth and Planetary Interiors*, 130, 71-101.
- Pondrelli, S., Salimbeni, S., Ekström, G., Morelli, A., Gasperini, P., and Vannucci, G., 2006. The Italian CMT dataset from 1977 to the present. *Phys. Earth Planet. Int.*, doi:10.1016/j.pepi.2006.07.008, 159/3-4, pp. 286-303.
- Pondrelli, S., Salimbeni, S., Morelli, A., Ekström, G., and Boschi, E., 2007. European-Mediterranean Regional Centroid Moment Tensor catalog: Solutions for years 2003 and 2004. *Physics of the Earth and Planetary Interiors*, 164, 90-112.
- Pondrelli, S., Salimbeni, S., Morelli, A., Ekström, G., Postpischl, L., Vannucci, G., and Boschi, E., 2011. European-Mediterranean Regional Centroid Moment Tensor Catalog: solutions for 2005-2008. *Phys. Earth Planet. Int.*, 185, 74-81.
- Pondrelli, S., Salimbeni, S., Perfetti, P., and Danecek, P., 2012. Quick regional centroid moment tensor solutions for the Emilia 2012 (northern Italy) seismic sequence. *Annals of Geophysics*, 55, 4, doi: 10.4401/ag-6146.
- Portner, D. E., Delph, J. R., Biryol, C. B., Beck, S. L., Zandt, G., Özacar, A. A., Sandvol, E., and Türkelli, N., 2018. Subduction termination through progressive slab deformation across Eastern Mediterranean subduction zones from updated P-wave tomography beneath Anatolia. *Geosphere*, v. 14, no. 3, p. 1–19, <https://doi.org/10.1130/GES01617.1>.
- Pourteau, A., Candan, O., and Oberhänsli, R., 2010. High-pressure metasediments in central Turkey: Constraints on the Neotethyan closure history. *Tectonics*, Vol. 29, doi:10.1029/2009TC002650.

- Reasenber, P., 1985. Second-order moment of central California seismicity, 1969-82. *J. Geophys. Res.*, 90, 5479–5495.
- Reches, Z., 1987. Determination of the tectonic stress tensor from slip along faults that obey the coulomb yield condition. *Tectonics*, Vol. 6, No. 6, pp. 849-861.
- Reilinger, R., McClusky, S., Vernant, P., Lawrence, S., Ergintav, S., Cakmak, R., Ozener, H., Kadirov, F., Guliev, I., Stepanyan, R., Nadariya, M., Hahubia, G., Mahmoud, S., Sakr, K., ArRajehi, A., Paradissis, D., Al-Aydrus, A., Prilepin, M., Guseva, T., Evren, E., Dmitrotsa, A., Filikov, S. V., Gomez, F., Al-Ghazzi, R., and Karam, G., 2006. GPS constraints on continental deformation in the Africa-Arabia-Eurasia continental collision zone and implications for the dynamics of plate interactions. *Jour. of Geophy. Res.*, v. 111, B05411, <https://doi.org/10.1029 /2005JB004051>.
- Rivera, L., and A. Cisternas, 1990. Stress tensor and fault plane solutions for a population of earthquakes. *Bull. Seismol. Soc. Am.*, 80, 600 – 614, 1990.
- Robertson, A. H. F., Ustaömer, T., Parlak, O., Ünlügenç, U. C., Taşlı, K., and İnan, N., 2006. The Berit transect of the Tauride thrust belt, S Turkey: Late Cretaceous–Early Cenozoic accretionary/collisional processes related to closure of the Southern Neotethys. *Jour. of Asian Earth Sci.*, 27, 108–145.
- Rojay, B., Heimann, A., and Toprak, V., 2001. Neotectonic and volcanic characteristics of the Karasu fault zone (Anatolia,Turkey):The transition zone between the Dead Sea transform and the East Anatolian fault zone. *Geodinamica Acta*, 14, 1-17.
- Salamon, A., Hofstetter, A., Garfunkel, Z., and Ron, H., 2003. Seismotectonics of the Sinai subplate–the eastern Mediterranean region. *Geophys. J. Int.*, 155, 149-173.
- Sanchez, J. J., McNutt, S. R., Power, J. A., and Wyss, M., 2004. Spatial variations in the frequency – magnitude distribution of earthquakes at Mount Pinatubo Volcano. *Bull. of the Seism. Soc. of America*, V. 94, No. 2, pp. 430-438.
- Schwarz, J., Lang, D. H., Raschke, M., Schmidt, G. H., Wuttke, F., Baumbach, M., and Zschau, J., 2000. Lessons from recent earthquakes – field missions of German task force. 12WCEE2000.
- Shah, S. T., 2015. Stress tensor inversion from focal mechanism solutions and

- earthquake probability analysis of Western Anatolia, Turkey. M.Sc. Thesis, Middle East Technical University.
- Shi, Y., and Bolt, B., 1982. The standard error of the magnitude-frequency b-value. *Bull. of the Seism. Soc. of America*, V. 72, N. 5, pp. 1677-1687.
- Sokos, E. N., and Zahradnik, J., 2008. ISOLA a Fortran code and a Matlab GUI to perform multiple-point source inversion of seismic data. *Computers & Geosciences* 34, 967-977. ISSN 0098-3004, doi: 10.1016/j.cageo.2007.07.005.
- Sokos, E., and Zahradnik, J., 2009. A Matlab GUI for use with ISOLA Fortran codes, User's guide. Ver 4.0.
- Sokos, E., and Zahradník, J., 2013. Evaluating Centroid-Moment-Tensor Uncertainty in the New Version of ISOLA Software. *Seis. Res. Letters*, V.84, P.656-665.
- Sokos, E., Zahradnik, J., Kiratzi, A., Jansky, J., Gallovic, F., Novotny, O., Kostelecky, J., Serpetsidaki, A., and Tselentis, G. A., 2012. The January 2010 Efpalio earthquake sequence in the western Corinth Gulf (Greece). *Tectonophysics*, 530-531, 299-309.
- Stampfli, G. M., 2000. Tethyan oceans. In: Bozkurt, E., Winchester, J.A., and Piper, J.D.A. (eds), *Tectonics and Magmatism in Turkey and the Surrounding Area*. *Geol. Soc.*, London, Spec. Publ., n. 173, p. 1-23.
- Stein, S., and Wysession, M., 2003. *An introduction to seismology, earthquakes, and earth structure*. Blackwell Publishing, UK.
- Şahin, G., 2016. 1938 Kırşehir (Akpınar) Depremi ve Bölgeye Etkileri. *Journal of History School (JOHS)*. Year 9, Iss. XXVI, pp.289-321.
- Şaroğlu, F., Emre, Ö., and Kuşçu. İ., 1992. The East Anatolian fault zone of Turkey, *Annal. Tecton.*, 6, 99–125.
- Şaroğlu, F., Emre, Ö., Kuşçu, İ., 1992. Turkish Active Faults Map. *Directorate of Mineral Research and Exploration*, Ankara, Turkey.
- Şen, A. T., 2014. Inversion of seismic source parameters for weak mining-induced and natural earthquakes. Ph.D. Dissertation, Potsdam University.
- Şengör, A. M. C., 1979a. Mid-Mesozoic closure of Permo-Triassic Tethys and its implications. *Nature*, v. 279, p. 590-593.
- Şengör, A. M. C., 1987. Tectonics of the Tethysides: orogenic collage development in

- a collisional setting. *Ann. Rev. Earth Planet. Sci.*, v. 15, p. 213-244.
- Şengör, A. M. C., and Yılmaz, Y., 1981, Tethyan evolution of Turkey, a plate tectonic approach. *Tectonophysics*, v. 75, p. 181–241, [https://doi.org/10.1016/0040-1951, 90275-4](https://doi.org/10.1016/0040-1951(81)90275-4).
- Şengör, A. M. C., Görür, N., and Şaroğlu, F., 1985. Strike-slip faulting and related basin formation in zones of tectonic escape: Turkey as a case study, in Biddle, K.T., and Christie-Blick, N., eds., *Strike-Slip Deformation, Basin Formation, and Sedimentation. Soc. of Economic Paleontologists and Mineralogists Spec. Publ.*, 37, p. 227–264, doi: 10.2110/pec.85.37.0227.
- Talbi, A., Nanjo, K., Satake, K., Zhuang, J., and Hamdache, M., 2013. Comparison of seismicity declustering methods using a probabilistic measure of clustering. *J. of Seismol.*, 17, 1041–1061.
- Taymaz, T., Eyidoğan, H., and Jackson, J., 1991b. Source parameters of large earthquakes in the East Anatolian Fault Zone (Turkey). *Geophysical Journal International*, 106, 537–550.
- Taymaz, T., Jackson, J. A., and McKenzie, D., 1991. Active tectonics of the North and Central Aegean Sea, *Geophys. J. Int.*, 106, 433–490.
- Tekeli, O., 1981. Subduction complex of pre-Jurassic age, northern Anatolia, Turkey, *Geology*, 9, 68–72. doi:10.1130/0091-7613(1981)9<68: SCOPAN>2.0.CO;2.
- Temiz, H., Guezou, J. C., Poisson, A. M., and Tutkun, Z., 1993. Tectonostratigraphy and kinematics of the eastern end of the Sivas Basin (central eastern Turkey): implications for the so-called ‘Anatolian block’. *Geol. J.*, V. 28, 239-250.
- The Regional Moment Tensor Catalog of the Swiss Seismological Service (SRMT).
- Toprak, V., and Göncüoğlu, M. C., 1993b. Tectonic control on the development of Neogene–Quaternary Central Anatolian Volcanic province, Turkey. *Geol. J.*, 28, 357–369.
- Triantafyllis, N., Sokos, E., Ilias, A., and Zahradnik, J., 2016. Scisola: automatic moment solution for SeisComP3, *Seism. Res. Let.*, 87, 157-163.
- Tselentis, G. A., Sokos, E., Martakis, N., and Serpetsidaki, A., 2006. Seismicity and seismotectonic in Epirus, Western Greece: results from a microearthquake survey. *Bull. of the Seism. Soc. of America*, Vol. 96, No.5, pp.1706-1717.
- Turcotte, D. L., 1986. Fractals and Fragmentation. *J. Geophys. Res-solid*, 91:1921.

- Tülüveli, G., 2015. Historical seismicity in the Middle East: new insights from Ottoman primary sources (sixteenth to mid-eighteenth centuries). *J. Seismol.*, 1003-1008.
- Tüysüz, O., 2005. Neotectonics and Seismicity of Turkey. Eurasia Institute of Earth Sciences, ITU.
- Udias, A., Madariaga, R., and Bufom, E., 2014. Source mechanisms of earthquakes: theory and practice. Cambridge University Press, New York.
- Utsu, T., 1965. A method for determining the value of b in the formula  $\log n = a - bM$  showing the magnitude-frequency relation for earthquakes (with English summary). *Geophys. Bull.*, Hokkaido Univ. 13, 99-103.
- Utsu, T., 1969. Aftershock and earthquake statistics (I): Some parameters which characterize an aftershock sequence and their interrelations. *J. Fac. Sci. Hokkaido Univ. Ser. VII*, 129-195.
- van Hinsbergen, D. J. J., Maffione, M., Plunder, A., Kaymakçı, N., Ganerod, M., Hendriks, B. W. H., Corfu, F., Gürer, D., de Gelder, G. I. N. O., Peters, K., McPhee, P. J., Brouwer, F. M., Advokaat, E. L., and Vissers, R. L. M., 2016. Tectonic evolution and paleogeography of the Kırşehir Block and the Central Anatolian Ophiolites, Turkey. *Tectonics*, 35, doi:10.1002/2015TC004018.
- Wang, J. H., 1994. On the correlation of observed Gutenberg–Richter’s b-value and Omori’s p-value for aftershocks. *Bull. Seismol. Soc. Am.*, 84:2008–2011.
- Wdowinski, S., Ben-Avraham, Z., Arvidsson, R., and Ekström, G., 2006. Seismotectonics of the Cyprian Arc. *Geophys. J. Int.*, 176–181.
- Wessel, P., Smith, W. H. F., Scharroo, R., Luis, J. F., and Wobbe, F., 2013. Generic Mapping Tools: Improved version released, *EOS Trans. AGU*, 94, 409-410.
- Westaway, R., 1994. Present-day kinematics of the Middle East and eastern Mediterranean. *J. of Geophys. Res.*, Vol. 99, No: B6, Pages 12071-12090.
- Westaway, R., 1999. Comment on ‘a new intracontinental transcurrent structure: the Central Anatolian Fault Zone, Turkey’ by A. Koçyiğit and A. Beyhan, *Tectonophysics*, 314, 469–479.

- Westaway, R., 2004. Kinematic consistency between the Dead Sea Fault Zone and the Neogene and Quaternary left-lateral faulting in SE Turkey. *Tectonophysics*, 391, 203 – 237.
- Westaway, R., and Arger, J., 1996. The Gölbaşı basin, southeastern Turkey: A complex discontinuity in a major strike-slip fault zone. *J. Geol. Soc.*, 153, 729–743.
- Westaway, R., and Arger, J., 1998. Kinematics of the Malatya–Ovacık Fault Zone, Third International Turkish Geology Symposium, METU-Ankara, Abstracts, 1998, p. 197.
- Westaway, R. and Arger, J., 2001. Kinematics of the Malatya – Ovacık Fault Zone. *Geodinamica Acta*, 103 – 131.
- Westaway, R., Demir, T., and Seyrek, A., 2008. Geometry of the Turkey-Arabia and Africa-Arabia plate boundaries in the latest Miocene to Mid-Pliocene: the role of the Malatya-Ovacık Fault Zone in eastern Turkey. *eEarth*, 3, 27–35.
- Wiemer, S., 2001. A software package to analyze seismicity: ZMAP. *Seismol. Res. Lett.*, 72, 374–383.
- Wiemer, S., and Wyss, M., 1997. Mapping the frequency-magnitude distribution in asperities: an improved technique to calculate recurrence times?. *Journal of Geophysical Research*, Vol. 102, No. B7, pp.15115-15128.
- Wiemer, S., and Wyss, M., 2000. Minimum magnitude of completeness in earthquake catalogs: Examples from Alaska, the Western United States, and Japan. *Bulletin of the Seismological Society of America*, 90, pp.859-869.
- Wiemer, S., Gerstenberg, M., and Hauksson, E., 2002. Properties of the aftershock sequence of the 1999 Mw 7.1 Hector Mine earthquake: implications for aftershock hazard. *Bul. of the Seism. Soc. of America*, V.92, N.4, 1227-1240.
- Wiemer, S., McNutt, S. R., and Wyss, M., 1998. Temporal and threedimensional spatial analysis of the frequency–magnitude distributions near Long Valley Caldera California. *Geophys. J. Int.*, 134:409–421.
- Woessner, J., Hardebeck, J. L., and Hauksson, E., 2010. What is an instrumental seismicity catalog, Community Online Resource for Statistical Seismicity Analysis, doi:10.5078/corssa-38784307. Available at <http://www.corssa.org>.
- Wyss, M., Schorlemmer, D., and Wiemer, S., 2000. Mapping asperities by minima of

- local recurrence time: San Jacinto–Elsinore Fault Zones. *J. Geophys. Res.*, 105:7829–7844.
- Yalınız, M. K., Floyd, P. A., and Göncüoğlu, M. C., 1996. Supra-subduction zone ophiolites of Central Anatolia: geochemical evidence from the Sarıkaman Ophiolite, Aksaray, Turkey. *Mineralogical Magazine*, Vol. 60, pp. 697-710.
- Yılmaz, Y., 1993. New evidence and model on the evolution of the southeast Anatolian orogen. *Geol. Soc. of Am. Bull.*, v. 105, p. 251-271.
- Yılmaz, Y., and Yıldırım, M., 1996. Geology and evolution of the nappe region (the metamorphic massifs) of the southeast Anatolian orogenic belt. *Turkish Journal of Earth Science*, v. 5, p. 21-38.
- Yılmaz, A., and Yılmaz, H., 2006. Characteristic features and structural evolution of a post collisional basin: The Sivas Basin, Central Anatolia, Turkey, *J. Asian Earth Sci.*, 27, 164–176.
- Yılmaztürk, A., and Burton, P. W., 1999. An evaluation of seismic hazard parameters in southern Turkey. *J. Seismol.*, 3. 61-81.
- Yurtmen, S., Rowbotham, G., İşler, F., and Floyd, P. A., 2000. Petrogenesis of basalts from southern Turkey: the Plio-Quaternary volcanism to the north of Iskenderun, in: Bozkurt E., Winchester J.A., Piper J.D.A. (Eds.), *Tectonics and magmatism in Turkey and the surrounding area. Geological Society Special Publication*, v. 173, pp. 489–512.
- Yürür, M. T., and Chorowicz, J., 1998. Recent volcanism, tectonics and plate kinematics near the junction of the African, Arabian, and Anatolian plates. *J. Volcan. Geother. Res.*, 85, 1–15.
- Zahradnik, J., and Sokos, E., 2016. ISOLA Costa Rica 2016 course (user’s guide).
- Zahradnik, J., Jansky, J., and Plicka, V., 2008. Detailed waveform inversion for moment tensors of  $M \sim 4$  events: Examples from the Corinth Gulf, Greece. *Bulletin of the Seismological Society of America*, V. 98, N. 6, 2756-2771.
- Zhang, J., and Lay, T., 1990. Effects of centroid location on determination of earthquake mechanisms using long-period surface waves. *Bulletin of the Seismological Society of America*. Vol. 80, No. 5, pp. 1205-1231.
- Zhao, S., and Müller, R. D., 2001. The tectonic stress field in Eastern Australia. PESA Eastern Australasian Basins Symposium Melbourne, Vic, 25-28 Nov. 2001.

- Zoback, M. L., 1992. Stress-field constraints on intraplate seismicity in eastern North America. *J. of Geophys. Res. Solid Earth*, 97, B8, 11761-11782.
- Zohar, M., and Salamon, A., 2016. Supplementary material - Reappraised list of historical earthquakes that affected Israel and its close surroundings. *Journal of Seismology*, Vol. 20, Issue 3, p. 971-985.



## APPENDIX A

**Table A. 1** The list of earthquakes with focal mechanism solutions occurred in the study area. (1 = Jackson, and McKenzie, 1984; 2 = Salamon et al., 2003; 3 = Canitez and Üçer, 1967; 4 = Taymaz et al., 1991; 5 = Yılmaztürk and Burton, 1999; 6 = Dziewonski et al., 1981; Ekström et al., 2012 (CMT, GCMT); 7 = Ergin et al., 2004; 8 = Pondrelli et al., 1999 (EMSC); 9 = Pondrelli et al., 2002; 2004; 2006; 2007; 2011; 2015 (RCMT, MedNet); 10 = Örgülü et al., 2003; 11 = Regional Moment Tensor of the Swiss Seismological Service (SRMT); 12 = Karasözen, 2010; 13 = General Directorate of Disaster Affairs Earthquake Research Department (GDDA-ERD), 14 = National Earthquake Information Center of the United States Geological Survey (NEIC-USGS); 15 = Kandilli Observatory and Earthquake Research Institute National Earthquake Monitoring Center (KOERI-NEMC); 16 = GEOFON Data Centre, 1993 (GFZ).

No	Date	Time	Lon. E (°)	Lat. N (°)	Mag.	Dep. (km)	Strike (°)	Dip (°)	Rake (°)	Ref.
1	19.4.1938	10:59	33.70	39.50	6.8	10.0	30	60	4	1
2	20.1.1941	03:37	33.60	35.20	6.0	100.0	248	46	144	2
3	8.4.1951	21:38	36.10	36.60	6.0	15.0	30	68	15	3
4	14.6.1964	12:15	38.48	38.08	5.5	10.5	227	29	-28	4
5	7.4.1967	17:07	36.13	37.37	4.8	38.0	266	70	-10	2
6	7.4.1967	18:33	36.18	37.37	4.9	32.0	245	80	20	2
7	4.7.1967	18:33	36.20	37.40	5.1	39.0	156	30	-159	1
8	6.11.1968	13:41	32.78	35.16	4.8	65.0	80	45	120	2
9	5.10.1970	14:53	38.99	35.13	4.8	34.0	40	35	90	2
10	29.6.1971	09:08	36.86	37.13	5.0	35.2	70	40	130	2
11	11.7.1971	20:12	36.83	37.16	5.0	18.7	82	88	8	5
12	17.8.1971	04:29	36.79	37.11	4.9	35.3	50	78	99	2
13	1.1.1975	00:30	36.48	36.78	5.2	35.4	26	77	-74	2
14	9.2.1978	21:10	36.80	37.08	4.5	42.3	80	30	60	2
15	28.12.1979	03:09	35.85	37.49	5.4	47.1	141	90	180	6
16	2.1.1980	12:52	36.33	36.57	4.7	31.9	258	77	74	2
17	30.6.1981	07:59	35.89	36.17	4.7	63.3	76	82	40	2
18	20.5.1982	03:28	33.69	35.09	4.6	71.5	110	45	70	2
19	24.11.1983	00:14	36.13	37.05	4.7	37.4	226	70	-10	2
20	18.12.1984	13:59	35.30	35.26	4.7	39.1	215	58	42	2
21	5.5.1986	03:35	37.78	38.00	6.0	4.4	260	54	9	6
22	6.6.1986	10:39	37.91	38.01	5.8	10.6	160	90	180	6
23	16.6.1987	06:17	35.25	35.55	4.7	33.0	163	77	-105	2
24	24.6.1989	03:09	35.94	36.75	5.1	46.4	203	28	-93	6

**Table A. 1 (cont'd)**

No	Date	Time	Lon. E (°)	Lat. N (°)	Mag.	Dep. (km)	Strike (°)	Dip (°)	Rake (°)	Ref.
25	10.4.1991	01:08	36.12	37.30	5.3	33.0	160	27	-136	6
26	10.2.1994	06:15	35.89	36.93	4.9	32.0	285	85	-140	7
27	21.1.1995	03:48	36.25	37.37	4.5	15.0	350	40	-100	7
28	23.2.1995	21:03	32.27	35.06	5.9	20.2	239	21	140	6
29	23.2.1995	21:40	32.30	35.01	5.4	30.4	71	34	-9	8
30	13.4.1995	20:23	36.20	37.42	4.9	14.0	170	40	-90	7
31	29.5.1995	04:58	32.25	35.05	5.3	28.9	224	20	132	6
32	22.1.1997	17:57	35.96	36.21	5.7	45.4	243	39	-15	6
33	22.1.1997	18:22	36.03	36.26	4.3	13.0	50	90	40	7
34	22.1.1997	18:24	36.06	36.13	5.2	4.0	219	41	-39	7
35	23.1.1997	14:53	36.05	36.26	4.2	4.8	45	85	-40	7
36	3.1.1998	21:15	35.77	37.20	4.1	15.8	125	85	150	7
37	28.3.1998	00:30	38.75	38.20	4.5	6.1	235	46	-15	9
38	9.5.1998	15:38	38.95	38.25	5.1	26.5	251	83	-7	6
39	27.6.1998	13:55	35.33	36.53	6.2	32.0	50	85	10	7
40	28.6.1998	03:59	35.49	36.92	4.9	10.0	223	71	-12	9
41	4.7.1998	02:15	35.44	36.90	5.1	37.6	60	90	20	7
42	4.12.1998	04:59	35.58	37.01	4.0	22.8	65	80	20	7
43	14.12.1998	13:06	35.79	38.92	4.7	15.0	339	64	166	9
44	15.1.1999	02:04	35.85	37.04	4.2	23.5	35	75	-10	7
45	6.4.1999	00:08	38.23	39.37	5.4	30.7	326	49	175	6
46	10.6.1999	23:25	35.96	37.38	4.5	19.5	50	85	10	7
47	11.6.1999	05:25	36.80	39.53	4.9	6.2	67	45	-39	9
48	24.8.1999	17:33	32.68	39.41	4.9	10.0	27	53	-2	9
49	2.1.2000	20:28	38.96	38.30	3.7	13.1	345	72	-147	10
50	2.4.2000	11:41	37.08	37.61	4.2	12.8	44	80	38	10
51	2.4.2000	17:26	37.32	37.54	4.0	10.0	224	89	-15	10
52	7.5.2000	09:08	38.83	38.26	4.2	22.7	53	82	16	10
53	7.5.2000	23:10	38.91	38.27	4.4	22.3	320	87	167	10
54	12.5.2000	03:01	36.06	36.99	4.7	32.7	10	45	-106	9
55	27.5.2000	07:49	35.28	36.23	4.2	6.9	65	45	-10	7
56	17.1.2001	12:09	36.21	37.07	4.4	9.6	60	65	-20	7
57	25.6.2001	13:28	36.27	37.22	4.6	7.9	320	50	-110	7
58	25.9.2001	11:53	32.33	35.97	4.5	40.3	326	75	-173	9
59	18.10.2001	15:50	35.22	36.86	4.5	10.0	161	34	-175	9

**Table A. 1 (cont'd)**

No	Date	Time	Lon. E (°)	Lat. N (°)	Mag.	Dep. (km)	Strike (°)	Dip (°)	Rake (°)	Ref.
60	31.10.2001	12:33	36.25	37.26	4.9	6.7	35	35	-90	7
61	23.5.2002	01:08	36.35	37.41	4.4	10.3	231	58	-37	9
62	19.11.2002	01:25	38.39	38.02	4.7	10.0	338	74	-177	9
63	14.12.2002	01:02	36.19	37.47	4.8	29.2	30	41	-79	9
64	26.2.2003	03:08	36.27	35.86	4.4	10.0	295	84	-2	9
65	13.7.2003	01:48	38.95	38.28	5.5	12.9	72	89	1	6
66	24.9.2003	08:13	38.23	39.55	4.7	0.9	275	74	7	9
67	26.2.2004	04:13	38.25	37.91	4.8	5.0	334	44	155	9
68	18.8.2004	05:57	34.40	36.80	4.3	13.6	26	15	-95	9
69	4.7.2005	21:33	36.08	39.16	4.5	3.4	58	52	-61	11
70	30.7.2005	21:45	33.11	39.39	5.2	15.7	214	87	-2	6
71	31.7.2005	23:41	33.10	39.44	4.8	11.5	205	73	1	9
72	31.7.2005	00:45	33.13	39.43	4.3	2.0	8	62	14	11
73	31.7.2005	15:18	33.08	39.42	4.6	11.7	20	73	-20	11
74	1.8.2005	00:45	33.07	39.44	4.7	19.3	119	82	172	9
75	6.8.2005	09:09	33.10	39.39	4.7	6.0	111	74	171	9
76	18.10.2005	07:17	39.00	38.78	4.3	10.0	273	71	4	9
77	26.11.2005	15:56	38.86	38.21	5.1	10.0	237	51	-20	6
78	29.3.2006	22:05	35.44	35.28	5.0	10.0	219	43	-10	6
79	9.10.2006	05:01	35.56	35.88	4.1	18.3	137	28	-113	9
80	14.2.2007	11:59	34.14	39.76	3.9	18.8	349	38	-47	12
81	18.5.2007	23:27	33.26	37.32	4.6	8.3	176	43	-26	9
82	24.8.2007	02:53	37.45	38.15	4.4	1.2	334	43	-170	9
83	15.9.2007	05:26	37.00	37.81	4.4	8.5	334	43	105	9
84	15.9.2007	23:28	36.92	37.79	4.3	10.8	244	19	5	9
85	24.9.2007	23:21	35.47	39.77	3.5	6.8	242	45	0	12
86	13.12.2007	18:06	33.07	38.83	4.9	7.9	224	55	1	6
87	20.12.2007	09:48	33.16	39.41	5.7	11.3	214	73	17	6
88	26.12.2007	23:47	33.11	39.42	5.6	10.8	231	67	5	6
89	27.12.2007	13:48	33.14	39.44	4.7	3.8	150	57	-140	9
90	15.3.2008	10:15	33.05	39.50	4.8	12.5	41	66	-6	9
91	14.4.2008	15:16	35.91	39.95	3.4	9.7	220	45	45	12
92	3.9.2008	02:22	38.50	37.51	5.0	5.7	219	79	-10	6
93	12.11.2008	14:03	35.52	38.84	5.1	10.0	227	70	-13	6
94	17.6.2009	04:29	36.02	36.05	4.6	10.4	174	32	-113	9

**Table A. 1 (cont'd)**

No	Date	Time	Lon. E (°)	Lat. N (°)	Mag.	Dep. (km)	Strike (°)	Dip (°)	Rake (°)	Ref.
95	10.9.2009	18:29	32.52	37.94	4.8	2.0	28	42	-82	6
96	11.9.2009	01:58	32.44	37.94	4.9	5.0	26	39	-76	6
97	1.2.2010	04:01	38.12	39.56	4.5	21.5	85	82	-22	9
98	1.2.2010	04:01	37.99	39.56	4.5	6.0	178	68	-171	9
99	23.3.2010	19:33	38.65	39.89	3.7	11.0	48	57	-33	13
100	16.8.2010	06:41	38.92	39.72	3.6	13.0	335	86	-165	13
101	17.9.2010	10:17	38.95	38.14	4.9	10.0	322	74	-165	9
102	14.11.2010	23:08	36.08	36.48	4.9	12.0	24	53	-94	6
103	14.11.2010	23:08	36.01	36.59	4.9	2.5	212	33	-99	9
104	16.11.2010	10:50	36.32	37.33	4.7	7.6	5	17	-48	9
105	29.6.2011	19:48	35.87	37.41	4.4	20.6	95	40	78	9
106	16.8.2011	07:53	35.90	39.08	4.1	5.0	65	70	-20	14
107	22.9.2011	03:22	38.60	39.68	5.6	16.1	239	77	-5	6
108	16.2.2012	11:01	37.46	38.65	4.6	15.3	22	31	-107	9
109	25.5.2012	11:22	38.72	38.16	4.4	14.8	70	85	-11	9
110	22.7.2012	09:26	36.23	37.34	4.8	19.2	38	53	-78	6
111	16.9.2012	07:54	35.77	37.44	4.6	21.0	163	86	161	9
112	19.9.2012	09:17	37.12	37.28	5.0	21.4	210	48	-11	6
113	5.10.2012	10:25	33.80	39.35	4.6	17.7	198	62	-32	9
114	16.10.2012	01:16	37.11	37.30	4.5	14.7	211	71	-27	9
115	16.10.2012	10:25	37.16	37.27	4.5	25.0	146	90	153	9
116	13.11.2012	23:55	37.12	37.20	4.9	24.9	119	90	153	9
117	14.11.2012	00:02	37.14	37.28	4.4	10.0	46	83	44	9
118	18.11.2012	19:18	37.13	37.33	3.9	28.0	187	74	108	13
119	1.12.2012	03:51	38.35	37.47	4.1	17.9	133	65	124	13
120	25.12.2012	15:35	34.10	39.85	3.9	17.1	276	48	110	13
121	30.12.2012	09:11	35.72	37.48	4.1	8.0	247	79	49	15
122	8.1.2013	06:05	37.96	37.93	4.3	13.8	51	88	1	9
123	8.1.2013	06:15	37.96	37.92	4.4	21.1	150	90	172	9
124	12.2.2013	20:20	36.95	37.11	3.7	13.0	314	74	-154	13
125	4.4.2013	06:34	37.12	37.32	3.7	9.0	140	68	-156	13
126	14.4.2013	18:25	36.21	37.31	3.5	20.0	59	51	19	13
127	1.5.2013	06:47	37.10	37.31	3.7	7.9	290	81	157	13
128	1.5.2013	06:50	37.11	37.30	3.9	13.3	0	44	-58	13
129	6.5.2013	18:33	37.13	37.30	3.8	12.4	109	74	-167	13

**Table A. 1 (cont'd)**

No	Date	Time	Lon. E (°)	Lat. N (°)	Mag.	Dep. (km)	Strike (°)	Dip (°)	Rake (°)	Ref.
130	16.6.2013	20:31	37.08	38.11	4.6	13.1	347	75	160	13
131	26.7.2013	00:22	35.87	36.06	4.0	25.8	345	78	-95	13
132	28.8.2013	06:26	38.91	38.38	3.6	18.2	340	70	-162	13
133	23.10.2013	12:24	34.43	36.23	4.5	10.1	22	54	45	9
134	30.12.2013	00:02	38.33	37.88	3.5	19.9	333	81	-131	13
135	10.1.2014	13:20	36.23	37.28	4.0	6.0	282	85	173	15
136	14.2.2014	00:33	36.07	36.23	4.9	18.0	35	70	-59	6
137	22.2.2014	15:42	36.38	37.42	4.4	20.0	193	60	-45	9
138	2.3.2014	04:25	35.18	36.79	4.2	10.0	69	45	63	9
139	26.3.2014	14:00	38.59	38.14	3.9	4.0	216	69	-38	15
140	9.6.2014	03:38	36.06	36.29	4.8	20.9	164	36	-135	6
141	20.9.2014	02:52	38.70	39.16	4.1	10.0	250	87	-43	9
142	8.1.2015	18:44	36.86	37.03	4.5	21.6	106	75	170	9
143	22.1.2015	19:27	36.30	37.40	3.9	6.0	3	69	-99	15
144	10.2.2015	04:01	36.02	35.80	4.3	10.0	228	70	-27	9
145	28.3.2015	10:08	36.41	37.49	4.1	22.0	306	70	-150	15
146	28.3.2015	05:04	35.63	38.88	3.6	7.0	144	73	-167	15
147	17.4.2015	11:49	38.81	37.53	3.7	10.9	226	71	40	13
148	29.7.2015	22:01	34.94	36.58	4.9	23.7	193	68	-75	9
149	29.7.2015	22:01	34.87	36.44	5.0	33.4	195	64	-76	6
150	29.7.2015	00:56	34.95	36.58	4.9	34.0	149	50	-128	14
151	26.8.2015	23:01	36.93	37.33	4.0	7.0	353	43	-100	15
152	3.10.2015	21:08	38.93	38.18	3.8	9.8	324	71	160	15
153	29.11.2015	00:28	37.75	38.82	5.1	20.2	74	72	-19	6
154	29.11.2015	00:28	37.87	38.90	5.0	17.0	339	77	173	16
155	9.12.2015	09:03	37.92	38.88	4.5	22.8	65	73	-8	9
156	10.1.2016	17:40	34.33	39.72	5.0	21.2	7	79	-6	6
157	2.2.2016	14:21	37.84	38.84	4.1	10.2	184	88	-167	13
158	18.2.2016	07:56	35.84	39.01	3.9	5.4	46	69	-49	13
159	31.3.2016	21:33	35.85	36.97	4.2	14.0	142	77	-171	15
160	7.4.2016	11:11	35.09	37.92	3.8	12.9	27	53	-65	13
161	23.4.2016	19:51	36.62	36.91	3.7	5.8	312	39	-176	13
162	17.8.2016	01:07	38.15	38.70	4.2	11.2	271	40	66	13
163	16.9.2016	05:12	36.90	37.21	3.6	7.8	216	53	-26	13
164	20.11.2016	22:52	38.59	39.95	3.8	6.4	41	74	-62	13

**Table A. 1 (cont'd)**

<b>No</b>	<b>Date</b>	<b>Time</b>	<b>Lon. E (°)</b>	<b>Lat. N (°)</b>	<b>Mag.</b>	<b>Dep. (km)</b>	<b>Strike (°)</b>	<b>Dip (°)</b>	<b>Rake (°)</b>	<b>Ref.</b>
165	3.2.2017	06:33	38.09	38.69	3.7	17.9	71	65	8	13
166	25.2.2017	21:06	36.10	37.01	4.5	3.8	351	45	-79	13
167	2.3.2017	11:07	38.45	37.53	5.6	17.2	225	78	-21	6
168	2.3.2017	17:03	38.50	37.58	3.7	7.7	45	86	26	13
169	10.3.2017	22:23	38.51	37.58	3.7	9.3	33	86	-31	13
170	28.3.2017	21:53	37.18	38.29	4.0	12.0	70	86	-31	13
171	18.8.2017	04:30	37.54	37.57	4.0	9.0	233	55	-9	13

**Table A. 2** List of stations.

Station Code	Station Location (in Turkey)	WGS84 (Lat / Lon)		Elevation (m)
		N (Y) (°)	E (X) (°)	
AT01	Kalın, Sivas	39.7240	36.7109	1340.26
AT02	Karataş, Sivas	39.3806	37.0573	1524.20
AT03	Kuzyaka, Sivas	39.0301	37.5955	1700.65
AT04	Fethiye, Malatya	38.6278	38.1386	931.45
AT05	Ormaniçi, Malatya	38.2174	38.7937	1162.01
AT06	Çampınar, Yozgat	39.6731	35.6665	1287.25
AT07	Kartalkaya, Sivas	39.1454	36.2223	1448.92
AT08	Yazyurdu, Sivas	38.8040	36.9266	1905.73
AT09	Yukarılupınar, Malatya	38.4019	37.5696	1650.75
AT10	Hudutköy, Malatya	38.0119	37.8609	1415.45
AT11	Ardıçoluk, Adıyaman	37.7579	38.3758	660.38
AT12	Hamzalı, Yozgat	39.4523	34.7451	1026.57
AT13	Yazıçepni, Yozgat	39.0770	35.3153	1213.87
AT14	Samagir, Kayseri	38.6277	36.0603	1464.92
AT15	Arıtış, Kahramanmaraş	38.3476	36.7763	1608.30
AT16	Ekinözü, Kahramanmaraş	38.0842	37.1361	1265.31
AT17	Aşağıazaplı, Adıyaman	37.7466	37.5200	1037.59
AT18	Akbudak, Gaziantep	37.4427	37.9589	579.60
AT19	Kurşunkaya, Kırıkkale	39.7352	33.5811	1017.11
AT20	Kırkpınar, Kırşehir	39.3639	34.1573	1206.79
AT21	Aşıklar, Nevşehir	38.9269	34.5246	1190.40
AT22	Karain, Nevşehir	38.5906	34.9903	1385.31
AT23	Ayvazhacı, Kayseri	38.3631	35.5500	1429.01
AT24	Sarıkaya, Kayseri	38.1646	35.9024	1704.98
AT25	Değirmendere, K.Maraş,	37.9181	36.4592	1718.88
AT26	Kurtul, Kahramanmaraş	37.6299	36.7315	595.56
AT27	Söğütlü, K.Maras	37.4836	37.1963	835.73
AT28	Süleymanobası, Gaziantep	37.2527	37.5501	761.62
AT29	Acıöz, Ankara	39.1790	33.3776	918.63
AT30	Akpınar, Aksaray	38.7640	34.0045	1283.20
AT31	Inallı, Nevşehir	38.5727	34.5084	1266.06
AT32	Orhanlı, Niğde	38.2967	34.8891	1454.10
AT33	Sulucaova, Niğde	38.0292	35.1502	1784.20
AT34	Yeşilköy, Adana	37.9051	35.5147	1503.36
AT35	Çulluuşağı, Adana	37.6727	35.8772	776.44

**Table A. 2 (cont'd).** List of stations.

Station Code	Station Location (in Turkey)	WGS84 (Lat / Lon)		Elevation (m)
		N (Y) (°)	N (Y) (°)	
AT37	Yenigün, Osmaniye	37.2442	36.4915	671.05
AT38	Karlıca, Osmaniye,	37.0361	36.8080	693.84
AT39	Bayraktepe, Gaziantep	36.9320	37.2230	843.86
AT40	Beylioiva, Konya	38.8489	32.4513	1118.06
AT41	Konya	38.4684	33.2447	939.07
AT42	Kutlu, Aksaray	38.2752	33.8726	968.70
AT43	Çömlekçi, Niğde	38.0579	34.3305	1607.63
AT44	Bahçeli, Niğde	37.8467	34.6120	1188.82
AT45	Yelatan, Niğde	37.6876	35.0198	1740.87
AT46	Hacıhaslani, Adana	37.3027	35.5761	173.42
AT47	Hamidiye, Osmaniye	36.9920	35.9910	93.86
AT48	Saylak, Hatay	36.6193	36.4138	257.46
AT49	Kolukısa, Konya	38.5137	32.2530	993.00
AT50	Altınekin, Konya	38.2999	32.8781	1013.60
AT51	Esentepe, Konya	38.0085	33.3798	1047.43
AT52	Emirgazi, Konya	37.9145	33.8631	1090.87
AT53	Şeyhömerli, Konya	37.5773	34.3336	1305.73
AT54	Alpu-Pozantı, Adana	37.4756	34.8818	1356.97
AT55	Fadıl, Adana	37.0837	35.0873	123.57
AT56	Kaldırım, Adana	36.7020	35.5469	4.19
AT57	Yarma, Konya	37.8143	32.8774	1001.26
AT58	İslik, Konya	37.5650	33.3254	1009.81
AT59	Üçarman, Konya	37.2833	33.8196	1433.46
AT60	Yavca, Mersin	37.0163	34.3637	1473.70
AT61	Akören, Konya	37.4195	32.3623	1135.21
AT62	Pınarbası, Karaman	37.1030	33.0534	1284.89
AT63	Topluca, Mersin	36.7125	33.4720	770.55
AT64	Esenpınar, Mersin	36.6013	34.1213	774.08
AT65	Edikli, Niğde	38.2210	34.9630	1377.41
AT66	Yenigün, Osmaniye	37.4212	36.1750	259.80
AT67	Erzin, Hatay	36.9517	36.2478	375.64
AT68	Hudutkoy, Malatya	38.0245	37.8338	1427.86
AT69	Söğütlü, Kahramanmaraş	37.4842	37.1970	837.83
AT70	Okçu, Niğde	37.9336	34.5432	1209.89
AT71	Karasaray, Konya	37.3780	34.2590	1963.74

**Table A. 3** P- T-, SHmax, SHmin axes and stress regimes of the focal mechanism solutions in the study area (data given in Table A.1). NF = normal faulting, NS = predominately normal faulting with strike-slip component, SS = strike-slip faulting, TS = predominately reverse faulting with strike-slip component, TF = thrust (reverse) faulting, UF = undefined.

No	Date	Time	Lon. E (°)	Lat. N (°)	P axis		T axis		SH axis		Regime Code
					Paz	Ppl	Taz	Tpl	Max az.	Min az.	
1	19.4.1938	10:59	33.70	39.50	348	18	250	23	164	74	SS
2	20.1.1941	03:37	33.60	35.20	122	11	227	52	126	36	UF
3	8.4.1951	21:38	36.10	36.60	343	5	251	26	162	72	SS
4	14.6.1964	12:15	38.48	38.08	222	51	92	27	14	104	UF
5	7.4.1967	17:07	36.13	37.37	224	21	131	8	42	132	SS
6	7.4.1967	18:33	36.18	37.37	17	7	109	21	18	108	SS
7	4.7.1967	18:33	36.20	37.40	348	47	115	29	12	102	UF
8	6.11.1968	13:41	32.78	35.16	329	4	69	69	150	60	TF
9	5.10.1970	14:53	38.99	35.13	310	10	130	80	130	40	TF
10	29.6.1971	09:08	36.86	37.13	312	11	65	62	136	46	TF
11	11.7.1971	20:12	36.83	37.16	217	4	307	7	37	127	SS
12	17.8.1971	04:29	36.79	37.11	133	32	331	56	123	33	TF
13	1.1.1975	00:30	36.48	36.78	317	55	103	30	180	90	NF
14	9.2.1978	21:10	36.80	37.08	12	18	234	67	7	97	TF
15	28.12.1979	03:09	35.85	37.49	186	1	96	1	6	96	SS
16	2.1.1980	12:52	36.33	36.57	1	30	147	55	14	104	TF
17	30.6.1981	07:59	35.89	36.17	201	21	306	34	28	118	UF
18	20.5.1982	03:28	33.69	35.09	34	2	298	76	34	124	TF
19	24.11.1983	00:14	36.13	37.05	184	21	91	8	2	92	SS
20	18.12.1984	13:59	35.30	35.26	336	2	69	51	157	67	TS
21	5.5.1986	03:35	37.78	38.00	218	19	116	30	33	123	SS
22	6.6.1986	10:39	37.91	38.01	205	1	115	1	25	115	SS
23	16.6.1987	06:17	35.25	35.55	54	55	265	30	9	99	NF
24	24.6.1989	03:09	35.94	36.75	299	73	115	17	25	115	NF
25	10.4.1991	01:08	36.12	37.30	327	58	104	24	4	94	NF
26	10.2.1994	06:15	35.89	36.93	156	31	51	23	148	58	UF
27	21.1.1995	03:48	36.25	37.37	137	81	267	6	176	86	NF
28	23.2.1995	21:03	32.27	35.06	110	30	256	55	123	33	TF
29	23.2.1995	21:40	32.30	35.01	47	40	286	32	30	120	UF
30	13.4.1995	20:23	36.20	37.42	260	85	80	5	170	80	NF
31	29.5.1995	04:58	32.25	35.05	101	29	252	58	112	22	TF

**Table A. 3 (cont'd)**

No	Date	Time	Lon. E (°)	Lat. N (°)	P axis		T axis		SH axis		Regime Code
					Paz	Ppl	Taz	Tpl	Max az.	Min az.	
32	22.1.1997	17:57	35.96	36.21	219	41	104	26	24	114	UF
33	22.1.1997	18:22	36.03	36.26	177	27	283	27	5	95	UF
34	22.1.1997	18:24	36.06	36.13	206	55	94	14	10	100	NF
35	23.1.1997	14:53	36.05	36.26	354	31	99	23	2	92	UF
36	3.1.1998	21:15	35.77	37.20	175	17	77	25	171	81	SS
37	28.3.1998	00:30	38.75	38.20	206	39	98	21	15	105	UF
38	9.5.1998	15:38	38.95	38.25	207	10	117	0	27	117	SS
39	27.6.1998	13:55	35.33	36.53	184	4	275	11	4	94	SS
40	28.6.1998	03:59	35.49	36.92	181	21	89	5	180	90	SS
41	4.7.1998	02:15	35.44	36.90	193	14	287	14	15	105	SS
42	4.12.1998	04:59	35.58	37.01	197	7	289	21	18	108	SS
43	14.12.1998	13:06	35.79	38.92	205	9	300	28	27	117	SS
44	15.1.1999	02:04	35.85	37.04	352	18	261	3	172	82	SS
45	6.4.1999	00:08	38.23	39.37	185	24	291	31	12	102	UF
46	10.6.1999	23:25	35.96	37.38	184	4	275	11	4	94	SS
47	11.6.1999	05:25	36.80	39.53	49	54	303	11	37	127	NF
48	24.8.1999	17:33	32.68	39.41	349	27	246	24	162	72	UF
49	2.1.2000	20:28	38.96	38.30	208	36	112	8	24	114	SS
50	2.4.2000	11:41	37.08	37.61	170	18	272	33	175	85	SS
51	2.4.2000	17:26	37.32	37.54	178	11	270	10	179	89	SS
52	7.5.2000	09:08	38.83	38.26	186	6	278	17	7	97	SS
53	7.5.2000	23:10	38.91	38.27	6	7	275	11	5	95	SS
54	12.5.2000	03:01	36.06	36.99	196	79	291	1	21	111	NF
55	27.5.2000	07:49	35.28	36.23	34	36	285	24	23	113	UF
56	17.1.2001	12:09	36.21	37.07	21	31	288	5	19	109	SS
57	25.6.2001	13:28	36.27	37.22	165	74	64	3	155	65	NF
58	25.9.2001	11:53	32.33	35.97	189	16	281	6	10	100	SS
59	18.10.2001	15:50	35.22	36.86	7	39	129	33	24	114	UF
60	31.10.2001	12:33	36.25	37.26	125	80	305	10	35	125	NF
61	23.5.2002	01:08	36.35	37.41	197	48	107	1	17	107	NS
62	19.11.2002	01:25	38.39	38.02	201	13	294	9	22	112	SS
63	14.12.2002	01:02	36.19	37.47	55	81	292	5	23	113	NF
64	26.2.2003	03:08	36.27	35.86	250	6	160	3	70	160	SS
65	13.7.2003	01:48	38.95	38.28	207	0	297	1	27	117	SS
66	24.9.2003	08:13	38.23	39.55	230	6	138	16	49	139	SS
67	26.2.2004	04:13	38.25	37.91	202	18	311	46	29	119	TS

**Table A. 3 (cont'd)**

No	Date	Time	Lon. E (°)	Lat. N (°)	P axis		T axis		SH axis		Regime Code
					Paz	Ppl	Taz	Tpl	Max az.	Min az.	
68	18.8.2004	05:57	34.40	36.80	123	60	300	30	28	118	NF
69	4.7.2005	21:33	36.08	39.16	30	68	128	3	37	127	NF
70	30.7.2005	21:45	33.11	39.39	169	4	79	1	169	79	SS
71	31.7.2005	23:41	33.10	39.44	161	11	69	13	160	70	SS
72	31.7.2005	00:45	33.13	39.43	322	11	226	29	139	49	SS
73	31.7.2005	15:18	33.08	39.42	338	26	68	1	158	68	SS
74	1.8.2005	00:45	33.07	39.44	164	0	74	11	164	74	SS
75	6.8.2005	09:09	33.10	39.39	336	5	68	18	157	67	SS
76	18.10.2005	07:17	39.00	38.78	229	10	136	16	48	138	SS
77	26.11.2005	15:56	38.86	38.21	206	39	104	15	18	108	SS
78	29.3.2006	22:05	35.44	35.28	189	37	78	26	177	87	UF
79	9.10.2006	05:01	35.56	35.88	276	69	64	18	150	60	NF
80	14.2.2007	11:59	34.14	39.76	345	61	229	14	144	54	NF
81	18.5.2007	23:27	33.26	37.32	154	46	44	18	141	51	NS
82	24.8.2007	02:53	37.45	38.15	184	37	295	26	16	106	UF
83	15.9.2007	05:26	37.00	37.81	233	3	340	79	54	144	TF
84	15.9.2007	23:28	36.92	37.79	221	40	77	44	16	106	UF
85	24.9.2007	23:21	35.47	39.77	206	29	97	31	16	106	UF
86	13.12.2007	18:06	33.07	38.83	184	23	83	25	178	88	UF
87	20.12.2007	09:48	33.16	39.41	167	1	76	24	167	77	SS
88	26.12.2007	23:47	33.11	39.42	187	12	93	20	5	95	SS
89	27.12.2007	13:48	33.14	39.44	2	50	92	0	2	92	NS
90	15.3.2008	10:15	33.05	39.50	360	20	265	13	178	88	SS
91	14.4.2008	15:16	35.91	39.95	161	8	57	58	158	68	TF
92	3.9.2008	02:22	38.50	37.51	175	15	85	1	175	85	SS
93	12.11.2008	14:03	35.52	38.84	186	23	93	5	5	95	SS
94	17.6.2009	04:29	36.02	36.05	322	70	101	15	7	97	NF
95	10.9.2009	18:29	32.52	37.94	55	82	292	4	22	112	NF
96	11.9.2009	01:58	32.44	37.94	52	80	286	7	17	107	NF
97	1.2.2010	04:01	38.12	39.56	40	21	133	10	42	132	SS
98	1.2.2010	04:01	37.99	39.56	40	21	133	10	42	132	SS
99	23.3.2010	19:33	38.65	39.89	15	45	281	4	12	102	NS
100	16.8.2010	06:41	38.92	39.72	200	13	109	8	19	109	SS
101	17.9.2010	10:17	38.95	38.14	185	21	275	1	5	95	SS
102	14.11.2010	23:08	36.08	36.48	274	82	117	8	27	117	NF
103	14.11.2010	23:08	36.01	36.59	332	78	129	12	38	128	NF

**Table A. 3 (cont'd)**

No	Date	Time	Lon. E (°)	Lat. N (°)	P axis		T axis		SH axis		Regime Code
					Paz	Ppl	Taz	Tpl	Max az.	Min az.	
104	16.11.2010	10:50	36.32	37.33	37	57	242	31	163	73	NF
105	29.6.2011	19:48	35.87	37.41	14	6	249	80	13	103	TF
106	16.8.2011	07:53	35.90	39.08	24	28	293	1	24	114	SS
107	22.9.2011	03:22	38.60	39.68	195	13	104	6	14	104	SS
108	16.2.2012	11:01	37.46	38.65	157	74	305	15	33	123	NF
109	25.5.2012	11:22	38.72	38.16	25	11	116	4	25	115	SS
110	22.7.2012	09:26	36.23	37.34	353	77	120	7	28	118	NF
111	16.9.2012	07:54	35.77	37.44	210	10	117	16	29	119	SS
112	19.9.2012	09:17	37.12	37.28	178	35	71	22	169	79	UF
113	5.10.2012	10:25	33.80	39.35	161	42	71	0	161	71	NS
114	16.10.2012	01:16	37.11	37.30	169	32	262	4	170	80	SS
115	16.10.2012	10:25	37.16	37.27	194	19	98	19	11	101	SS
116	13.11.2012	23:55	37.12	37.20	167	19	71	19	164	74	SS
117	14.11.2012	00:02	37.14	37.28	169	24	278	35	177	87	UF
118	18.11.2012	19:18	37.13	37.33	263	27	121	57	72	162	TF
119	1.12.2012	03:51	38.35	37.47	199	14	88	56	14	104	TF
120	25.12.2012	15:35	34.10	39.85	352	1	258	75	172	82	TF
121	30.12.2012	09:11	35.72	37.48	7	23	119	41	16	106	UF
122	8.1.2013	06:05	37.96	37.93	6	1	276	2	6	96	SS
123	8.1.2013	06:15	37.96	37.92	195	6	105	6	15	105	SS
124	12.2.2013	20:20	36.95	37.11	177	30	84	6	175	85	SS
125	4.4.2013	06:34	37.12	37.32	0	32	90	0	0	90	SS
126	14.4.2013	18:25	36.21	37.31	13	15	270	39	8	98	SS
127	1.5.2013	06:47	37.10	37.31	339	10	245	23	157	67	SS
128	1.5.2013	06:50	37.11	37.30	351	68	248	5	160	70	NF
129	6.5.2013	18:33	37.13	37.30	331	20	62	3	152	62	SS
130	16.6.2013	20:31	37.08	38.11	35	3	304	24	34	124	SS
131	26.7.2013	00:22	35.87	36.06	248	57	79	33	176	86	NF
132	28.8.2013	06:26	38.91	38.38	201	27	292	2	22	112	SS
133	23.10.2013	12:24	34.43	36.23	322	1	231	55	142	52	TF
134	30.12.2013	00:02	38.33	37.88	206	40	94	25	13	103	UF
135	10.1.2014	13:20	36.23	37.28	328	1	237	9	148	58	SS
136	14.2.2014	00:33	36.07	36.23	343	54	103	19	5	95	NF
137	22.2.2014	15:42	36.38	37.42	157	52	253	5	162	72	NS
138	2.3.2014	04:25	35.18	36.79	358	3	259	71	177	87	TF
139	26.3.2014	14:00	38.59	38.14	174	41	272	9	179	89	NS

**Table A. 3 (cont'd)**

No	Date	Time	Lon. E (°)	Lat. N (°)	P axis		T axis		SH axis		Regime Code
					Paz	Ppl	Taz	Tpl	Max az.	Min az.	
140	9.6.2014	03:38	36.06	36.29	345	61	105	16	10	100	NF
141	20.9.2014	02:52	38.70	39.16	197	31	305	26	26	116	UF
142	8.1.2015	18:44	36.86	37.03	332	3	63	18	152	62	SS
143	22.1.2015	19:27	36.30	37.40	258	65	100	23	15	105	NF
144	10.2.2015	04:01	36.02	35.80	187	33	279	3	8	98	SS
145	28.3.2015	10:08	36.41	37.49	168	35	74	5	166	76	SS
146	28.3.2015	05:04	35.63	38.88	6	21	98	3	7	97	SS
147	17.4.2015	11:49	38.81	37.53	350	11	90	41	174	84	TS
148	29.7.2015	22:01	34.94	36.58	127	64	272	22	176	86	NF
149	29.7.2015	22:01	34.87	36.44	132	68	275	18	1	91	NF
150	29.7.2015	00:56	34.95	36.58	352	62	85	2	175	85	NF
151	26.8.2015	23:01	36.93	37.33	161	82	270	3	180	90	NF
152	3.10.2015	21:08	38.93	38.18	12	0	282	27	12	102	SS
153	29.11.2015	00:28	37.75	38.82	32	26	302	0	32	122	SS
154	29.11.2015	00:28	37.87	38.90	204	4	296	14	24	114	SS
155	9.12.2015	09:03	37.92	38.88	22	18	290	6	21	111	SS
156	10.1.2016	17:40	34.33	39.72	323	12	232	4	143	53	SS
157	2.2.2016	14:21	37.84	38.84	50	11	318	8	49	139	SS
158	18.2.2016	07:56	35.84	39.01	0	49	107	14	12	102	NS
159	31.3.2016	21:33	35.85	36.97	6	16	96	3	6	96	SS
160	7.4.2016	11:11	35.09	37.92	357	69	99	5	8	98	NF
161	23.4.2016	19:51	36.62	36.91	162	36	278	31	176	86	UF
162	17.8.2016	01:07	38.15	38.70	198	7	83	73	16	106	TF
163	16.9.2016	05:12	36.90	37.21	185	42	86	11	179	89	NS
164	20.11.2016	22:52	38.59	39.95	344	53	110	24	10	100	NF
165	3.2.2017	06:33	38.09	38.69	27	12	292	23	25	115	SS
166	25.2.2017	21:06	36.10	37.01	347	82	253	1	163	73	NF
167	2.3.2017	11:07	38.45	37.53	181	24	274	6	2	92	SS
168	2.3.2017	17:03	38.50	37.58	176	15	272	21	179	89	SS
169	10.3.2017	22:23	38.51	37.58	345	24	83	18	169	79	SS
170	28.3.2017	21:53	37.18	38.29	22	24	120	18	26	116	SS
171	18.8.2017	04:30	37.54	37.57	196	29	95	19	10	100	SS



## **APPENDIX B**

### **MOMENT TENSOR INVERSION SOLUTIONS**



**EVENT#1**

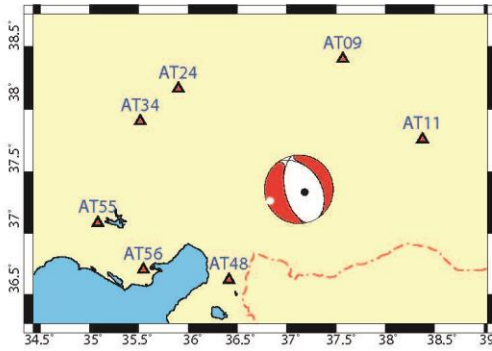
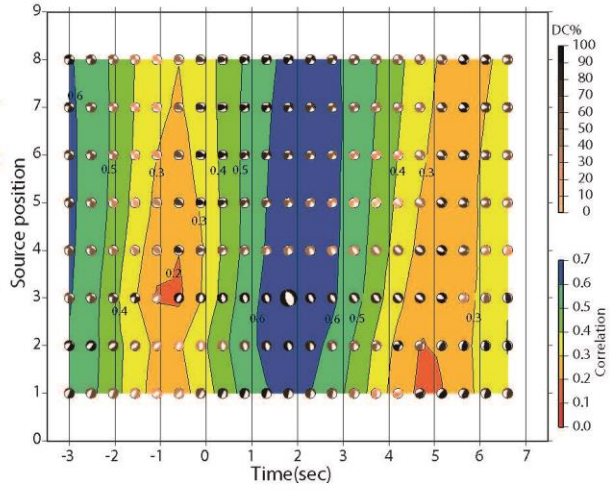
Origin time 20130525 16:05:00.94  
 Lat 37.3373 Lon 37.1407 Depth 4.9 km

Moment (Nm) : 4.519e+14  
 Mw : 3.7  
 VOL% : 0  
 DC% : 92.4  
 CLVD% : 7.6  
 Var.red.: (for stations used in inversion): 0.45  
 Corr.% : 70

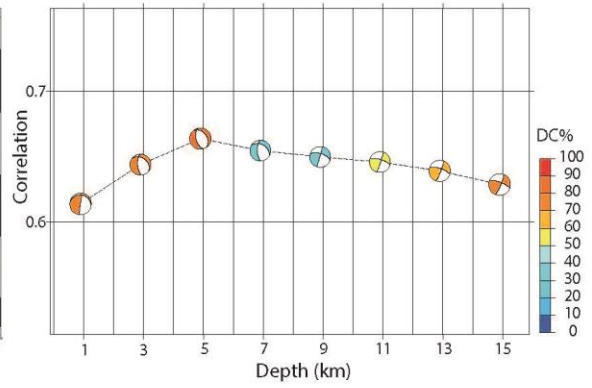
CN FMVAR STVAR  
 3.4 51±32 0.18

Strike Dip Rake Mrr Mtt Mpp  
 324 37 -110 -3.999 0.400 3.599  
 Strike Dip Rake Mrt Mrp Mtp  
 168 56 -76 0.234 1.679 -1.731

P-axis Azimuth Plunge Exponent (Nm): 14  
 119 75  
 T-axis Azimuth Plunge  
 248 10

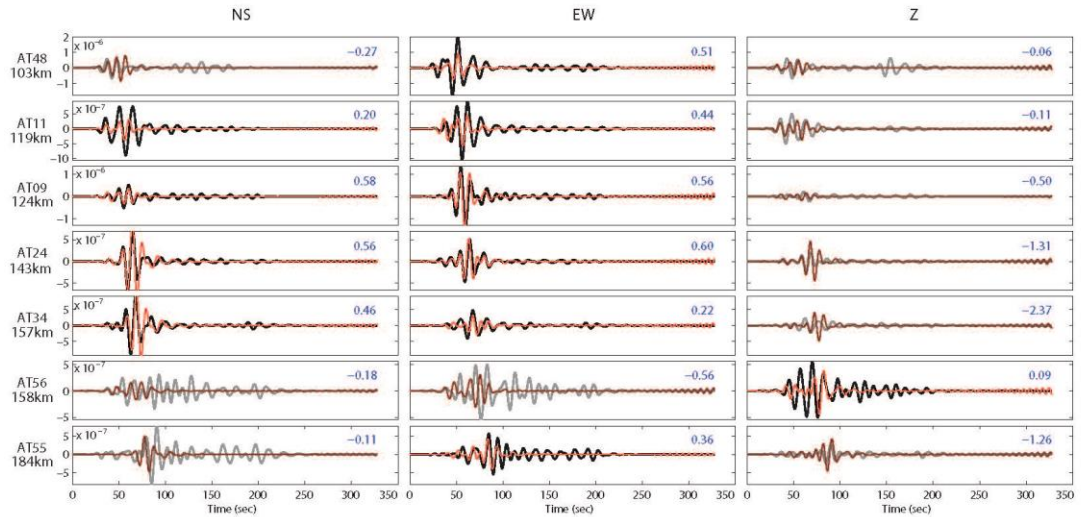


Correlation vs Depth Plot



Displacement (m). Inversion band (Hz) 0.06 – 0.12

— Observed  
 — Synthetic  
 Gray waveforms weren't used in inversion.  
 Blue numbers are variance reduction



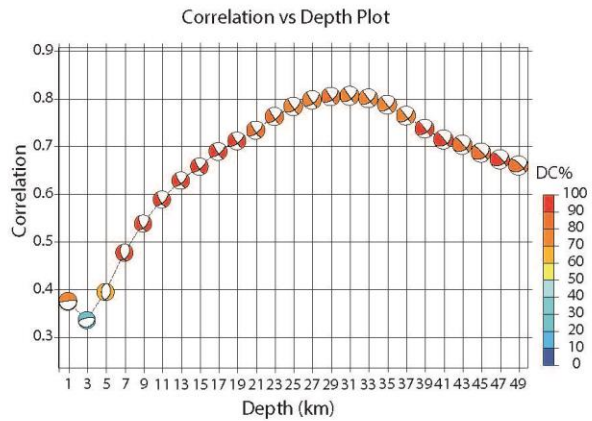
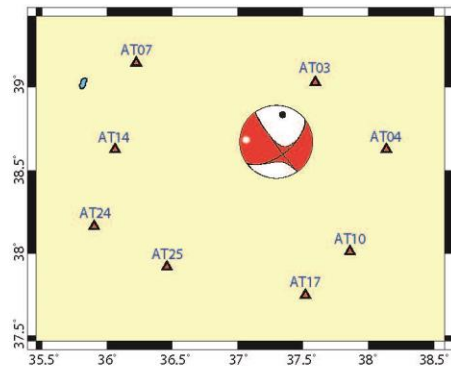
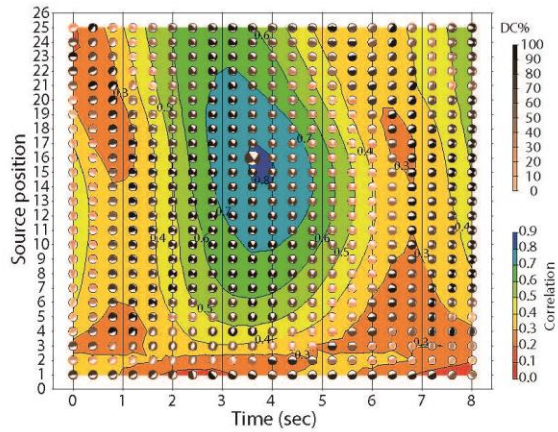
**EVENT#2**

Origin time 20130604 04:12:27.08  
 Lat (N) 38.6253 Lon (E) 37.3287 Depth 30.9 km

Moment (Nm): 4.489e+15  
 Mw: 4.4 CN FMVAR STVAR  
 VOL%: 0 2.0 5±2 0.07  
 DC%: 79.8  
 CLVD%: 20.2  
 Var.red.: (for stations used in inversion): 0.66  
 Corr.%: 90

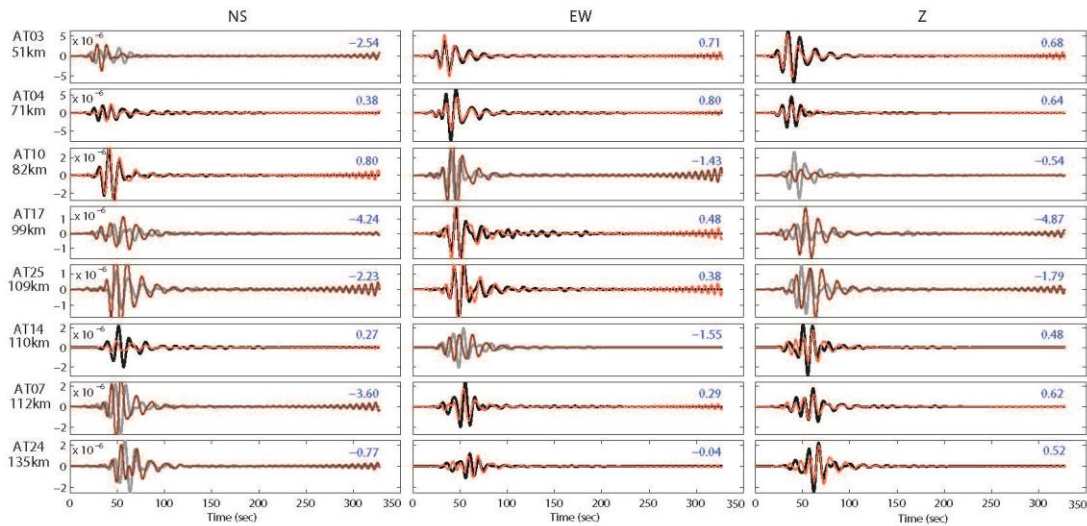
Strike Dip Rake Mrr Mtt Mpp  
 52 58 -5 -0.106 -3.514 3.620  
 Strike Dip Rake Mrt Mrp Mtp  
 145 85 -148 -1.881 1.585 1.172

P-axis Azimuth Plunge Exponent (Nm): 15  
 13 25  
 T-axis Azimuth Plunge  
 274 18



Displacement (m). Inversion band (Hz) 0.06 - 0.12

— Observed  
 — Synthetic  
 Gray waveforms weren't used in inversion.  
 Blue numbers are variance reduction



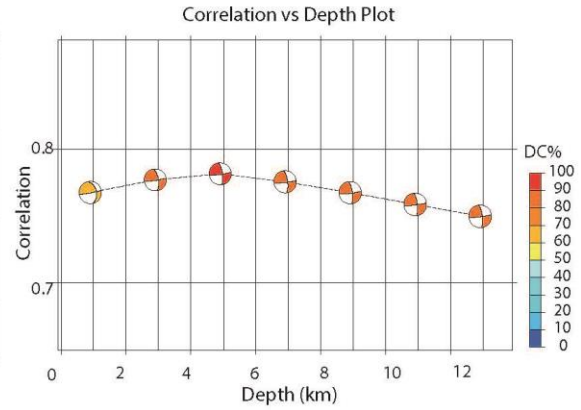
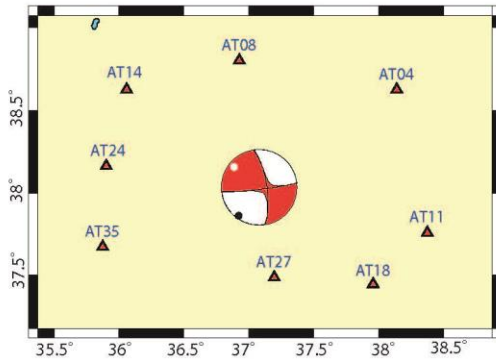
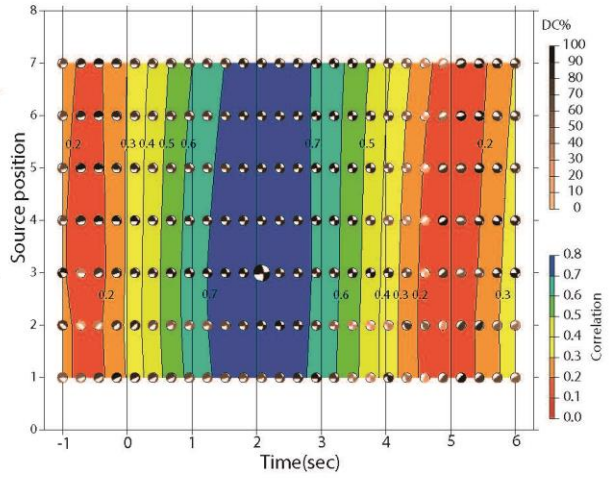
**EVENT#3**

Origin time 20130616 20:31:38.38  
 Lat 38.092 Lon 37.1075 Depth 4.9

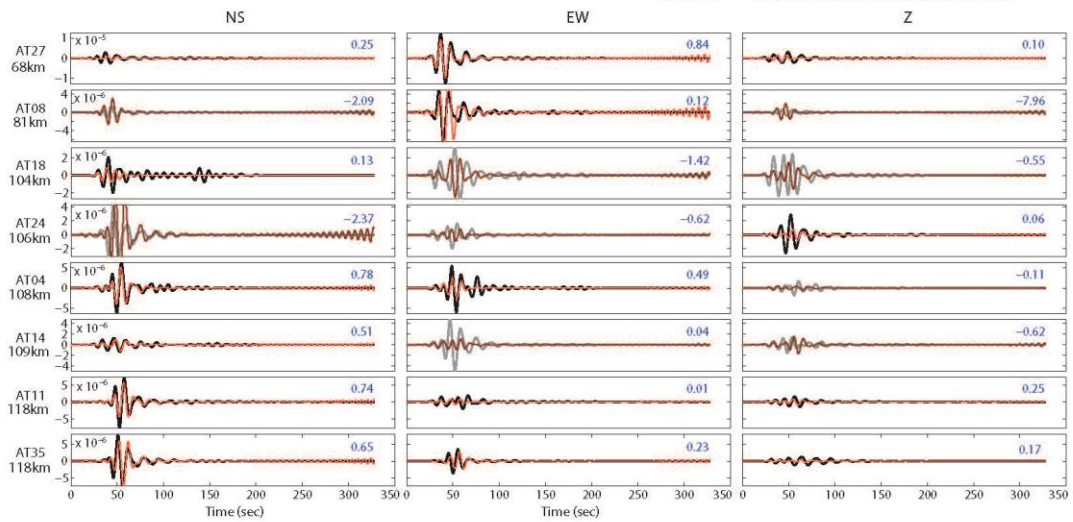
Moment (Nm) : 1.579e+15  
 Mw : 4.1  
 VOL% : 0  
 DC% : 90.1  
 CLVD% : 9.9  
 Var.red.: (for stations used in inversion): 0.61  
 Corr.% : 80

Strike	Dip	Rake	Mrr	Mtt	Mpp
352	73	175	0.152	-0.468	0.317
Strike	Dip	Rake	Mrt	Mrp	Mtp
83	85	17	0.420	0.155	1.457

P-axis Azimuth Plunge      Exponent (Nm): 15  
 216    8  
 T-axis Azimuth Plunge  
 309    15



Displacement (m). Inversion band (Hz) 0.06 – 0.12



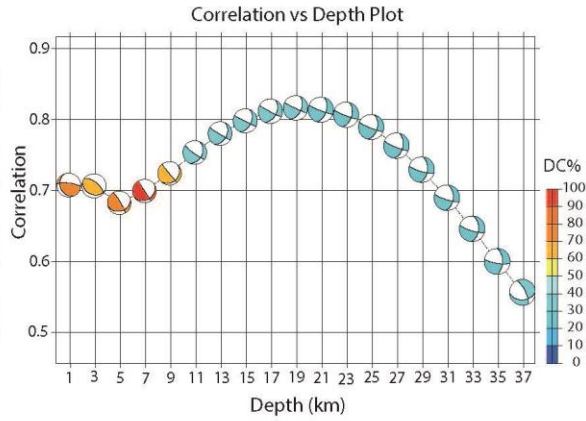
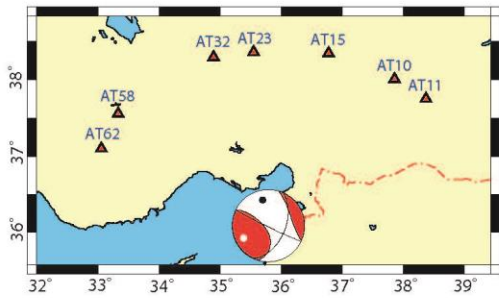
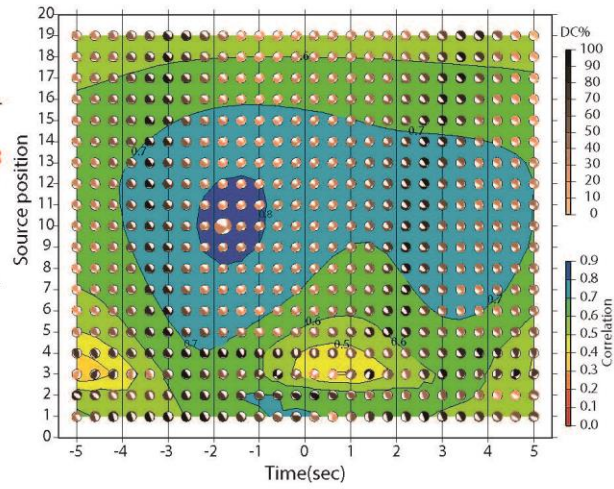
**EVENT#4**

Origin time 20130726 00:22:55.47  
 Lat 36.03 Lon 35.89 Depth 18.9

Moment (Nm): 3.815e+15  
 M<sub>w</sub>: 4.3  
 VOL%: 0  
 DC%: 32.3  
 CLVD%: 67.7  
 Var.red.: (for stations used in inversion): 0.67  
 Corr.%: 90

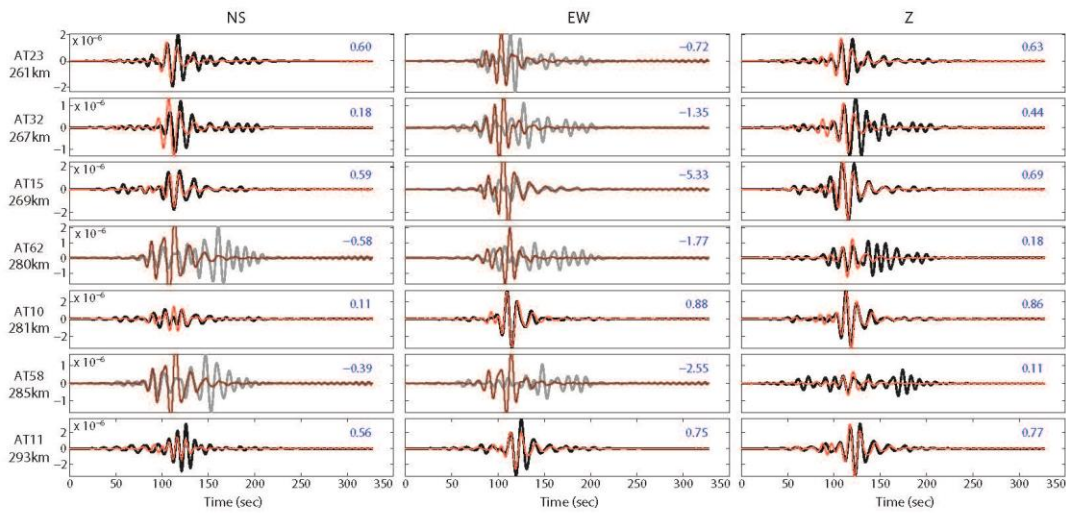
Strike Dip Rake Mrr Mtt Mpp  
 116 88 -142 -0.796 -1.525 2.321  
 Strike Dip Rake Mrt Mrp Mtp  
 24 52 -3 -1.540 1.807 -2.179

P-axis Azimuth Plunge Exponent (Nm): 15  
 347 28  
 T-axis Azimuth Plunge  
 243 24



Displacement (m). Inversion band (Hz) 0.06 - 0.12

— Observed  
 — Synthetic  
 Gray waveforms weren't used in inversion.  
 Blue numbers are variance reduction



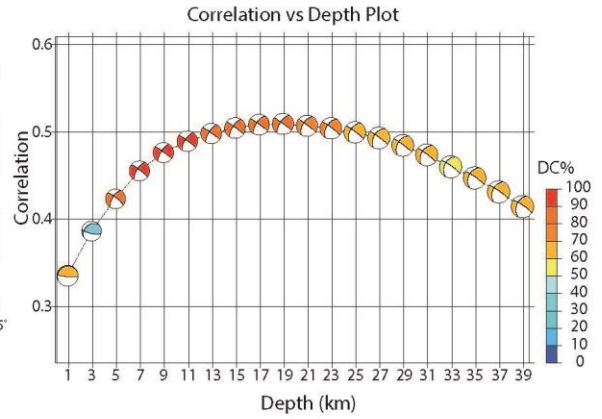
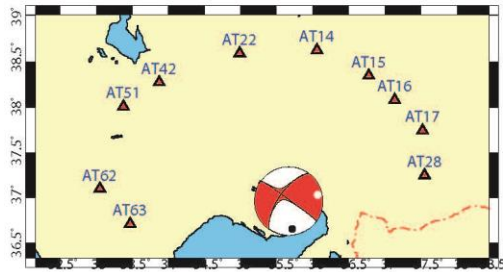
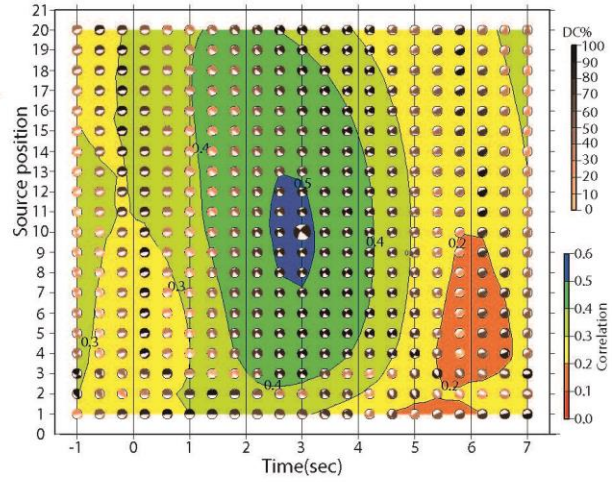
**EVENT#5**

Origin time 20130727 20:13:53.96  
 Lat 36.9697 Lon 35.5473 Depth 18.9

Moment (Nm) : 4.257e+14  
 VOL%: 0  
 DC%: 87.9  
 CLVD%: 12.1  
 Var.red.: (for stations used in inversion): 0.26  
 Corr.%: 60

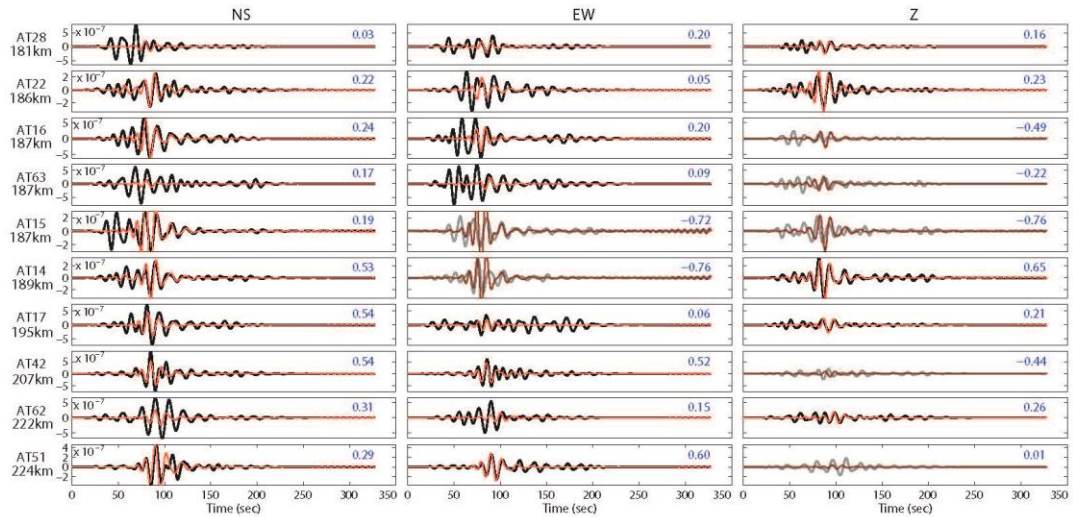
Strike Dip Rake Mrr Mtt Mpp  
 215 66 -3 0.008 -3.663 3.655  
 Strike Dip Rake Mrt Mrp Mtp  
 306 87 -156 1.626 -0.739 -1.244

P-axis Azimuth Plunge Exponent (Nm): 14  
 173 19  
 T-axis Azimuth Plunge  
 78 15



Displacement (m). Inversion band (Hz) 0.06 - 0.12

— Observed  
 — Synthetic  
 Gray waveforms weren't used in inversion.  
 Blue numbers are variance reduction



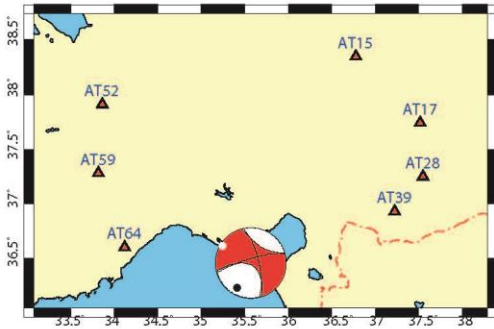
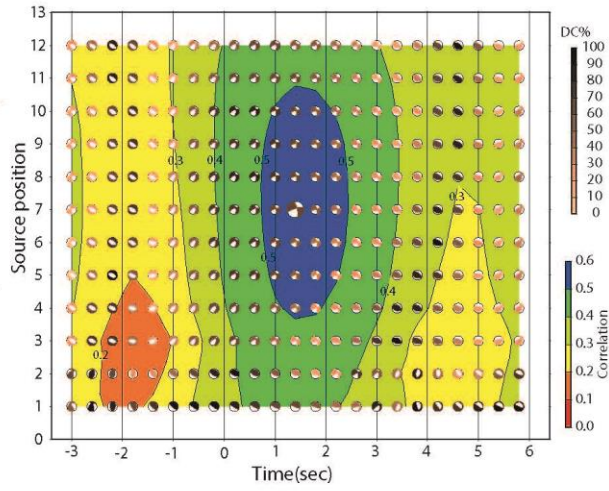
**EVENT#6**

Origin time 20130806 14:54:47.27  
 Lat 36.42 Lon 35.5873 Depth 12.9

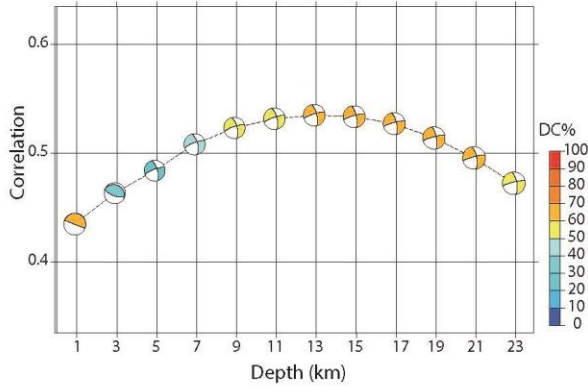
Moment (Nm): 6.160e+14  
 Mw: 3.8  
 VOL%: 0  
 DC%: 60.5  
 CLVD%: 39.5  
 Var.red.: (for stations used in inversion): 0.29  
 Corr.%: 60

Strike Dip Rake	Mrr Mtt Mpp
347 72 -170	0.439 -3.043 2.604
Strike Dip Rake	Mrt Mrp Mtp
253 80 -18	2.451 -0.906 4.796

P-axis Azimuth Plunge      Exponent (Nm): 14  
 209 20  
 T-axis Azimuth Plunge  
 301 6

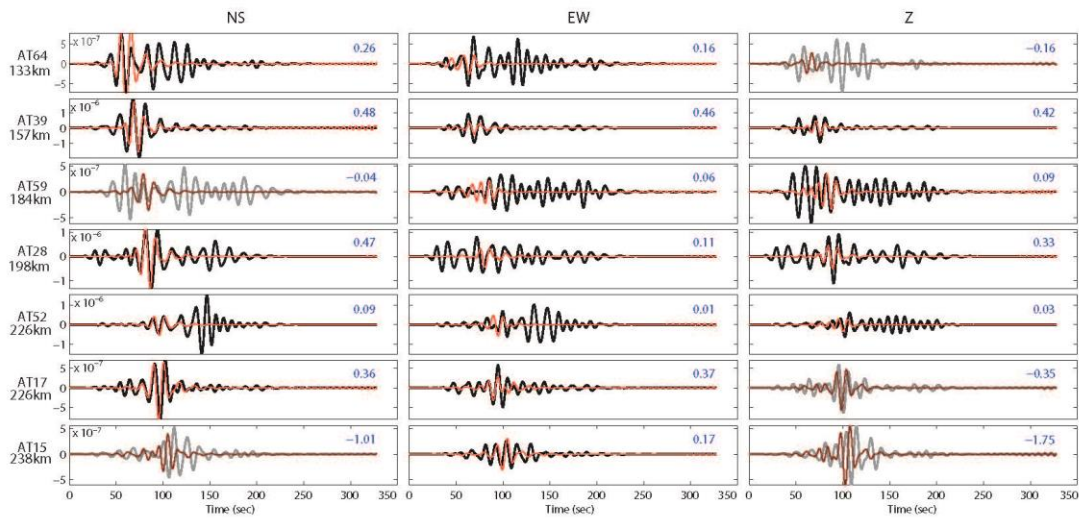


Correlation vs Depth Plot



Displacement (m). Inversion band (Hz) 0.06 - 0.12

— Observed  
 — Synthetic  
 Gray waveforms weren't used in inversion.  
 Blue numbers are variance reduction



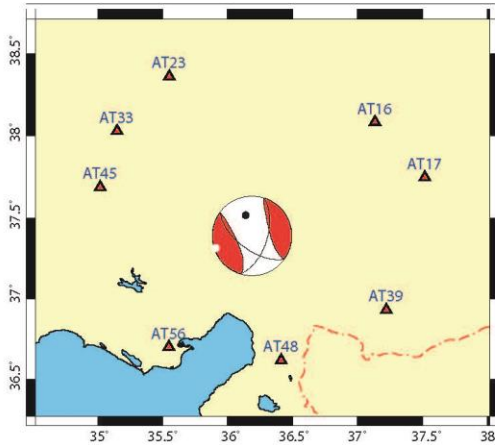
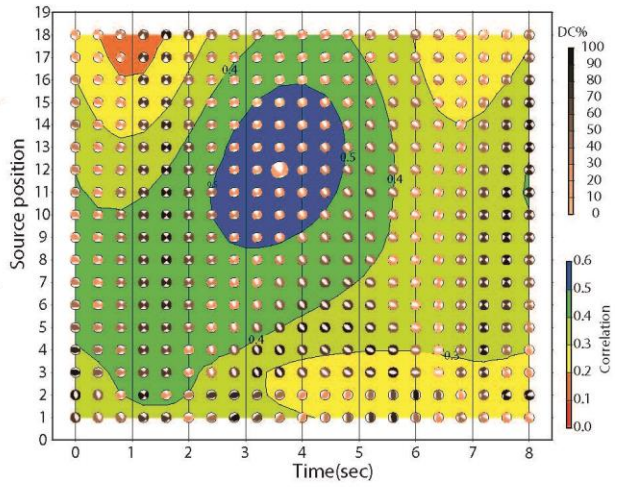
**EVENT#7**

Origin time 20130918 21:10:04.86  
 Lat 37.378 Lon 36.1963 Depth 22.9

Moment (Nm) : 3.264e+15  
 VOL% : 0 CN FMVAR STVAR  
 DC% : 18.8 2.5 16±10 0.08  
 CLVD% : 81.2  
 Var.red.: (for stations used in inversion): 0.31  
 Corr.% : 60

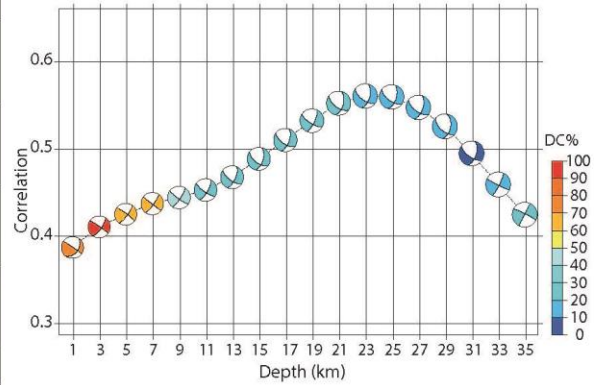
Strike Dip Rake Mrr Mtt Mpp  
 127 61 -144 -1.868 -1.301 3.168  
 Strike Dip Rake Mrt Mrp Mtp  
 17 59 -34 -0.391 0.056 -1.699

P-axis Azimuth Plunge Exponent (Nm): 15  
 343 45  
 T-axis Azimuth Plunge  
 251 2

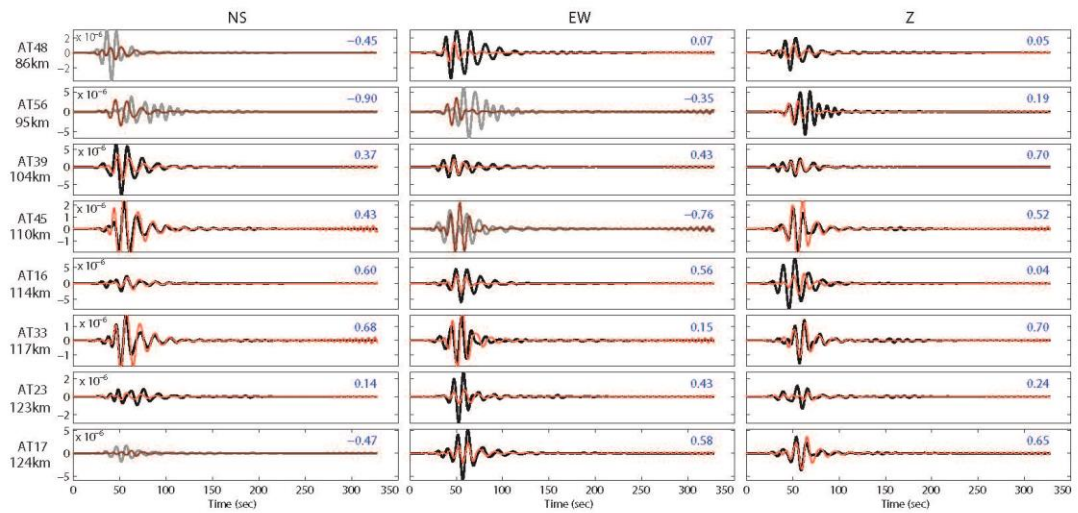


Displacement (m). Inversion band (Hz) 0.06 - 0.12

Correlation vs Depth Plot



— Observed  
 — Synthetic  
 Gray waveforms weren't used in inversion.  
 Blue numbers are variance reduction



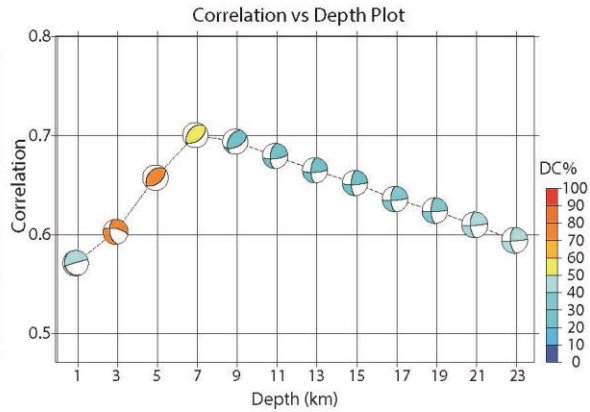
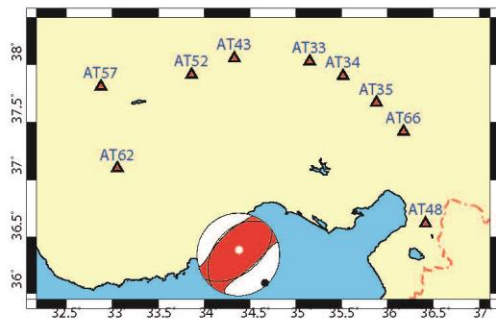
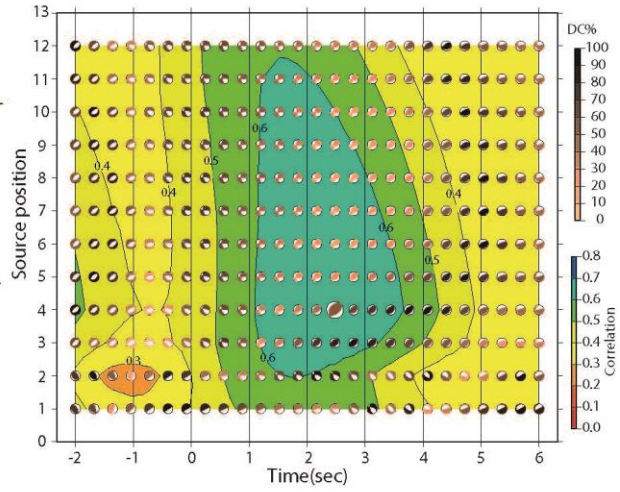
**EVENT#8**

Origin time 20131023 12:24:22.67  
 Lat 36.3023 Lon 34.3252 Depth 6.9

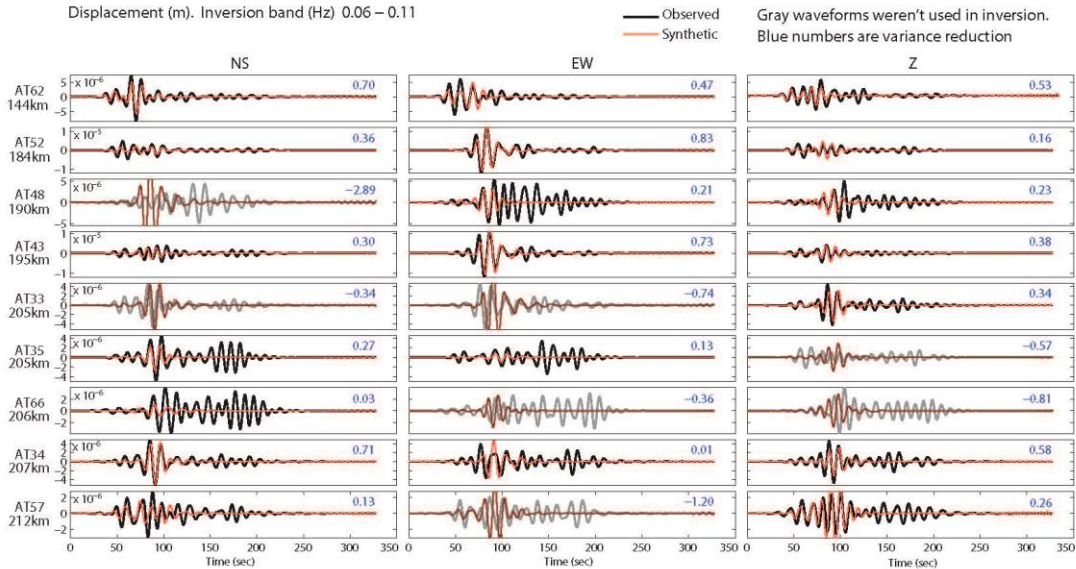
Moment (Nm): 6.155e+15  
 Mw: 4.5  
 VOL%: 0  
 DC%: 53.1  
 CLVD%: 46.9  
 Var.red.: (for stations used in inversion): 0.49  
 Corr.%: 80

Strike Dip Rake Mrr Mtt Mpp  
 53 51 99 5.022 -2.713 -2.309  
 Strike Dip Rake Mrt Mrp Mtp  
 219 40 79 1.187 0.511 -4.154

P-axis Azimuth Plunge Exponent (Nm): 15  
 137 6  
 T-axis Azimuth Plunge  
 7 81



Displacement (m). Inversion band (Hz) 0.06 - 0.11



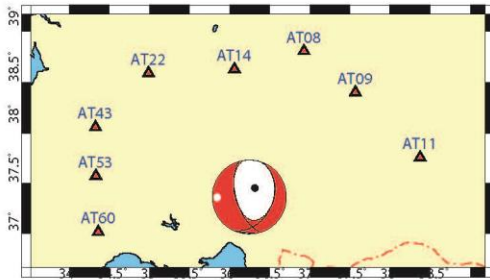
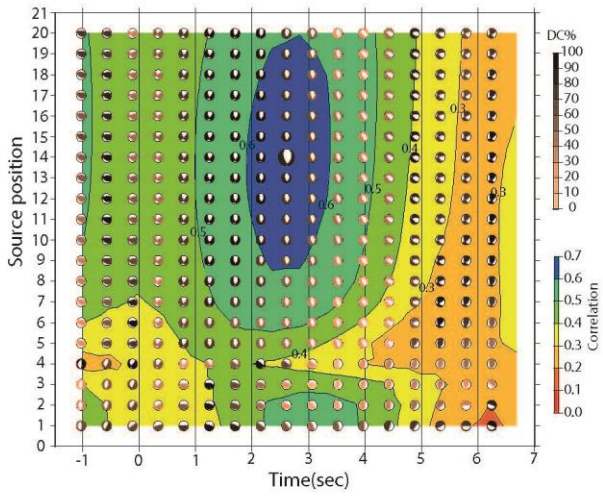
**EVENT#9**

Origin time 20131107 06:39:28.49  
 Lat 37.396 Lon 36.2358 Depth 13.9

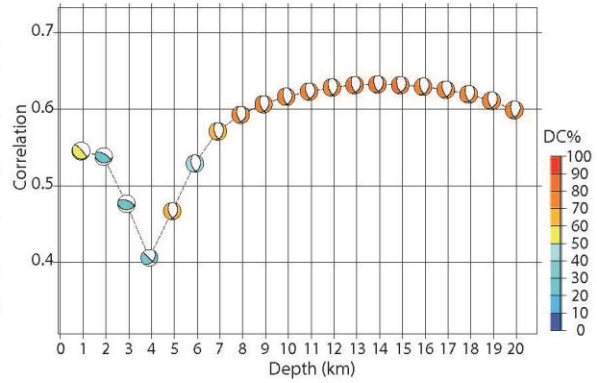
Moment (Nm) : 1.122e+15  
 VOL% : 0 CN FMVAR STVAR  
 DC% : 82.5 2.0 9±6 0.15  
 CLVD% : 17.5  
 Var.red.: (for stations used in inversion): 0.40  
 Corr.% : 70

Strike Dip Rake Mrr Mtt Mpp  
 23 36 -56 -9.214 -0.463 9.677  
 Strike Dip Rake Mrt Mrp Mtp  
 163 60 -112 -4.019 4.438 0.770

P-axis Azimuth Plunge Exponent (Nm): 14  
 31 67  
 T-axis Azimuth Plunge  
 269 13

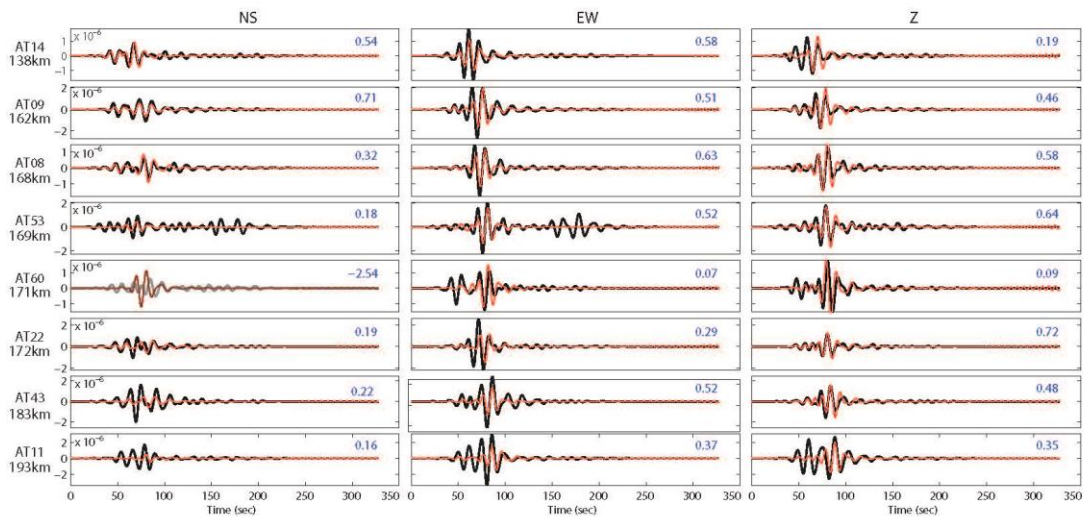


Correlation vs Depth Plot



Displacement (m). Inversion band (Hz) 0.06 – 0.12

— Observed  
 — Synthetic  
 Gray waveforms weren't used in inversion.  
 Blue numbers are variance reduction



**EVENT#10**

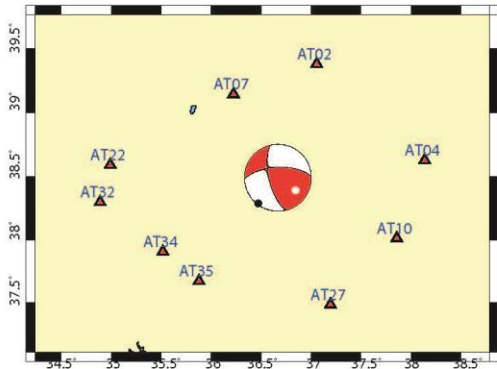
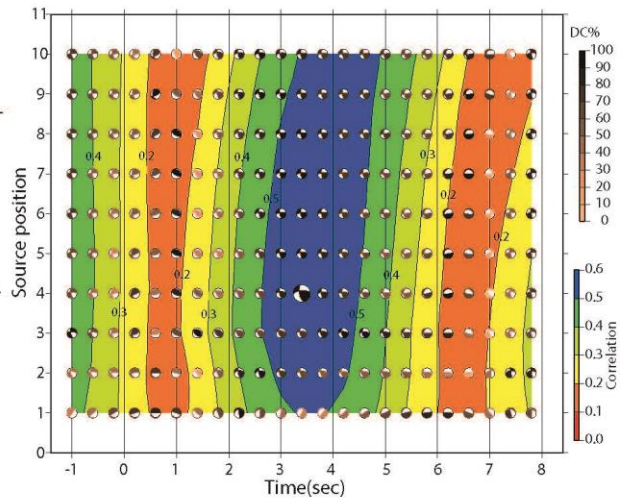
Origin time 20131108 05:55:33.82  
 Lat 38.5147 Lon 36.7787 Depth 6.9

Moment (Nm): 3.191e+14

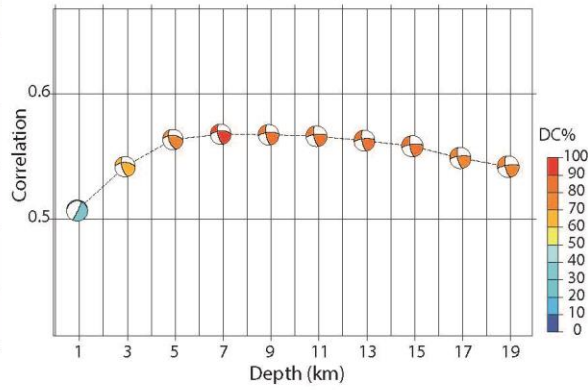
Mw: 3.6  
 VOL%: 0  
 DC%: 97.8  
 CLVD%: 2.2  
 Var.red.: (for stations used in inversion): 0.32  
 Corr.%: 60

Strike Dip Rake Mrr Mtt Mpp  
 167 68 152 1.078 -1.247 0.169  
 Strike Dip Rake Mrt Mrp Mtp  
 268 64 25 -0.775 -1.271 2.568

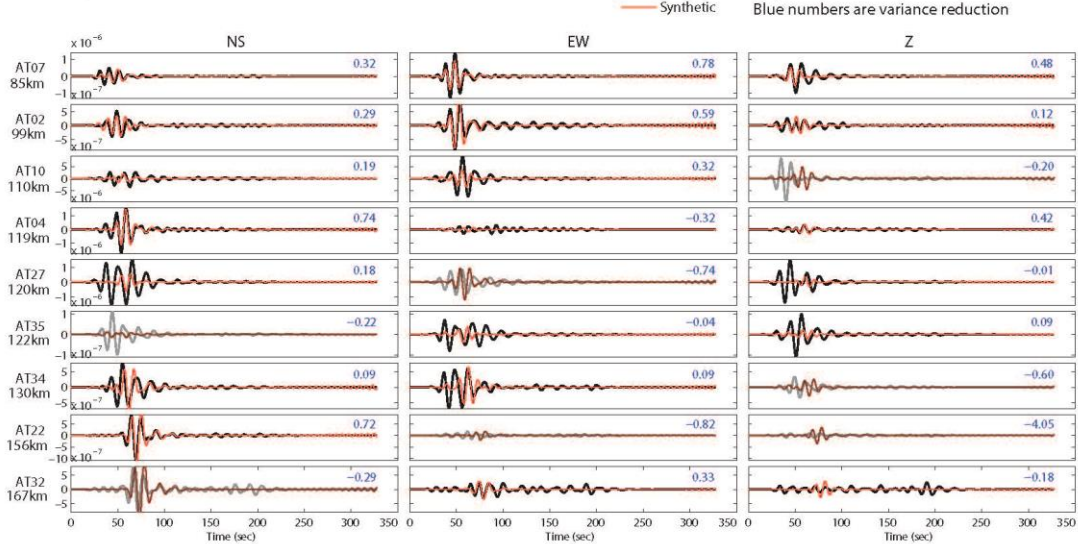
P-axis Azimuth Plunge Exponent (Nm): 14  
 218 2  
 T-axis Azimuth Plunge  
 126 35



Correlation vs Depth Plot



Displacement (m). Inversion band (Hz) 0.06 - 0.12



**EVENT#11**

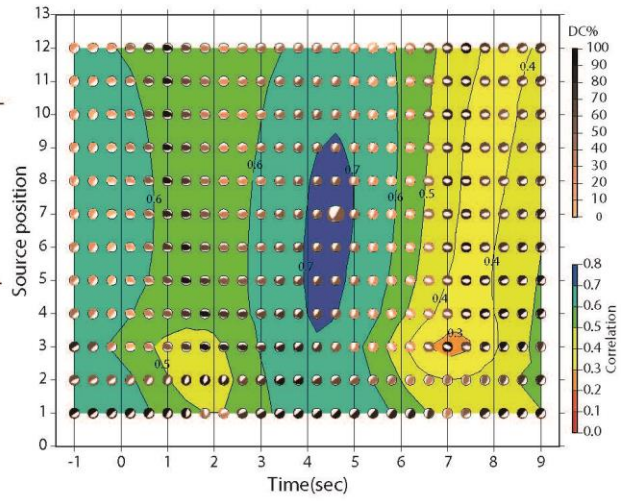
Origin time 20140110 13:20:46.44  
 Lat 37.3065 Lon 36.2035 Depth 12.9

Moment (Nm) : 1.239e+15  
 Mw: 4.0  
 VOL%: 0  
 DC%: 51.8  
 CLVD%: 48.2  
 Var.red.: (for stations used in inversion): 0.51  
 Corr.%: 80

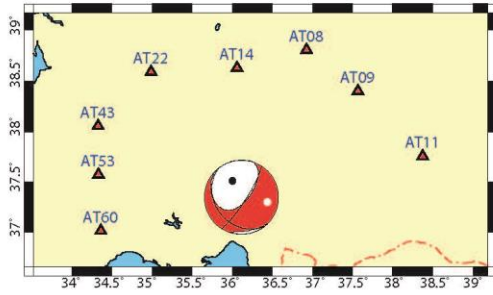
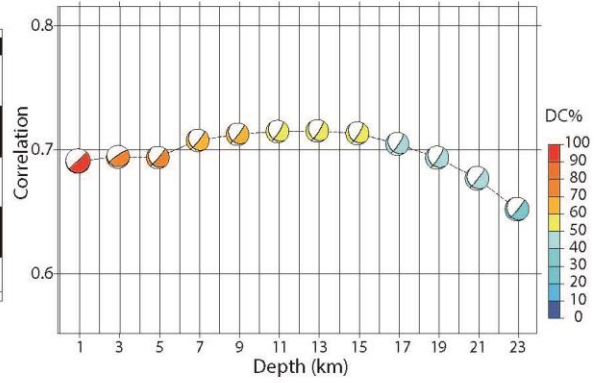
CN FMVAR STVAR  
 1.9 35±34 0.27

Strike Dip Rake Mrr Mtt Mpp  
 33 80 -63 -4.379 -2.327 6.706  
 Strike Dip Rake Mrt Mrp Mtp  
 142 29 -159 -7.989 -7.075 -2.199

P-axis Azimuth Plunge Exponent (Nm): 14  
 331 48  
 T-axis Azimuth Plunge  
 101 30

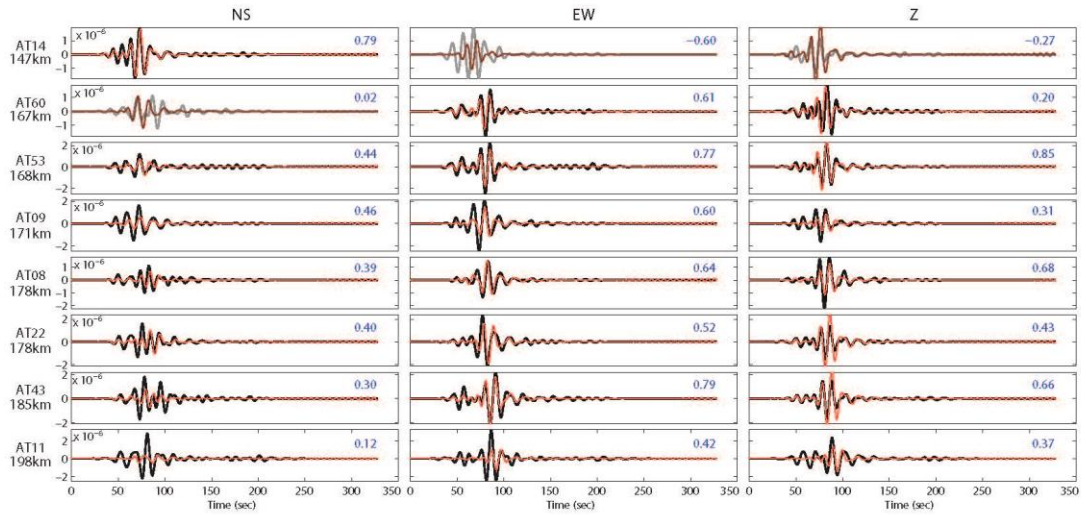


Correlation vs Depth Plot



Displacement (m). Inversion band (Hz) 0.06 – 0.12

— Observed  
 — Synthetic  
 Gray waveforms weren't used in inversion.  
 Blue numbers are variance reduction



**EVENT#12**

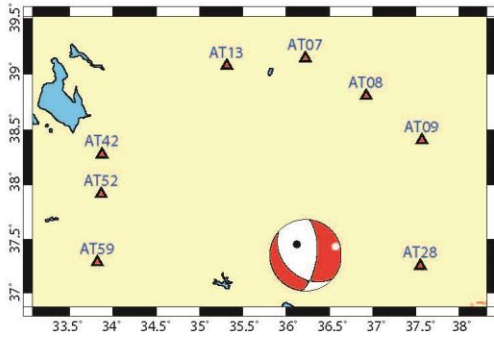
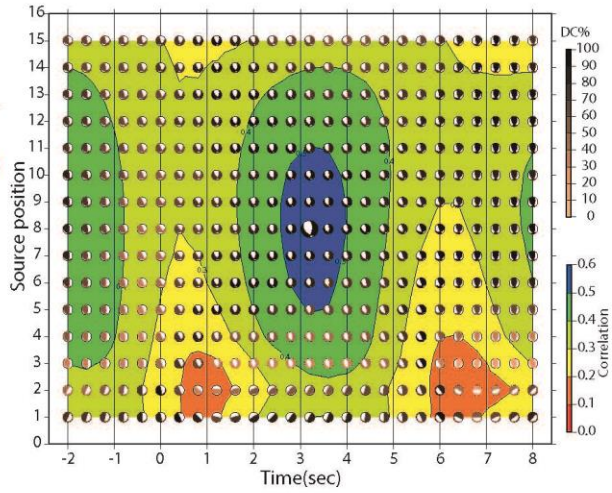
Origin time 20140207 04:48:08.80  
 Lat 37.3015 Lon 36.2037 Depth 14.9

Moment (Nm): 7.598e+14  
 Mw: 3.9  
 VOL%: 0  
 DC%: 99.1  
 CLVD%: 0.9  
 Var.red.: (for stations used in inversion): 0.28  
 Corr.%: 60

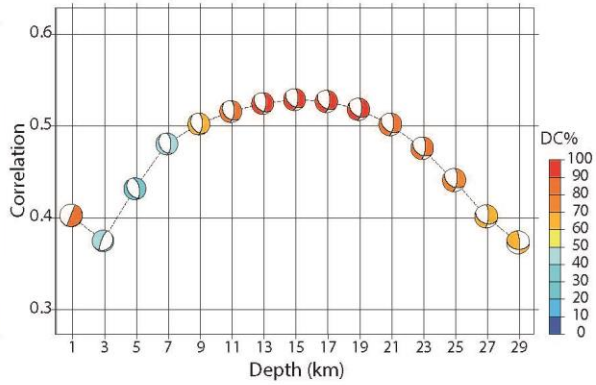
CN FMVAR STVAR  
 2.2 13±21 0.10

Strike Dip Rake Mrr Mtt Mpp  
 6 64 -59 -5.054 -0.666 5.720  
 Strike Dip Rake Mrt Mrp Mtp  
 131 39 -137 -2.063 -3.905 -2.979

P-axis Azimuth Plunge Exponent (Nm): 14  
 320 58  
 T-axis Azimuth Plunge  
 74 14

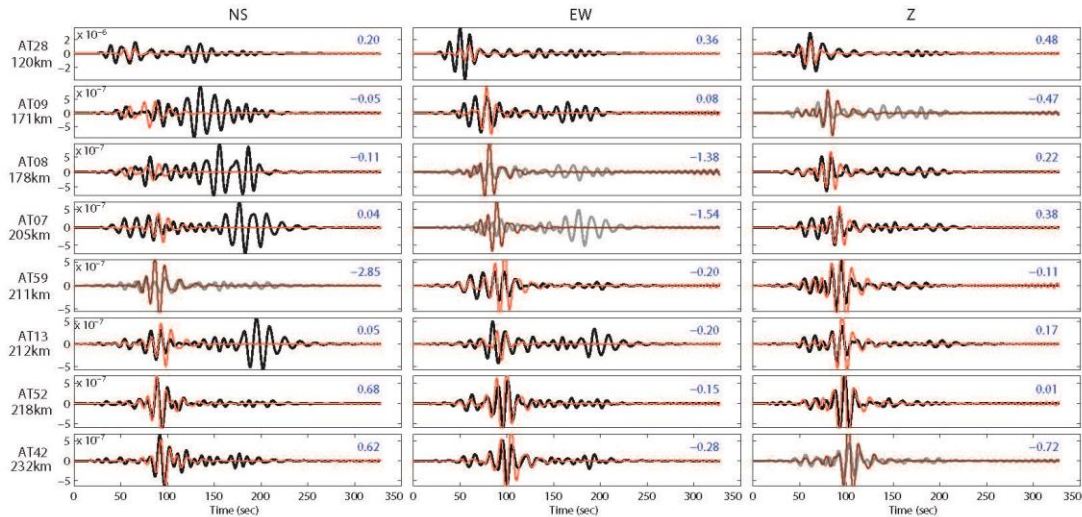


Correlation vs Depth Plot



Displacement (m). Inversion band (Hz) 0.06 - 0.12

— Observed  
 — Synthetic  
 Gray waveforms weren't used in inversion.  
 Blue numbers are variance reduction



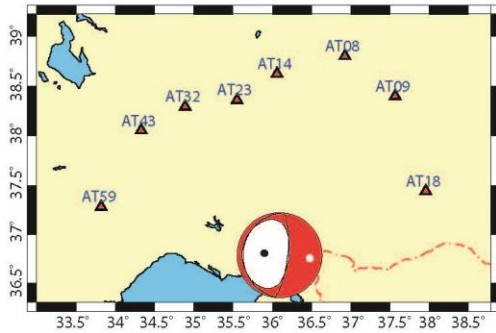
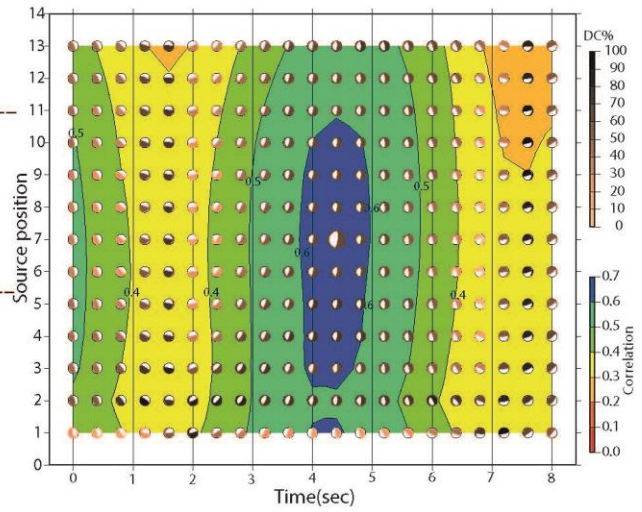
**EVENT#13**

Origin time 20140214 00:33:37.76  
 Lat 36.7218 Lon 36.0273 Depth 14.9

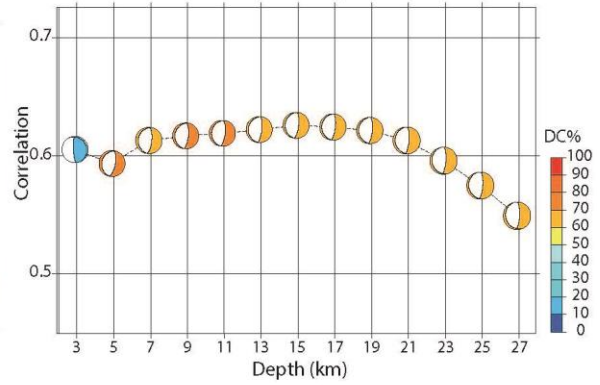
Moment (Nm) : 9.500e+15  
 Mw : 4.6  
 VOL% : 0  
 DC% : 68.1  
 CLVD% : 31.9  
 Var.red.: (for stations used in inversion): 0.39  
 Corr.% : 70

Strike Dip Rake Mrr Mtt Mpp  
 6 75 -90 -5.628 1.665 3.964  
 Strike Dip Rake Mrt Mrp Mtp  
 187 15 -89 -0.856 -8.021 0.297

P-axis Azimuth Plunge Exponent (Nm): 15  
 276 60  
 T-axis Azimuth Plunge  
 96 30

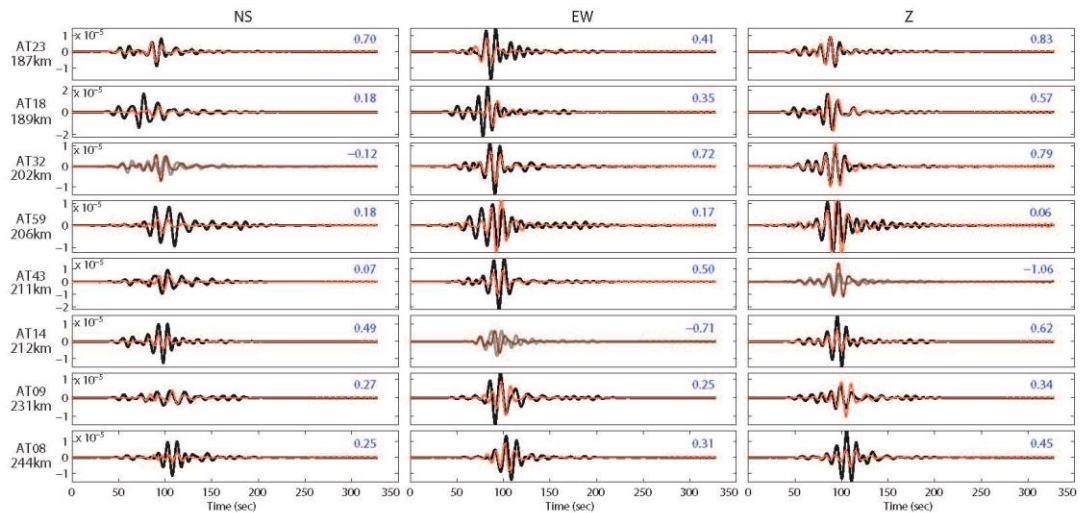


Correlation vs Depth Plot



Displacement (m). Inversion band (Hz) 0.06 – 0.12

— Observed  
 — Synthetic  
 Gray waveforms weren't used in inversion.  
 Blue numbers are variance reduction



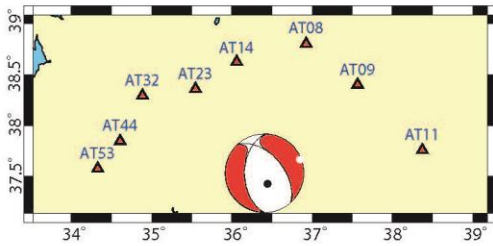
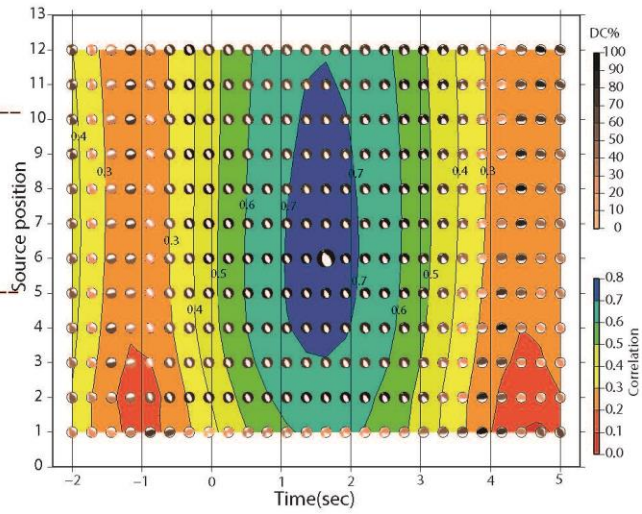
**EVENT#14**

Origin time 20140222 15:42:06.62  
 Lat 37.4095 Lon 36.3998 Depth 8.9

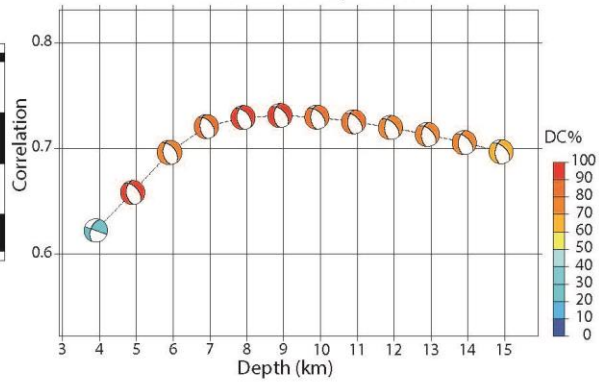
Moment (Nm): 2.732e+15  
 Mw: 4.2 CN FMVAR STVAR  
 VOL%: 0 1.8 9±7 0.20  
 DC%: 90.9  
 CLVD%: 9.1  
 Var.red.: (for stations used in inversion): 0.53  
 Corr.%: 80

Strike Dip Rake Mrr Mtt Mpp  
 318 51 -120 -2.277 -0.105 2.382  
 Strike Dip Rake Mrt Mrp Mtp  
 181 47 -58 0.918 0.135 -1.080

P-axis Azimuth Plunge Exponent (Nm): 15  
 164 67  
 T-axis Azimuth Plunge  
 69 2

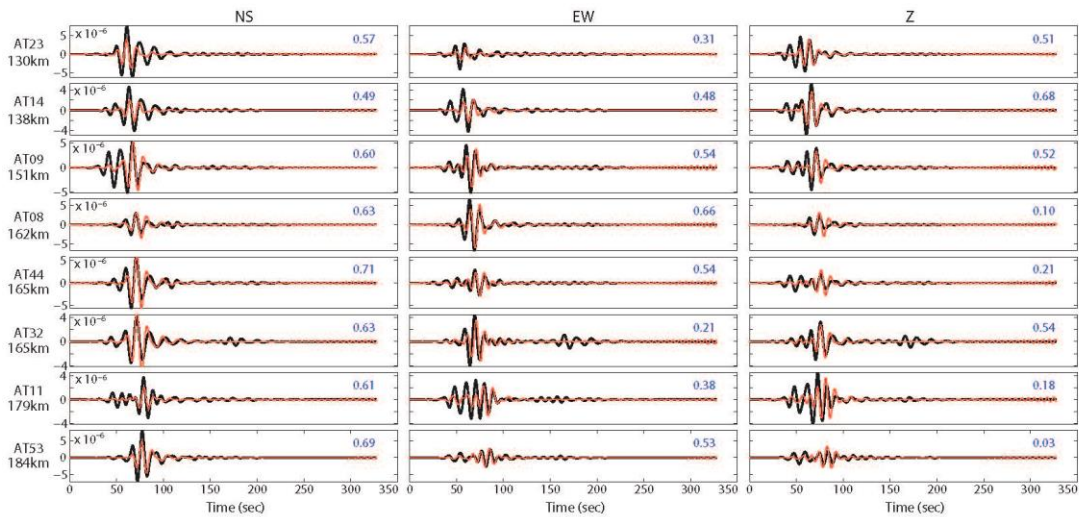


Correlation vs Depth Plot



Displacement (m). Inversion band (Hz) 0.06 - 0.12

— Observed  
 — Synthetic  
 Gray waveforms weren't used in inversion.  
 Blue numbers are variance reduction



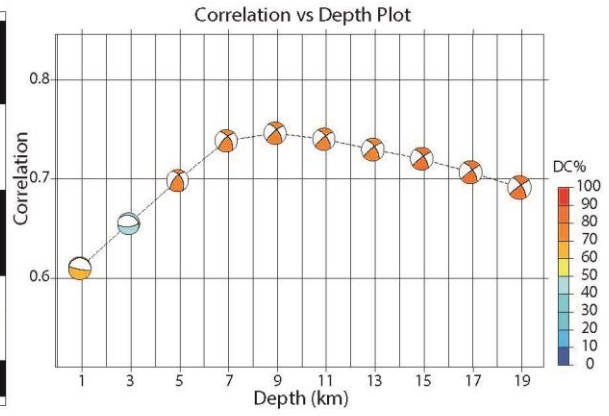
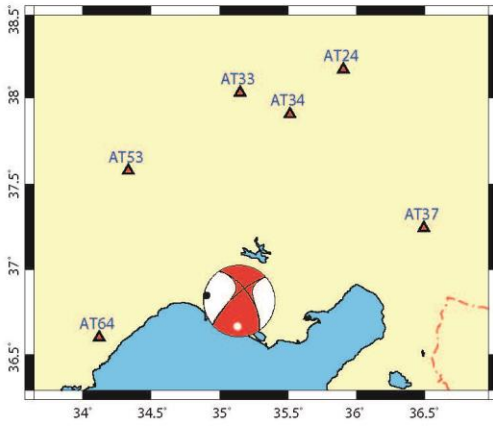
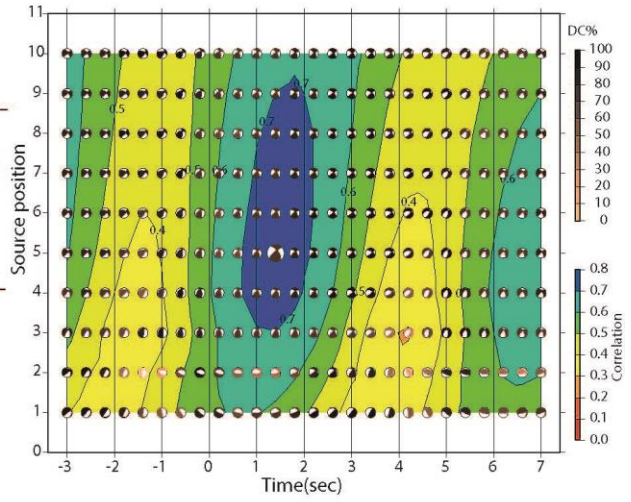
**EVENT#15**

Origin time 20140302 04:29:09.38  
 Lat 36.776 Lon 35.1588 Depth 8.9

Moment (Nm) : 7.245e+14  
 Mw : 3.8  
 VOL% : 0  
 DC% : 78.1  
 CLVD% : 21.9  
 Var.red.: (for stations used in inversion): 0.56  
 Corr.% : 80

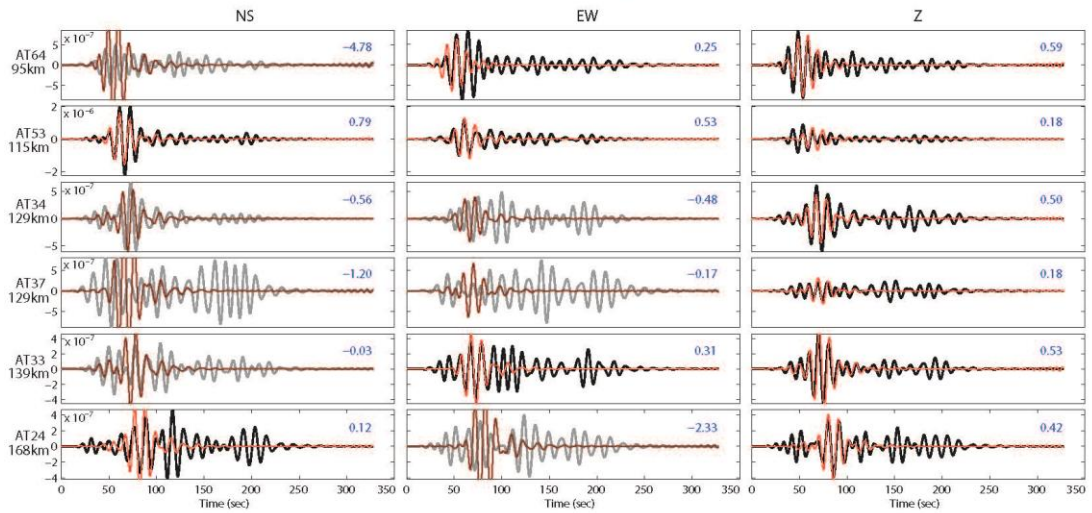
CN FMVAR STVAR  
 3.4 51±32 0.18  
 Mrr Mtt Mpp  
 2.046 5.209 -7.256  
 Mrt Mrp Mtp  
 -2.671 -0.950 -1.569

Strike Dip Rake  
 325 64 16  
 228 76 153  
 P-axis Azimuth Plunge  
 279 8  
 T-axis Azimuth Plunge  
 184 29  
 Exponent (Nm): 14



Displacement (m). Inversion band (Hz) 0.07 – 0.11

— Observed  
 — Synthetic  
 Gray waveforms weren't used in inversion.  
 Blue numbers are variance reduction



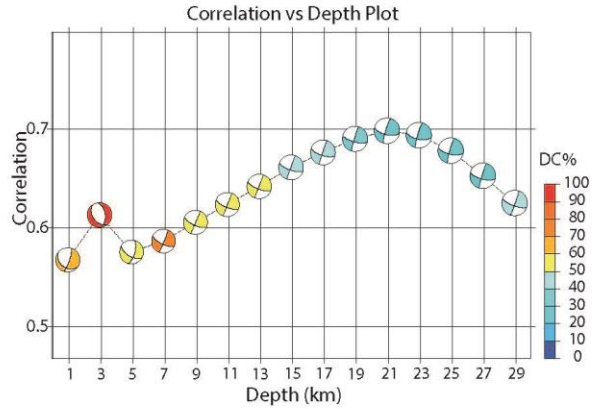
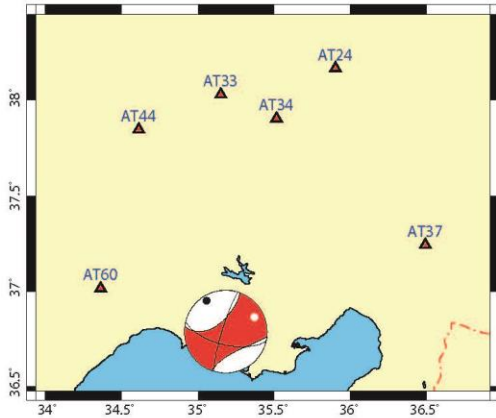
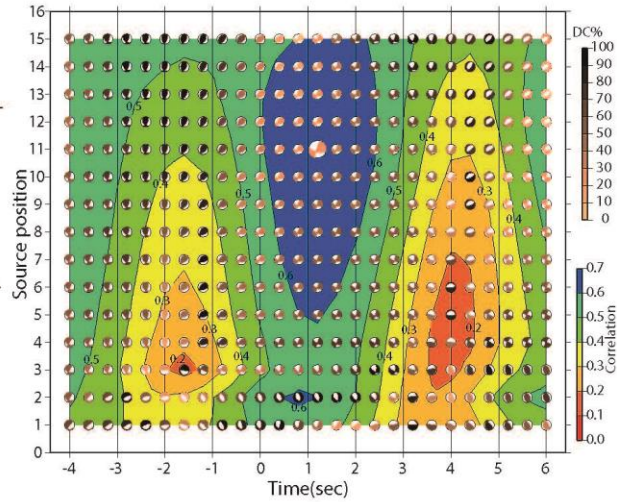
**EVENT#16**

Origin time 20140302 04:25:57.84  
 Lat 36.7573 Lon 35.1748 Depth 20.9

Moment (Nm): 6.279e+15  
 Mw: 4.5  
 VOL%: 0  
 DC%: 29.2  
 CLVD%: 70.8  
 Var.red.: (for stations used in inversion): 0.49  
 Corr.%: 70

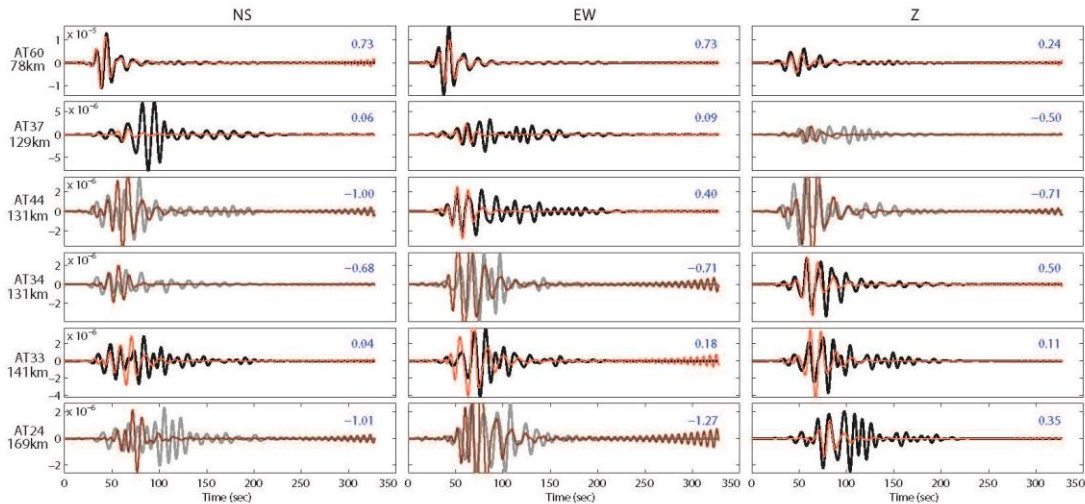
Strike Dip Rake Mrr Mtt Mpp  
 103 64 172 2.413 -3.682 1.270  
 Strike Dip Rake Mrt Mrp Mtp  
 197 82 26 -1.386 -1.787 -4.880

P-axis Azimuth Plunge Exponent (Nm): 15  
 328 13  
 T-axis Azimuth Plunge  
 63 24



Displacement (m). Inversion band (Hz) 0.06 - 0.12

— Observed  
 — Synthetic  
 Gray waveforms weren't used in inversion.  
 Blue numbers are variance reduction



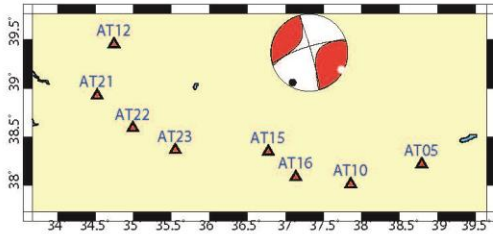
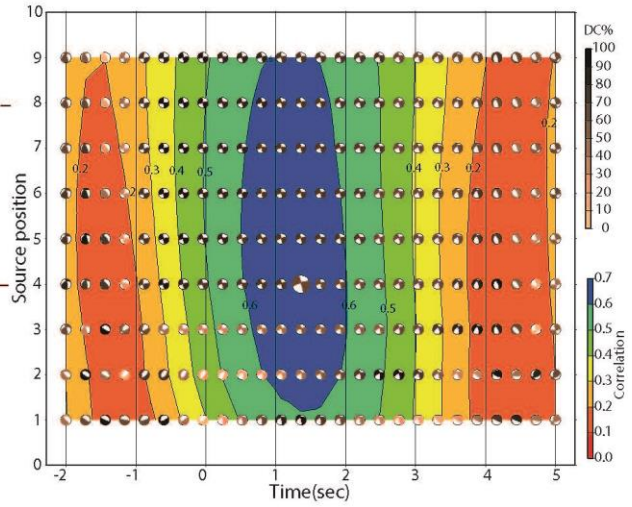
**EVENT#17**

Origin time 20140501 07:36:08.75  
 Lat 39.473 Lon 37.3525 Depth 6.9

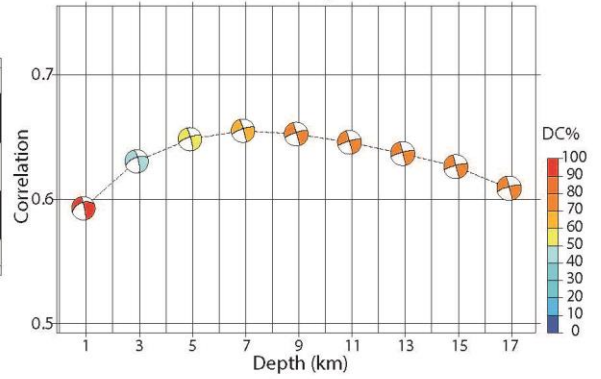
Moment (Nm) : 2.002e+15  
 Mw: 4.1  
 VOL%: 0  
 DC%: 69.7  
 CLVD%: 30.3  
 Var.red.: (for stations used in inversion): 0.43  
 Corr.%: 70

Strike Dip Rake Mrr Mtt Mpp  
 344 86 -167 -0.360 -0.894 1.254  
 Strike Dip Rake Mrt Mrp Mtp  
 253 77 -4 0.143 -0.396 1.606

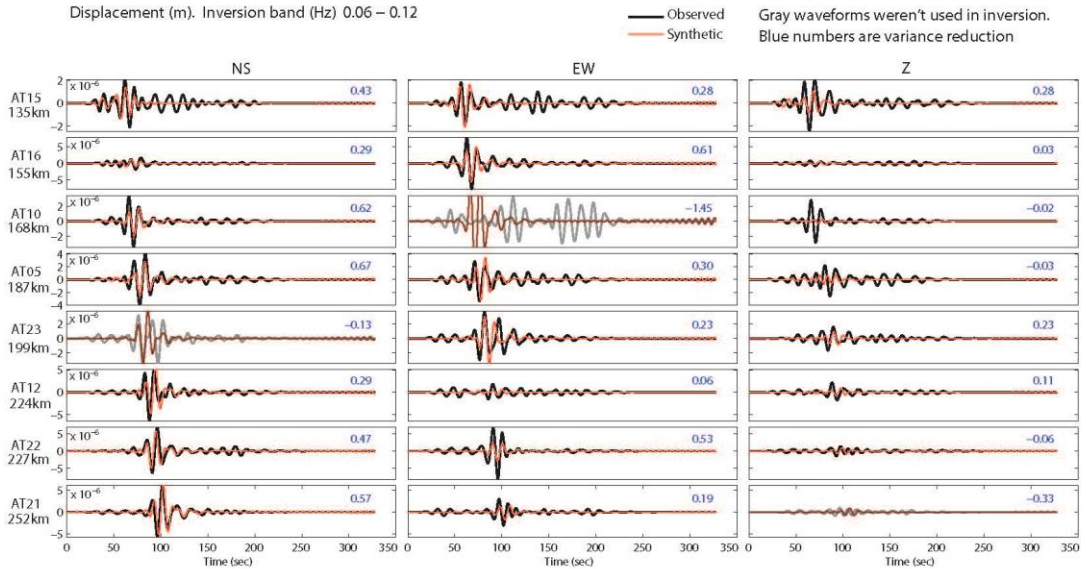
P-axis Azimuth Plunge Exponent (Nm): 15  
 209 12  
 T-axis Azimuth Plunge  
 118 6



Correlation vs Depth Plot



Displacement (m). Inversion band (Hz) 0.06 – 0.12



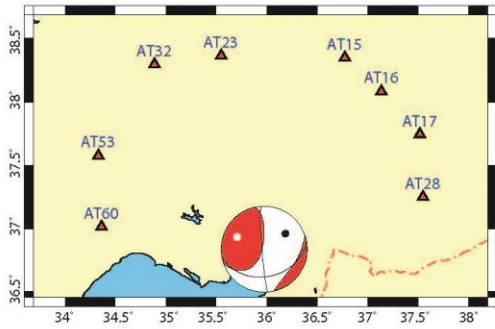
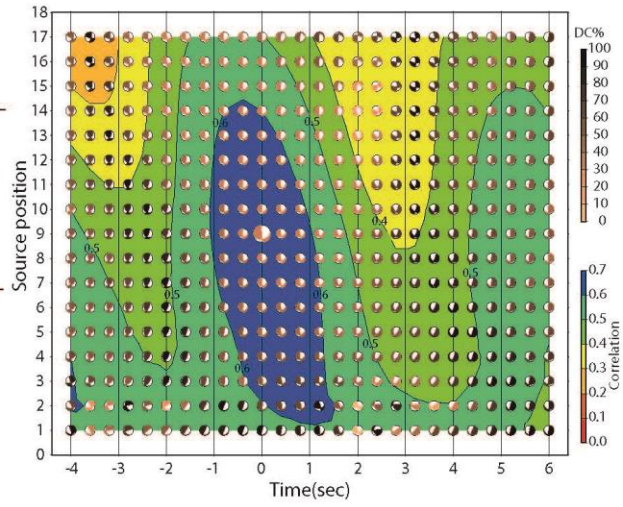
**EVENT#18**

Origin time 20140609 03:38:35.00  
 Lat 36.7702 Lon 36.0077 Depth 16.9

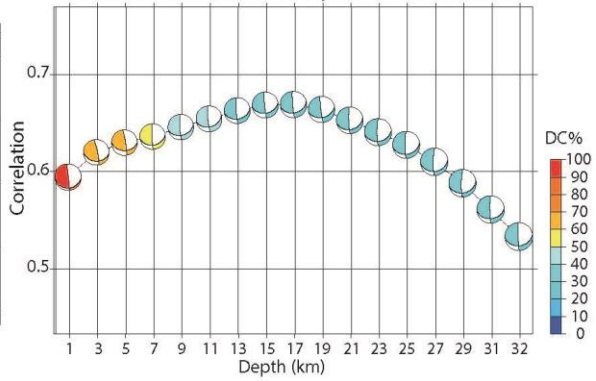
Moment (Nm): 1.077e+16  
 Mw: 4.6  
 VOL%: 0  
 DC%: 35.4  
 CLVD%: 64.6  
 Var.red.: (for stations used in inversion): 0.45  
 Corr.%: 70

Strike Dip Rake Mrr Mtt Mpp  
 176 85 -125 -1.410 -2.817 4.227  
 Strike Dip Rake Mrt Mrp Mtp  
 79 36 -8 1.687 8.188 5.684

P-axis Azimuth Plunge Exponent (Nm): 15  
 54 39  
 T-axis Azimuth Plunge  
 294 31

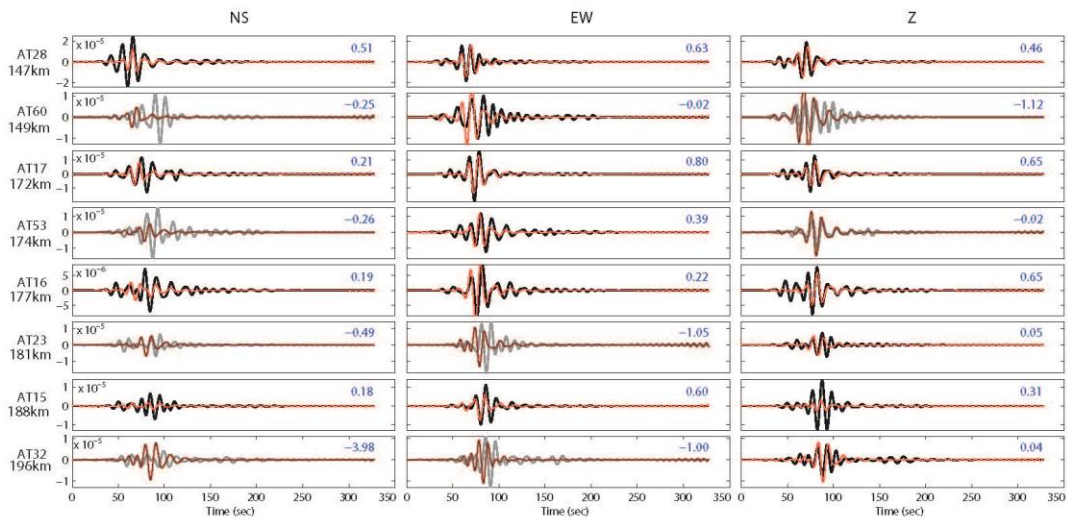


Correlation vs Depth Plot



Displacement (m). Inversion band (Hz) 0.06 - 0.12

— Observed  
 — Synthetic  
 Gray waveforms weren't used in inversion.  
 Blue numbers are variance reduction



**EVENT#19**

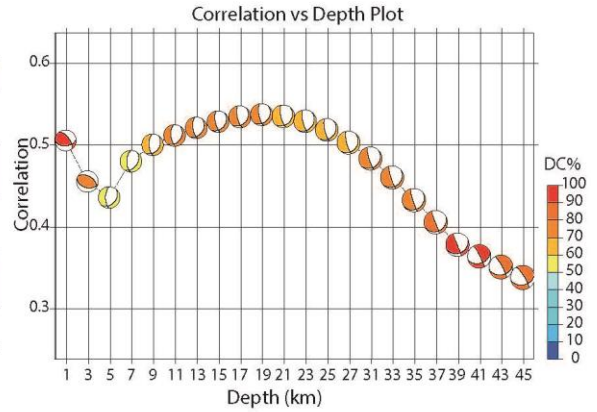
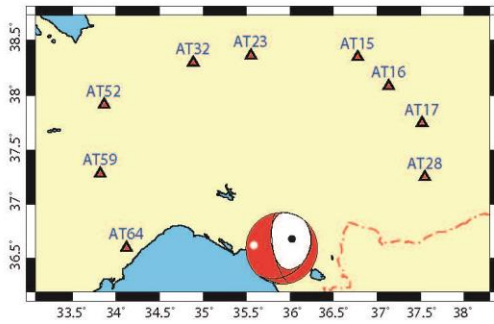
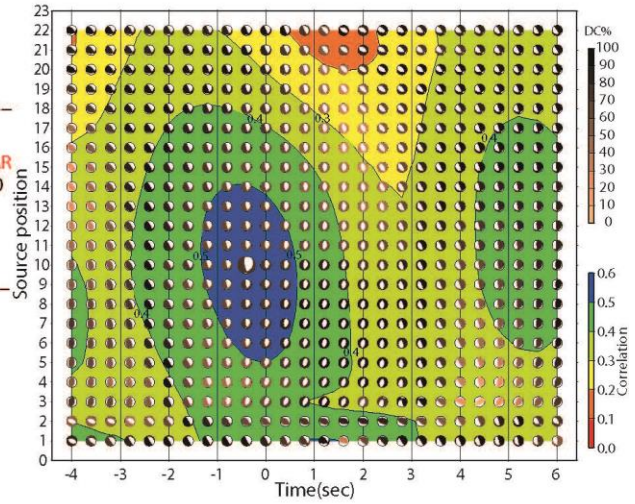
Origin time 20140712 21:58:22.33  
 Lat 36.5533 Lon 35.901 Depth 18.9

Moment (Nm) : 8.082e+14  
 VOL% : 0  
 DC% : 71.8  
 CLVD% : 28.2  
 Var.red.: (for stations used in inversion): 0.29  
 Corr.% : 60

CN FMVAR STVAR  
 1.9 14±18 0.10

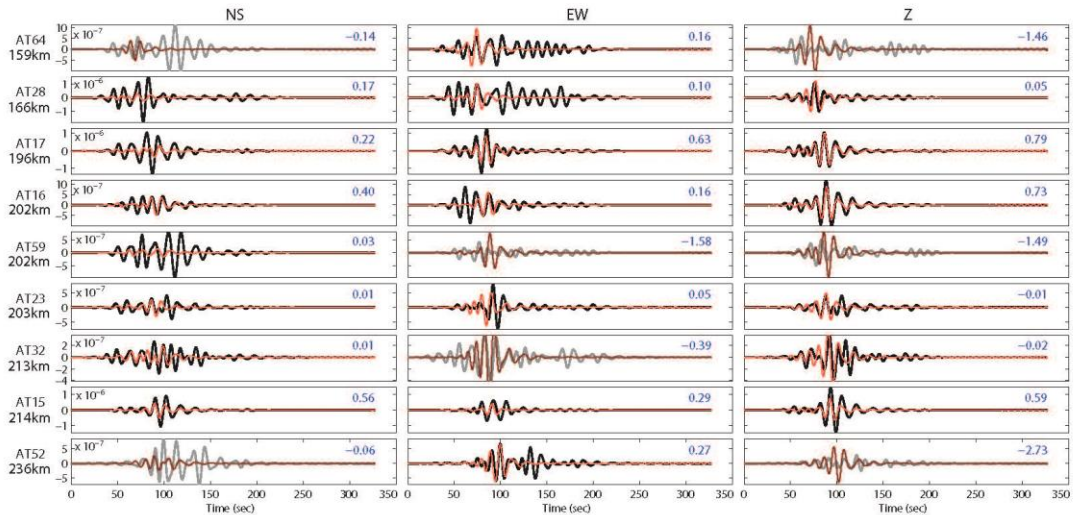
Strike Dip Rake Mrr Mtt Mpp  
 39 30 -44 -5.201 0.142 5.059  
 Strike Dip Rake Mrt Mrp Mtp  
 170 70 -112 -2.643 5.343 1.859

P-axis Azimuth Plunge Exponent (Nm): 14  
 48 59  
 T-axis Azimuth Plunge  
 276 22



Displacement (m). Inversion band (Hz) 0.06 - 0.12

— Observed  
 — Synthetic  
 Gray waveforms weren't used in inversion.  
 Blue numbers are variance reduction



**EVENT#20**

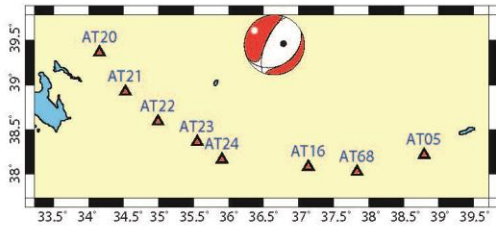
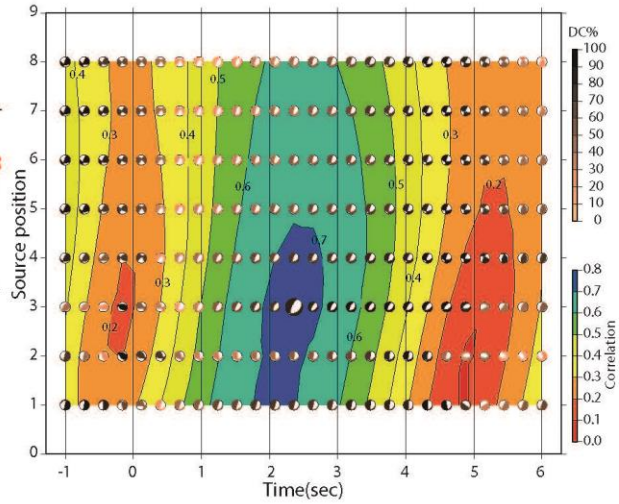
Origin time 20140811 04:22:43.97  
 Lat 39.4825 Lon 36.681 Depth 4.9

Moment (Nm): 5.681e+14  
 Mw: 3.8  
 VOL%: 0  
 DC%: 83.0  
 CLVD%: 17.0  
 Var.red.: (for stations used in inversion): 0.53  
 Corr.%: 80

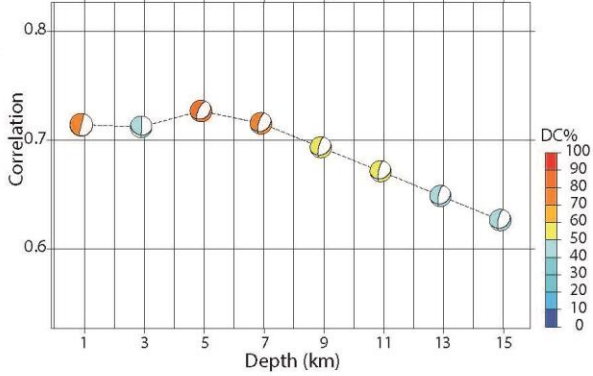
CN FMVAR STVAR  
 2.7 16±12 0.13

Strike Dip Rake Mrr Mtt Mpp  
 60 30 -56 -3.848 1.427 2.420  
 Strike Dip Rake Mrt Mrp Mtp  
 203 66 -107 0.910 3.478 2.829

P-axis Azimuth Plunge Exponent (Nm): 14  
 83 65  
 T-axis Azimuth Plunge  
 306 19

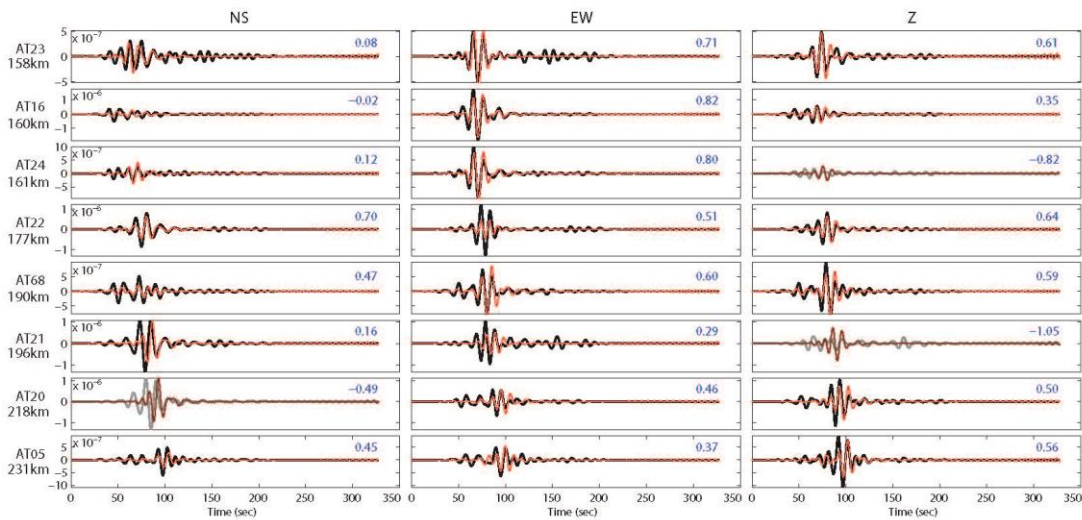


Correlation vs Depth Plot



Displacement (m). Inversion band (Hz) 0.06 – 0.12

— Observed  
 — Synthetic  
 Gray waveforms weren't used in inversion.  
 Blue numbers are variance reduction



**EVENT#21**

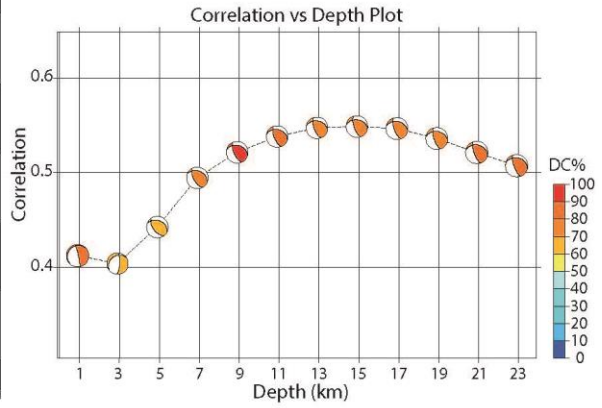
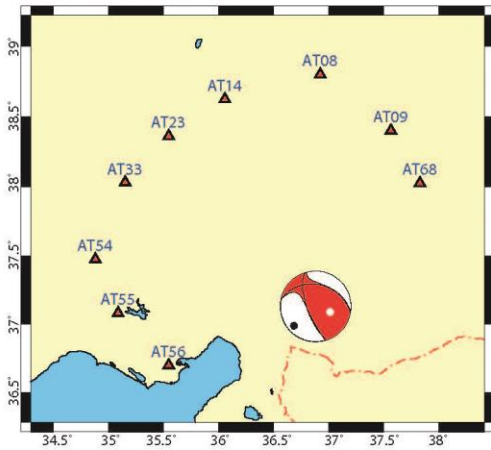
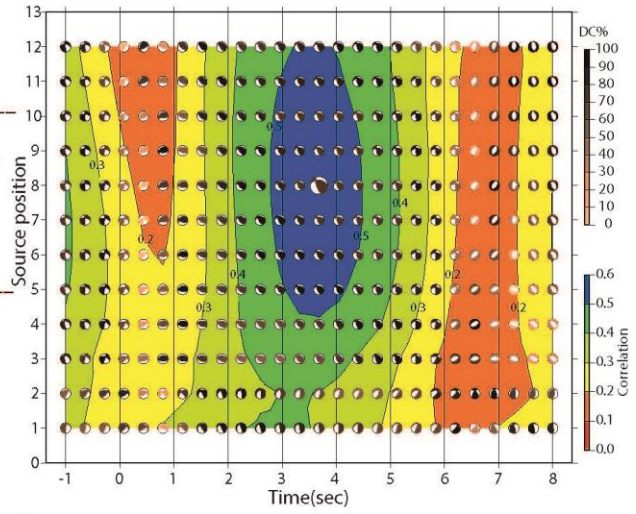
Origin time 20140828 10:22:00.79  
 Lat 37.113 Lon 36.8968 Depth 14.9

Moment (Nm) : 6.307e+14  
 VOL%: 0  
 DC%: 74.6  
 CLVD%: 25.4  
 Var.red.: (for stations used in inversion): 0.30  
 Corr.%: 60

CN FMVAR STVAR  
 2.2 6±3 0.12

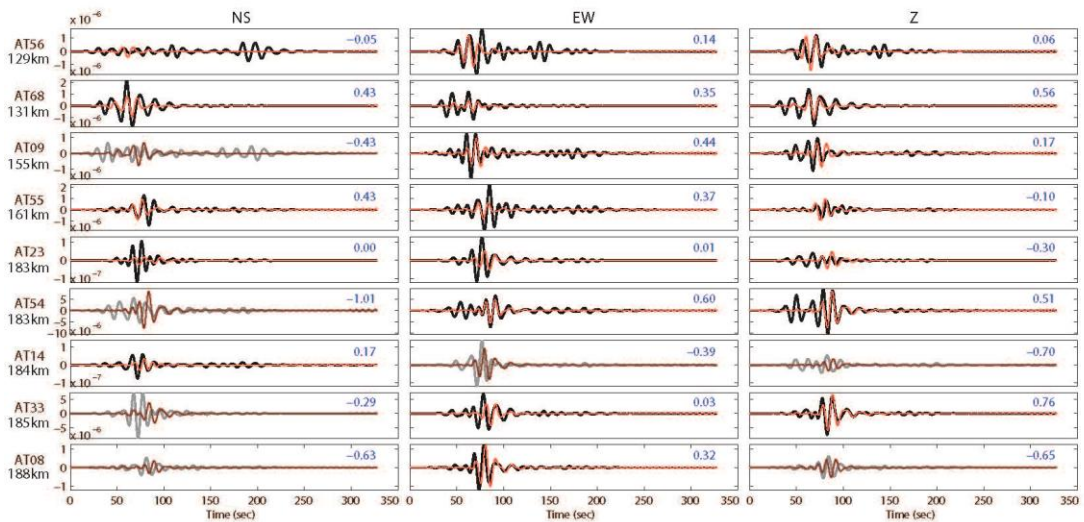
Strike Dip Rake Mrr Mtt Mpp  
 161 69 122 3.427 -2.053 -1.374  
 Strike Dip Rake Mrt Mrp Mtp  
 280 37 36 0.670 -3.847 3.950

P-axis Azimuth Plunge Exponent (Nm): 14  
 228 18  
 T-axis Azimuth Plunge  
 111 54



Displacement (m). Inversion band (Hz) 0.06 – 0.12

— Observed  
 — Synthetic  
 Gray waveforms weren't used in inversion.  
 Blue numbers are variance reduction



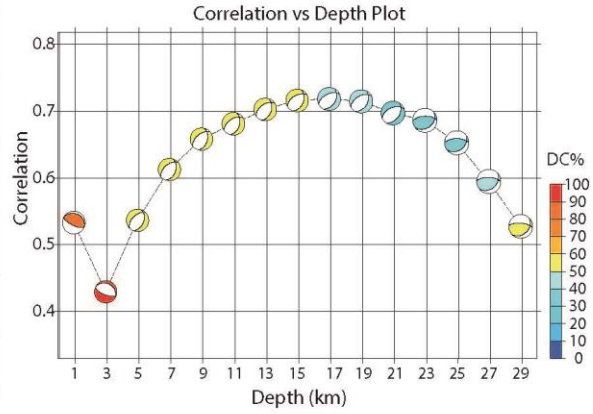
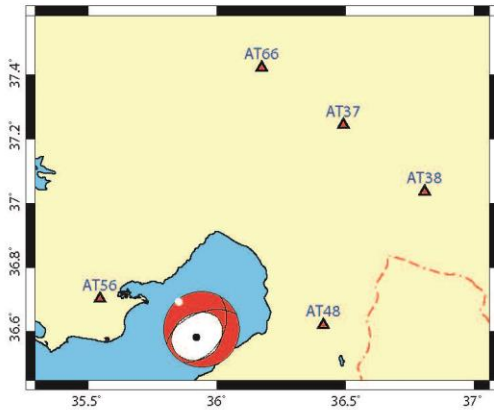
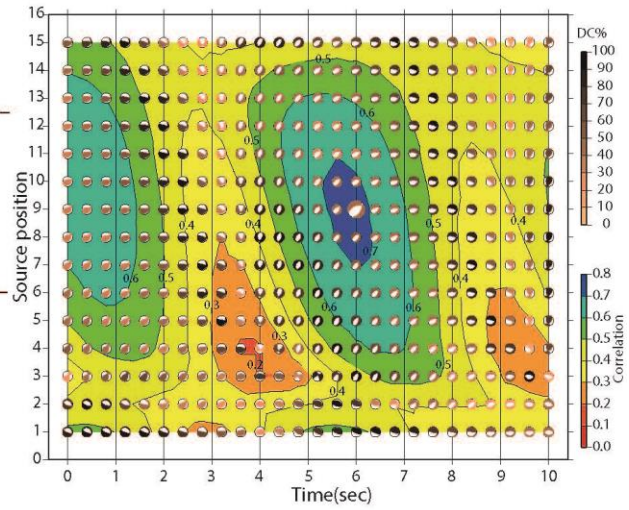
**EVENT#22**

Origin time 20140903 03:15:29.00  
 Lat 36.6083 Lon 35.928 Depth 16.9

Moment (Nm): 1.257e+15  
 Mw: 4.1  
 VOL%: 0  
 DC%: 44.0  
 CLVD%: 56.0  
 Var.red.: (for stations used in inversion): 0.52  
 Corr.%: 80

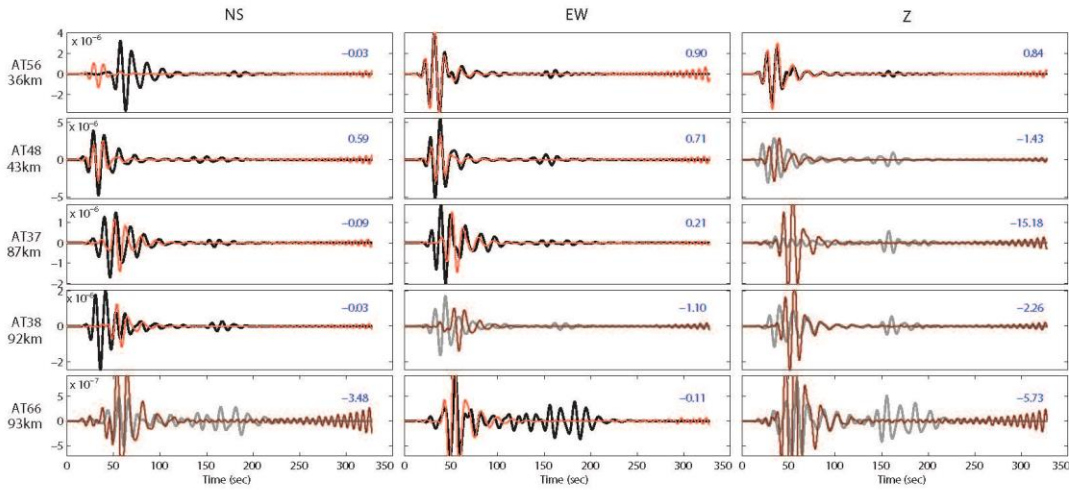
Strike Dip Rake Mrr Mtt Mpp  
 29 42 -120 -1.431 0.715 0.716  
 Strike Dip Rake Mrt Mrp Mtp  
 246 54 -66 0.674 -0.326 0.488

P-axis Azimuth Plunge Exponent (Nm): 15  
 212 69  
 T-axis Azimuth Plunge  
 320 6



Displacement (m). Inversion band (Hz) 0.06 – 0.12

— Observed  
 — Synthetic  
 Gray waveforms weren't used in inversion.  
 Blue numbers are variance reduction



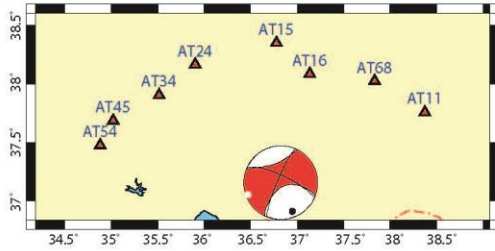
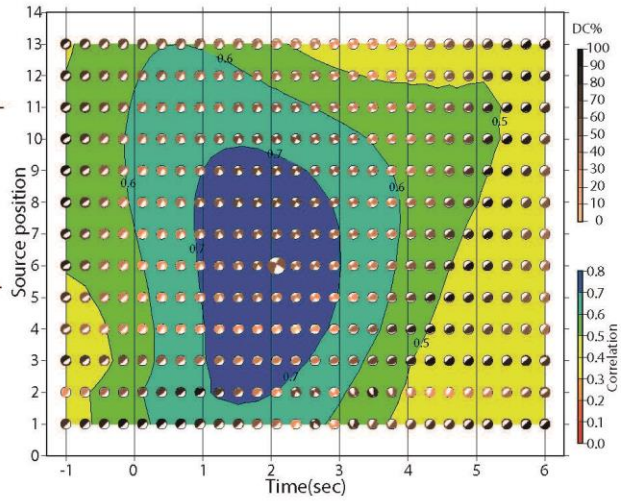
**EVENT#23**

Origin time 20150108 18:44:46.00  
 Lat 37.0822 Lon 36.8465 Depth 10.9

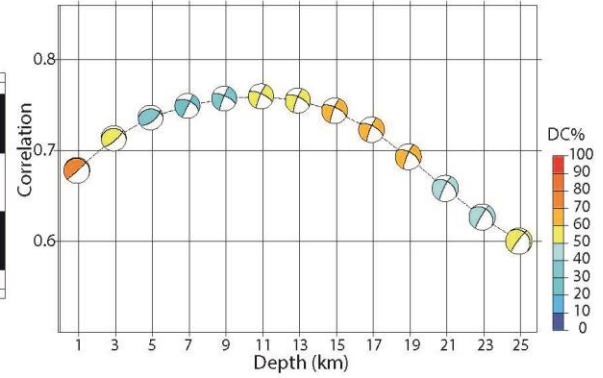
Moment (Nm) : 4.977e+15  
 Mw : 4.4  
 VOL% : 0  
 DC% : 50.4  
 CLVD% : 49.6  
 Var.red.: (for stations used in inversion): 0.58  
 Corr.% : 80

Strike Dip Rake Mrr Mtt Mpp  
 295 74 -171 0.775 -3.686 2.910  
 Strike Dip Rake Mrt Mrp Mtp  
 203 82 -16 1.736 0.982 -3.077

P-axis Azimuth Plunge Exponent (Nm): 15  
 158 17  
 T-axis Azimuth Plunge  
 250 5

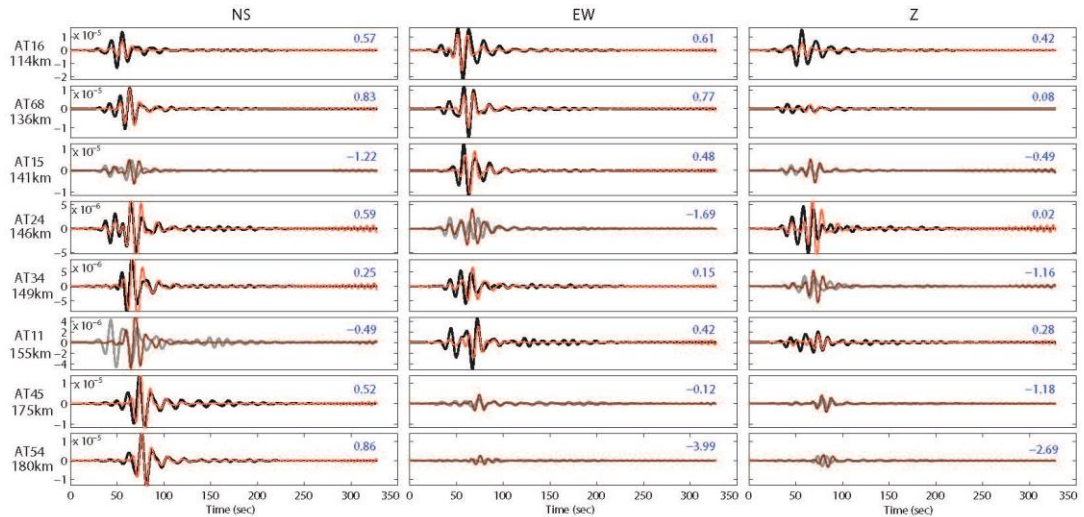


Correlation vs Depth Plot



Displacement (m). Inversion band (Hz) 0.06 - 0.12

— Observed  
 — Synthetic  
 Gray waveforms weren't used in inversion.  
 Blue numbers are variance reduction



**EVENT#24**

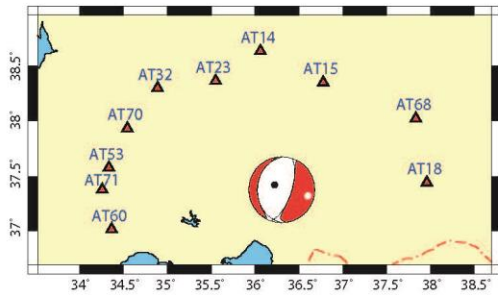
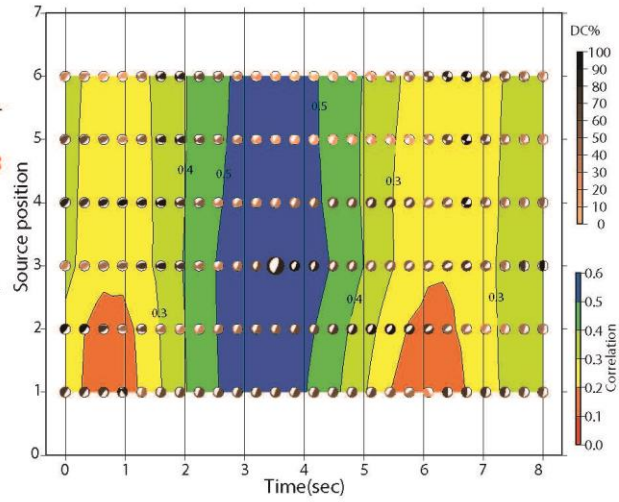
Origin time 20150122 19:27:45.64  
 Lat 37.3995 Lon 36.3053 Depth 4.9

Moment (Nm): 1.032e+15

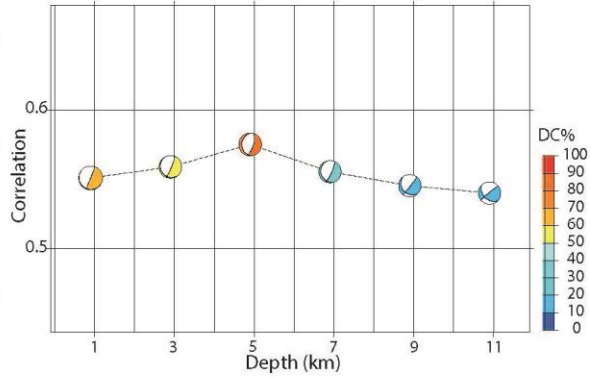
Mw: 3.9  
 VOL%: 0  
 DC%: 87.9  
 CLVD%: 12.1  
 Var.red.: (for stations used in inversion): 0.33  
 Corr.%: 60

Strike Dip Rake Mrr Mtt Mpp  
 19 65 -83 -7.410 -0.495 7.906  
 Strike Dip Rake Mrt Mrp Mtp  
 182 26 -105 -2.531 -6.207 1.627

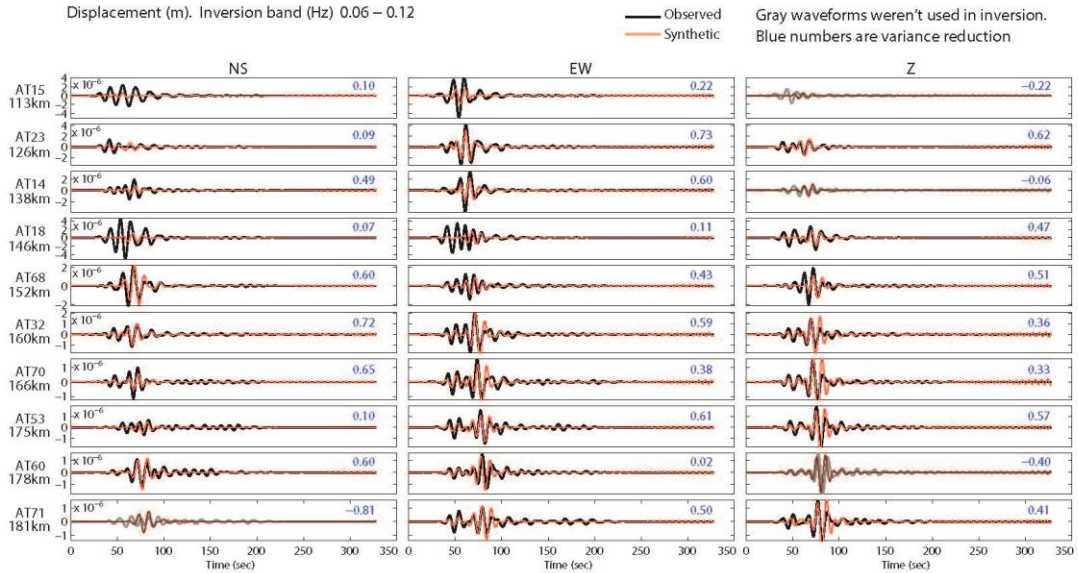
P-axis Azimuth Plunge Exponent (Nm): 14  
 303 69  
 T-axis Azimuth Plunge  
 103 20



Correlation vs Depth Plot



Displacement (m). Inversion band (Hz) 0.06 – 0.12



— Observed  
 — Synthetic  
 Gray waveforms weren't used in inversion.  
 Blue numbers are variance reduction

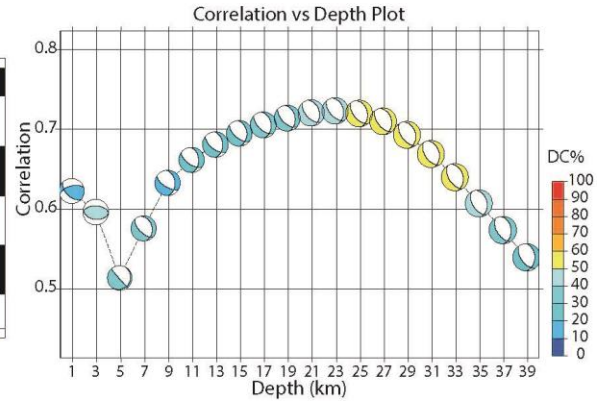
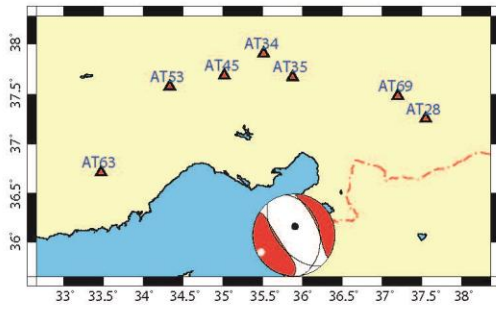
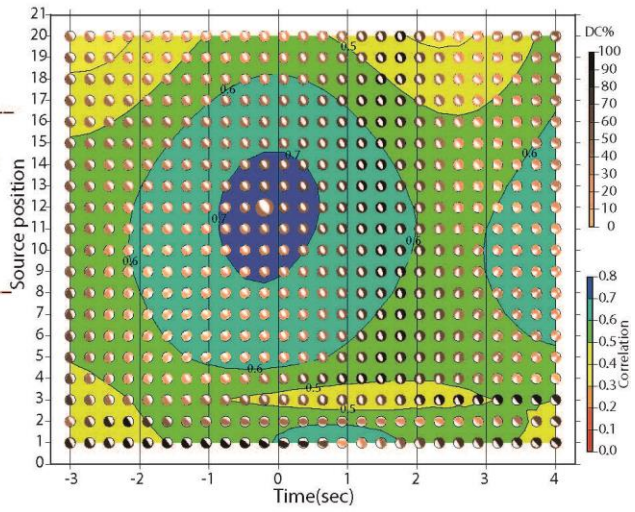
**EVENT#25**

Origin time 20150210 04:01:54.41  
 Lat 36.0278 Lon 35.975 Depth 22.9

Moment (Nm) : 1.214e+16  
 VOL% : 0  
 DC% : 47.0  
 CLVD% : 53.0  
 Var.red.: (for stations used in inversion): 0.52  
 Corr.% : 80

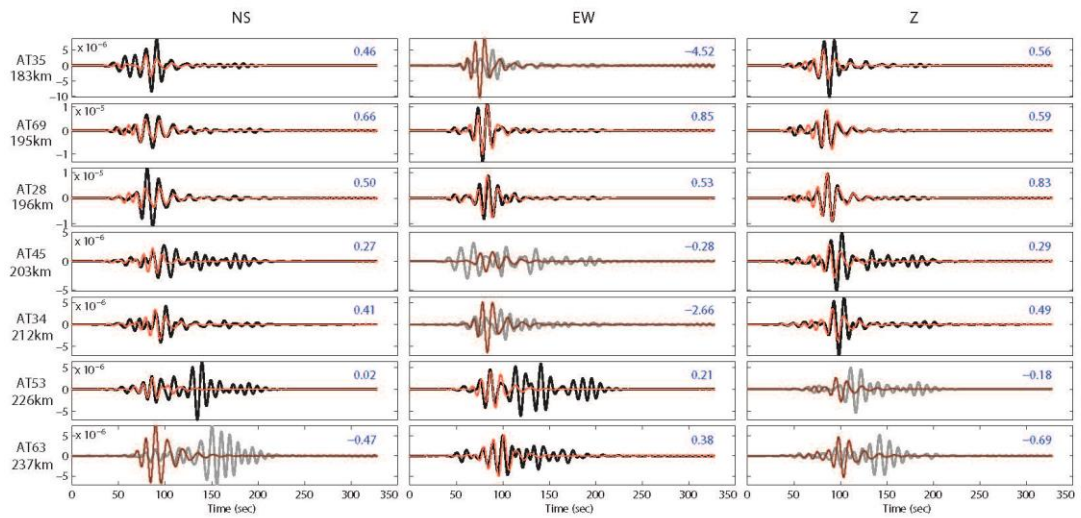
Strike Dip Rake Mrr Mtt Mpp  
 348 37 -67 -8.948 -0.340 9.289  
 Strike Dip Rake Mrt Mrp Mtp  
 140 56 -106 -3.066 2.654 -6.908

P-axis Azimuth Plunge Exponent (Nm): 15  
 6 73  
 T-axis Azimuth Plunge  
 242 10



Displacement (m). Inversion band (Hz) 0.06 - 0.12

— Observed  
 — Synthetic  
 Gray waveforms weren't used in inversion.  
 Blue numbers are variance reduction



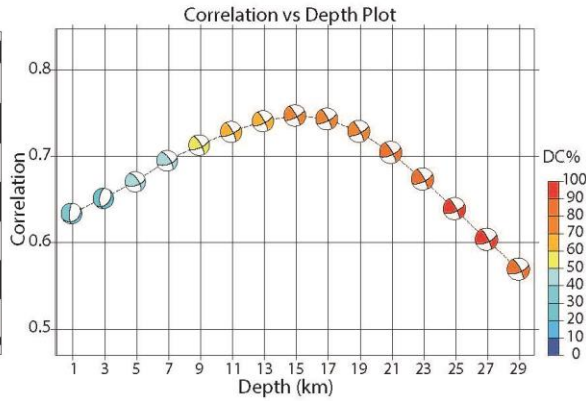
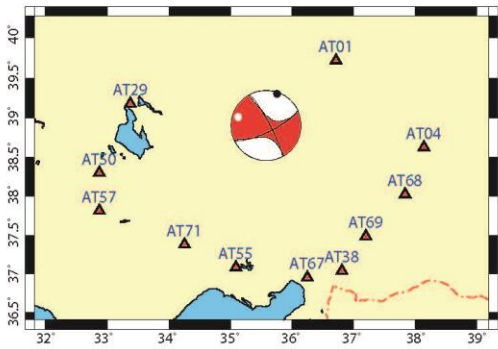
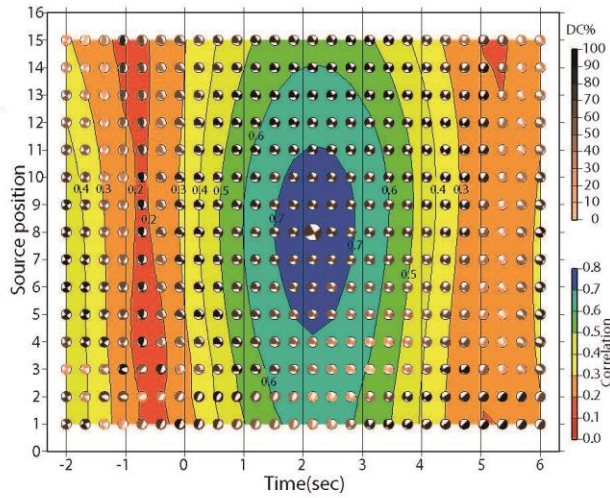
**EVENT#26**

Origin time 20150326 02:23:06.36  
 Lat 38.8912 Lon 35.607 Depth 14.9

Moment (Nm): 5.972e+14  
 Mw: 3.8  
 VOL%: 0 CN FMVAR STVAR  
 DC%: 70.8 1.6 6±6 0.10  
 CLVD%: 29.2  
 Var.red.: (for stations used in inversion): 0.56  
 Corr.%: 80

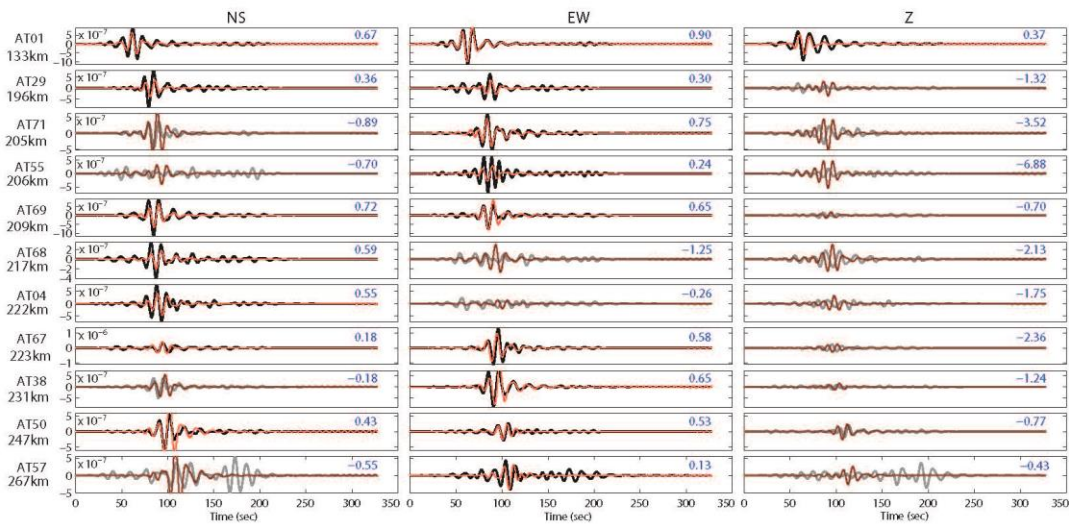
Strike Dip Rake Mrr Mtt Mpp  
 332 82 165 1.243 -5.211 3.968  
 Strike Dip Rake Mrt Mrp Mtp  
 64 75 8 -0.230 1.382 3.388

P-axis Azimuth Plunge Exponent (Nm): 14  
 19 5  
 T-axis Azimuth Plunge  
 287 17



Displacement (m). Inversion band (Hz) 0.06 – 0.12

— Observed  
 — Synthetic  
 Gray waveforms weren't used in inversion.  
 Blue numbers are variance reduction



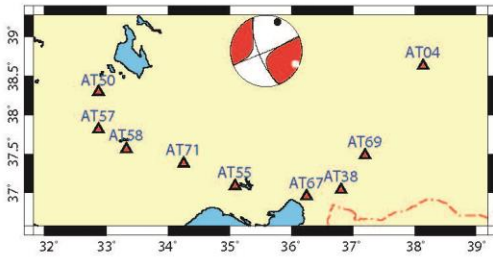
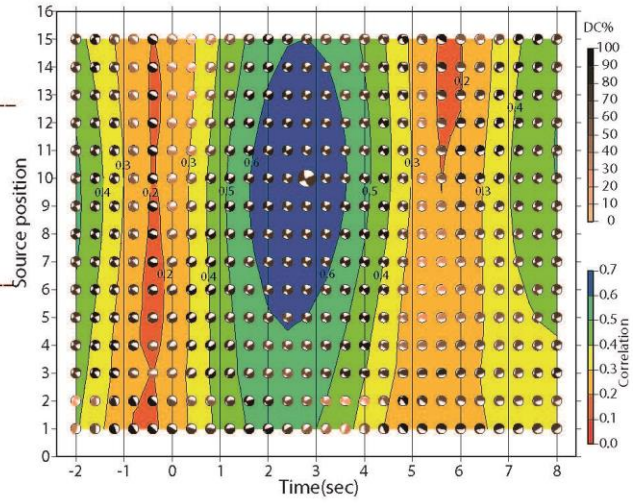
**EVENT#27**

Origin time 20150326 02:14:31.43  
 Lat 38.8892 Lon 35.5953 Depth 18.9

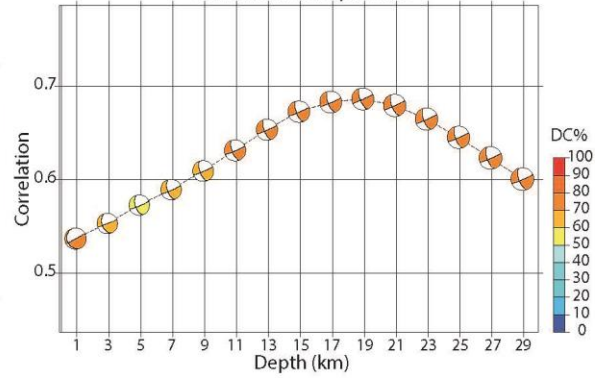
Moment (Nm) : 7.556e+14  
 VOL% : 0  
 DC% : 76.8  
 CLVD% : 23.2  
 Var.red.: (for stations used in inversion): 0.47  
 Corr.% : 70

Strike Dip Rake Mrr Mtt Mpp  
 158 72 -178 -0.945 -4.548 5.493  
 Strike Dip Rake Mrt Mrp Mtp  
 67 88 -18 -2.061 -1.061 5.084

P-axis Azimuth Plunge Exponent (Nm): 14  
 21 14  
 T-axis Azimuth Plunge  
 114 11

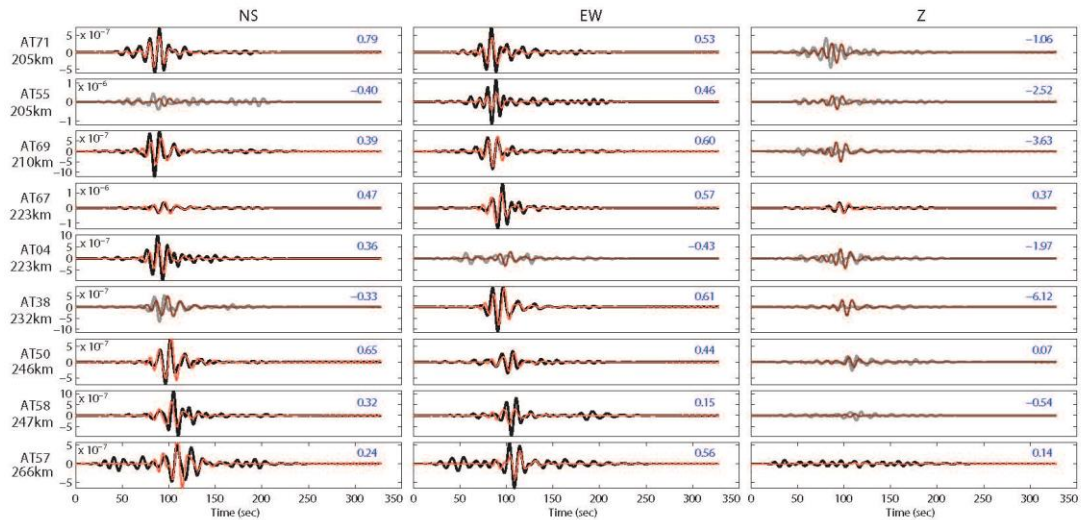


Correlation vs Depth Plot



Displacement (m). Inversion band (Hz) 0.06 - 0.12

— Observed  
 — Synthetic  
 Gray waveforms weren't used in inversion.  
 Blue numbers are variance reduction



**EVENT#28**

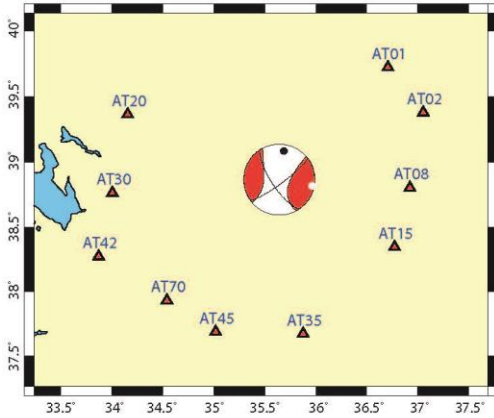
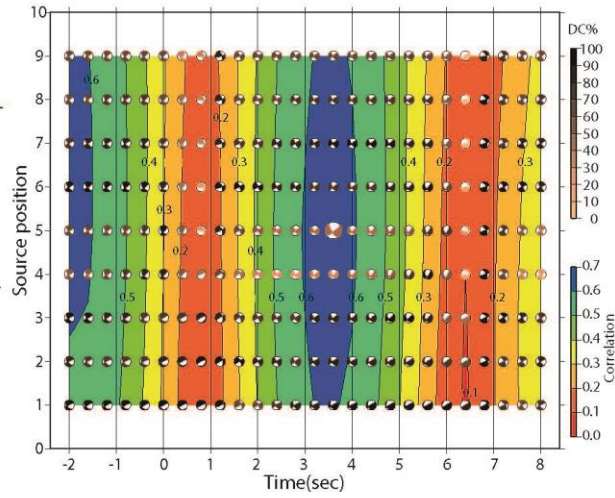
Origin time 20150328 05:04:15.09  
 Lat 38.8895 Lon 35.6162 Depth 4.9

Moment (Nm): 6.894e+14  
 Mw: 3.8  
 VOL%: 0  
 DC%: 41.0  
 CLVD%: 59.0  
 Var.red.: (for stations used in inversion): 0.40  
 Corr.%: 70

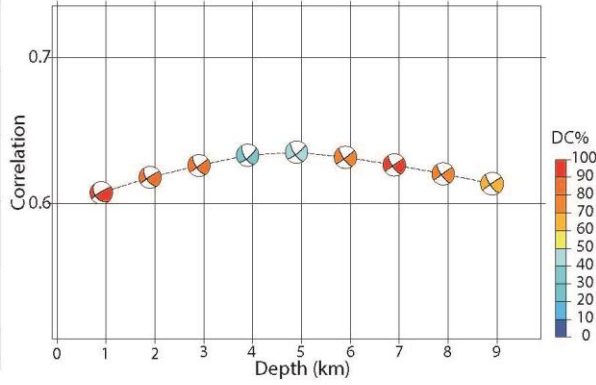
CN FMVAR STVAR  
 3.0 40±37 0.23

Strike Dip Rake Mrr Mtt Mpp  
 146 72 -170 -2.540 -4.673 7.213  
 Strike Dip Rake Mrt Mrp Mtp  
 53 80 -19 -1.200 -0.877 2.270

P-axis Azimuth Plunge Exponent (Nm): 14  
 9 20  
 T-axis Azimuth Plunge  
 101 6

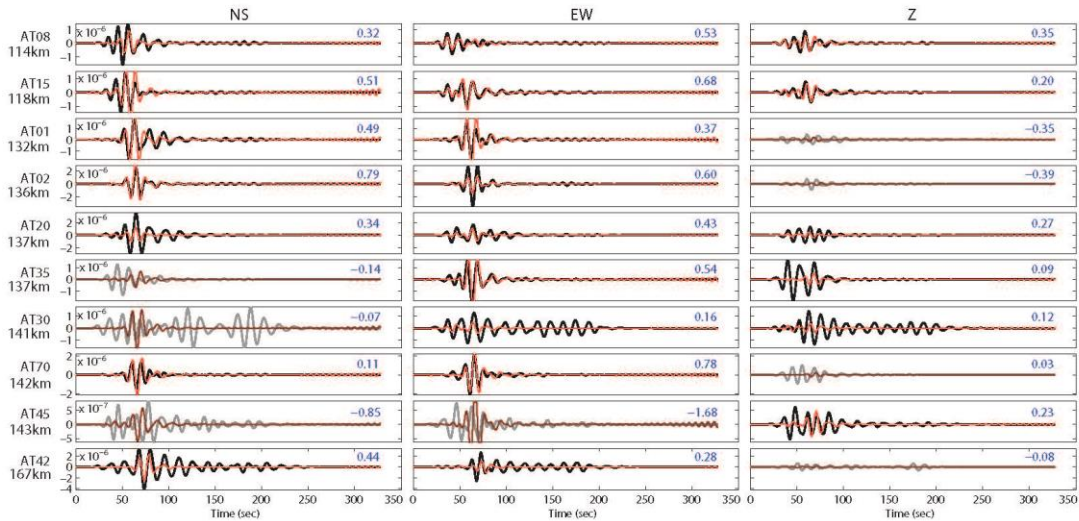


Correlation vs Depth Plot



Displacement (m). Inversion band (Hz) 0.06 - 0.12

— Observed  
 — Synthetic  
 Gray waveforms weren't used in inversion.  
 Blue numbers are variance reduction



**EVENT#29**

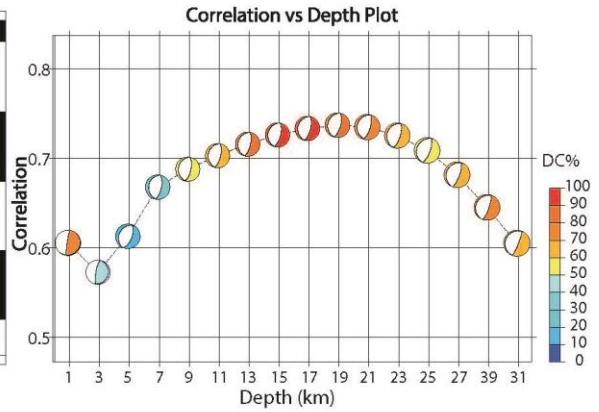
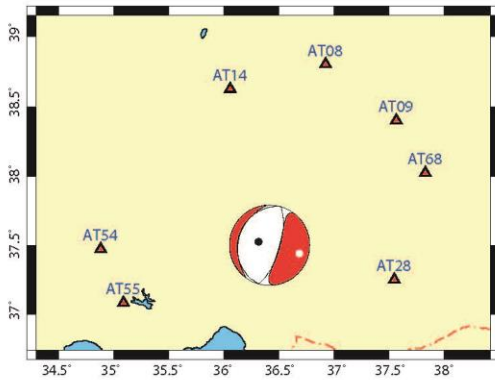
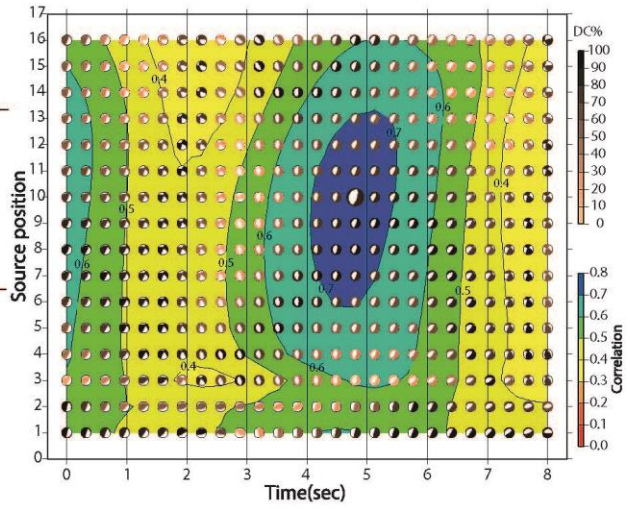
Origin time 20150328 10:08:16.10  
 Lat 37.482 Lon 36.4072 Depth 18.9

Moment (Nm) : 3.811e+15  
 Mw : 4.3  
 VOL% : 0  
 DC% : 80.1  
 CLVD% : 19.9  
 Var.red.: (for stations used in inversion): 0.54  
 Corr.% : 80

CN FMVAR STVAR  
 3.3 8±5 0.14

Strike Dip Rake Mrr Mtt Mpp  
 16 69 -90 -2.354 -0.170 2.524  
 Strike Dip Rake Mrt Mrp Mtp  
 195 21 -90 -0.761 -2.703 0.816

P-axis Azimuth Plunge Exponent (Nm): 15  
 286 66  
 T-axis Azimuth Plunge  
 106 24



Displacement (m). Inversion band (Hz) 0.07 – 0.11

— Observed  
 — Synthetic  
 Gray waveforms weren't used in inversion.  
 Blue numbers are variance reduction

